

STUDY OF HOMOGENEOUS THERMAL DECOMPOSITION OF TRIETHYLGALLIUM,  
TRIETHYLALUMINUM WITH AMMONIA AND TUNGSTEN DIMETHYLHYDRAZIDO  
COMPLEX USING *IN SITU* RAMAN SPECTROSCOPY AND COMPUTATIONAL  
CHEMISTRY

By

JOOYOUNG LEE

A DISSERTATION PRESENTED TO THE GRADUATESCHOOL  
OF THE UNIVERSITY OF FLORIDA IN PARTIAL FULFILLMENT  
OF THE REQUIREMENTS FOR THE DEGREE OF  
DOCTOR OF PHILOSOPHY

UNIVERSITY OF FLORIDA

2011

© 2011 Jooyoung Lee

To my parents, wife and son

## ACKNOWLEDGMENTS

First of all, I'd like to thank God. Whatever I do and however I do, He has been with me.

I have been pleased to work with Dr. Anderson including all group members. Dr. Anderson always has kept his eyes on my research and has encouraged the progress. Due to his belief in my studies, I could finish my doctoral research. I have enjoyed discussion with group members and that always gives me good ideas and breakthroughs. The morning coffee with them refreshes my thinking and gives me energy to work efficiently.

I feel five years in Gainesville is very short. My wife, Hankyung Seong, always has given encouragement and energy to my research and I'd like to dedicated this dissertation to her. My only son, Geon, has been everything to my family and I hope five years of Gainesville life would be his blessings from the heavenly God.

## TABLE OF CONTENTS

	<u>page</u>
ACKNOWLEDGMENTS.....	4
LIST OF TABLES.....	8
LIST OF FIGURES.....	10
LIST OF ABBREVIATIONS.....	15
ABSTRACT .....	18
INTRODUCTION.....	20
APPLICATIONS OF RAMAN SCATTERING TO GAS PHASE DECOMPOSITION REACTIONS.....	24
Theoretical Background of Raman Scattering .....	25
Classical Theory of Raman Scattering .....	26
Selection Rule .....	27
Raman Scattering Intensity and Cross-section.....	28
Signal-to-Noise.....	30
CVD Reactor with Raman Spectrometer .....	31
Reactor Setup .....	31
Characteristics of Spectroscopic System .....	32
Applications of Raman Scattering.....	34
Gas Phase.....	34
Temperature determination.....	34
Concentration measurement.....	39
Liquid Phase.....	40
Solid Phase .....	42
Summary .....	47
COMPUTATIONAL CALCULATIONS .....	59
Vibrational Frequency .....	61
Classical Approach.....	61
Quantum Mechanical Approach .....	62
Potential Energy Surfaces .....	65
Thermodynamic Properties.....	66
Contribution from Translation .....	66
Contribution from Electronic Motion .....	67
Contribution from Rotational Motion .....	67
Contribution from Vibration.....	68
Kinetic Parameters .....	69

Theoretical Raman Intensity and Absolute Differential Raman Cross-section .....	72
The Selection of Basis Set.....	74
<b>REACTOR MODELING AND PARAMETER ESTIMATION .....</b>	<b>83</b>
Mathematical Description of CVD Reactor.....	84
Parameter Estimation .....	86
Solving Inverse Problem Using Optimization Algorithm.....	91
Summary .....	93
<b>INVESTIGATION OF THE THERMAL DECOMPOSITION OF TRIETHYLGALLIUM USING IN SITU RAMAN SPECTROSCOPY AND DFT CALCULATIONS .....</b>	<b>103</b>
Overview.....	103
Experimental and Theoretical Methods.....	104
Results and Discussion.....	109
TEGa Thermal Decomposition Experiments Using <i>in situ</i> Raman Spectroscopy .	113
The Comparison of DFT Calculation with Experimental Results.....	115
Concluding Remarks.....	116
<b>HOMOGENEOUS THERMAL DECOMPOSITION STUDIES OF TRIETHYLALUMINUM (TEAL): EFFECT OF NH<sub>3</sub>.....</b>	<b>127</b>
Overview.....	127
Experimental and Theoretical Methods.....	128
Results and Discussion.....	130
Homogeneous TEAI Thermal Decomposition Experiments.....	130
DFT Calculations.....	134
The Comparison of Experimental Results with DFT Calculations .....	136
Concluding Remarks.....	137
<b>EXPERIMENTAL AND COMPUTATIONAL STUDIES OF THE HOMOGENEOUS THERMAL DECOMPOSITION OF THE TUNGSTEN DIMETHYLHYDRAZIDO COMPLEX CL<sub>4</sub>(CH<sub>3</sub>CN)W(NNME<sub>2</sub>) DURING DEPOSITION OF WN<sub>x</sub>C<sub>y</sub> THIN FILMS .....</b>	<b>145</b>
Overview.....	145
Experimental and Theoretical Methods.....	146
Results and Discussion.....	148
Kinetics of Acetonitrile Dissociation from 1a.....	148
Ion Cyclotron Resonance Experiments .....	148
<i>In situ</i> Raman Experiments .....	149
DFT Calculations.....	151
Comparison of Experimental Results with DFT calculations .....	153
Concluding Remarks.....	158
<b>DESIGN, SIMULATION AND SETUP OF ULTRA HIGH VACUUM SYSTEM FOR SURFACE SCIENCE AND ITS APPLICATION .....</b>	<b>171</b>

Overview.....	171
Characterization of Surface Kinetics in UHV.....	172
Temperature Programmed Desorption (TPD) .....	172
Low Electron Energy Diffraction (LEED) .....	173
Auger Electron Spectroscopy (AES) .....	174
Attenuated Total Reflection Using FTIR Spectroscopy (ATR-FTIR).....	175
Current state of ATR-FTIR technique .....	175
FT-IR (Fourier Transform Infrared) spectroscopy .....	176
Applications of ATR-FTIR technique to thin film research.....	177
UHV System Design and Sample Probe Simulation Using CFD Software .....	182
UHV System Design.....	182
Sample Probe Simulation Using CFD Software .....	183
CONCLUSIONS AND RECOMMENDATIONS .....	198
LIST OF REFERENCES .....	201
BIOGRAPHICAL SKETCH.....	212

## LIST OF TABLES

<u>Table</u>		<u>page</u>
2-1	Absolute differential Raman scattering cross-section of the vibrational-rotational band of gas-phase nitrogen of Q-branch .....	49
2-2	Absolute differential Raman scattering cross-section of widely used liquids using the laser wavelength of 514.5nm .....	50
2-3	Selected principal plasma lines in the argon ion laser .....	51
2-4	Vales of rotational constant $B_0$ and centrifugal distortion $D_0$ for nitrogen and oxygen from Butcher <i>et al.</i> [21].....	53
2-5	Vales of $\chi$ and $B_e / \omega_e$ for various simple diatomic molecules .....	53
2-6	Raman shifts for single wall carbon nanotubes in two kinds of organic solvents .....	57
2-7	Observed Raman shift of CuInSe <sub>2</sub> nanopowder and proposed assignment.....	57
2-8	Penetration depth according to laser wavelength in Si, Ge, Si <sub>0.78</sub> Ge <sub>0.22</sub> , 4H-, 6H-SiC and CdS .....	58
3-1	Rotational symmetry numbers for molecular point groups[62].....	78
4-1	Dimensionless groups in modeling equations .....	95
4-2	Comparison of experimental and kinetic theory derived diffusivities for H <sub>2</sub> -gas pairs and collision diameters.....	95
4-3	Deviations of heat capacity between experimental and calculated values .....	97
4-4	A-factor and activation energy value of homolysis and $\beta$ -hydride elimination reaction before and after optimization .....	101
5-1	Experimental and calculated rate parameters for first ethyl group dissociation	118
5-2	Reported relative Raman cross section for group II, III metal-organic sources	119
5-3	Computed enthalpies, entropies and Gibbs free energies for selected gas-phase decomposition reactions .....	121
5-4	Calculated and corrected Raman active Ga-C stretching frequencies only for the symmetric motions.....	126
6-1	Calculated and corrected Raman active stretching frequencies.....	143

7-1	Experimental and computationally optimized bond lengths (Å) and bond angles (°) for complex 1a.....	164
7-2	Calculated bond dissociation enthalpy ( $\Delta H^\circ$ ) and Gibbs energy change ( $\Delta G^\circ$ ) for the W-N1 and N1-N2 bonds .....	166
7-3	Calculated and corrected Raman active stretching frequencies.....	170
8-1	The thermal properties used in CFD simulation.....	192
8-2	The temperature difference between both ends of Si wafer according to each design.....	195

## LIST OF FIGURES

<u>Figure</u>		<u>page</u>
2-1	Comparison of three most widely used spectroscopic methods .....	48
2-2	Jablonski energy level diagram for typical IR and Raman scattering. The line thickness is roughly proportional to the signal strength .....	48
2-3	A graphical representation of 1 steradian .....	49
2-4	Raman scattering results of pure liquid benzonitrile in the range of 500 ~ 1150 cm <sup>-1</sup> .....	50
2-5	Schematic drawing of the chemical vapor deposition reactor for <i>in situ</i> Raman spectroscopic measurements .....	51
2-6	A schematic diagram of a Raman spectroscopic system .....	52
2-7	Conventional schematic diagram of photomultiplier tube .....	52
2-8	Conventional diagram of a CCD .....	53
2-9	Temperature determination process.....	54
2-10	Overlapped rotational Raman spectra of nitrogen and ammonia, and the rotational Raman spectrum of ammonia.....	55
2-11	Raman scattering measurement for single wall carbon nanotubes .....	56
2-12	Raman spectrum of CuInSe <sub>2</sub> nanopowder measured at room temperature .....	57
3-1	Potential energy diagram of simple harmonic oscillator.....	76
3-2	Potential energy diagram for harmonic and anharmonic oscillator .....	76
3-3	Morse potential. (D <sub>e</sub> -D <sub>o</sub> ) means zero-point energy .....	77
3-4	Example of potential energy surface with two variables. Figure was taken from Ref. [79].....	77
3-5	Relative energy diagram according to the change of rotation angle of ethyl group in triethylgallium.....	78
3-6	The nature of simple reaction including transition-state A <sup>‡</sup> .....	79
3-7	The first β-hydride elimination process of triethylgallium with geometry optimized transition state using B3LYP/LanL2DZ level of chemistry .....	79

3-8	Comparison of experimental and simulated results .....	80
3-8	Continued .....	82
4-1	Experimental and calculated heat capacity .....	96
4-2	Simulated temperature contours (unit is shown as °C) and streamlines and concentration contours in the reactor .....	98
4-3	Radial triethylgallium temperature and concentration profile at different axial positions .....	99
4-4	Optimization process using genetic algorithm followed by simplex method for solving inverse problem .....	100
4-4	Continued .....	101
4-5	Concentration and temperature profile of gas phase triethylgallium.....	102
5-1	Schematic of the experimental reactor for <i>in situ</i> Raman spectroscopic measurements.....	118
5-2	Recorded Ga–C <sub>3</sub> vibrational measurement of 490cm <sup>-1</sup> line.....	119
5-3	Schematized TEGa structure and energetics during first β–hydride elimination with Wiberg indices.....	120
5-4	Schematics of β–hydride elimination transition state structures .....	122
5-5	Calculated energetics of the two major thermal decomposition pathways of TEGa with reaction enthalpies [kcal/mol] listed .....	122
5-6	17 screened reaction pathways out of 34 with reaction enthalpies [kcal/mol] listed .....	123
5-7	Raman spectrum of gas-phase TEGa. Different horizontal line means different height measurement along the centerline.....	123
5-8	Simulated and experimental concentration profile of TEGa in the reactor.....	124
5-9	Optimized values of rate parameters of two main reactions for activation energy and A-factor (pre-exponential factor) .....	125
6-1	(Color online) Schematic drawing of the CVD reactor interfaced with <i>in situ</i> Raman spectrometer .....	139
6-2	(Color online) Raman spectrum of gas-phase TEAI .....	139
6-3	(Color online) Raman spectrum of gas-phase TEAI with ammonia .....	140

6-4	(Color online) Measured and simulated temperature and ammonia concentration profile (with and without reaction) in CVD reactor .....	140
6-5	Wiberg indices tracking of C <sub>2</sub> H <sub>6</sub> elimination from TEAI:NH <sub>3</sub> adduct.....	141
6-6	(Color online) Relative energy diagram of C <sub>2</sub> H <sub>6</sub> elimination from TEAI:NH <sub>3</sub> adduct (Energies in parenthesis are from Ref.[124]) .....	141
6-7	(Color online) Relative energy diagram of C <sub>2</sub> H <sub>6</sub> elimination in the case of excess ammonia (Energies in parenthesis are from Ref. [124]) .....	142
6-8	(Color online) Simulated tetramer and hexane formation from H <sub>2</sub> Al-NH <sub>2</sub> with enthalpy change and free energy change ( <u>underlined</u> ) at 298K .....	142
6-9	(Color online) Comparison of Raman spectra at 2840cm <sup>-1</sup> for two cases, without ammonia and with ammonia .....	144
6-10	Proposed overall decomposition mechanism from neat TEAI and TEAI with ammonia experiment (Et = ethyl group; -C <sub>2</sub> H <sub>5</sub> ).....	144
7-1	Schematic of the nebulizer-assisted experimental reactor for <i>in situ</i> Raman spectroscopic measurements .....	159
7-2	Plot of ln(k/T) vs. 1/T(K) for acetonitrile exchange in complex <b>1a</b> .....	160
7-3	Raman spectra of gas-phase dimethylhydrazido complex <b>1a</b> in benzonitrile as a function of distance below the heated susceptor .....	161
7-4	Relative species concentration and gas phase temperature profiles along the reactor centerline for benzonitrile (BN), <b>1b</b> , and <b>2</b> .....	162
7-5	Peak deconvolution results.....	163
7-6	Liquid Raman spectra of <b>1a</b> in benzonitrile solution (red) compared to pure liquid benzonitrile (black) .....	164
7-7	Computationally optimized geometry of <b>1a</b> .....	165
7-8	Products of cleavage of the W–N1 and N1–N2 bonds of complex <b>2</b> . Gibbs energy values ( $\Delta G^\circ$ ) are in kcal/mol .....	165
7-9	Limiting resonance structures of complexes <b>1a</b> and <b>1b</b> .....	166
7-10	Wiberg bond indices for <b>1a</b> and <b>1b</b> .....	166
7-11	Gibbs energy change ( $\Delta G^\circ$ ) for initial ligand substitution and dissociation reactions of complex <b>1</b> . All energy values are in kcal/mol at 298 K .....	167

7-12	Production of dimethylaminyl radical ( <b>3</b> ) after W–N1 cleavage to form <b>5</b> . Gibbs energy values are in kcal/mol.....	167
7-13	Known reactions of dimethylaminyl radicals and their calculated (B3LYP/LanL2DZ) reaction energies at 298 K.....	168
7-14	Suggested evolution of an atomized droplet as it approaches a heated susceptor.....	168
7-15	Detected Raman spectrum profile assigned to phenyl breathing mode of benzonitrile (1003 cm <sup>-1</sup> ).....	169
8-1	Desorption rate of argon from tungsten for various values of the incident ion energy. (taken from Ref. [163]).....	185
8-2	A multiple reflection ATR system (Figure was taken from Ref.[182]).....	185
8-3	Various types of ATR-FTIR system .....	186
8-4	Fluoride-based etching conditions, leading to hydride-terminated flat and porous silicon surfaces. (Figure was taken from Ref. [183]) .....	186
8-5	Internal reflection spectra of HF-treated Si(111) surfaces (Figure was taken from Ref. [184]).....	187
8-6	Ge-H vibrations observed by ATR-FTIR. Surfaces prepared by etching 10% HF solution. (Figure was taken from Ref. [170]) .....	187
8-7	[2+2] cyclo additions on Si surface, possible models for adsorption of ethylene and FTIR spectra for <i>cis</i> - and <i>trans</i> -1,2-dideuteroethylene .....	188
8-8	Si-H IR vibrational modes for the initial surface and after various precursor exposure doses of TDEAHf at 25 and 250 °C .....	188
8-9	Calculated vibrational spectra for the species present in the H transfer process and for surface species in the Si-H abstraction process .....	189
8-10	A time series of IR absorbance spectra of c-H and Si-H stretching vibrational modes. (Figure was taken from Ref. [178]) .....	190
8-11	Saturation infrared spectra of ED/Ge, PD/ED/Ge, ED/PD/ED/Ge, and PD/ED/PD/Ge, schematic illustration of PD on Ge and second layer reaction .	190
8-12	Proposed decomposition mechanism for Ti(O-iPr) <sub>2</sub> (dpm) <sub>2</sub> on a Pt surface. (Figure was taken from Ref. [179]) .....	191
8-13	Four chamber UHV system and process flow diagram.....	191

8-14	Perspective view of CAD drawing for deposition chamber, ATR-FTIR chamber and analysis chamber.....	192
8-15	Proposed design of sample probe for perspective view, CFD simulation profile, and beveled edge Si wafer .....	193
8-16	Temperature profile simulations at 1000 K for the modified designs .....	194
8-17	Quadrangular grid mesh for Fig. 8-16E .....	195
8-18	CAD drawing of sample probe for perspective, front, side, and top view.....	196
8-19	CAD drawing of designed UHV system .....	197

## LIST OF ABBREVIATIONS

AACVD	Aerosol-assisted Chemical Vapor Deposition uses aerosol produced by nebulizer or high pressure spraying system as low vapor pressure reactant delivery method.
Ab initio	Ab initio is Latin word and it means “from the beginning”. In quantum chemistry, ab initio method means basic and fundamental laws of nature that doesn’t count on additional assumptions or models.
AES	Auger Electron Spectroscopy
ATR	Attenuated Total Reflection
Basis set	A set of MO functions that is used to create the molecular orbitals. Typically these functions are combined with atomic orbitals. There are several categories according to type of fundamental function such as minimal basis set (STO-nG; n=3, 4, 6), split valence basis set, and Pople basis set (3-21G, 6-31G, 6-311+G*).
CCD	Charge Coupled Device
CFD	Computational Fluid Dynamics
CH	Chalcopyrite
CVD	Chemical Vapor Deposition. CVD is a chemical process that is used to deposit high-purity, high-performance solid film materials.
DFT	Density functional theory. DFT is a quantum chemical modeling method used in physics and chemistry to simulate the electronic structure of N-body systems.
DMABEE	4-(dimethylamino)benzoate
FEM	Finite Element Method is a numerical technique to find solutions of partial differential equations. It is also known as FEA (Finite Element Analysis). FEM can provide good method to find solutions for complicated domains, especially for changing or moving domains.
FIB	Focused ion beam
FT-IR	Fourier Transform-Infrared
FWHH	Full width at half-height
HEMT	High Electron Mobility Transistor

HF	Hartree-Fock method is an approximate technique for determining the ground-state wave function and ground-state energy of a quantum many-body system. Hartree-Fock method assumes that $N$ -body wave function can be simplified by a single Slater determinant.
IRC	Internal reaction coordinate is a simplified one dimensional diagram that represents reaction progress along with reaction process.
IRE	Internal Reflection Element
LED	Light Emitting Diode
LEED	Low Electron Energy Diffraction
LOD	Limit of Detection is the lower limit of detection of species.
LOQ	Limit of Quantitation is the smallest concentration of a measuring unit that can be reliably measured by an analytical procedure.
LO mode	Longitudinal mode is a particular electromagnetic field pattern of radiation or crystal vibration measured along with the propagation direction.
MOCVD	Metalorganic Chemical Vapor Deposition is one of CVD technique using metalorganic precursors.
MP	Møller-Plesset Perturbation theory is a post Hartree-Fock ab initio method. It is improved by adding electron correlation to HF method.
NA	Numerical aperture
NBO	Natural Bond Orbital. The orbital which is formed from natural hybrid orbital (definition by IUPAC).
Nd:YAG	Neodymium doped yttrium aluminum garnet is a lasing medium for a solid state laser. The triply ionized Nd replaces yttrium in the crystal of the YAG as dopant. Typically dopant concentration of Nd is around 1 at. %.
NIR	Near Infrared
NMR	Nuclear Magnetic Resonance
OFHC	Oxygen Free High Conductivity
PCM	Polarized Continuum Model

PES	Potential Energy Surface
PL	Photoluminescence
PMT	Photo Multiplier Tube is a sensitive photon detector multiplying the number of photons as much as $10^8$ .
QMS	Quadrupole Mass Spectroscopy is a method of mass analysis using four highly parallel circular rods to detect mass to charge ratio.
SCF	Self-consistent Field is another term for the Hartree-Fock method.
TDEAHf	Tetrakis(diethylamino) hafnium; $\text{Hf}[\text{N}(\text{C}_2\text{H}_5)_2]_4$
TDMAHf	Tetrakis(dimethylamino) hafnium; $\text{Hf}[\text{N}(\text{CH}_3)_2]_4$
TEAI	Triethylaluminum; $(\text{C}_2\text{H}_5)_3\text{Al}$
TEGa	Triethylgallium; $(\text{C}_2\text{H}_5)_3\text{Ga}$
TEIn	Triethylindium; $(\text{C}_2\text{H}_5)_3\text{In}$
TMAI	Trimethylaluminum; $(\text{CH}_3)_3\text{Al}$
TO mode	Transverse mode is a particular electromagnetic field pattern of radiation or crystal vibration measured in a plane perpendicular to the propagation direction.
TPD	Temperature Programmed Desorption
TPRS	Temperature Programmed Reaction Spectroscopy
UHV	Ultra High Vacuum means the pressure $< 10^{-10}$ Torr.
XPS	X-ray Photoelectron Spectroscopy

Abstract of Dissertation Presented to the Graduate School  
of the University of Florida in Partial Fulfillment of the  
Requirements for the Degree of Doctor of Philosophy

STUDY OF HOMOGENEOUS THERMAL DECOMPOSITION KINETICS OF  
TRIETHYLGALLIUM, TRIETHYLALUMINUM WITH AMMONIA AND TUNGSTEN  
DIMETHYLHYDRAZIDO COMPLEX IN CVD REACTOR USING IN SITU RAMAN  
SPECTROSCOPY AND COMPUTATIONAL CHEMISTRY

By

Jooyoung Lee

August 2011

Chair: Timothy J. Anderson  
Major: Chemical Engineering

The gas phase thermal decomposition pathways for the metal-organic precursor of TEGa ( $(C_2H_5)_3Ga$ , Triethylgallium) were followed using *in situ* Raman spectroscopy in an up-flow, cold-wall CVD (Chemical Vapor Deposition) reactor. Raman shift located at  $490\text{cm}^{-1}$ ,  $517\text{cm}^{-1}$ ,  $537\text{cm}^{-1}$ , and  $555\text{cm}^{-1}$  were assigned to the vibrational frequencies between gallium and the  $\alpha$ -carbon of  $(Et)_3Ga$ ,  $(DEGa)_2$ ,  $(Et)GaH-Ga(Et)_2$  and  $(Et)GaH-GaH_2$ , respectively. DFT (Density Functional Theory) calculations were in good agreement with experimental observations. Identification of intermediates by Raman spectroscopy confirmed that both  $\beta$ -hydride elimination and homolysis homogeneous thermal decomposition reactions occur under the reactor conditions. The mass transport simulation using the finite element method supports the presence of both reactions. In addition to the peak assignments, DFT calculations using the B3LYP/LanL2DZ (Becke, three-parameter, Lee-Yang-Par/Los Alamos National Laboratory 2-Double-Zeta) model chemistry were performed to screen 17 envisioned routes from 34 reactions.

Homogeneous thermal decomposition pathways for triethylaluminum ( $(C_2H_5)_3Al$ ; TEAI) were investigated. Raman scattering experiments were performed on TEAI neat and in the presence of ammonia in the reactor. Raman shifts were observed for the decomposition products TEAI:NH<sub>3</sub>, DEAIH, TEAI:NH<sub>3</sub> TS, H<sub>2</sub>N-AlH-NH-AlH<sub>2</sub>, H<sub>2</sub>Al-NH<sub>2</sub>, MEAIH<sub>2</sub>, MEAIH-AlH<sub>2</sub> and DEAI-AlH<sub>2</sub>. DFT calculations using the B3LYP/LanL2DZ level of theory were carried out to optimize the geometry of each intermediate and likely transition structures to estimate activation energies.

The gas-phase decomposition pathways of the tungsten dimethylhydrazido complexes Cl<sub>4</sub>(RCN)W(NNMe<sub>2</sub>) (**1a**: R=CH<sub>3</sub>; **1b**: R=Ph), precursors for single source deposition of WN<sub>x</sub>C<sub>y</sub>, were investigated using a combination of Raman scattering experiments and DFT calculations. DFT calculations (B3LYP/LanL2DZ) were used to estimate Raman active frequencies and explore the reaction surface. Dimethylamine and methylmethylenimine, products from N-N cleavage of the hydrazido ligand, were observed under deposition conditions and identified by comparison with previously reported Raman shifts and calculated frequencies. Combining experimental thermal decomposition studies by Raman spectroscopy with DFT calculations and FEM (Finite Element Method) reactor modeling is a powerful approach for quantitative CVD kinetics analysis.

## CHAPTER 1 INTRODUCTION

When the semiconductor industry bloomed, Gordon Moore predicted a long-term trend in computing hardware, so called Moore's law[1]. Moore's law suggests that the number of transistors that can be placed onto an integrated circuit will double every two years. Although various semiconductor materials and devices were devised, new applications motivate the search for new semiconductor materials. Recent applications include light emitting devices, power electronics, and Cu metalgates ICs (Integrated Circuits). These potential new applications have spurred the development of compound semiconductors formed by combining elements from group III and group V or ones from group II and group IV.

Amongst a large spectrum of applications for compound semiconductors, optoelectronic compound semiconductor devices that covers blue and green LEDs (Light Emitting Diodes) and UV (Ultraviolet) light detectors are two of the most important areas. After group III-nitrides semiconductors proved their superiority over II-VI semiconductor (e.g. ZnSe), they have been under intensive research and development.

The bandgaps of InN, GaN, and AlN are 0.7[2], 3.4[3], and 6.2 eV [4], respectively, which span the UV and the full visible ranges. This suggests that one can select bandgap energy when alloyed by manipulating the composition of In, Ga, and Al (e.g.  $\text{Al}_x\text{Ga}_y\text{In}_{1-x-y}\text{N}$ ). Moreover, group III-nitrides have good thermal conductivity, chemical stability, and high mechanical strength[5]. Based on the outstanding physical properties of group III-nitrides, a range of devices has been developed, including LEDs, detectors, lasers, and transistors.

Amongst a large number of film growth technologies, metalorganic chemical vapor deposition (MOCVD hereafter) is the most widely used technique for many materials. However, most MOCVD film growth results have been empirical, focused on film quality with variation in reaction conditions such as the III/V ratio and growth temperature. This is a long and expensive route to optimizing growth conditions. Supplementing experimental results with modeling would be more efficient, but kinetics are necessary. Unfortunately the MOCVD reaction mechanism and associated rate parameter (reaction order, rate constant, and activation energy) are not well known. There are a few examples, however, in the literature[6-9]. It should be noted that several obstacles, for example, homogeneity of reactions, physical sampling of reactant, non-intrusive temperature measurement, and wall deposition in flow reactors must be addressed.

In this study, MOCVD kinetics for triethylgallium (TEGa), triethylaluminum (TEAl) and the dimethylhydrazido tungsten complex are investigated using *in situ* Raman spectroscopy. Raman spectroscopy is a nondestructive probe similar to infrared spectroscopy. It can detect reactants, reaction intermediates and products during film growth and gather information from Raman signal to estimate temperature. Although Raman spectroscopy is less sensitive than infrared, it can detect an induced dipole of a molecule and measure local temperature remotely with high accuracy.

This study consists of eight chapters including this chapter. In Chapter 2, the characteristics of Raman scattering and its relationship with CVD are described. Details of gas phase temperature measurements in the reactor and concentration measurements for gas phase chemical species, as well as Raman applications for gas, liquid, and solid phase research with experimental results are also described. Chapter

3 gives an overview of the procedures and techniques for applying computational chemistry to interpret Raman spectra. In this chapter, practical quantum chemical calculations used for Raman cross section, calculation of vibrational frequency, thermodynamic properties that contain molecular motions such as rotational, translational, vibrational and electronic motions, and potential energy surfaces are covered. In the next two chapters, two group III metal alkyls that used in chemical vapor deposition of group III-V compound semiconductors.

In Chapter 4, CVD reactor modeling and parameters estimation are carried out. Computational chemistry with an appropriate method and basis set is used to obtain fundamental reaction or thermodynamic parameters for reaction intermediates. Data from Raman scattering experiment are optimized by simplex and genetic algorithms. In Chapter 5, the behavior of triethylgallium ( $\text{Ga}(\text{C}_2\text{H}_5)_3$ ) in CVD reactor is examined. Both homolysis and  $\beta$ -hydride elimination are considered and the activation energy and pre-exponential factor are estimated for the first Ga-C bond breakage of triethylgallium. The measured and simulated parameters are optimized using a FEM reactor model. In Chapter 6, the gas phase thermal decomposition of triethylaluminum ( $\text{Al}(\text{C}_2\text{H}_5)_3$ ) with and without ammonia in CVD reactor is studied.

In the next chapter, the thermal decomposition of a low volatility organometallic compound is examined. The tungsten dimethylhydrazido complex ( $\text{Cl}_4(\text{CH}_3\text{CN})\text{W}(\text{NNMe}_2)$ , “**1a**” hereafter) is of interest for deposition of WN, which has potential as a diffusion barrier in Cu metallization[10]. To investigate the behavior and decomposition mechanism of **1a**, experiments and quantum chemical calculations are performed.

This chapter also includes a brief review of temperature programmed desorption (TPD), low electron energy diffraction (LEED), Auger electron spectroscopy (AES) and a detailed review of attenuated total reflection using FT-IR (Fourier Transform Infrared). To assist design of the UHV system, commercial CFD (Computational Fluid Dynamics) software is used to optimize and verify the temperature distribution of a rotatable sample probe. In chapter 9, this thesis is concluded and recommendations for future studies are given.

## CHAPTER 2

### APPLICATIONS OF RAMAN SCATTERING TO GAS PHASE DECOMPOSITION REACTIONS

Raman scattering has been studied for over 70 years and its applicability to material characterization and chemical analysis has been demonstrated for a variety of systems. In particular, there has been a considerable use of Raman scattering to study gas phase reactions.

Some advantages of Raman spectroscopy over Infrared spectroscopy include easy preparation of sample, the ability to obtain higher spatial resolution from visible light instead of infrared light, and the ability to identify molecules. For the gas phase kinetics research, Raman spectroscopy shows the strength especially in homonuclear species such as N<sub>2</sub>, O<sub>2</sub>, H<sub>2</sub>. These species do not appear in infrared spectroscopy since those are symmetric molecules. Moreover, Raman shows good spatial resolution, although infrared has the resolution no better than 4 cm<sup>-1</sup>. And the visible laser used for Raman can be focused more tightly than infrared beams since it is visible. Typically, the cross section for Raman scattering and IR (Infrared)absorption are in the order of 10<sup>-29</sup> and 10<sup>-18</sup>cm<sup>2</sup>, respectively. Recent technological advances such as low noise multichannel detectors and efficient spectrographs,have boosted the Raman signal strength by ~10<sup>4</sup>, thus increasing its sensitivity.

Among various techniques that probe molecular vibrations, FTIR is the oldest and most developed technique. FTIR spectra have narrow line widths and rich spectral detail, i.e. a distinguishable fingerprint. Currently, FTIR instrumentation is highly refined due to its widespread use, however, it has some disadvantages. Mid-IR light cannot penetrate many common optical material, thus it has sampling difficulty. Due to the time consuming and/or destructive sample preparation as a KBr pellet, Nujol null, and the

like, application of FTIR can be interrupted. Although NIR (Near Infrared) is not as informative as FTIR, NIR has many advantages, for example, noninvasive measurement, simplicity of sampling, and remote sampling with fiber optic cable[11]. The comparison of Raman scattering with FTIR and NIR is schematized in Fig. 2-1.

In this chapter, the theory of Raman scattering for an experimental view point is described and its applications to the three phases (gas, liquid and solid) are discussed for the methodology of following experimental chapters. Lastly, the CVD reactor system that is interfaced with the Raman spectrometer is described in detail.

### **Theoretical Background of Raman Scattering**

In 1928, Indian physicist Raman discovered that a very small portion of light is scattered off from the molecules as red-shifted or blue-shifted, and the frequency difference between the incident light (at frequency  $v_L$ ) and scattered light (at frequency  $v_0$ ) equals to the molecular vibrational frequency,

$$v_L = v_L' \pm v_0 \quad (2 - 1)$$

In other words, if the frequency or wavelength of the scattered light is analyzed, not only is the incident light wavelength seen (i.e., Rayleigh scattering), but also a small amount of light that has scattered at some different wavelength (i.e., Stokes and Anti-Stokes Raman scattering). This phenomenon described above is called Raman effect and shown in Fig. 2-2.

Rayleigh scattering was named after Lord Rayleigh who described this process from the blue color of the sky. Depending on the vibrational state of the molecule, photons of light can have either higher or lower frequency by the Raman effect.

Based on these principles, there has been explosive progress in the field of Raman spectroscopy of materials with the invention of lasers in the 1960's. Today,

Raman scattering is one of the most powerful and widely-used tools for materials study in all fields, even in archaeology[12].

### Classical Theory of Raman Scattering

Assume a plane of electromagnetic wave is traveling along the positive direction of the z-axis. As a consequence of Maxwell's equations, such a wave has only transverse components. And thus the electric field intensity is given by

$$E_x = E_0 \cos(\omega t + \theta_x) \quad (2-2)$$

where  $\omega$  is the angular frequency. And it is noted that  $\omega = 2\pi\nu$ , where  $\nu$  is the frequency; that  $\nu = c/\lambda$  where  $\lambda$  is the wavelength. If the phase is not an issue, Eq.2-2 can be simplified as follows by replacing  $\theta_x$  with zero.

$$E_x = E_0 \cos(\omega t) \quad (2-3)$$

If an electric field,  $E$ , is applied to a molecule, the distribution of electrons is slightly changed and thus the dipole moment,  $P$ , is polarized. When the electromagnetic field is weak,  $P$  is proportional to the electric field intensity  $E$  and is given by:

$$P = \alpha E = E_0 \cos(\omega t) \quad (2-4)$$

where  $\alpha$  is polarizability tensor and has 9 components for three-dimensional space. According to the periodic vibration of a molecule,  $\alpha$  also has a periodic change as follows:

$$\alpha = \alpha_0 + \alpha_1 \cos(\omega_l t) \quad (2-5)$$

where  $\alpha_0$  and  $\alpha_1$  are the time-independent and time-dependent term, respectively. Eq. 2-6 results from inserting Eq. 2-5 into Eq. 2-4.

$$P = E_0 \cos(\omega t) E_0 \cos(\omega_0 t + \frac{1}{2} \alpha_1 \omega_l t) = \frac{1}{2} E_0^2 \alpha_1 (\cos(\omega - \omega_l)t + \cos(\omega + \omega_l)t) \quad (2-6)$$

The first term on the right-hand side (R.H.S) of Eq. 2-6 reflects Rayleigh scattering that is not affected by the change of polarizability tensor, the second term is for Stokes scattering and the third term expresses Anti-Stokes scattering.

### Selection Rule

Suppose a transition between two quantum states of a molecule, initial state,  $i$ , and final state,  $f$ . The wave functions of the initial and final state are expressed as  $\psi_i$  and  $\psi_f$ , respectively. When the relevant transition dipole moment  $\mu_{i,f}$  is non-zero, transition can be observed since dipole moment is given by:

$$\mu_{i,f} = \langle \psi_f | \hat{\mu} | \psi_i \rangle \quad (2-7)$$

Other than the form of Eq. (2-5), polarizability can be expanded as

$$\alpha_{ij} = (\alpha_{ij})_0 + \sum_k \left( \frac{\partial \alpha_{ij}}{\partial Q_k} \right)_0 Q_k + \frac{1}{2} \sum_{l,m} \left( \frac{\partial^2 \alpha_{ij}}{\partial Q_l \partial Q_m} \right)_0 Q_l Q_m + \dots \quad (2-8)$$

where  $Q_j$  denotes the normal coordinate of a vibration mode with frequency  $\nu_j$ .

By separating the vibrational and rotational motion from the electronic part, a space-fixed component of the polarizability tensor  $\alpha_{xy}$  can be expanded as the form given by:

$$\begin{aligned} [\alpha_{xy}]_{f,i} &= (\alpha_{xy})_0 \left\langle \prod_k \phi_f(Q_k) \middle| \prod_k \phi_i(Q_k) \right\rangle \\ &\quad + \sum_k \left( \frac{\partial \alpha_{xy}}{\partial Q_k} \right)_0 \left\langle \prod_k \phi_f(Q_k) \middle| Q_k \left| \prod_k \phi_i(Q_k) \right. \right\rangle \end{aligned} \quad (2-9)$$

where  $\phi_j$  denotes the vibrational wave function of quantum state  $j$ .

To proceed further, the following relations are required for harmonic oscillator functions:

$$\langle \phi_f(Q_k) | \phi_i(Q_k) \rangle = \begin{cases} 0 & \text{for } \nu_i \neq \nu_j \\ 1 & \text{for } \nu_i = \nu_j \end{cases} \quad (2-10)$$

and

$$\langle \phi_f(Q_k) | Q_k | \phi_i(Q_k) \rangle = \begin{cases} 0 & \text{for } \nu_i = \nu_j \\ b_k \sqrt{\nu_k^i + 1} & \text{for } \Delta \nu_k = 1 \\ b_k \sqrt{\nu_k^i} & \text{for } \Delta \nu_k = -1 \end{cases} \quad (2-11)$$

where  $b_k = h / 4\pi\omega$ .

Eq. 2-10 is for the Rayleigh scattering and the Raman selection rule is  $|\Delta \nu_k| = 1$  while the second and third case of Eq. 2-11 is for the Stokes and anti-Stokes Raman scattering, respectively[13].

### Raman Scattering Intensity and Cross-section

The intensity of a Raman line is closely related to the scattering cross-section of the transition between the two energy levels. And various factors such as scattering angle, temperature, and the wavelength of incident light are correlated with the intensity of Raman scattering. Taking into account the thermal population at temperature, T, and a  $90^\circ$  scattering angle, one can obtain following relation:

$$I_{rot} = NI_0 \left( \frac{d\sigma_{rot}}{d\Omega} \right) \quad (2-12)$$

where  $N$  is the number of scattered molecules,  $\sigma_{rot}$  is the rotational scattering cross-section,  $\Omega$  is the solid angle, and  $(d\sigma_{rot} / d\Omega)$  is called the differential cross-section[14].

The total scattering cross-section  $\sigma$  consists of numerous partial cross-sections, for instance,  $\sigma_{elastic}$ ,  $\sigma_{fission}$ , and  $\sigma_{\pi production}$ . Therefore, it should be noted that the total cross-section for a particular process is the integral over all angles of the differential cross-

section for that specific process. The direct measurement of absolute Raman scattering cross-section is challenging and laborious. To this end, using a relative Raman cross-section technique has been developed by many researchers for several decades. As for earlier efforts, Hyatt and his coworkers focused on establishing the absolute Raman cross-section for molecular nitrogen gas [15], and Fenner and his coworkers performed absolute measurement for some simple gases like N<sub>2</sub>, O<sub>2</sub>, H<sub>2</sub>, CO, NH<sub>3</sub>, CH<sub>4</sub>, C<sub>2</sub>H<sub>6</sub>, and C<sub>6</sub>H<sub>6</sub>[16]. The scattering cross section of the rotational lines of gas-phase hydrogen can be measured easily, since the optical anisotropy  $\gamma_0^2$  and its wavelength dependence are well known. The differential scattering cross-section of a Stokes rotational Raman line is expressed in the S-branch ( $\Delta J = 2$ ).

$$\frac{d\sigma_{rot}}{d\Omega} = \frac{16\pi^4}{45} (\nu_0 - \nu_{rot})^4 \frac{3(J+1)(J+2)}{2(2J+3)(2J+1)} 7\gamma_0^2 \quad (2-13)$$

Since the measured Raman intensity of a molecule is directly proportional to the absolute Raman cross-section as seen in Eq. 2-12, a useful and appropriate equation for species  $j$  versus nitrogen reference can be derived as follows:

$$\left( \frac{d\sigma_j}{d\Omega} \right) / \left( \frac{d\sigma_{N_2}}{d\Omega} \right) = \Phi(J) \frac{I_j}{I_{N_2}} \quad (2-14)$$

where  $\Phi(J)$  is the thermal population of the J-th level with a Boltzmann distribution.

$$\Phi(J) = \frac{N_j}{N_0} = \frac{g_J (2J+1) \exp(-F(J)hc/kT)}{\sum_{J=0}^{\infty} g_J (2J+1) \exp(-F(J)hc/kT)} \quad (2-15)$$

where  $g_J$  is the nuclear-statistics factor and  $F(J)$  is the term value for the J-th level.

After obtaining a firm base for simple gases, one can measure the relative Raman cross-section of target molecule with ease. For convenience, the results of the

measurements of the absolute differential Raman scattering cross-section of the Q-branch of nitrogen at  $2331\text{cm}^{-1}$  are tabulated in Table 2-1.

It should be noted that the wavelength dependence of Raman scattering cross-section is quite large since it has the  $(\nu_0 - \nu_j)^4$  dependence. The Raman scattering cross-section has units of  $\text{cm}^2/\text{sr}$ , where the sr is the SI unit of solid angle. The steradian(sr) is dimensionless and is the unit angle of the cone, it is depicted in Fig. 2-3.

Cross-sections in liquids are usually higher than those for the same vibration in gases by a factor of 2 to 4 and some reference values are tabulated in Table 2-2. Usually  $(d\sigma/d\Omega)$  is larger for molecules with extended  $\pi$ -systems, because the electrons in those molecules are more easily polarized whereas molecules with only single C–H, C–O, and C–C bonds have small cross-sections. Also multiple bond stretches have high  $(d\sigma/d\Omega)$  values.

### Signal-to-Noise

The noise in analytical spectroscopy is defined as the fluctuation in the signal level due to different causes. It is generally associated with the standard deviation, or the root mean square noise. Noise types can be shot and flicker, the former being proportional to the square root of the signal and the last being proportional to the signal. In a typical experiment, background, detector and readout noises add to the signal noise. Therefore, within the assumption of independent, non correlated noises, the total noise of the observed signal is defined as follows:

$$\text{Noise} = \sigma_y = \sqrt{(\sigma_s^2 + \sigma_B^2 + \sigma_d^2 + \sigma_r^2)} \quad (2-16)$$

where  $\sigma_s$ ,  $\sigma_B$ ,  $\sigma_d$  and  $\sigma_r$  are the standard deviation of signal, the background, dark signal, and readout noise, respectively. Normally the signal-to-noise ratio for the peak

intensity of a Raman signal is the average peak height,  $\bar{S}$ , divided by the total noise as defined above, i.e.,

$$\begin{aligned}\text{Signal-to-Noise Ratio} &= \frac{\bar{S}}{\sigma_y} \\ &= \frac{\bar{S}}{\sqrt{(\sigma_s^2 + \sigma_B^2 + \sigma_d^2 + \sigma_r^2)}}\end{aligned}\tag{2-17}$$

Generally, the limit of detection in quantitative analysis is often considered to be a signal-to- root mean square noise ratio of 3 for the concentration of the sample. It should be noted that the signal-to-noise ratio is calculated relative to the background, since it is this noise that determines the limit of detection. If a signal peak is below a certain background noise level, it is indistinguishable from the noise. In addition, if a peak is too weak, it cannot accurately be quantified. Therefore, the Limit of Detection (LOD) corresponds to the value over which a peak can be identified with a certain statistical confidence factor (usually 3). As an example for both detectable and quantifiable signals, a liquid benzonitrile Raman scattering measurement was performed using a liquid chamber with pure benzonitrile as shown in Fig. 2-4.

From the magnified inset, it can be seen that the peak noise intensity is 15 counts. The peak at  $929 \text{ cm}^{-1}$  has the intensity of 62 counts with a corrected baseline. In this context, signal-to-peak to peak noise ratio is 4.1 ( $=62/15$ ) and the S/N RMS is  $\sim 21$ .

### CVD Reactor with Raman Spectrometer

#### Reactor Setup

A schematic diagram of the chemical vapor deposition reactor used in this study is shown in Fig. 2-5. This CVD reactor is an up-flow, impinging jet, and cold-wall reactor which was custom-designed to study the gas-phase decomposition kinetics of

metalorganic precursors. Since quartz is optically transparent, the outermost body is constructed with optical flat quartz that is shaped as a rectangular parallelepiped. Inside of the parallelepiped reactor, there is a cylindrical reactor that is also made of quartz and it has four longitudinal narrow slits to secure beam pathways. This cylindrical arrangement permits a stable flow pattern in the reactor.

The inlet tube consists of three parts – center, annular and sweeping flows. Using three inlet tubes enables various combinations of reaction kinetic studies. For example, when triethylaluminum is introduced in the center inlet by nitrogen, as a carrier gas, and ammonia is introduced in the annulus inlet, one can study diffusivity between triethylaluminum and ammonia at specific temperatures, as well as aluminum nitride deposition mechanisms. Each tube is packed with 3mm glass beads confined by stainless steel screens to provide parallel flow streams. A metalorganic precursor is introduced through the center line via a N<sub>2</sub> carrier gas envelops the metal-organic gas to limit wall deposition of precursors that interrupts homogeneous reaction.

To help reach reaction temperatures, Boralectric® sample heating material provided by tectra GmbH is used for all experiments in this study. To prevent deposition on the heating material, the sample heater is enclosed with a ceramic cap and a Ni-Cr thermocouple measures the temperature of the sample heater and it is located between the heater and this ceramic enclosure.

### **Characteristics of Spectroscopic System**

The MOCVD reactor used in this study is interfaced with a Raman spectroscopic system (Jobin-Yvon Ramanor U-1000). The excitation light sources are an argon ion laser that emits 488 nm of wavelength (Innova 90, Coherent Inc.) and the frequency-doubled Nd:YAG (Neodymium doped Yttrium-Aluminum-Garnet) solid-state laser

(Verdi-8, Coherent Inc.) for 532.08 nm. Among numerous plasma lines, the argon ion laser predominantly produces 488 and 514 nm lines and partly selected principal plasma lines from Ref. [17] are tabulated in Table 2-3.

A laser line is focused by a lens that has 110mm focal length and directs it into the CVD reactor described above. Scattered light from the sample which is perpendicular to the incident laser line is reflected into the double monochromator. The spectrometer is equipped with two gratings which have a groove density of 1800 lines/mm and its schematic diagram is shown in Fig. 2-6.

Scattered light is dispersed and then observed with either a liquid nitrogen cooled CCD (Charge Coupled Device) or a PMT (Photo Multiplier Tube). PMTs are devised to count photons to achieve high sensitivity and low enough dark noise to avoid overwhelming the signal of interest. Basically, PMT uses the photoelectron effect that was first discovered out in 1887 by Heinrich Hertz. When the photon strikes a photocathode and thus the energy of this photon exceeds the work function of the photocathode, a photoelectron is ejected from the metal surface. The ejected electron is accelerated and amplified by striking sequential dynodes under high negative voltage. Conventional schematic diagram of PMT is shown in Fig. 2-7.

In this study, the R943-02 PMT model (Hamamatsu Photonics K.K.) that has a 51 mm diameter head-on type and has GaAs photocathode is used. A typical gain is  $2 \times 10^6$  at a temperature 25 °C and cathode to anode voltage of 1750 V is the typical value of this study. The PMT used is cooled with cold water to decrease dark counts. The CCD was invented in 1969 at AT&T Bell Labs by Willard Boyle and George E. Smith. As integrated circuit technology progressed at a rapid rate for the past a few

decades, CCD gets utilized due to its convenience and high capability to detect spectroscopic signals. CCD is based on the storage and manipulation of electrons and holes in a photosensitive silicon semiconductor. The photosensitive area in CCD, which is covered by the circuit mask, is constructed of pixel arrays in columnar form. The pixels in this column detect Raman shift as a form of slit image. Tall and narrow pixels corresponds to a Raman shift value, in other words, each pixel location is rigidly related to a specific wavelength. When CCD gets Raman shift information, it accumulates photoelectrons in its array of potential wells and the electrons accumulated are converted to a digital value. Each packet of stored electrons is amplified and digitized by a converter. Usually the number of stored electrons in CCD is stated as electrons per count ( $e^-/count$ ). As a multichannel detector, the CCD used is cooled with liquid nitrogen that holds 1 liter with a down-looking Dewar and is of the Symphony Spectrum One model provided by Jobin Yvon (Horiba scientific). Conventional CCD unit is shown in Fig. 2-8.

### **Applications of Raman Scattering**

#### **Gas Phase**

#### **Temperature determination**

A variety of techniques are available for measuring the local temperature of the sample. It might depend on the sample states (gas, liquid, and solid-phase) as well as the heat sensitivity or sample stability[18]. By using *in situ* Raman spectroscopy, one can monitor a local temperature of a gas molecule with high accuracy and without thermocouple.

There are two basic methods for determining the temperature by Raman scattering and those are the Stokes to anti-Stokes ratio method and the Stokes Raman

method. Since the intensities of the Stokes and anti-Stokes lines depend on the population of the ground and excited state of the specific vibrations, the relative occupation of both states can be described by Boltzmann distribution,

$$\frac{I_S}{I_{AS}} \propto \exp(-h\nu_1 / kT) \quad (2-18)$$

where T is absolute temperature and  $h\nu_1$  is the energy gap between two states. In addition to this, since photon count is the most frequently measured quantity in a Raman experiment rather than photon intensity, scattered intensity is governed by a third power of the optical frequency (fourth power for photon intensity) [19] and thus the frequency dependence of the Stokes and anti-Stokes Raman scattering can be described by:

$$I_S \propto \nu_0(\nu_0 - \nu_1)^3 \quad (2-19a)$$

$$I_{AS} \propto \nu_0(\nu_0 + \nu_1)^3 \quad (2-19b)$$

where  $\nu_0$  is the frequency of the exciting laser line. From Eqs. 2-18, 2-19a and 2-19b, the ratio of the Stokes and anti-Stokes Raman intensity is

$$\frac{I_S}{I_{AS}} = \frac{(\nu_0 - \nu_1)^3}{(\nu_0 + \nu_1)^3} \exp(-h\nu_1 / kT) \quad (2-20)$$

This method seems relatively easy and convenient, however, the accuracy of temperature determination decreases drastically since the anti-Stokes Raman scattering lines are very weak[20]. A more detailed study on the measurement of uncertainty over this method has been reported by LaPlant and his coworkers[19]. Briefly speaking, the absolute temperature error  $\Delta T$  is expressed as  $\Delta T = \sigma_r kT^2 / h\nu_1 c$  by using Eq.2-20, where  $\sigma_r$  is the relative uncertainty and defined as

$\sigma_r = \Delta(I_S / I_{AS})/(I_S / I_{AS})$ . At low temperatures, the relative uncertainty becomes large due to the loss of anti-Stokes line intensity. At high temperatures, the  $T^2$  term dominates the temperature error, the uncertainty becomes high as well.

Secondly, in the Stokes Raman method, the temperature of the gas can be extracted from a measured rotational distribution of the gas, mainly N<sub>2</sub> or H<sub>2</sub>, since a rotational state distribution of gas is governed by temperature. Usually nitrogen or hydrogen is used as a carrier gas for CVD systems, and this is advantageous for a Raman scattering experiment. Rotational transitions at the ground state of vibration can be correlated with temperature of the gas by using Eqs.2-12 and 2-13. Combining those two equations produces:

$$I = \frac{16\pi^4}{45} (\tilde{\nu}_0 - \tilde{\nu}_{rot})^4 g_s N I_0 7\gamma_0^2 \frac{\exp(-F(J)hc/k_B T)}{\sum \exp(-F(J)hc/k_B T)} \times \frac{3(J+1)(J+2)(2J+1)}{2(2J+3)(2J+1)} \quad (2-21)$$

where  $\gamma_0^2$  the anisotropy of the polarizability tensor,  $J$  is the rotational quantum number and  $g_s$  is the statistical weight factor (equal to 6 and 3 for even and odd nitrogen lines), and  $\tilde{\nu}_0$  and  $\tilde{\nu}_{rot}$  is the wavenumber shift of the incident light and rotational line, respectively.  $F(J)$  denotes the rotational term and it becomes:

$$F(J) = B_0 J(J+1) - D_0 J^2(J+1)^2 + \dots \quad (2-22)$$

where  $B_0$  and  $D_0$  is the rotational constant and the centrifugal distortion constant, respectively. Values of  $B_0$  and  $D_0$  were taken from Butcher *et al.*[21] and those values are shown in Table 2-4.

As shown in Table 2-4, the magnitude of  $D_0$  is much smaller than the magnitude of  $B_0$  where typically  $B_0 / D_0 \approx 10^{-6}$  [22]. With Eq. 2-22, one can calculate the frequency shift  $\omega(J)$  of the  $J$ th rotational Raman line as follows [22, 23]:

$$\omega(J) = F(J+2) - F(J) = B_0(4J+6) - D_0\{3(2J+3) + (2J+3)^3\} \quad (2-23)$$

Therefore, the rotational Raman spectrum is specified by the frequencies of  $\omega_0 \pm \omega(J)$ , where  $\omega_0$  is the wavenumber of the incident light. In addition, for taking into consideration of non-ideality, a few correction factors are required for Eq. 2-21. In other words, the anisotropy influenced by the centrifugal distortion and spectral response of the spectroscopic system should be considered for real gas molecular behavior. From these considerations, Eq. 2-21 can be rewritten as follows:

$$I = \frac{16\pi^4}{45} (\tilde{\nu}_0 - \tilde{\nu}_{rot})^4 g_s N I_0 7\gamma_0^2 \frac{\exp(-F(J)hc/k_B T)}{\sum \exp(-F(J)hc/k_B T)} \times \frac{3(J+1)(J+2)(2J+1)}{2(2J+3)(2J+1)} R(J, \nu_0) f(J) \quad (2-24)$$

where  $R(J, \tilde{\nu}_0)$  is the spectral response as a function of wavenumber and  $f(J)$  is the correction term for the anisotropy and is theoretically described as follows [24]:

$$f(J) = 1 + \frac{4}{\chi} \left( \frac{B_e}{\omega_e} \right)^2 [J(J+1) + J'(J'+1)] \quad (2-25)$$

Values of  $\chi$  and  $B_e / \omega_e$  for various simple diatomic molecules are tabulated in Table 2-5. However, these two functions are needed only at high temperatures and these corrections are not necessary up to approximately 1000K for nitrogen. When taking natural logarithm of Eq. 2-24 and rearranging the result, one can obtain Eq. 2-26b via Eq. 2-26a:

$$\frac{I}{g_s(\tilde{\nu}_0 - \tilde{\nu}_{rot})^4} \frac{(2J+3)}{(J+1)(J+2)} = \frac{8\pi^4}{15} \frac{NI_0 7\gamma_0^2}{\sum \exp(-F(J)hc/k_B T)} \times \exp(-F(J)hc/k_B T) \quad (2-26a)$$

$$\ln \left\{ \frac{I}{g_s(\tilde{\nu}_0 - \tilde{\nu}_{rot})^4} \frac{(2J+3)}{(J+1)(J+2)} \right\} = C_0 - \left\{ \frac{F(J)hc/k_B}{k_B} \right\} \frac{1}{T} \quad (2-26b)$$

where  $C_0 = \frac{8\pi^4}{15} \frac{NI_0 7\gamma_0^2}{\sum \exp(-F(J)hc/k_B T)}$  and this is the constant for a given experimental condition. As an example, the nitrogen rotational Raman spectrum measured at 300 K and linear fit were shown in Fig. 2-9.

As one can see, very good linearity is kept for the entire nitrogen rotational spectrum and one can calculate gas temperature with the unit of Kelvin from the slope of  $-1/T$ .

When using a mixed gas, for example, nitrogen and ammonia for group III-nitride deposition or nitrogen and hydrogen, it should be noted that the rotational Raman spectra of two gases overlap each other. Fig. 2-10 shows that the rotational Raman spectra of 95 % nitrogen and 5 % ammonia overlap so the gas temperature cannot be measured.

Generally, since the interval between each rotational band for ammonia is  $39$  or  $38 \text{ cm}^{-1}$ , as shown in Fig. 2-10B, one should be careful for temperature measurement under this experimental condition, or a peak deconvolution technique can be applied to screen the nitrogen rotational Raman spectrum.

Even though uncertainty in temperature measurements using Raman spectroscopy over 3000K increases drastically (more than 300K) [25], the temperature measurement technique with Raman scattering is effective in the range of approximately 20-2230 °C and has 7 % accuracy[18].

## Concentration measurement

One of the most outstanding advantages of Raman spectroscopy, compared to infrared spectroscopy, is the capability of measuring sample concentration. Fundamental formulation starts from Eq. 2-27.

$$I_{rot} = NI_0 \left( \frac{d\sigma_{rot}}{d\Omega} \right) \quad (2-27)$$

The term in parenthesis is expressed by some experimental variables.

$$\left( \frac{d\sigma}{d\Omega} \right)_k = C_k \frac{(\tilde{\nu}_0 - \tilde{\nu}_k)^4}{\tilde{\nu}_k [1 - \exp(-hc\tilde{\nu}_k / kT)]} \quad (2-28)$$

where  $C_k$  is a constant and it includes  $k$ -th vibrational mode information such as Raman scattering activity. Calculation of absolute Raman cross-section described previously, at known concentration, allows for us to calculate the constant  $C_k$ . For experimental simplicity, the relative normalized differential Raman cross-section is defined as follows:

$$\Sigma_k \equiv \frac{(d\sigma_k / d\Omega)}{(d\sigma_{N_2} / d\Omega)} \cdot \frac{(\tilde{\nu}_0 - \tilde{\nu}_{N_2})^4}{(\tilde{\nu}_0 - \tilde{\nu}_k)^4} \frac{1 - \exp(-hc\tilde{\nu}_k / kT)}{1 - \exp(-hc\tilde{\nu}_{N_2} / kT)} \quad (2-29)$$

In Eq. 2-29, the exponential Boltzmann factor for nitrogen can be omitted at ambient temperature. Note that the quantity  $\Sigma_k$  is closely related to the relative scattering coefficient and the scattering activity. When performing concentration measurements with Raman spectroscopy, measured Raman apparent intensity and the number density ratio are to be calculated at the region of interest. Using Eqs. 2-27 and 2-29, the relationship between the number density ratio,  $N_{N_2} / N_k$ , and the intensity ratio is described as follows:

$$\frac{N_{N_2}}{N_k} = \frac{I_{N_2}}{I_k} \frac{(d\sigma_{N_2} / d\Omega)}{(d\sigma_k / d\Omega)}$$

$$= \frac{I_{N_2}}{I_k} \frac{(\tilde{\nu}_0 - \tilde{\nu}_k)^4}{(\tilde{\nu}_0 - \tilde{\nu}_{N_2})^4} \frac{1 - \exp(-hc\tilde{\nu}_{N_2}/kT)}{1 - \exp(-hc\tilde{\nu}_k/kT)} \Sigma_k \quad (2-30)$$

For a binary system, the mole fraction of component k is given by

$$\begin{aligned} x_k &= \frac{N_k}{N_k + N_{N_2}} \\ &= 1 / \left[ 1 + \frac{N_{N_2}}{N_k} \right] \\ &= 1 / \left[ 1 + \frac{I_{N_2}}{I_k} \frac{(\tilde{\nu}_0 - \tilde{\nu}_k)^4}{(\tilde{\nu}_0 - \tilde{\nu}_{N_2})^4} \frac{1 - \exp(-hc\tilde{\nu}_{N_2}/kT)}{1 - \exp(-hc\tilde{\nu}_k/kT)} \Sigma_k \right] \end{aligned} \quad (2-31)$$

However, the relative normalized Raman cross-section has to be measured to use Eq. 2-31. A more detailed example for gas concentration measurement of group-III precursor will be discussed in later chapters.

### Liquid Phase

Typically, a liquid phase sample is more concentrated than a gas phase sample, consequently a liquid sample can show much stronger Raman scattering intensity. Due to this distinguishing feature, Raman spectroscopy reveals its suitability to the characterization for liquid phase samples. The association between acrylonitrile ( $\text{CH}_2=\text{CH}-\text{CN}$ ) and the  $\text{Ni}^{2+}$  ion in aqueous solution was studied by Ramanspectroscopy[26]. By changing the nickel nitrate hexahydrate concentration in the range 30~70 % (w/w) and temperature in the range 248~338 K as well, Raman shift was observed and enthalpy change was calculated. In addition to above experiment, Alía et al. have reported spectroscopic behavior for various combinations of silver nitrate solutions in four nitriles (e.g. acetonitrile, benzonitrile, ethylcyanoacetate, and acrylonitrile) to elucidate the relationship between the silver ion and the nitrile[27]. An

interaction between nitriles and cations was revealed and solvation spheres around the silver ion are identified spectroscopically. A new solvation number of acetonitrile was calculated based on the band deconvolution and component-fitting in the  $\nu(CN)$  region. Yin *et al.*[28] measured the Raman spectral intensities of  $CCl_4$  in  $CS_2$  at concentrations ranging from 90 to 0.05%(v/v) for tracing Raman scattering cross-sections of the 218, 314 and  $459\text{ cm}^{-1}$  of  $CCl_4$  bands. Also from the Raman scattering observations, the Raman scattering cross-sections of three  $CCl_4$  bands were increased with decreasing concentration of  $CCl_4$  over the entire range. Raman spectroscopy is widely used in carbon nanotube research[29-32]. Rao *et al.*[33] have measured the Raman spectrum of single walled carbon nanotubes in  $CS_2$  where the tubes are present in ordered bundles or ropes. From the typical tube diameter estimation formula of  $\omega_R \approx 224\text{cm}^{-1} \cdot nm / d$  where  $\omega_R$  and  $d$  is the radial mode frequency and the tube diameter, respectively, modified formula of  $\omega_R \approx (224\text{cm}^{-1} \cdot nm / d) + \Delta\omega_R$ . Interestingly, the radial mode frequencies for the tubes in solution are found to be approximately  $10\text{ cm}^{-1}$  higher than those observed for tubes in a rope.

For the solvent effect, single walled carbon nanotubes were placed in two types of solvents and liquid phase scattering experiments were performed with a Raman spectrometer. Two sets of experiments were performed using only sodium dodecyl sulfate (SDS) and a mixed solution of sodium cholate (SC) and SDS in the ratio of 4:1, and the measured Raman spectra of two experiments are shown in Fig. 2-11.

Among various measured Raman shifts, peaks compared in Fig. 2-11 show outstanding difference. Peaks around  $270$  and  $1500\text{ cm}^{-1}$  suggest metallic characteristics of carbon nanotube and those around  $1600\text{ cm}^{-1}$  shows semiconducting

characteristics. Raman measurements reveal that sodium cholate downshifts the metallic band rather than semiconducting features. Other than these features, the measured Raman shift for two cases are tabulated in Table 2-6.

Mitambo and Loppnow recorded Raman spectra of 4-(dimethylamino)benzoate (DMABEE) in 18 solvents of varying polarity and hydrogen bond strength to find the molecular mechanism between solvent and solute[34]. Raman shifts of the C=O stretch of DMABEE in various solvents show large differences, as much as  $45\text{cm}^{-1}$ . Other than this, Raman spectroscopy can give reaction kinetic information as Jeon *et al.* reported[35]. By observing time-dependent Raman spectra of  $\alpha$ -Bromo-o-toluic acid at  $25 \sim 55^\circ\text{C}$ , they estimated the rate constant for the product of phthalide in an 80 % ethanol solution. In addition, far after the early trial of polymerization of the styrene monomer to polystyrene[36], a detailed polymerization kinetic study was revealed by Chu *et al.* by observing Raman spectra of three initial temperatures[37]. Lee *et al.* performed *in situ* monitoring of benzylideneaniline formation from benzaldehyde and aniline under chloroform in a glass microfluidic chip and compared experimental signals with calculated data using B3LYP/6-31G(d) level of chemistry[38]. Increasing C=N stretching of benzylideneaniline at  $1628\text{ cm}^{-1}$  shows the progress of the imine formation reaction.

The variety of applications makes Raman spectroscopy more useful than before and its capability allows researchers to perform experiments more conveniently and accurately.

## Solid Phase

Raman spectroscopy can also provide various kinds of information for a solid phase as well as gas and liquid phase. Especially Raman shift measurement is

especially useful for layered heterostructure device studies. Since photoluminescence (PL) resolution is limited by carrier diffusion whereas Raman spectroscopy resolution is limited only by laser spot size, vibrations probed by Raman are very sensitive to changes in the lattice. Lattice order, stress and even chemical composition profiling can be measured by observing changes in peak width, position and relative peak strength. Lattices have steady vibrations even at a stable state and phonon modes explain those vibrations. Phonon modes consist of an acoustic mode and an optical mode and both may be transverse (TO) or longitudinal (LO). Lattice strain, order, structure, composition, and orientation can be confirmed by phonon mode analysis. Kim and Spitzer have reported Raman shift of a  $\text{Ga}_x\text{Al}_{1-x}\text{As}$  mixed crystal due to the influence of the surrounding lattice[39]. Also Wetzel and his coworkers showed the carrier density  $N$  in n-type GaN can be expressed as:

$$N = 1.1 \times 10^{17} (\Delta\tilde{\nu})^{0.764} \quad (2-32)$$

where  $\Delta\tilde{\nu}$  is the observed Raman frequency shift within the interesting range of  $N \leq 1 \times 10^{19} \text{ cm}^{-3}$  [40]. In addition, Kim *et al.* characterized GaN on sapphire after etching by Focused Ion Beam (FIB) with changing probe beam current near the etched ring area[41]. Even though it is a qualitative study, that research contributes to the field of Raman spectroscopy. Like gas phase temperature measurement, Cui *et al.* derived a noncontact temperature measurement function. It has the form of:

$$\Omega(T) = \Omega_0 - \frac{C}{\exp[D(hc\Omega_0/kT)] - 1} \quad (2-33)$$

where  $\Omega_0$  is the Raman line position at 0 K,  $C$  and  $D$  are free parameters decided by experiments[42]. Although it is a purely empirical function, its good linear dependency

shows it can be a good nondestructive technique for measuring device temperature. As an application, Kim *et al.* has reported contact free measurement of channel temperature of AlGaN/GaN HEMTs (High Electron Mobility Transistors) under different operation modes[43]. By plotting the plot of the peak position of the  $E_2^2$  phonon mode as a function of the passive heating temperature from 20 to 150°C, they provided a device temperature measurement reference so that Raman shift of an active heating device can be compared to that. Other than these applications, Raman spectroscopy can be conveniently used to identify crystalline structures, and evaluate material quality and composition.

As an example of identifying crystalline nanostructures, CuInSe<sub>2</sub> synthesized by a low temperature solution based method was characterized by micro-Raman spectrometer. The room temperature micro-Raman spectra were recorded by using a Jobin Yvon Ramanor U-1000 spectrometer equipped with an optical microscope BH-2, manufactured by the Olympus Company. All measurements were performed by using 532.08nm line of a Nd:YAG solid-state laser with 0.2W intensity. For better signal-to-noise ratio, 20 scans for each measurement were performed. The backscattered light is collected with the numerical aperture (NA) of the microscope and imaged to the double monochromator equipped with two 1800 grooves/mm gratings. The photomultiplier tube (PMT) equipped with a GaAs cathode (R943-02, Hamamatsu) was used as a detection unit.

For several years, various studies of the CuInSe<sub>2</sub> chalcopyrite (ch) structure ( $D_{2d}$ ) for thin film and powder characterization were reported[44-46]. The vibrational spectrum of CuInSe<sub>2</sub> chalcopyrite structure consists of 24 zone-centered vibrational

modes of  $1A_1 + 2A_2 + 3B_1 + 4B_2 + 7E$ . Besides two silent modes ( $2A_2$ ), 22 Raman active vibrations ( $1A_1 + 3B_1 + 4B_2 + 7E$ ) are expected from the  $\text{CuInSe}_2$  chalcopyrite structure. However, only the LO and TO modes with  $\Gamma_{15}$  symmetry are Raman active in a sphalerite structure ( $T_d$ ). The vibrational frequencies for the LO and TO modes with  $\Gamma_{15}$  symmetry in sphalerite structure were reported at  $210\sim217\text{cm}^{-1}$  and  $230\sim235\text{cm}^{-1}$ , respectively[45, 46].Besides,  $\text{Cu}_x\text{Se}_y$  (e.g.,  $\text{CuSe}$  and  $\text{Cu}_2\text{Se}$ ) and  $\text{In}_x\text{Se}_y$  (e.g.,  $\text{InSe}_2$  and  $\text{In}_2\text{Se}_3$ ) structures can coexist with  $\text{CuInSe}_2$  structures in the sample.

Raman spectra of various  $\text{CuInSe}_2$  nanopowder samples for this research, measured using the 532.08nm line, are shown in Fig. 2-12. In order to exploit a Raman spectrum, the main part from 50 to  $300\text{cm}^{-1}$  was extracted. Results are tabulated in Table 2-7.

Raman frequencies and proposed peak assignments were described. As described above, two major  $\text{CuInSe}_2$  sphalerite characteristic peaks and some binary peaks ( $\text{Cu}_x\text{Se}_y$  and  $\text{In}_x\text{Se}_y$ ) were measured. Although the highest intensity of the feature at  $124\text{cm}^{-1}$  from D in Fig. 2-12 was attributed to the  $B_1$  mode[47], it does not seem clearly assigned because  $124\text{cm}^{-1}$  of  $B_1$  mode is from chalcopyrite. Besides the feature at  $124\text{cm}^{-1}$ , the other four peaks are relatively clear. First of all, features at about  $200\text{cm}^{-1}$  can be attributed to  $\text{Cu}_3\text{Se}_2$ [48].And the peak at  $212$  and  $236\text{cm}^{-1}$  correspond to  $B_2$  and E modes of  $\text{CuInSe}_2$  phase as reported for sphalerite structure ( $T_d$ )[49]. As shown in Fig. 2-12,  $212\text{cm}^{-1}$ feature appears as shoulders, and two  $236\text{cm}^{-1}$  peaks were measured only from B and D. However, the possibility that the feature at  $236\text{cm}^{-1}$  could be overlapped with that of  $\text{Se}_n$  polymer moleculecannot be ruled out. As for the peaks from  $256$  to  $259\text{cm}^{-1}$ , there are three possibilities. Witte et al. reported  $260\text{cm}^{-1}$  as the

$\text{Cu}_{2-x}\text{Se}$  phase from a Cu-rich  $\text{Cu}(\text{In},\text{Ga})\text{Se}_2$  sample[50]. On the other hand, the Raman shift at  $260\text{cm}^{-1}$  can be attributed to  $\text{In}_2\text{Se}_3$ [51], and its frequency typically coincides with that of a  $\text{Se}_8$  ring structure observed from monoclinic and amorphous selenium. In addition to that, Lin *et al.*[52] recently reported Raman spectra of  $259\text{cm}^{-1}$  for  $\text{Cu}_2\text{Se}$  structure from the film deposited on copper in a hydrazine/water system. From the analysis of the micro-Raman spectra described above, the sample analyzed has a unique structure of sphalerite ( $T_d$ ) and it is confirmed by Raman shift analysis, although  $\text{CuInSe}_2$  usually has a chalcopyrite ( $D_{2d}$ ) structure.

When it comes to thin film characterization for semiconductor applications, note that each laser with a different wavelength has a different penetration depth. Moreover, penetration depth also depends on sample compositions. For strong absorption materials like semiconductors, the Raman signal originates from a volume defined by the penetration depth and the diameter of the laser beam. A shorter laser wavelength penetrates less and provides lattice strain information near the surface. Different penetration depths in silicon and germanium are tabulated for various wavelengths.

When deeper penetration is required, Raman measurement after sputtering is an available procedure. Ramsteiner and his coworkers sputtered the ion implanted  $\text{GaAs:Si}^+$  samples and performed Raman observations with various sputtering depth of 100, 150, 200 nm, and as grown film as well[53]. As shown in Table 2-8, penetration depth data according to laser wavelength is very limited and one can consult the calculation method. The optical penetration depth can be calculated as follows:

$$d_p = \frac{1}{2\alpha} \quad (2-34)$$

where  $\alpha$  denotes the absorption coefficient[54].

## **Summary**

Raman spectroscopy has numerous applications for most research fields even archeology, geology, or art. In the same context, Raman spectroscopy interfaced with CVD reactor can be used for elucidating reaction kinetics by measuring local temperature and species concentrations at precisely focused points inside the reactor. The principles of Raman scattering, detectors such as CCD and PMT were described. Moreover, Raman applications for gas, liquid, and solid phase research were explained and exemplified by experiments. In addition, practical information relevant to further research for each phase was stated.

Spectroscopic Method			
Advantages	Raman Scattering	FTIR Absorption	NIR Absorption
	Narrow linewidths Water compatible Easy sampling Noninvasive Low frequency mode observable Enhancement possible  Low sensitivity Interference	Narrow linewidths Good fingerprint - good libraries Fundamental vibrations  Sampling often difficult Strong water absorption	Noninvasive Water compatible Fiber optics, Remote sampling  Wide linewidths Calibration complex Poor fingerprint
Disadvantages			.....

Figure 2-1. Comparison of three most widely used spectroscopic methods.

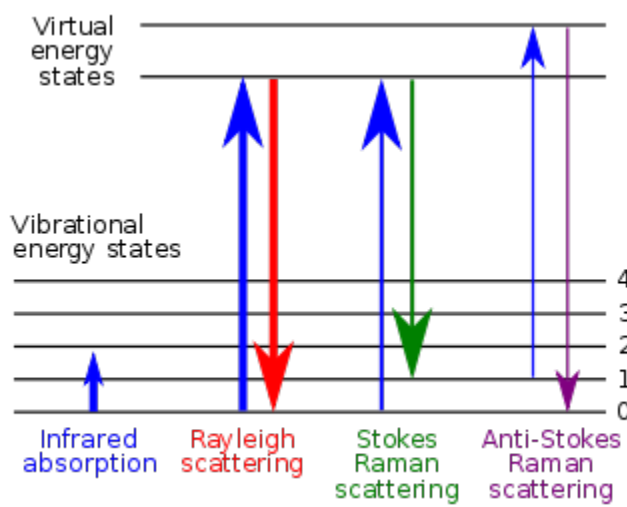


Figure 2-2. Jablonski energy level diagram for typical IR and Raman scattering. The line thickness is roughly proportional to the signal strength.

Table 2-1. Absolute differential Raman scattering cross-section of the vibrational-rotational band of gas-phase nitrogen of Q-branch (table is taken from Ref. [14])

Exciting line $\lambda_0$ (nm)	$\frac{d\sigma}{d\Omega}$ ( $10^{-32}$ cm $^2$ /sr)	$\frac{d\sigma}{d\Omega}(\nu_0 - 2331\text{cm}^{-1})^{-4}$ ( $10^{-48}$ cm $^6$ /sr)
632.8	21±3	6.4±1
514.5	44±17	5.1±2
	43±2	5.0±0.3
	42±2	4.9±0.3
	43.2±0.8	5.05±0.11
488.0	33±11	3.0±1
	43	4.0±1
	54±3	5.0±0.3
	55.8±2	5.13±0.2
457.9	76±5	5.2±0.4
	73.7±3	5.09±0.25
363.8	204±25	5.1±0.6
300.0	970	10.5

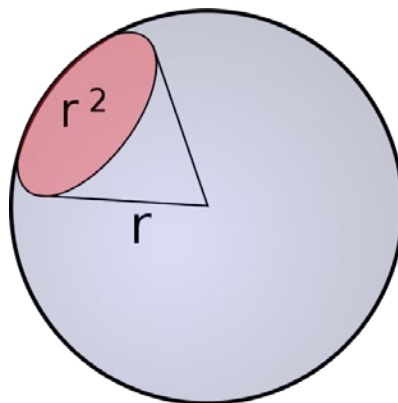


Figure 2-3. A graphical representation of 1 steradian.

Table 2-2. Absolute differential Raman scattering cross-section of widely used liquids using the laser wavelength of 514.5nm (table is taken from Ref. [11])

Sample	$\frac{d\sigma}{d\Omega} (10^{-30} \text{ cm}^2/\text{sr})$	$\frac{d\sigma}{d\Omega} (\nu_0 - 2331 \text{ cm}^{-1})^{-4} (10^{-48} \text{ cm}^6/\text{sr})$
Benzene		
992 $\text{cm}^{-1}$	30.6	235
3060 $\text{cm}^{-1}$	45.3	-
Cyclohexane		
802 $\text{cm}^{-1}$	5.2	-
All C-H	43	-
$\text{CHCl}_3$		
3032 $\text{cm}^{-1}$	4.4	-
758 $\text{cm}^{-1}$	3.2	-
667 $\text{cm}^{-1}$	6.6	-
364 $\text{cm}^{-1}$	6.3	-
261 $\text{cm}^{-1}$	7.0	-

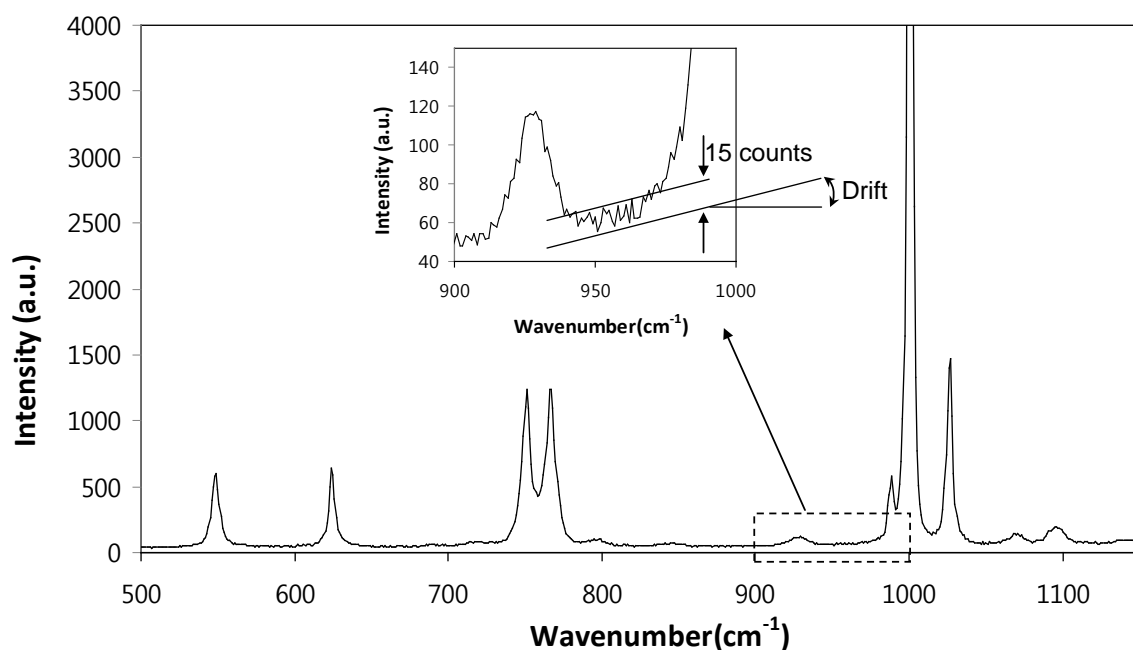


Figure 2-4. Raman scattering results of pure liquid benzonitrile in the range 500 ~ 1150  $\text{cm}^{-1}$ . The peak to peak noise (about 1/5 of the RMS noise) is shown, together with clearly visible drift, which has the character of flicker noise.

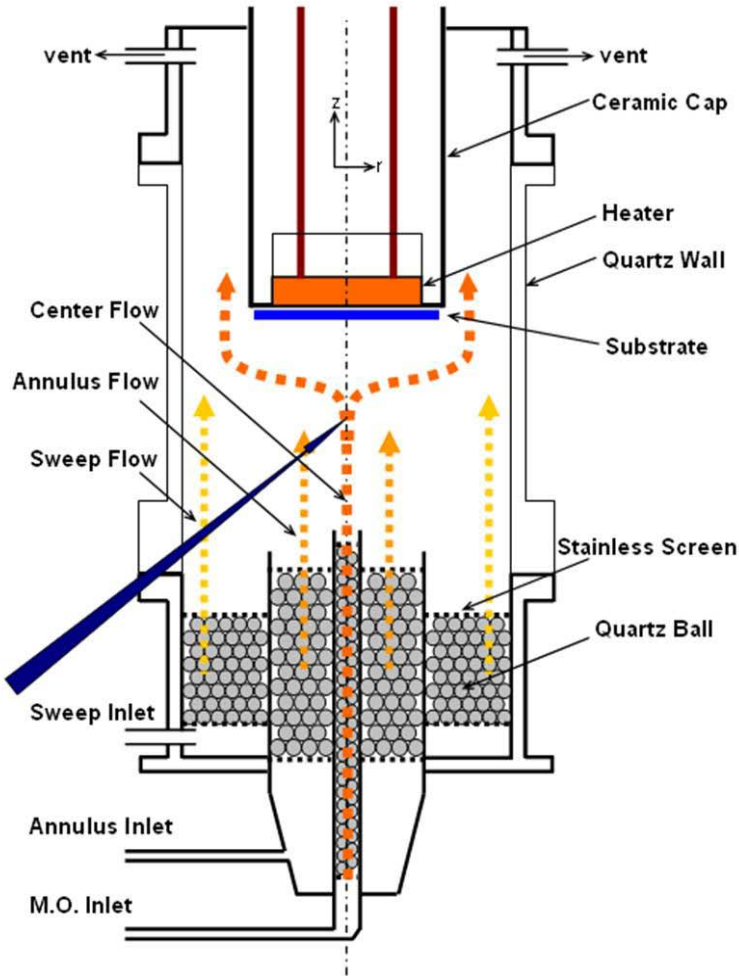


Figure 2-5. Schematic drawing of the chemical vapor deposition reactor for *in situ* Raman spectroscopic measurements.

Table 2-3. Selected principal plasma lines in the argon ion laser.

Relative Intensity	Wavelength (air) (nm)	Wavenumber (vac) (cm <sup>-1</sup> )	Shift (cm <sup>-1</sup> ) relative to 488.0 nm	Shift (cm <sup>-1</sup> ) relative to 514.5 nm
5000	487.9860	20486.67	0	
960	496.5073	20135.07	351.6	
1500	500.9334	19957.16	529.5	
1400	506.2036	19749.39	737.3	
1000	514.5319	19429.73	1056.9	0
>1750	611.4929	16348.90	4137.8	3080.8
1400	617.2290	16196.96	4289.71	3232.8

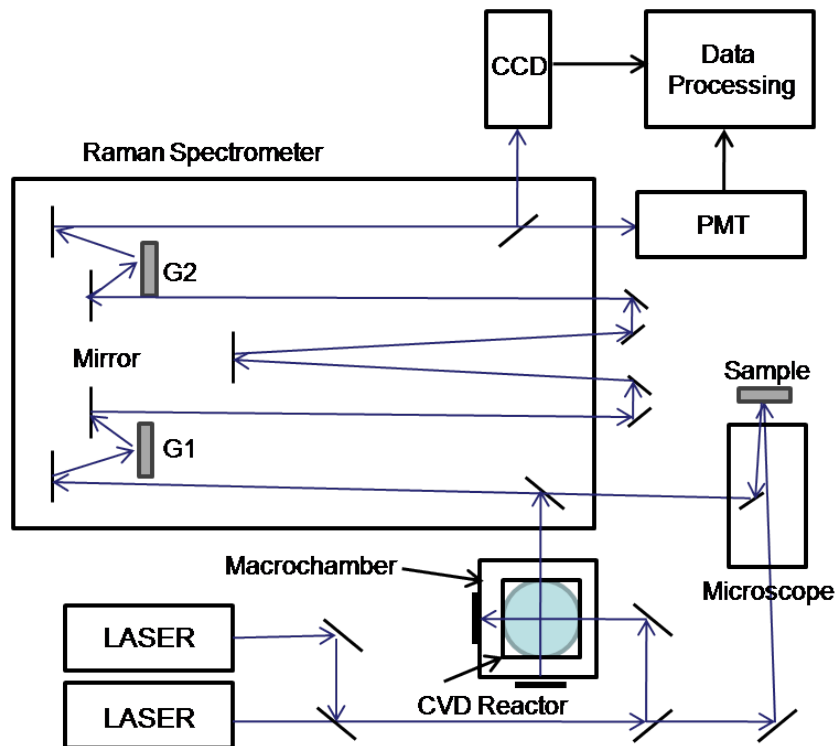


Figure 2-6. A schematic diagram of a Raman spectroscopic system.

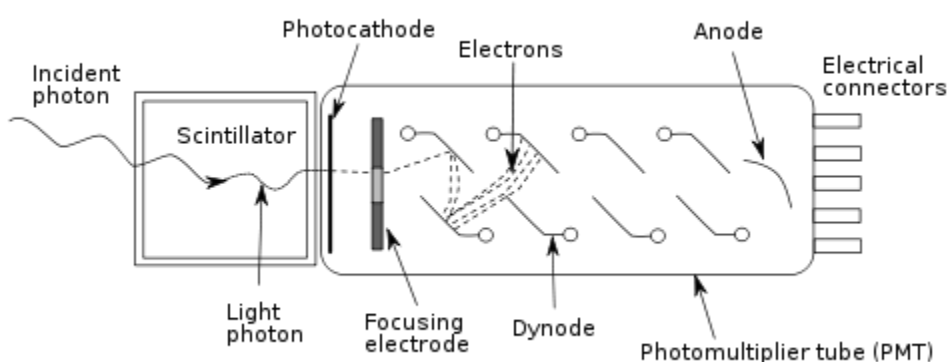


Figure 2-7. Conventional schematic diagram of photomultiplier tube.

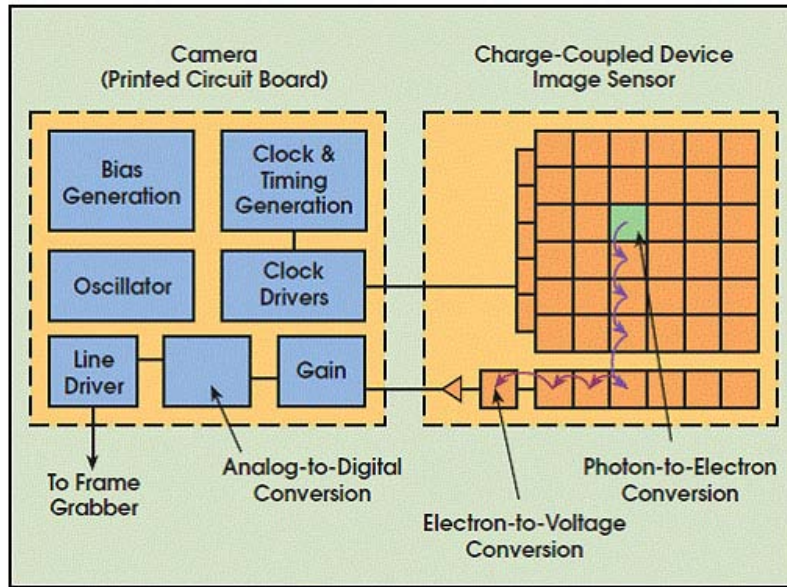


Figure 2-8. Conventional diagram of a CCD.

Table 2-4. Values of rotational constant  $B_0$  and centrifugal distortion  $D_0$  for nitrogen and oxygen from Butcher *et al.*[21]

Molecule	$B_0$ (cm $^{-1}$ )	$D_0$ ( $\times 10^6$ cm $^{-1}$ )
Nitrogen (N <sub>2</sub> )	1.98950 ± 0.00002	5.48 ± 0.05
Oxygen (O <sub>2</sub> )	1.43768 ± 0.00001	4.85 ± 0.01

Table 2-5. Values of  $\chi$  and  $B_e / \omega_e$  for various simple diatomic molecules

Molecule	$\chi$ <sup>a</sup>	$B_e / \omega_e$ <sup>b</sup>
H <sub>2</sub>	0.38 ± 0.01	1.383×10 <sup>-2</sup>
D <sub>2</sub>	0.38 ± 0.01	9.762×10 <sup>-3</sup>
N <sub>2</sub>	0.45 ± 0.09	8.476×10 <sup>-4</sup>
O <sub>2</sub>	0.23 ± 0.07	9.148×10 <sup>-4</sup>
CO	0.27 ± 0.13	8.901×10 <sup>-4</sup>

<sup>a</sup>Taken from Ref. [55]

<sup>b</sup>Spectroscopic data was taken from Ref. [56]

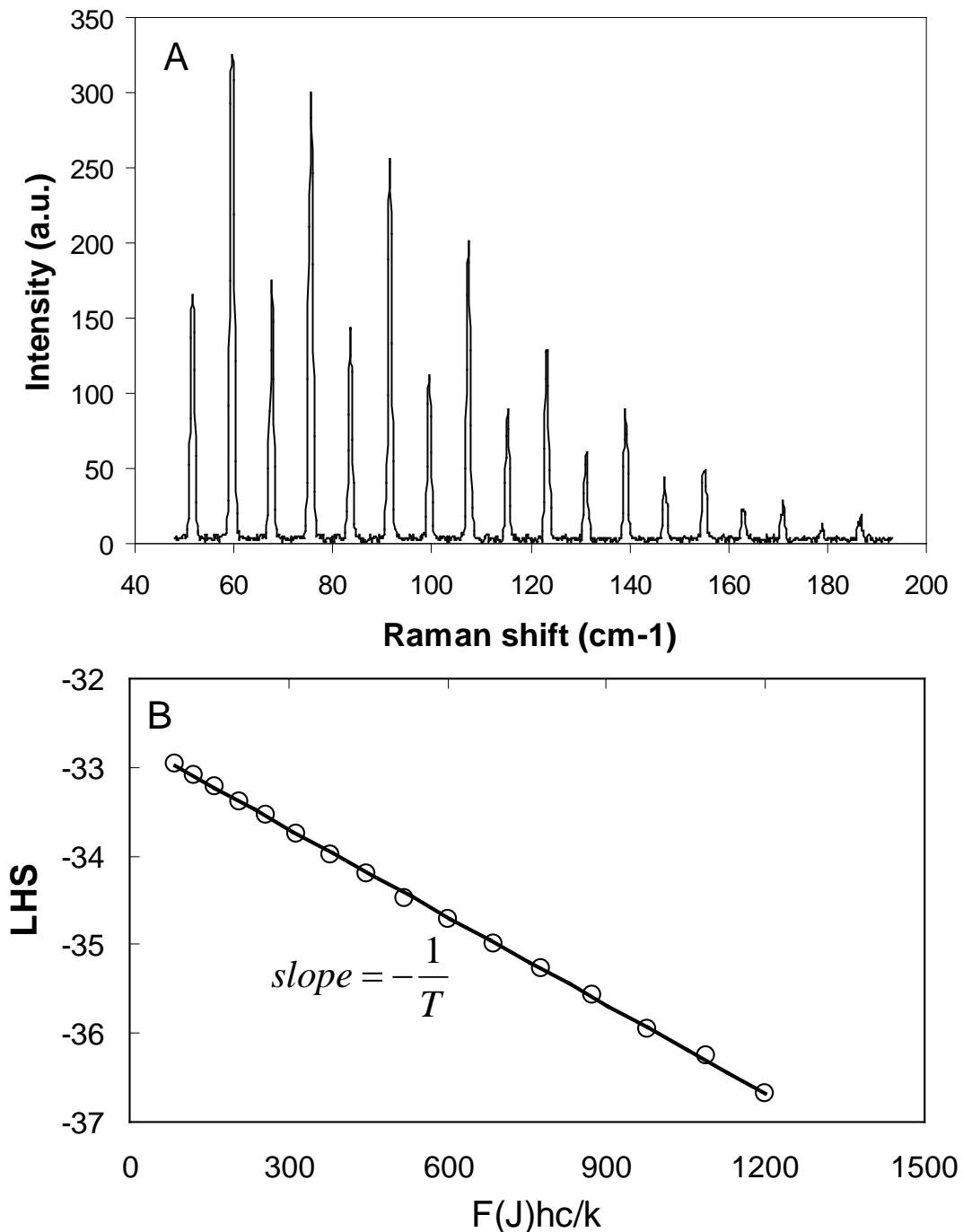


Figure 2-9. Temperature determination process: (A) a rotational Raman spectrum taken at 300 K and (B) linear relationship between LHS and  $F(J)hc/k_B$  in Eq. 2-26b.

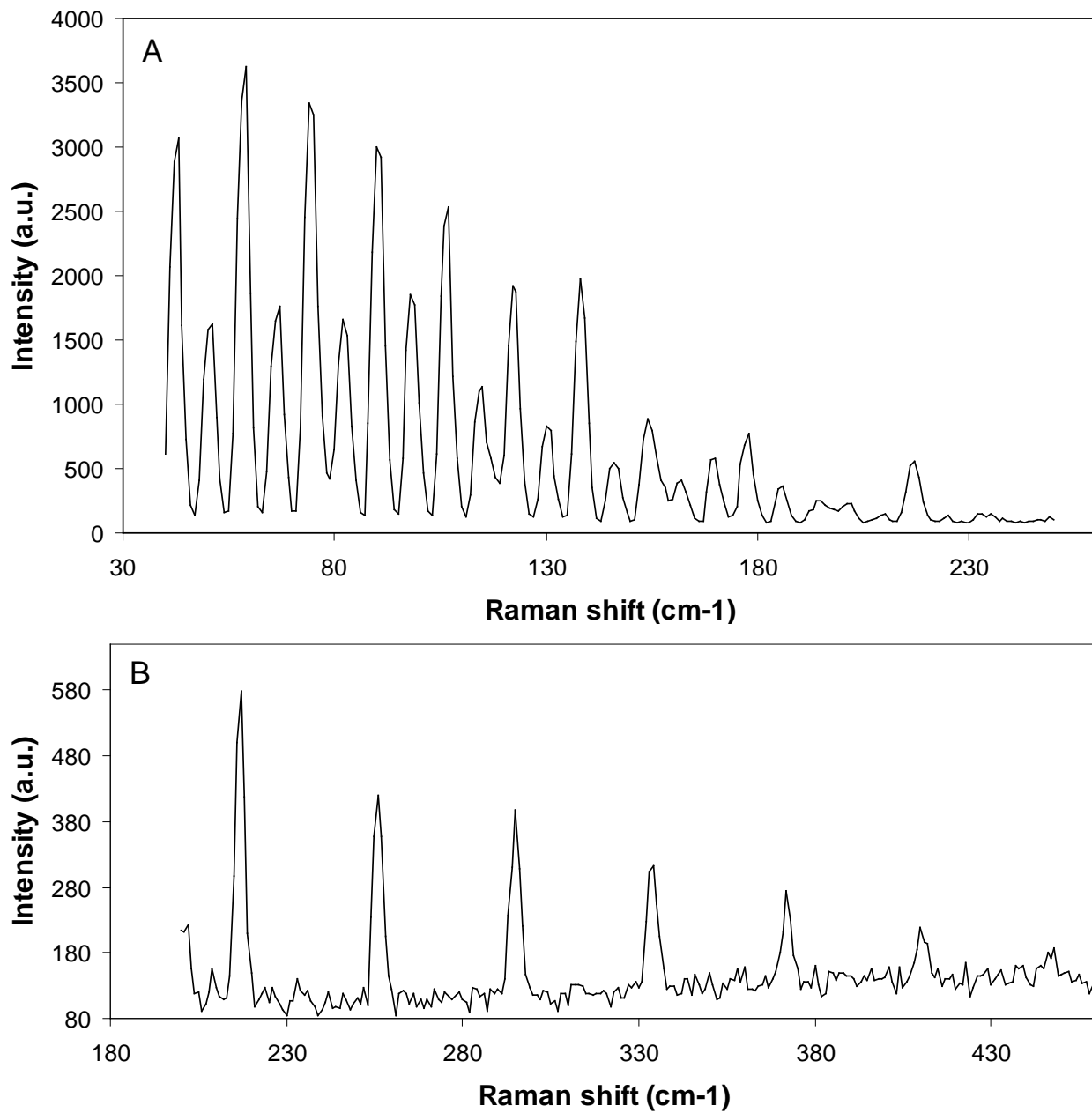


Figure 2-10. (A) Overlapped rotational Raman spectra of nitrogen and ammonia, (B) the rotational Raman spectrum of ammonia.

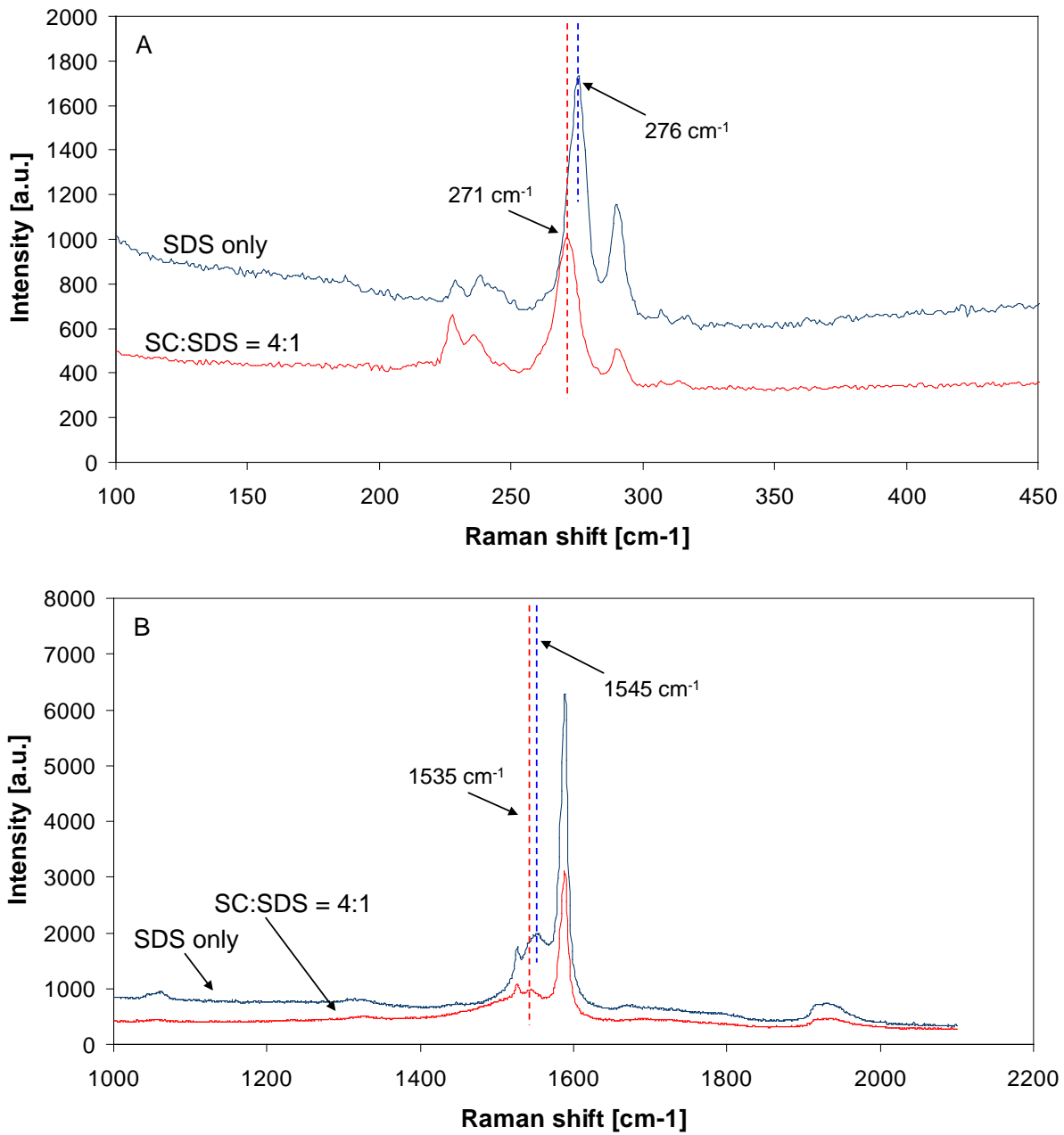


Figure 2-11. Raman scattering measurement for single wall carbon nanotubes in (A) sodium dodecyl sulfate (SDS) and (B) sodium cholate (SC) and SDS in the ratio of 4:1.

Table 2-6. Raman shifts for single wall carbon nanotubes in two kinds of organic solvents

Molecule	Raman shift [cm <sup>-1</sup> ]						
SDS only	229	238	276	290	1527	1545	1588 1928
SC:SDS=4:1	228	235	271	290	1526	1535	1588 1927
Difference	1	3	5	0	1	10	0 1

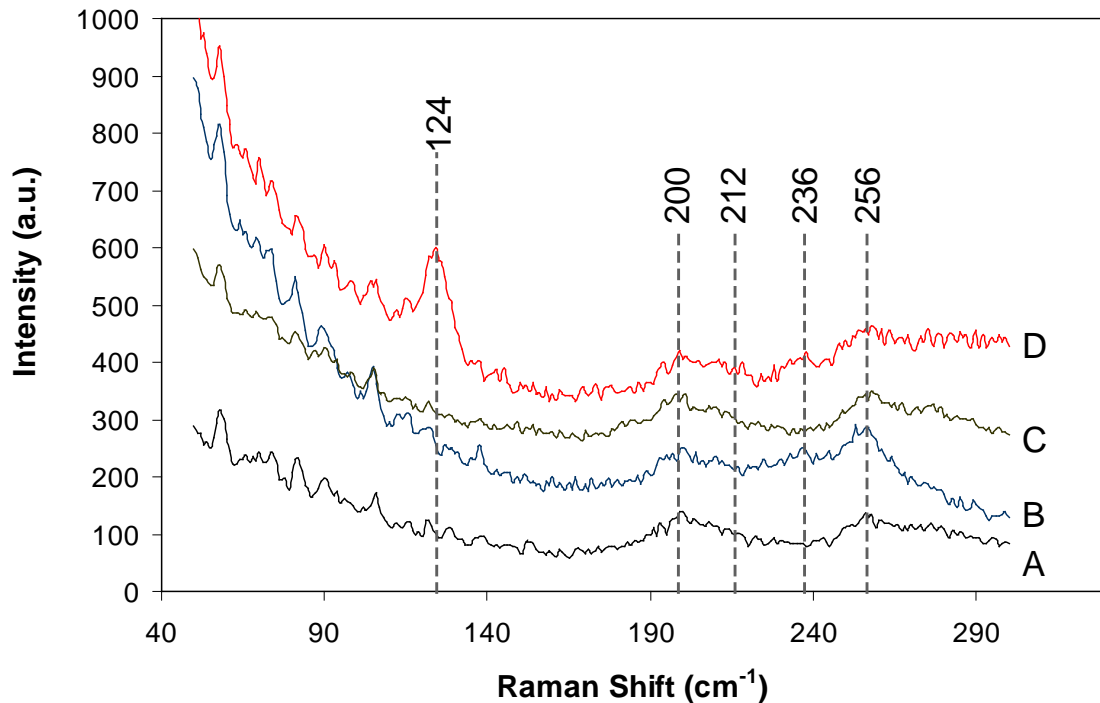


Figure 2-12. Raman spectrum of CuInSe<sub>2</sub> nanopowder measured at room temperature.

Table 2-7. Observed Raman shift of CuInSe<sub>2</sub> nanopowder and proposed assignment

Entry	A	B	C	D	Proposed assignment
1				124	B <sub>1</sub>
2	200	200	201	199	Cu <sub>3</sub> Se <sub>2</sub>
3	212	212	212	212	Γ <sub>15</sub> (LO)
4		237		236	Γ <sub>15</sub> (TO) / Se <sub>n</sub> polymer
5	256	257	258	259	Cu <sub>2-x</sub> Se/Cu <sub>2</sub> Se/In <sub>2</sub> Se <sub>3</sub> /Se <sub>8</sub> ring molecule

Table 2-8. Penetration depth according to laser wavelength in Si, Ge,  $\text{Si}_{0.78}\text{Ge}_{0.22}$ , 4H-, 6H-SiC and CdS

Laser wavelength (nm)	Penetration depth in Si (nm)	Penetration depth in $\text{Si}_{0.78}\text{Ge}_{0.22}$ (nm)	Penetration depth in Ge (nm)	Penetration depth in 4H-, 6H-SiC (nm)	Penetration depth in CdS (nm)
633	3000 <sup>c</sup>		32 <sup>c</sup>		
514	762 <sup>c</sup> , 340 <sup>a</sup>	300 <sup>d</sup>	19.2 <sup>c</sup> , 8 <sup>a</sup>		
~500				2mm <sup>e</sup>	
488	569 <sup>c</sup>		19 <sup>c</sup>		100 <sup>b</sup>
457	313 <sup>c</sup> , 140 <sup>a</sup>	65 <sup>d</sup>	18.7 <sup>c</sup> , 8 <sup>a</sup>		
413.1	61 <sup>a</sup>	12 <sup>d</sup>	7 <sup>a</sup>		
364				50~100 $\mu\text{m}$ <sup>e</sup>	
351	5 <sup>a</sup>	5 <sup>d</sup>	5 <sup>a</sup>		
325	~10 <sup>c</sup>		~9 <sup>c</sup>		
266				100~250 <sup>e</sup>	
244	~6 <sup>c</sup>		~7 <sup>c</sup>	50~100 <sup>e</sup>	

(Data were taken from a)Ref. [57], b) Ref. [58], c) Ref.[59], d) Ref. [60] and e) Ref.[61])

## CHAPTER 3 COMPUTATIONAL CALCULATIONS

Raman spectroscopy can detect various types of molecules such as adducts, molecules in a transition state, as well as the parent metalorganic precursor with its high spatial resolution. However, unfortunately Raman observation does not indicate what signals correspond to. This research involves quantifying Raman signal and calculating various properties, for example, rate constant, activation energy, free energy and so on, so an external method is required for these calculations. Typically IR measurement is used for organic molecules which has enormous database for assignment, so IR does not undergo this problem. Many theoretical chemists have studied and developed computational chemistry for predicting experimental results for several decades, and they achieved eye-opening progress with the help of developing computational performance.

A molecule's quantum states and its eigenvalues are expressed by wave functions for time independent case as follows:

$$\tilde{H}(\vec{R}, \vec{r})\Psi(\vec{R}, \vec{r}) = E\Psi(\vec{R}, \vec{r}) \quad (3-1)$$

where  $\tilde{H}(\vec{R}, \vec{r})$ ,  $\Psi(\vec{R}, \vec{r})$ , and  $E$  are the electronic wavefunction, the electronic Hamiltonian operator, and the electronic energy, respectively. Vector  $\vec{R}$  is vector notation for the coordinates of the N nuclei and  $\vec{r}$  represents the coordinates of the n electrons. To solve this well-known Schrödinger equation, many researchers have studied various approaches. Among them, there are four main approaches to calculating molecular properties –*ab initio* methods, semi empirical methods, the density functional method, and the molecular mechanics method[62]. Semi empirical methods do not use the correct molecular Hamiltonian, rather a simple Hamiltonian, and

parameters whose values are adjusted to fit experimental results. On the other hand, *ab initio* calculation uses the correct Hamiltonian and the value of the fundamental physical constants, while neglecting experimental data. Latin *ab initio* means “from the beginning” and it implies a calculation based on fundamental principles. The goal for a Hartree-Fock SCF (Self-consistent Field) calculation is to find the antisymmetrized product,  $\Phi$ , of one-electron functions which minimize  $\int \Phi^* \tilde{H} \Phi d\tau$ , where  $\tilde{H}$  is the true Hamiltonian.

The classical *ab initio* method based on Hartree-Fock (HF) formally scales as number of electrons to  $N^4$  or higher powers. The density functional method does not calculate the molecular wavefunction, instead, it calculates the molecular electron probability density and calculates the molecular electronic energy from the density. The properties of a many-electron system can be determined by using functionals which is the spatially dependent electron density. DFT methods have a better scaling of  $N^3$  or lower and it make calculations on typical CVD precursors more accessible, because the molecular mechanics method handles the molecule as a collection of atoms held together by bonds and molecular energy in terms of force constants. Strictly speaking, the molecular mechanics method is not a quantum mechanical method since it does not use a molecular Hamiltonian operator or wavefunction.

Applications of computational chemistry have expanded rapidly with the growth in computational speed and lower computing cost. These methods have been rendered effective in studying molecular properties of compounds especially in the areas of combustion and halogenated hydrocarbon chemistry[63]. When it comes to the CVD process, the *ab initio* method and DFT calculations have provided a thermodynamic and

kinetic perspective for the development of reaction mechanisms for deposition of Si and related compounds[64-66].

Applying computational chemistry to the gas-phase precursors in CVD reactors has been investigated less, partially because of the large number of electrons associated with the second, third, and fourth row elements of the metalorganic materials for compound semiconductors[67].

In this chapter, a practical study of computational chemistry will be considered for combining experimental results with theoretical values to secure their validity. At first, a vibrational frequency calculation method will be described with two types of approaches based on the harmonic vibration assumption, and then the estimation method for thermodynamic properties and kinetic parameters will be shown in detail. Lastly, a calculation method of theoretical Raman intensity and differential Raman cross section will be described as practical applications.

### Vibrational Frequency

#### Classical Approach

A single particle of mass  $m$  attracted toward the origin by a force proportional to the displacement from the origin as follows :

$$F = -kx \quad (3-2)$$

where  $k$  is the force constant and  $F$  is the force on the particle. The force,  $F$ , is the source that the spring is not stretched greatly from its equilibrium position. From Newton's second law,  $F = ma$ , Eq.3-2 gives

$$-kx = m \frac{d^2x}{dt^2} \quad (3-3)$$

where  $t$  is the time. By solving Eq. 3-3, one can have the solution of

$$x = A \sin(2\pi\nu t + b) \quad (3-4)$$

where  $A$  and  $b$  are the integration constants, and the vibrational frequency  $\nu$  is

$$\nu = \frac{1}{2\pi} \sqrt{\frac{k}{m}} \quad (3-5)$$

A photon can be absorbed by a molecule if the frequency of the photons is the same as one of the normal vibrational modes of the molecule. That suggests a molecule that is in its ground vibrational state can be excited, so that it vibrates at a given frequency.

### Quantum Mechanical Approach

As described earlier, a diatomic molecule vibrates like two masses on a spring with a potential energy that depends on the square of the displacement from equilibrium. However, the energy levels are quantized at equally spaced values in the case of simple harmonic oscillator as shown in Fig. 3-1.

The Schrödinger equation for a harmonic oscillator can be converted by using the classical spring potential

$$V(x) = \frac{1}{2}kx^2 = \frac{1}{2}m\omega^2x^2 \quad (3-6)$$

where  $\omega = \sqrt{k/m}$  is the angular frequency. The Schrödinger equation with this potential energy of Eq. 3-6 is expressed as

$$-\frac{\hbar^2}{2m} \frac{d^2\Psi(x)}{dx^2} + \frac{1}{2}m\omega^2x^2\Psi(x) = E\Psi(x) \quad (3-7)$$

Eq. 3-7 can be solved with a differential equation solving method by substituting wavefunction  $\Psi(x)$  for  $\Psi(x) = Ce^{-\alpha x^2/2}$ , where  $\alpha = m\omega/\hbar$ . This leads to the ground state energy for the quantum harmonic oscillator, which is nonzero. This energy is called the

zero-point energy and is expressed as  $\frac{1}{2}\hbar\nu$  or equally  $\frac{1}{2}\hbar\omega$  since  $\omega=2\pi\nu$  and  $\hbar=\frac{\hbar}{2\pi}$ ,

where  $\hbar$  is the Planck's constant and has the value of  $6.626\times10^{-34}\text{m}^2\text{kg/s}$ . Note that the energy levels of the quantum harmonic oscillator are

$$E_n = \left(n + \frac{1}{2}\right)\hbar\omega \quad n = 0, 1, 2, 3, \dots \quad (3-8)$$

This zero-point energy is the most outstanding difference with the classical approximation. This means, even at the ground state and absolute zero temperature, molecules are not completely at rest. One can make Eq. 3-6 more useful by replacing  $x$  with  $R - R_e$ .  $R$  is the distance between atoms and  $R_e$  is the equilibrium distance when being in the ground state.

$$V(R) = \frac{1}{2}k(R - R_e)^2 \quad (3-9)$$

The simple harmonic oscillator approximation closely matches energies at lower energy levels as shown in Fig. 3-1, however, it yields unmatched energy levels as energy increases. Since a real molecule has anharmonicity to some extent, additional terms should be considered[68].

$$E_n = \left(n + \frac{1}{2}\right)\hbar\omega - \left(n + \frac{1}{2}\right)^2 \hbar\omega\chi_1 + \left(n + \frac{1}{2}\right)^3 \hbar\omega\chi_2 + [\text{higher terms}] \quad (3-10)$$

where  $\chi_1$  and  $\chi_2$  are anharmonicity constants. These correction terms provide much better match of the calculated energies to the experimentally observed energies. And it is depicted in Fig. 3-2 as red dotted lines.

However, Fig. 3-2 does indicate one obvious deficiency. In reality, at some internuclear distance, which occurs at 4.748 eV for the H<sub>2</sub> molecule, two atoms dissociate and each

atom is not bound each other anymore. In that state, the bond is broken and they are isolated. A more realistic model which describes this condition is the Morse potential as shown in Fig. 3-3.

The Morse potential energy function is of the form

$$V(r) = D_e(1 - e^{-\alpha(R-R_e)})^2 \quad \text{for } \alpha = \sqrt{\frac{k}{2D_e}} \quad (3-11)$$

where  $D_e$  is the depth of the potential well and  $k$  is the bond force constant, so  $\alpha$  dictates potential well width. The Morse potential shows anharmonicity in its shape and converges to  $V(r) = D_e$  as the bond distance  $R \rightarrow \infty$ . In addition, the 1-D Schrödinger equation is analytically solvable if the potential well is expressed by the Morse potential with its eigenvalues described by Eq. 3-10. For simplicity, Eq. 3-10 can be truncated to the second-order term

$$E_n = \left(n + \frac{1}{2}\right)\hbar\omega - \left(n + \frac{1}{2}\right)^2 \hbar\omega\chi_1 \quad (3-10b)$$

where anharmonicity constant  $\chi_1$  can be expressed

$$\chi_1 = \frac{\alpha^2\hbar}{2\mu\omega} = \frac{\hbar\omega}{4D_e} \quad (3-12)$$

With the energy expression above, the hot band transition can be calculated. The harmonic oscillator approximation works fine with the light molecules because vibrational frequencies are very high, however, when it comes to heavy molecules, it could yield considerable error for metalorganic molecules. Therefore, it should be noted that the anharmonicity of the potential energy surface on hot band transition can affect frequency shifts.

## Potential Energy Surfaces

The potential energy surface (PES) is deeply related to the Born-Oppenheimer approximation and is a hypersurface defined by the potential energy of a collection of atoms. This approximation allows us to separate electronic and nuclear motion as a product form. In addition, the validity of this separation between electronic and nuclear motion is due to the large ratio between electronic and nuclear masses. Since the energy of molecule is a function of the positions of nuclei, the potential energy surface expresses energy of a molecule in terms of its structure. From the minimum energystate, reactants undergoes various energy gradient, i.e. hills or saddle points, as shown in Fig. 3-4. The potential energy surface has  $3N-6$  coordinate dimensions, where N is the number of atoms not less than 3. Due to a large number of dimensions, complete potential energy surface for polyatomic molecules are very difficult to visualize. Thus a potential energy surface of a molecule is very important for finding transition states and stable products. Various attempts have been done to find more easily find transition states[69] and the internal reaction coordinate (IRC) with relatively a simple molecule due to the reason described above[70]. As a one-variable example, there are two forms of stable triethylgallium structure, i.e. as reported by Mitzel and his coworkers[71]. According to crystallographic data, three of the four molecules are found in a propeller-like structure with  $C_3$  symmetry and only one molecule of the four has two ethyl groups pointing toward each other. Usually ethyl groups connected to metal centers can rotate and it has been known that the rotation has an energy barrier. The potential energy surface representing the changing of the dihedral angle of  $C_\beta-C_\alpha-Ga-C_\alpha$  was simulated and depicted in Fig. 3-5 and appropriate structures were also shown.

Since the maximum relative energy difference is only 1.97 kcal/mol, the ethyl group can rotate without much restriction. In addition, the structure at a rotation angle of 90° and 270° is the initial structure for β-hydride elimination and it seems located in the relatively stable region to proceed into further reactions.

### Thermodynamic Properties

As one of the most useful applications of quantum chemistry to metalorganics, estimation of thermodynamic properties plays a crucial role. For estimating thermodynamic properties, one should note that there are a few very important approximations to be aware of. Firstly, all the equations assume particles do not interact with each other, an ideal gas approximation. Secondly, it is assumed that the first and higher excited states are inaccessible. This approximation can introduce some error for systems with low lying electronic excited states.

Usually four constituents contribute to one thermodynamic property, i.e. translation, electronic motion, rotational motion, and vibrational motion[72]. Although among these four contributions vibrational motion plays the major role, all four components should be considered.

#### Contribution from Translation

The starting point for a thermodynamic analysis is from considering the partition function for the corresponding component of the total partition function. The usual partition function for the translational contribution is

$$q_t = \left( \frac{2\pi m k_B T}{h^2} \right)^{\frac{3}{2}} V \quad (3-13)$$

where  $k_B$  is Boltzmann constant and has the value of  $1.381 \times 10^{-23} \text{ m}^2 \text{ kg/s}^2 \text{ K}$ .

From Eq. 3-13, the contribution to the internal thermal energy due to translation is as follows:

$$E_t = N_A k_B T^2 \left( \frac{\partial \ln q}{\partial T} \right)_V = \frac{3}{2} RT \quad (3-14)$$

since  $\left( \frac{\partial \ln q}{\partial T} \right)_V = \frac{3}{2T}$ .

### Contribution from Electronic Motion

The usual electronic partition function is:

$$q_e = \omega_0 e^{-\varepsilon_0/k_B T} + \omega_1 e^{-\varepsilon_1/k_B T} + \omega_2 e^{-\varepsilon_2/k_B T} + \dots \quad (3-15)$$

where  $\omega_n$  is the degeneracy of the energy of the  $n$ -th level, and  $\varepsilon_n$  is the energy of the  $n$ -th level. From the assumption of inaccessibility between the first and higher excited states at any temperature, the energy of the ground state is set to zero. This assumption simplifies the electronic partition function so that the electronic components of internal energy and the electronic heat capacity are zero such as  $U_{elec} = 0$  and  $C_e = 0$ , respectively.

### Contribution from Rotational Motion

The molecular rotation contribution can be separated into several cases according to the molecule's type, i.e. single atom, linear polyatomic molecule and non-linear polyatomic molecule. For a single atom case, because  $q_r$  does not depend on temperature,  $q_r = 1$ . For a linear polyatomic molecule, the rotational partition function is as follows:

$$q_r = \frac{1}{\sigma_r} \left( \frac{T}{\Theta_r} \right) \quad (3-16)$$

where  $\sigma_r$  is 1 for asymmetric linear molecules and 2 for symmetric linear molecules.

Other than these values, rotational symmetry numbers are different according to the molecular point groups as shown in Table 3-1.  $\Theta_r = h^2 / 8\pi^2 I k_B$  and  $I$  is the molecular moment of inertia of the linear molecule.

From Eq.3-16, the contribution from rotational motion to the internal energy is:

$$\begin{aligned} E_r &= RT^2 \left( \frac{\partial \ln q_r}{\partial T} \right)_V \\ &= RT \end{aligned} \quad (3-17)$$

Lastly, for the general nonlinear polyatomic molecule, the rotational partition function is:

$$q_r = \frac{\pi^{1/2}}{\sigma_r} \left( \frac{T^{3/2}}{\sqrt{\Theta_{r,x} \Theta_{r,y} \Theta_{r,z}}} \right) \quad (3-18)$$

where  $\Theta_{r,x}$ ,  $\Theta_{r,y}$ , and  $\Theta_{r,z}$  are x, y, and z directional contribution at temperature  $T$ , respectively.

From Eq. 3-13, the contribution to the internal thermal energy due to rotation for the polyatomic linear molecule is as follows:

$$\begin{aligned} E_r &= RT^2 \left( \frac{\partial \ln q_r}{\partial T} \right)_V \\ &= \frac{3}{2} RT \end{aligned} \quad (3-19)$$

### Contribution from Vibration

The contributions to the partition function, internal energy, entropy, and heat capacity from vibrational motions are a little more complicated than those of other

motions and are composed of a product or sum of the contributions from each vibrational mode, K. As for the contributions from vibration, only the real frequencies are counted. Imaginary frequencies that were expressed with a minus sign in the quantum calculations output and describe imaginary bond such as one in the transition state would not be considered. A molecule with  $n$  atoms has  $3n - 6$  degree of freedom while linear molecule has  $3n - 5$ , and each mode has a characteristic vibrational temperature,  $\Theta_{v,K} = h\nu_K / k_B$ . And the partition function from a given vibrational mode is:

$$q_{v,K} = \frac{e^{-\Theta_{v,K}/2T}}{1 - e^{-\Theta_{v,K}/2T}} \quad (3-20)$$

and the overall vibrational partition function is described by a product of partition functions for each vibrational mode and expressed as follows:

$$q_v = \prod_K \frac{e^{-\Theta_{v,K}/2T}}{1 - e^{-\Theta_{v,K}/2T}} \quad (3-21)$$

From Eq. 3-21, the contribution to internal thermal energy resulting from molecular vibration is:

$$E_v = R \sum_K \Theta_{v,K} \left( \frac{1}{2} + \frac{1}{e^{-\Theta_{v,K}/2T} - 1} \right) \quad (3-22)$$

One should note that all four contributions are considered for estimating thermodynamic properties.

### Kinetic Parameters

Calculating kinetic parameters, such as rate constant and activation energy for the reaction depends on transition-state theory. Although the geometry and energy of stable molecules can be specified with experimentally to a greater accuracy, transition-states cannot be isolated experimentally since its lifetime is very short and it is

unstable[69]. Thus elucidating transition-states is one of the most advantageous targets for computational chemistry. Among a number of different methods to derive the fundamental equations of transition-state theory, one can follow the most intuitive way, with the example hereafter. First of all, consider the simple reaction depicted in Fig. 3-6.

The product B was produced from the reactant A via transition state  $A^\ddagger$ . A reversible first reaction has rate constants  $k_1$  and  $k_{-1}$  for forward and reverse reactions, respectively. For the relation between rate constants, molar concentration and equilibrium constant:

$$k_1 = \frac{k^+ [A^\ddagger]}{[A]} = k^+ K^+ \quad (3-23)$$

where  $K^+$  is the equilibrium constant between the transition-state complex and the reactant. From the relationship between Gibbs free energy and the equilibrium constant:

$$K^+ = e^{-(G^\ddagger - G_A)/k_B T} \quad (3-24)$$

where the difference of free energy,  $G^\ddagger - G_A$ , is meant for the activation free energy, i.e.  $\Delta G^\ddagger$ . From the relation  $G = U_o + PV - k_B T \ln Q$ , where  $Q$  is the partition function, Eqs. 3-23 and 3-24 can be combined as follows:

$$\begin{aligned} K^+ &= e^{-[(U^\ddagger + PV^\ddagger - k_B T \ln Q_+) - (U_A + PV_A - k_B T \ln Q_A)]/k_B T} \\ &= \frac{Q_+}{Q_A} e^{-(U^\ddagger - U_A)/k_B T} e^{-(PV^\ddagger - PV_A)/k_B T} \\ &\approx \frac{Q_+}{Q_A} e^{-(U^\ddagger - U_A)/k_B T} \end{aligned} \quad (3-25)$$

It can be assumed the changes in PV are negligible, thus from Eqs. 3-23 and 3-25:

$$k_1 = k^+ \frac{Q^+}{Q_A} e^{-(U^+ - U_A)/k_B T} \quad (3-26)$$

By separating the partition function for the reaction coordinate degree of freedom, it can be written

$$\begin{aligned} k_1 &= \frac{k_B T}{h} \frac{Q^+}{Q_A} e^{-(U^+ - U_A)/k_B T} \\ &= \frac{k_B T}{h} e^{-\Delta G^{o,+}/RT} \end{aligned} \quad (3-27)$$

or equally,

$$k_1 = \frac{k_B T}{h} e^{-\Delta H^{o,+}/RT} e^{-\Delta S^{o,+}/R} \quad (3-28)$$

By using Eq. 3-28, one can calculate rate constants based on following criteria:

$$\Delta G^+ = G^+ - G_A \quad (3-29)$$

For example, the first  $\beta$ -hydride elimination of triethylgallium follows reaction as shown in Fig. 3-7;

Since triethylgallium has an ethyl group and it is known to undergo  $\beta$ -hydride elimination with relatively low energy. The spin polarized hybrid density functional B3LYP with the LanL2DZ calculations using Gaussian 03 program suite[73] were performed. Isolation of  $\beta$ -hydride elimination during the thermal decomposition process of triethylgallium is difficult, and so information about kinetic parameters of  $\beta$ -hydride elimination is limiting. However, compared with experimental result of 38.7 kcal/mol reported by Wong and his coworkers[6] and calculated one of 43.6 kcal/mol by Tsuda and his coworkers[74] for  $E_{a,1}$ , the enthalpy change result of 38.3 kcal/mol in this study

agrees very well with reference data. In addition  $k_1$  was calculated to be  $30.6 \text{ s}^{-1}$  and it has been reported in the range  $11.3$  to  $36.1 \text{ s}^{-1}$  by other researchers and they reported  $E_{a,1}$  in the range  $22.7$  to  $47.2 \text{ kcal/mol}$ [7, 9, 75]. As McDaniel and his coworker reported[76], decomposition reaction kinetics of metalorganic precursors are inclined to change according to experimental condition such as carrier gas, reactor temperature, and reactor type. Complete decomposition mechanism of triethylgallium will be discussed more in detail in a later chapter.

### **Theoretical Raman Intensity and Absolute Differential Raman Cross-section**

The progress of computational chemistry for vibrational Raman spectral predictions allows us to estimate theoretical Raman intensity and absolute differential Raman cross-section among other values. Schrötter and Klöckner reported details of various gases and liquids for analytic calculations[14]. They provide an excellent review of experimental data with the Raman scattering model. The relationship of the absolute differential Raman scattering cross-section of a Stokes shifted vibrational Raman band  $\nu_j$ , is given by:

$$\frac{d\sigma_j}{d\Omega} \Big|_{\nu_0, \theta} = \frac{2^4 \pi^4}{45} \frac{(\nu_0 - \nu_j)^4 b_j^2}{1 - \exp(-hc\nu_j / kT)} S_j f(j, \theta) \quad (3-30)$$

where  $b_j^2 = h / 8\pi^2 c \nu_j$ , the square of the zero point amplitude, the angular factor  $f(j, \theta) = [2\rho_j + (1 - \rho_j) \sin^2 \theta] / (1 + \rho_j)$ , and the Raman activity  $S_j = g_j (45a_j^2 + 7\gamma_j^2)$ . Eq. 3-30 depends on the temperature through the exponential, which is negligible (less than 1%) for the region below  $1000 \text{ cm}^{-1}$ [14].  $g_j$  in Raman activity denotes the degree of degeneracy of the normal vibration  $\nu_j$ . Typically Raman experiments are set for  $90^\circ$

scattered angle where  $\theta$  is the angle between the direction of observation without polarization and the polarization vector of the linearly polarized exciting radiation and so the depolarization ratio  $\rho_j$  of the Raman band  $\nu_j$  is given by:

$$\rho_j = \frac{3\gamma_j^2}{45a_j^2 + 4\gamma_j^2} \quad (3-31)$$

and the angular factor  $f(j, \theta)$  approaches unity.

From this basis, the theoretical Raman intensity,  $I_j^R$ , which simulates the measured Raman spectrum can be calculated according to the formula

$$I_j^R = f \frac{(\nu_0 - \nu_j)^4}{\nu_j} \frac{S_i}{1 - \exp(-hcv_j/kT)} \quad (3-32)$$

where  $f$  is an appropriately chosen common scaling factor for all peak intensity[77].

Raman scattering activity,  $S_j$ , can be calculated *ab initio* or by the DFT method[78].

Using Eqs.3-30 and 3-32, the Raman scattering intensity and the absolute differential Raman scattering cross-section can be predicted. For comparison of experimental results with simulated ones, the liquid phase Raman experiment for neat benzonitrile was performed. Using the liquid chamber, the 0.1W Nd:YAG solid-state laser line was used to excite the neat benzonitrile source and vibrational Raman excitation lines were recorded through the range of 100~4000cm<sup>-1</sup>. Even at a low intensity of the excitation line, the measured intensity was sufficiently high and it shows a very good signal to noise (S/N) ratio. The experimental Raman scattering data and various simulated results are compared and shown in Fig. 3-8 with pure Lorentzian line shapes and a bandwidth (FWHH; Full Width at Half-Height) of 5 cm<sup>-1</sup>.

As one can find out, all three HF simulation results show large discrepancies in predicting vibrational frequencies and intensities, the B3LYP method shows relatively good results, and the MP2 method shows mid-performance.

### **The Selection of Basis Set**

Choosing a model of a chemical system always involves a trade-off between computational cost and accuracy because larger basis set runs longer. Even though larger basis set can describe the locations of the electrons in space more accurately, one cannot ignore computational cost. However, inappropriate basis set cannot give good description of electron state. Therefore, the selection of basis set is very important in computational calculations.

At an early stage of computational chemistry, minimal basis sets, for example STO-nG (Slater Type Orbital), where n is an integer, have been used. This approximates Slater orbitals with Gaussian functions. Other than this, one can increase the size of a basis set by adding more functions to each atom, for instance, split valence basis set. Similarly, triplet split valence basis set such like 6-311G uses three sizes of contracted functions for each orbital.

In this research, the B3LYP density functional model with LanL2DZ basis set was selected because it shows good performance on electron affinities, excellent performance on bond energy and reasonably good results on vibrational frequencies and geometries of ion and inorganic compounds. B3LYP is one of the hybrid functionals that approximate exchange-correlation energy functional by constructing a linear combination of the Hartree-Fock exact exchange functional and any number of exchange and correlation density functionals. It was developed by Hay and Wadt and has been widely used in quantum chemistry, especially in study of compounds that

contains heavy atoms. In addition to that, basis set superposition error was considered using counterpoise(CP) method to correct basis set overlapping especially in the case of ammonia adduct formation.

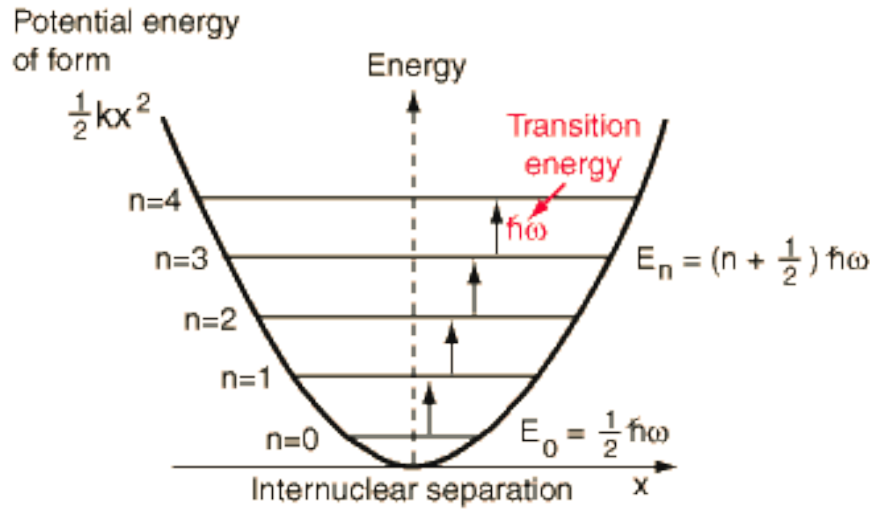


Figure 3-1. Potential energy diagram of simple harmonic oscillator.

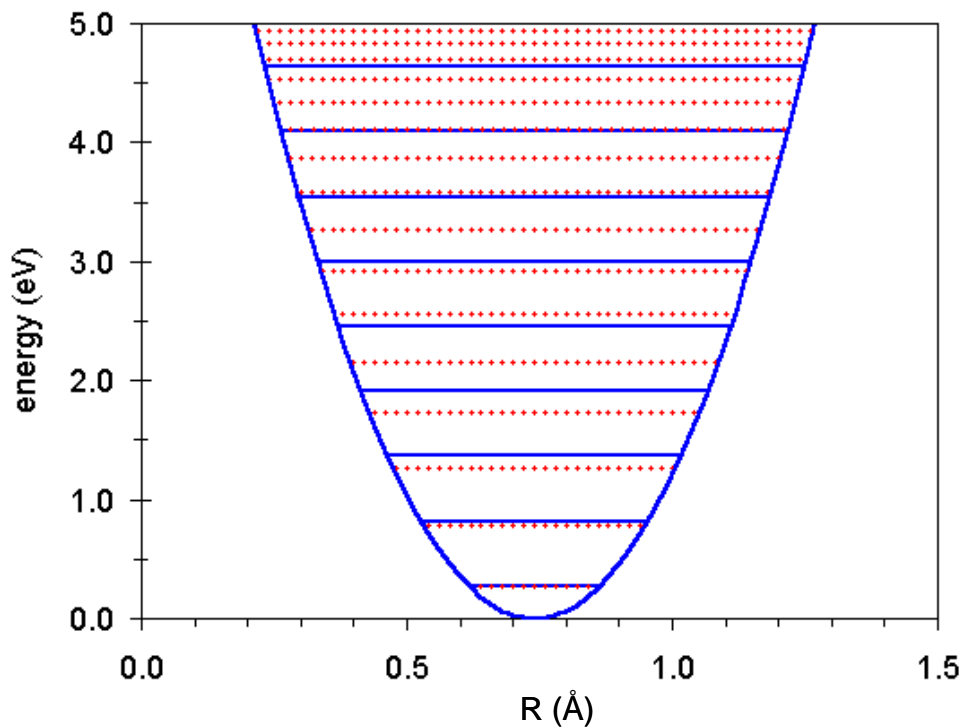


Figure 3-2. Potential energy diagram for harmonic and anharmonic oscillator.

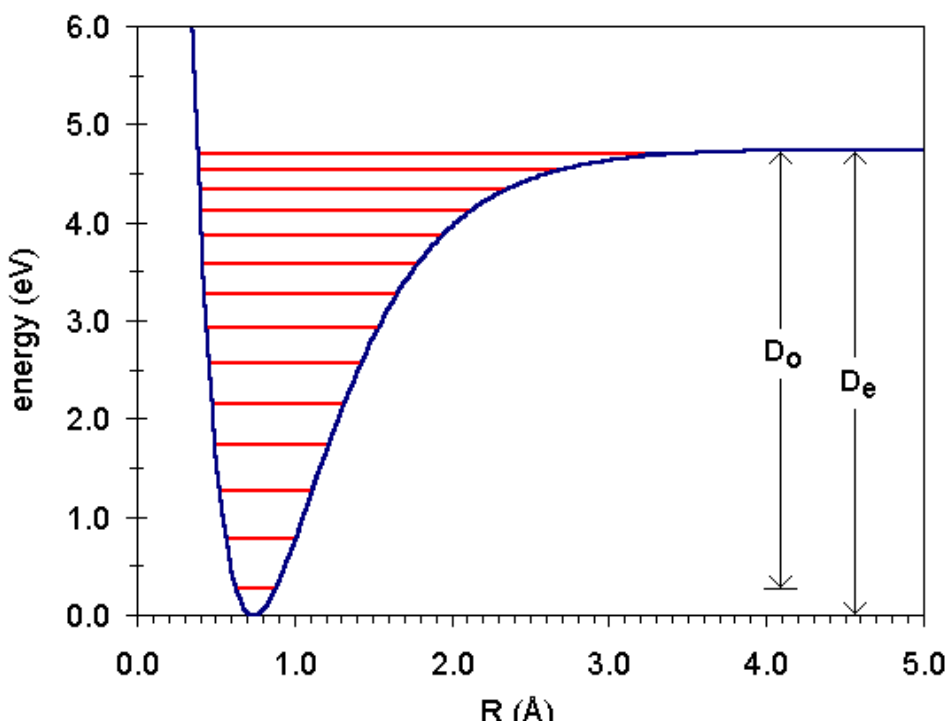


Figure 3-3. Morse potential.  $(D_e - D_0)$  means zero-point energy.

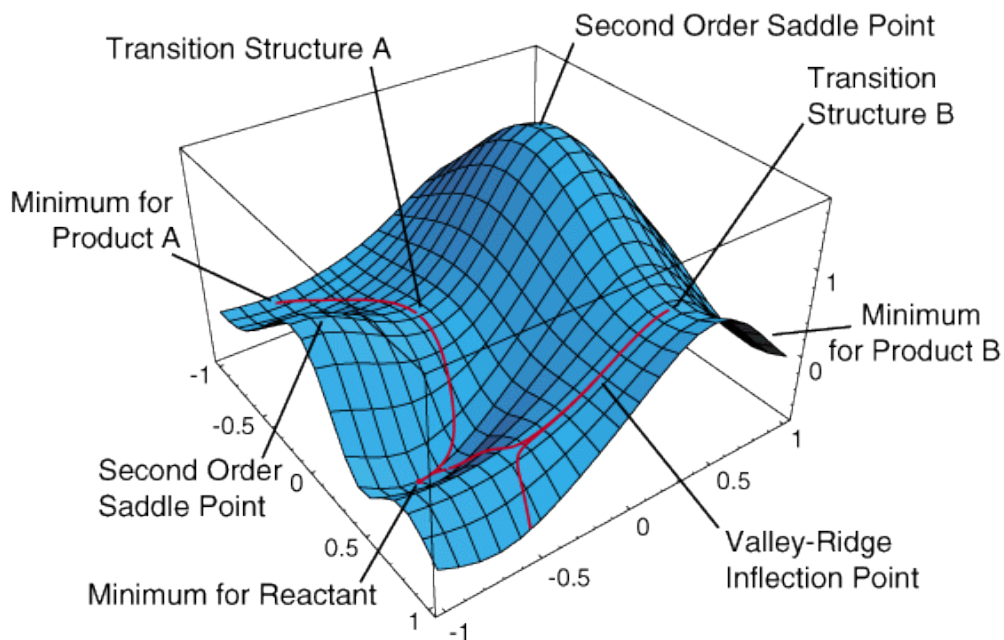


Figure 3-4. Example of potential energy surface with two variables. Figure was taken from Ref. [79].

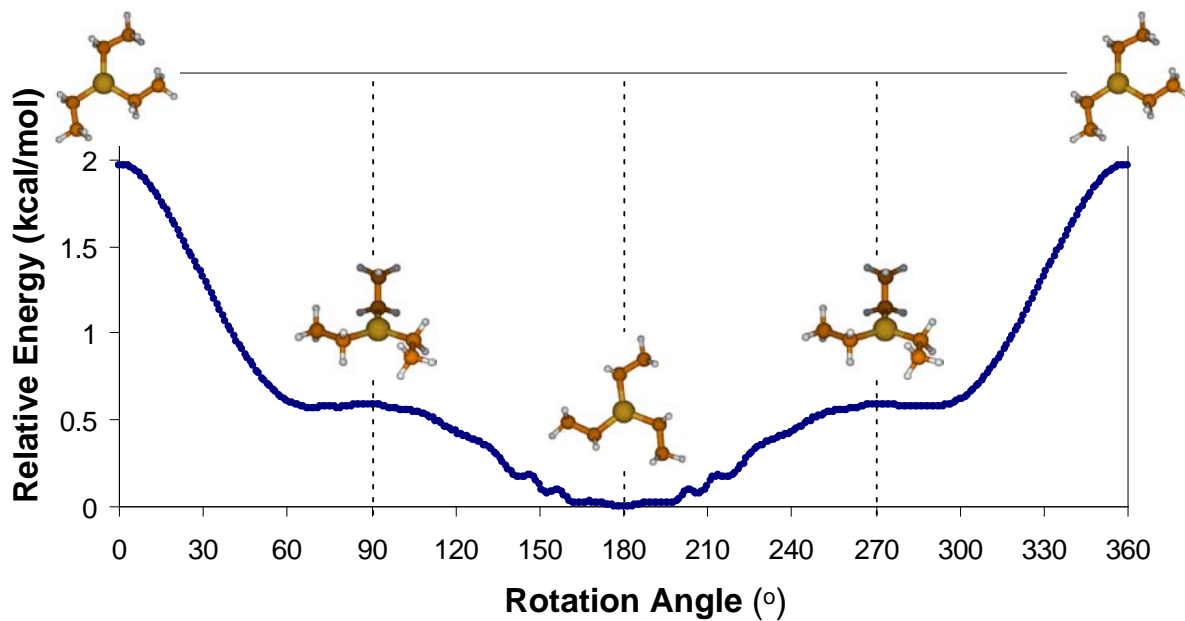


Figure 3-5. Relative energy diagram according to the change of rotation angle of ethyl group in triethylgallium.

Table 3-1. Rotational symmetry numbers for molecular point groups[62]

Point Group	$\sigma_r$
$C_{\infty v}$	1
$D_{\infty h}$	2
$S_n, n = 2, 4, 6, \dots$	$n/2$
$C_n, n = 2, 3, 4, \dots$	$n$
$C_{nh}, n = 2, 3, 4, \dots$	$n$
$D_n, n = 2, 3, 4, \dots$	$2n$
$D_{nh}, n = 2, 3, 4, \dots$	$2n$
$T$	12
$O_h$	24

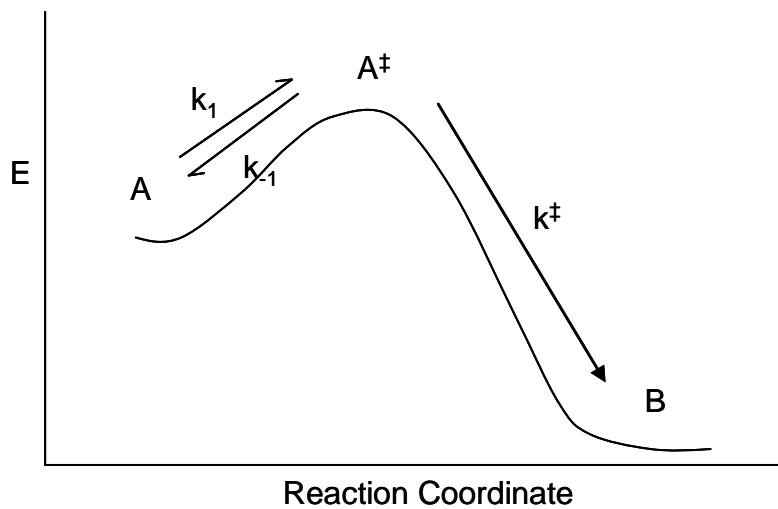


Figure 3-6. The nature of simple reaction including transition-state  $A^\ddagger$ .

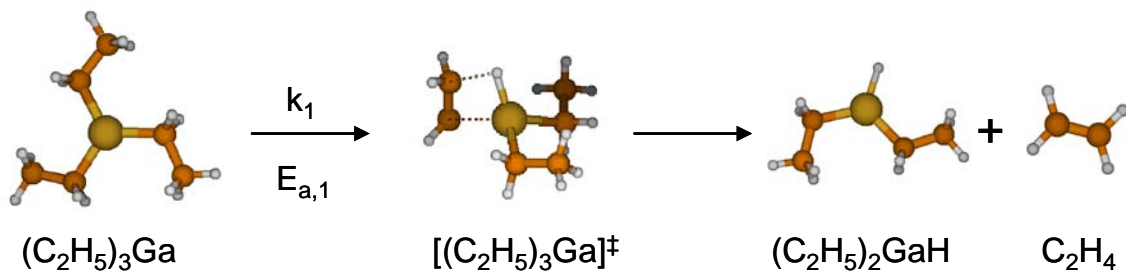


Figure 3-7. The first  $\beta$ -hydride elimination process of triethylgallium with geometry optimized transition state using B3LYP/LanL2DZ level of chemistry.

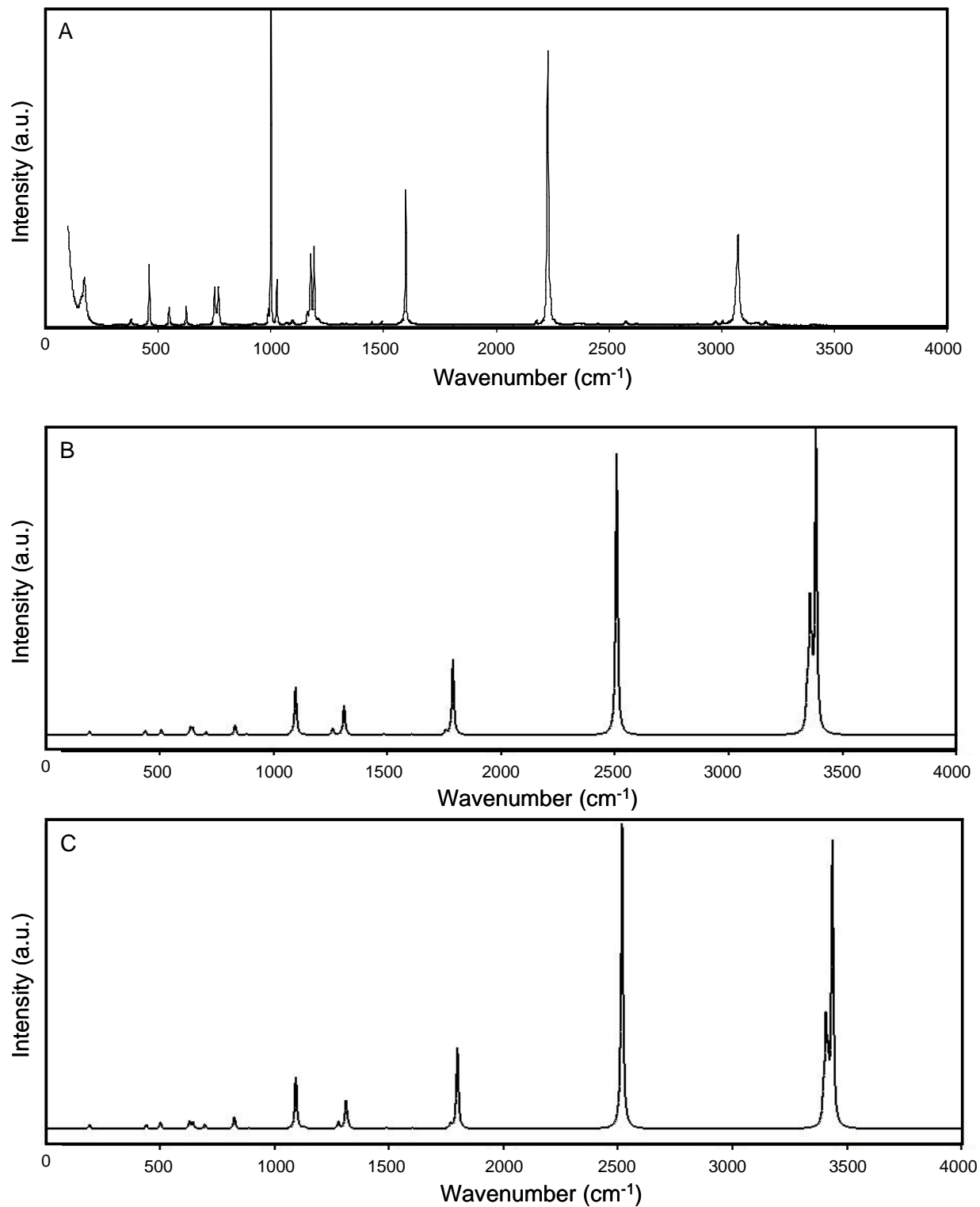


Figure 3-8. Comparison of experimental and simulated results. (A) experimental Raman spectra of liquid benzonitrile, (B) Simulated results using HF/6-311G level of chemistry, (C) HF/LanL2DZ, (D) HF/SDD, (E) B3LYP/6-311G, (F) B3LYP/LanL2DZ, (G) B3LYP/SDD, (H) MP2/LanL2DZ, (I) MP2/SDD.

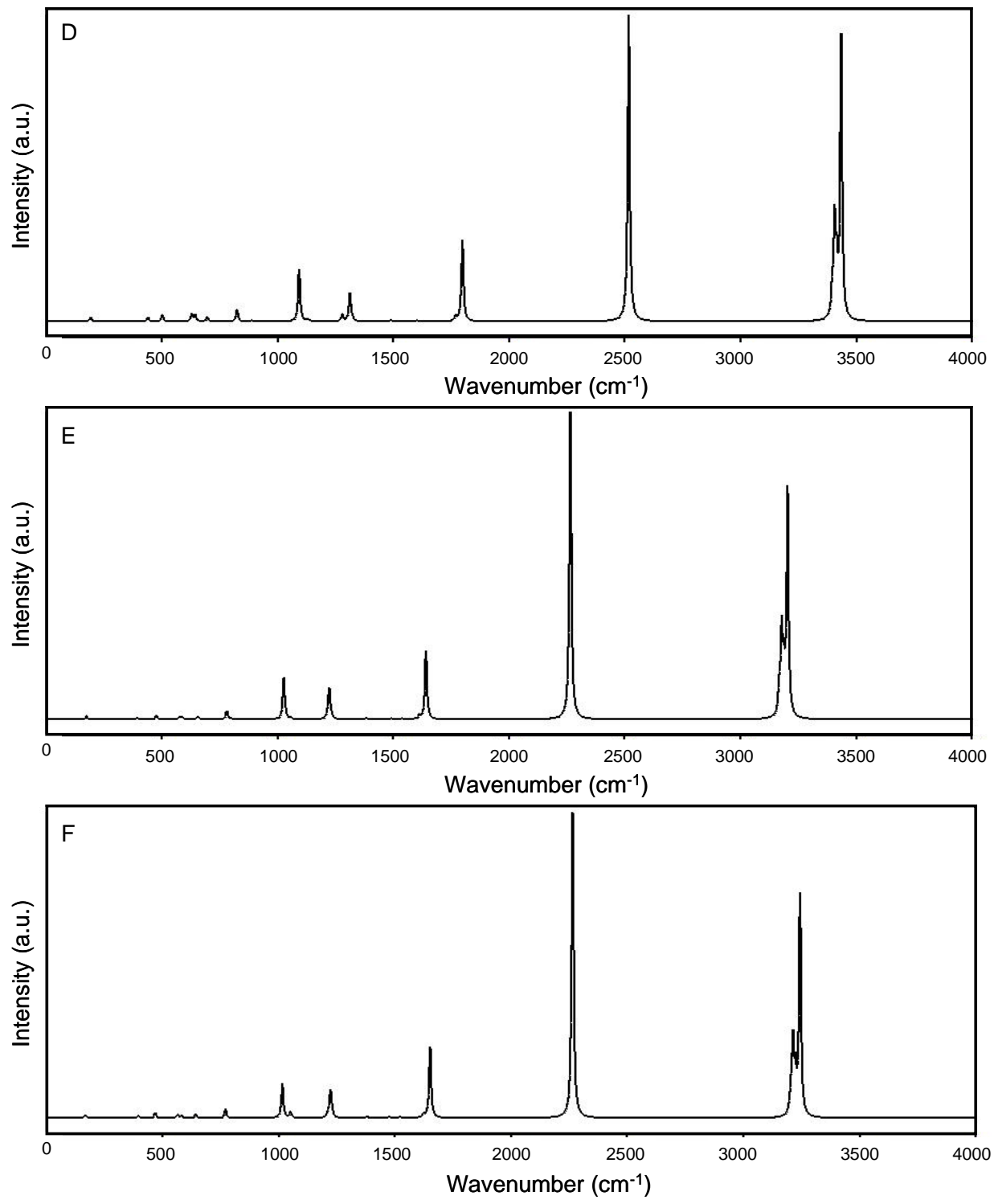


Figure 3-8. Continued

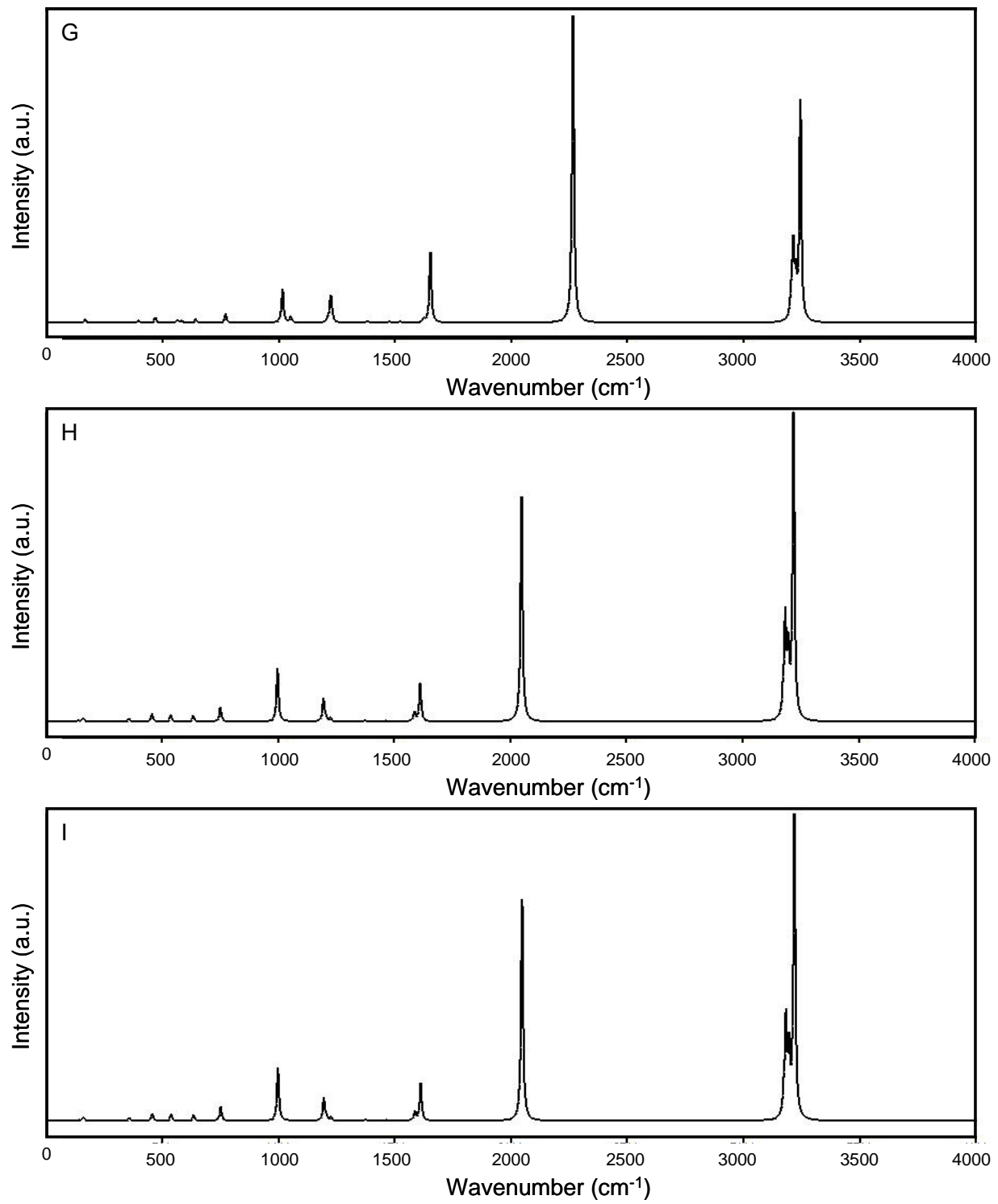


Figure 3-8. Continued.

## CHAPTER 4

### REACTOR MODELING AND PARAMETER ESTIMATION

Metalorganic Chemical vapor deposition (MOCVD) reactors have been widely used to deposit thin films in the semiconductor industry. Frequently, the performance of these films depends on their uniformity in thickness and composition. And this uniformity strongly depends on the heat and mass transfer conditions in the reactor, especially the region adjacent to the heated substrate since homogeneous reactions more readily occur in this layer. Reactor modeling is very useful because it can suggest efficient reactor designs, optimize reaction conditions, and thus improve device properties. However, factors important in reactor modelling are complex, and include buoyancy-driven convection, homogeneous and heterogeneous gas phase reactions of precursors, the strong temperature dependence of the physical properties of gases, and parasitic reactions at the cold-wall[80, 81].In particular, the limiting factor is most often the lack of reaction mechanism and quantitative rate parameters. In MOCVD, thermal decomposition reactions can produce hydrocarbon radicals that are responsible for carbon incorporation in films or the formation of undesired compounds consuming the desired metals. To minimize parasitic gas phase reactions and improve film deposition performance, transport processes are critical in this context. The large thermal gradient that is typical condition in a CVD reactor can produce buoyancy-driven recirculation flow leading to growth rate variation, inconsistent film quality, impurity incorporation and graded composition across the heterojunctions [82].In other words, those secondary flows adversely affect film thickness and composition uniformity by superimposing on the main flow. When it comes to recirculation flow of the CVD reactor used in this research, the upflow reactor geometry has advantage that the cold gas flows up toward

the heated substrate and it makes the flow stable since the buoyancy tends to progress upward. Due to the importance of transport phenomena, it has been studied extensively in experimental and modeling studies[83].

In the following, a brief mathematical description of transport phenomena, parameter estimation process using analytical and computational calculations, and the procedure for solving the inverse problem using optimization algorithm encoded FORTRAN language are described.

### **Mathematical Description of CVD Reactor**

Modeling a CVD reactor requires solving the equations for conservation of momentum, energy and mass. In the presence of homogeneous gas phase reactions, the steady-state transport processes within CVD reactors are described with the following set of equations[84].

- Conservation of momentum

$$\rho(\vec{v} \cdot \nabla \vec{v}) = -\nabla p + \nabla \cdot \mu(\nabla \vec{v} + (\nabla \vec{v})^T) + \rho \vec{g} \quad (4-1)$$

- Conservation of energy

$$\rho C_p \vec{v} \cdot \nabla T = \nabla \cdot k \nabla T \quad (4-2)$$

- Conservation of mass for species k

$$\rho \vec{v} \cdot \nabla w_k = \nabla \cdot \left( \sum_{i=1}^{\lambda-1} L_{ki} \nabla w_i + G_k \nabla \ln T \right) + r_k, \quad k = 1, \dots, \lambda-1 \quad (4-3)$$

- Continuity equation

$$\nabla \cdot \rho \vec{v} = 0 \quad (4-4)$$

- Ideal gas law (equation of state)

$$\rho = \frac{MP}{RT} \quad (4-5)$$

where  $\rho$ ,  $M$ ,  $P$ ,  $R$ ,  $T$  are the density, molecular weight of the gas, the nominal pressure of the reactor, gas constant, and reactor temperature, respectively. And  $\mu$ ,  $C_p$ ,  $\vec{v}$ ,  $p$ ,  $k$  and  $\vec{g}$  are the viscosity, heat capacity of the gas, pressure within the reactor, thermal conductivity and gravity vector, respectively. In addition,  $L_{ki}$ ,  $G_k$ ,  $w_k$  and  $r_k$  represent the multi component diffusion effect, thermal diffusion effect, the mass fraction and production rate of species k, respectively[84].

Based on those governing equations, appropriate boundary conditions must be set to describe reactor conditions correctly, and natural boundary conditions were applied along the reactor centerline and reactor walls. First of all, due to the axisymmetry of the reactor, the right half of the reactor was set for the modeling domain. For the momentum calculations, the no-slip condition was applied to the walls of the reactor and the susceptor surface. Three temperatures at the heater, ambient, and inlet region are given for the energy conservation. The ambient temperature is contributed to consider Newton's law of cooling. Because the reactor walls and susceptor are impenetrable and non-reacting surfaces (chemically inert), mass diffusion flux normal to the surface of component k is zero.

More often than not, the equations in dimensionless form are helpful in analysis of mass transport phenomena[85]. Since these dimensionless equations give approximate orders of magnitude, dimensionless groups are sometimes very useful. Typical useful dimensionless groups for describing CVD reactor with typical order of magnitude and physical meaning are tabulated in Table 4-1. For example, the Peclet number can be expressed as follows:

$$Pe = Re Pr = \frac{\langle v \rangle L}{\nu} \cdot \frac{\nu}{\alpha} = \frac{\langle v \rangle L}{\alpha} \quad (4-6)$$

$$\text{or } Pe = Re Pr = \frac{\rho C_p v_0 (T_1 - T_0) / l_0}{k(T_1 - T_0) / l_0^2} \quad (4-7)$$

The calculated Peclet number value for the CVD reactor used in this study at typical experimental conditions is approximately 99.96 at 375.15 K and this value is almost identical to the results for an infinite Peclet number. At the higher temperature, Peclet number is increased. In other words, heat transport by convection is far more dominant than that by conduction in this system[80].

### Parameter Estimation

To predict the kinetic behavior of gases, various kinetic theories have been studied. Among widely used theories, elementary kinetic theory characterized by a mean molecular velocity and a mean free path for low density gases describes three useful properties, i.e., thermal conductivity( $k$ ), binary diffusivity( $D_{AB}$ ), viscosity( $\mu$ ), at temperature  $T$  as follows[86]:

$$k = \frac{1}{3} \sqrt{\frac{RT}{\pi^3}} \frac{2M_A M_B}{(M_A + M_B)} \frac{C_p}{N_A d^2} \quad (4-8)$$

$$D_{AB} = \frac{1}{3} \sqrt{\frac{R^3 T^3}{\pi^3}} \frac{(M_A + M_B)}{2M_A M_B} \frac{1}{p N_A d^2} \quad (4-9)$$

$$\mu = \frac{1}{3} \sqrt{\frac{RT}{\pi^3}} \frac{2M_A M_B}{(M_A + M_B)} \frac{1}{N_A d^2} \quad (4-10)$$

where,  $M_A$ ,  $M_B$ ,  $C_p$ ,  $N_A$ ,  $p$ , and  $d$  are molecular weight of molecule A and B, heat capacity, Avogadro number, pressure, and molecular diameter, respectively. However, one should note that these relationships show discrepancies and can be corrected by

the rigorous kinetic theory of Chapman and Enskog, which considers in some detail the effect of intermolecular potential energies on the interactions between colliding molecules. By applying Chapman-Enskog theory to binary gas mixture, the kinetic parameters mentioned above can be predicted more accurately since Chapman-Enskog theory takes into account the force field between molecules and their finite diameter[87]. In addition the Chapman-Enskog theory treats the molecules as symmetric spheres and assumes that all collisions are binary and elastic and that molecular motion during collisions can be described by classical mechanics.

$$k = 5.9073 \times 10^{-2} \frac{\sqrt{T(M_A + M_B)/M_A M_B}}{\sigma_{AB}^2 \Omega_{k,AB}} \quad [\text{J/m}\cdot\text{s}\cdot\text{K}] \quad (4-11)$$

$$D_{AB} = 1.8583 \times 10^{-7} \frac{\sqrt{T^3(M_A + M_B)/M_A M_B}}{p \sigma_{AB}^2 \Omega_{D,AB}} \quad [\text{m}^2/\text{s}] \quad (4-12)$$

$$\mu = 3.7750 \times 10^{-6} \frac{\sqrt{T M_A M_B / (M_A + M_B)}}{p \sigma_{AB}^2 \Omega_{D,AB}} \quad [\text{Pa}\cdot\text{s}] \quad (4-13)$$

where  $\sigma$  and  $\Omega$ 's are the collision diameter and collision integrals. In addition the collision integral for thermal conductivity,  $\Omega_k$ , is identical to that for viscosity,  $\Omega_\mu$  and values of  $\Omega_\mu = \Omega_k$  are given for the Lennard-Jones intermolecular potential as a function of the dimensionless temperature,  $kT/\varepsilon$  [85]. These collision integrals are interpreted as describing the deviation from the rigid sphere behavior. The  $\varepsilon$  quantity in the Lennard-Jones potential is a characteristic energy denoting the maximum energy of attraction between a pair of molecules. For binary mixtures  $\varepsilon_{AB}$  is usually approximated by a geometric average of the contributions from the two species as  $\varepsilon_{AB} = \sqrt{\varepsilon_A \varepsilon_B}$  and  $\sigma_{AB}$

is approximated as  $\sigma_{AB} = \frac{1}{2}(\sigma_A + \sigma_B)$  [88]. Relevant collision diameters, actual and calculated binary diffusivities are tabulated in Table 4-2.

The Lennard-Jones potential parameters of  $\varepsilon$  ( $\text{\AA}$ ) and  $\sigma$  (J/mol) are estimated using the method of Le Bas[84].

$$\sigma = 1.18V_B^{1/3} \quad (4-14)$$

$$\varepsilon = 1.15kT_B \quad (4-15)$$

where  $T_B$  and  $V_B$  are the normal boiling point (K) and the Le Bas volume ( $\text{cm}^3/\text{mol}$ ). In addition Lennard-Jones parameter  $\varepsilon$  is used to calculate the dimensionless collision integrals  $\Omega^{(1,1)*}$ ,  $\Omega^{(1,2)*}$ , and  $\Omega^{(2,2)*}$  and these are calculated empirically by Neufeld and his coworkers. In this work following collision integrals are used among 16 collision integrals suggested[89].

$$\Omega_\mu = \Omega_k = \frac{1.16145}{T_*^{0.14874}} + \frac{0.52487}{e^{0.7732T_*}} + \frac{2.16178}{e^{2.43787T_*}} \quad (4-16)$$

$$\Omega_D = \frac{1.06036}{T_*^{0.15610}} + \frac{0.19300}{e^{0.47635T_*}} + \frac{1.03587}{e^{1.52996T_*}} + \frac{1.76474}{e^{3.89411T_*}} \quad (4-17)$$

where  $T_* = kT / \varepsilon$ . A simple semi empirical method which accounts for the energy exchange in polyatomic gases was developed by Eucken [90] and thermal conductivity of a polyatomic gas at low density is described as:

$$k = \left( C_p + \frac{5}{4}R \right) \frac{\mu}{M} \\ = 4.1772 \times 10^{-2} \frac{\sqrt{T M_A M_B / (M_A + M_B)}}{\sigma_{AB}^2 \Omega_{k,AB}} \quad [\text{J/m}\cdot\text{s}\cdot\text{K}] \quad (4-18)$$

where  $M = 2M_A M_B / (M_A + M_B)$ . Eq. 4-11 can be replaced with Eq. 4-18 for more accuracy since target system consists of polyatomic molecules.

For CVD modeling, heat capacities of metalorganic sources and their reaction intermediates are required. Rotational and vibrational contributions to the heat capacities can be calculated based on quantum chemistry, which has been discussed in Chapter 3 in detail. As examples, the comparison of calculated results with experimental values of heat capacity at 1 atm for N<sub>2</sub>, C<sub>2</sub>H<sub>4</sub>, C<sub>4</sub>H<sub>10</sub> are shown in Fig. 4-1. For these calculations, Gaussian 03 program was used with same level of chemistry (B3LYP/LanL2DZ) for consistency.

Obviously, calculated estimations for heat capacity show good agreement with experimental observations. For N<sub>2</sub>, although difference between two sets of data increases as temperature rise, the maximum calculated deviation from experimental results is at most 0.55 % at 800K. The deviation was calculated based on the following expression:

$$\text{Deviation}(\%) = \frac{(\text{Experiment value} - \text{Calculation value})}{\text{Experiment value}} \times 100 \quad (4-19)$$

Deviations of all available temperatures are tabulated in Table 4-3.

Even though deviation of butane at 300K is 10.21 %, it shows a decreasing trend as temperature increases and thus using the calculation data would not be problematic since the typical temperature range in which butane is produced as an intermediate from parent metalorganic precursors used in this study is at least higher than 400K. As one can see in Table 4-3, the calculated values for nitrogen are underestimated, while those for ethane and butane are overestimated.

For the triethylgallium case, boundary conditions were set as follows: 5 % triethylgallium was introduced through center inlet and pure nitrogen was used as a carrier gas with the velocity of 2.5 cm/s for all three gas inlets. The heater, inlet, and wall temperatures were set at 700, 200, and 22 °C, respectively. The heater temperature was measured with a thermocouple underneath the heating material, the inlet temperature with rotational Raman spectrum of nitrogen as described in chapter 2, and the wall temperature with handheld thermocouple. Fig. 4-2 shows temperature and concentration contours in the reactor. One should note that Fig. 4-2 shows time independent case, which means sufficient time has been allowed to make stable stream in the reactor. In addition, one can certify any directional profiles such as radial, axial or even diagonal positions. In Fig. 4-2A, continuous arrows show velocity vector notation of gas flow and it obviously confirms there is no eddy or recirculation flow that inhibits good quality film deposition by occurring flow instability.

Temperature and concentration profiles versus the radial position are extracted and shown in Fig. 4-3 with 10 mm intervals from 50 mm to 110 mm of z-altitude. Obviously, the temperature profile decreases as distance from susceptor increases, however, concentration propagation in the direction of reactor wall can be confirmed and the interval between each profile at zero radial position increases and then decreases. One can presume the steady increase of triethylgallium concentration at 15 mm through 20 mm is due to the diffusion from the centerline to the reactor wall since pure nitrogen is the only component in the annulus and sweep flows. Due to this phenomenon, axial concentration profiles show sigmoidal shape.

From these results, one can estimate reaction parameters such as A-factor (pre-exponential factor) and activation energy of each reaction associated with a specific CVD reaction mechanism. For example, for two major initial reactions of triethylgallium, homolysis and  $\beta$ -hydride elimination of the ethyl group, the A-factors were estimated as 65.0 kcal/mol and 40.3 kcal/mol for these two reactions. And activation energy was estimated using DFT calculations as  $4.68 \times 10^{22} \text{ s}^{-1}$  and  $1.95 \times 10^{13} \text{ s}^{-1}$ , respectively. One can find more details about these calculation results from next chapter.

The overall process of CVD, including gas phase hydrodynamics, mass transport, homogeneous and surface-mediated chemistry, and physical diffusion and nucleation on the surface, is so complex that one cannot elucidate all the processes clearly. However, CVD modeling helps to examine each step individually so that the relative importance of each step can be established.

### **Solving Inverse Problem Using Optimization Algorithm**

From aforementioned initial guesses for A-factor and activation energy by DFT calculations, the numerical reactor model can simulate the triethylgallium decomposition process considering two major reactions, homolysis and  $\beta$ -hydride elimination. For solving parameter estimation problem, maximum likelihood estimation is used. Introducing an optimization scheme into inverse problem solution process ensures a global minimum. As an optimization scheme, genetic algorithm followed by simplex method was implemented for the parameter estimation. As described in detail elsewhere[91], due to the high nonlinearity of heat, mass and energy transport model, genetic algorithms are chosen to solve this optimization problem since it has been shown to be successful for solving highly nonlinear space[92]. Eq. 4-20 describes objective function for the rate constants and activation energy.

$$\min \left\{ \sum_{i=1}^N \left( 1 / \left( 1 + \frac{(\tilde{\nu}_0 - \tilde{\nu}_j)^4}{(\tilde{\nu}_0 - \tilde{\nu}_{N_2})^4} \frac{1 - \exp(-hc\tilde{\nu}_{N_2}/kT_i)}{1 - \exp(-hc\tilde{\nu}_j/kT_i)} \left( \frac{I_{N_2}}{I_j} \right) \Sigma_j \right) - \hat{f}_i \right)^2 \right\} \quad (4-20)$$

where  $\tilde{\nu}$ ,  $h$ ,  $c$ ,  $k$ ,  $T$ ,  $I$ , and  $\Sigma_j$  represent wavenumber, Planck constant, speed of light, Boltzmann constant, temperature, scattering intensity, and the relative Raman cross-section of species  $j$ , respectively. In addition  $\hat{f}_i$  is the model function.

By minimizing the difference between experimental and simulated results, one can set the binary diffusion coefficient and/or relative Raman cross-section of species  $j$ . Also optimization process of A-factor and activation energy can be performed through reparametrization[92]. From well-known equation of following empirical equation,

$$k = A \exp \left[ -\frac{E_a}{RT} \right] \quad (4-21)$$

where  $k$ ,  $A$ ,  $E_a$ , and  $T$  represent rate constant at temperature  $T$ , A-factor (pre-exponential factor), activation energy of a reaction and reaction temperature, respectively. By reparametrizing the Eq. 4-21 with newly introduced parameters,  $\phi_1$  and  $\phi_2$ ,

$$k = \exp \left[ \phi_1 - \phi_2 \left( \frac{1}{T} - \frac{1}{T_m} \right) \right] \quad (4-22)$$

nonlinear relation between  $A$  and  $E_a$  was changed into linear relation between  $\phi_1$  and  $\phi_2$ , where  $\phi_1 = \ln(A) - \frac{E_a}{RT_m}$  and  $\phi_2 = \frac{E_a}{R}$ . And  $T_m$  denotes the mean temperature of measurement. Optimization processes for A-factor and activation energy of homolysis and  $\beta$ -hydride elimination are shown in Fig. 4-4. Though homolysis and  $\beta$ -hydride elimination processes are shown in different panel in Fig. 4-4, those were simulated in

one system. In other words, each system has influence on another system in the reactor simulated.

In Fig. 4-4C, the goodness of fit is the internal criterion that describes conversion threshold. A total of 43 iterations was made and optimized activation energies are 60.0 and 44.0 kcal/mol and A-factors are  $1.26 \times 10^{21} \text{ s}^{-1}$  and  $8.9 \times 10^{13} \text{ s}^{-1}$  for homolysis and  $\beta$ -hydride elimination, respectively, as tabulated in Table 4-4.

From Table 4-4, one can find the difference between the values before and after the optimization process. The values of before optimization were calculated from DFT calculations are shown to be a good initial guess for reactor modeling. For comparison of optimized values, the concentration and temperature profiles of triethylgallium are depicted in Fig. 4-5. The dots with error bars were measured experimentally, and dotted and solid line mean calculated profile of before optimization and after optimization, respectively.

As obviously shown above, profiles that use values after optimization (black solid line) shows better performance than that before optimization case (blue dotted line).

### Summary

In this chapter, the CVD reactor simulation adopting the Galerkin FEM model was described and applied to experimental data for the homogeneous decomposition of triethylgallium. The FEM model used in this study was described by five major governing equations, i.e., conservation of momentum, energy, and mass for species k, continuity equation and ideal gas law. By estimating the transport properties thermal conductivity, binary diffusivity, viscosity, heat capacity, as well as others by DFT calculations, appropriate initial values were estimated. Aforementioned DFT calculations showed only small deviations with experimental data in the wide range of

temperature, which indicates that DFT calculations can provide good estimates for unknown parameters. In addition the inverse problem was resolved by using a genetic algorithm followed by simplex method to estimate rate parameters for triethylgallium thermal decomposition. Compared with the pre-optimized triethylgallium concentration profile, the optimized profile shows better accordance with experimental measurements. After the 43 iterations, optimized activation energies are 60.0 and 44.0 kcal/mol and pre-exponential factors are  $1.26 \times 10^{21}$  and  $8.9 \times 10^{13}$  for homolysis and  $\beta$ -hydride elimination, respectively.

Table 4-1. Dimensionless groups in modeling equations

Name	Definition	Physical meaning	Typical order of magnitude
Prandtl	$\text{Pr} = \frac{\nu}{\alpha}$	Momentum diffusivity Thermal diffusivity	0.7
Schmidt	$Sc = \frac{\nu}{D}$	Momentum diffusivity Mass diffusivity	$1 \sim 10$
Reynolds	$Re = \frac{\langle v \rangle L}{\nu}$	Momentum flux by convection Momentum flux by diffusion	$10^{-1} \sim 10^2$
Peclet	$Pe = Re \text{Pr}$	Thermal flux by convection Thermal flux by diffusion	$10^{-1} \sim 10^2$
Grashof	$Gr = \frac{g \beta L^3 \Delta T}{\nu^2}$	Buoyancy force Viscous force	$1 \sim 10^5$
Rayleigh	$Ra = Gr \text{Pr}$	Buoyancy force Viscous force	$1 \sim 10^5$
Damköhler	$Da = \frac{R(C, T)_{ref} L}{C_{ref} \langle v \rangle}$	Characteristic time for flow Characteristic time for gas phase reaction	$10^{-3} \sim 10^3$

(Table was taken from Ref. [82])

Table 4-2. Comparison of experimental and kinetic theory derived diffusivities for H<sub>2</sub>-gas pairs and collision diameters

Gas	Collision diameter (Å)	Actual binary diffusivity (m <sup>2</sup> /s)	Calculated binary diffusivity (m <sup>2</sup> /s)
H <sub>2</sub>	1.41	$1.02 \times 10^{-4}$	$2.73 \times 10^{-4}$
He	1.13	$1.13 \times 10^{-4}$	$2.91 \times 10^{-4}$
C <sub>2</sub> H <sub>6</sub>	2.22	$5.37 \times 10^{-5}$	$1.20 \times 10^{-4}$
C <sub>4</sub> H <sub>10</sub>	2.34	$3.61 \times 10^{-5}$	$1.11 \times 10^{-4}$
C <sub>6</sub> H <sub>12</sub>	3.09	$3.19 \times 10^{-5}$	$7.67 \times 10^{-5}$

(Table was taken from Ref. [87])

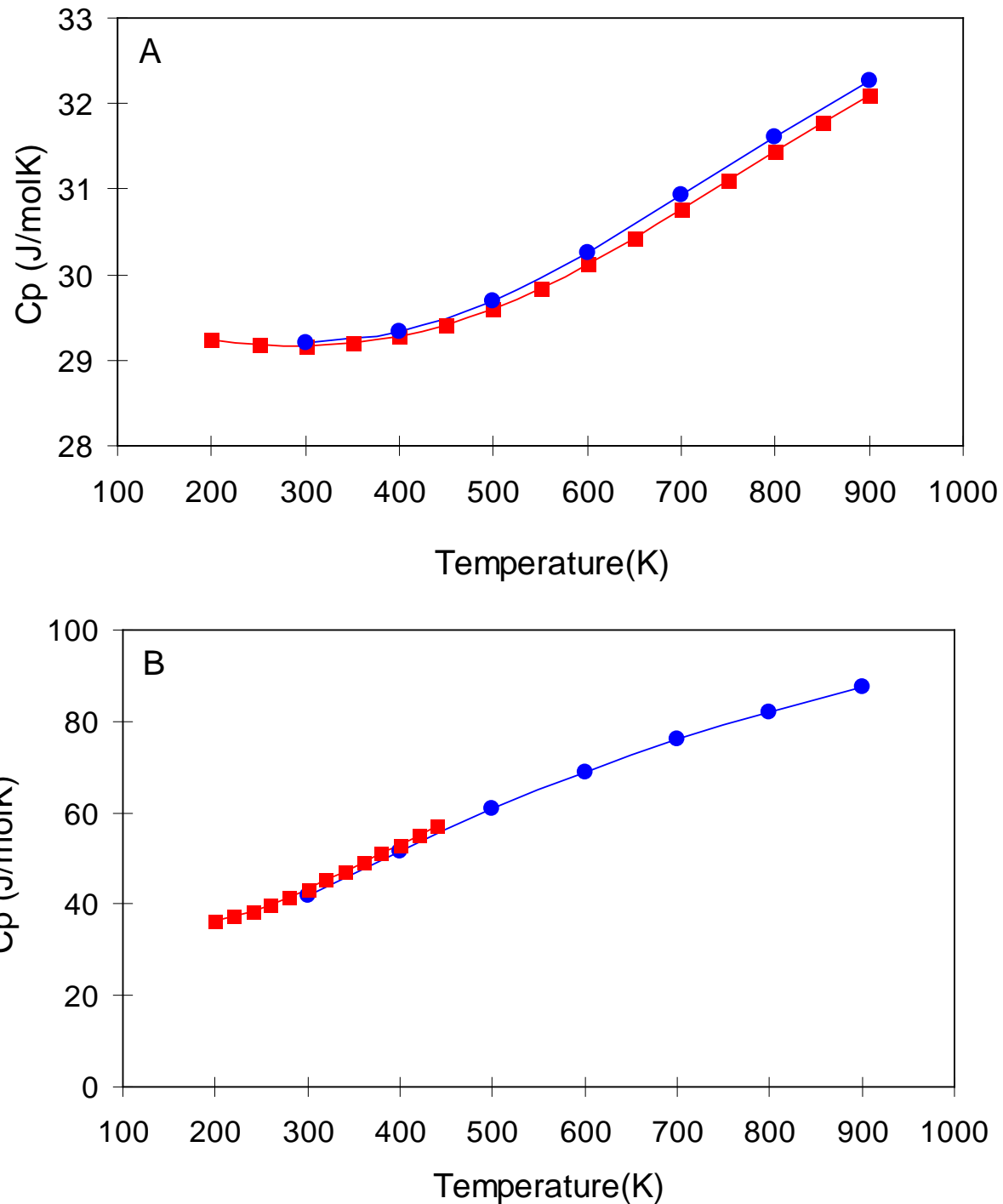


Figure 4-1. Experimental and calculated heat capacity of (A) nitrogen, (B) ethene, and (C) butane. Blue circles show calculation data and red rectangles experimental data. All data are based on gas phase. Experimental data were taken from Ref.[93] for nitrogen, Ref.[94] for ethane, and Ref.[95] for butane.

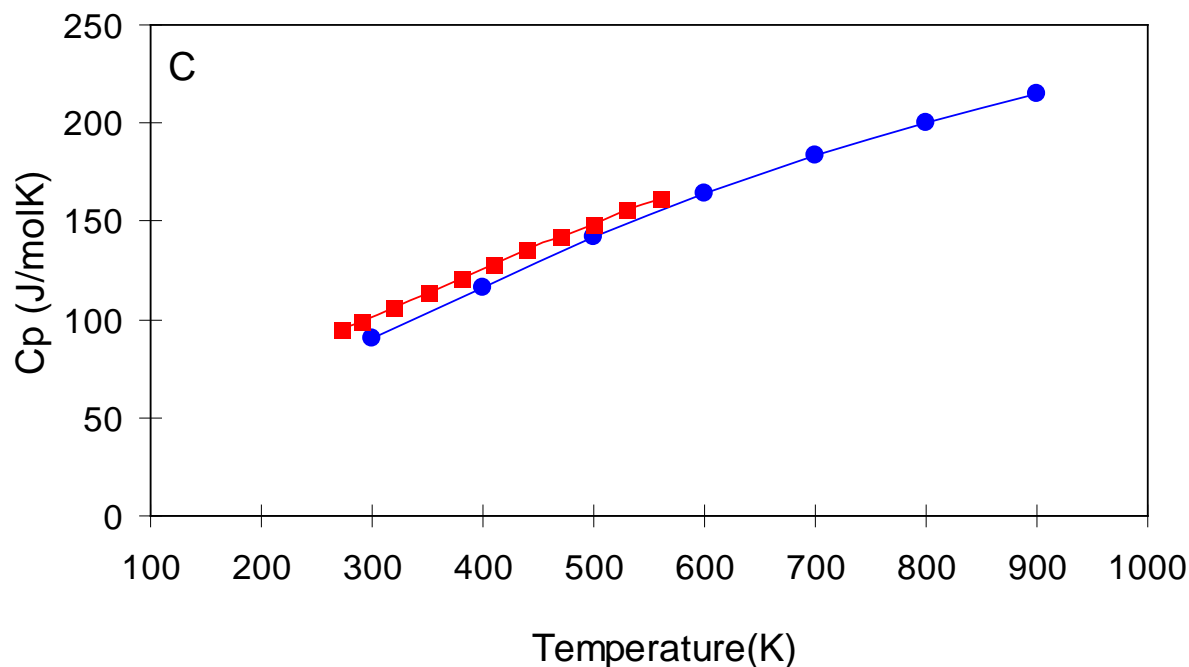


Figure 4-1. Continued.

Table 4-3. Deviations of heat capacity between experimental and calculated values

Temperature (K)	Deviation for $\text{N}_2$ (%)	Deviation for $\text{C}_2\text{H}_4$ (%)	Deviation for $\text{C}_4\text{H}_{10}$ (%)
300	-0.08	2.91	10.21
400	-0.23	2.78	7.08
500	-0.36	-	4.83
600	-0.48	-	-
700	-0.54	-	-
800	-0.55	-	-
900	-0.52	-	-

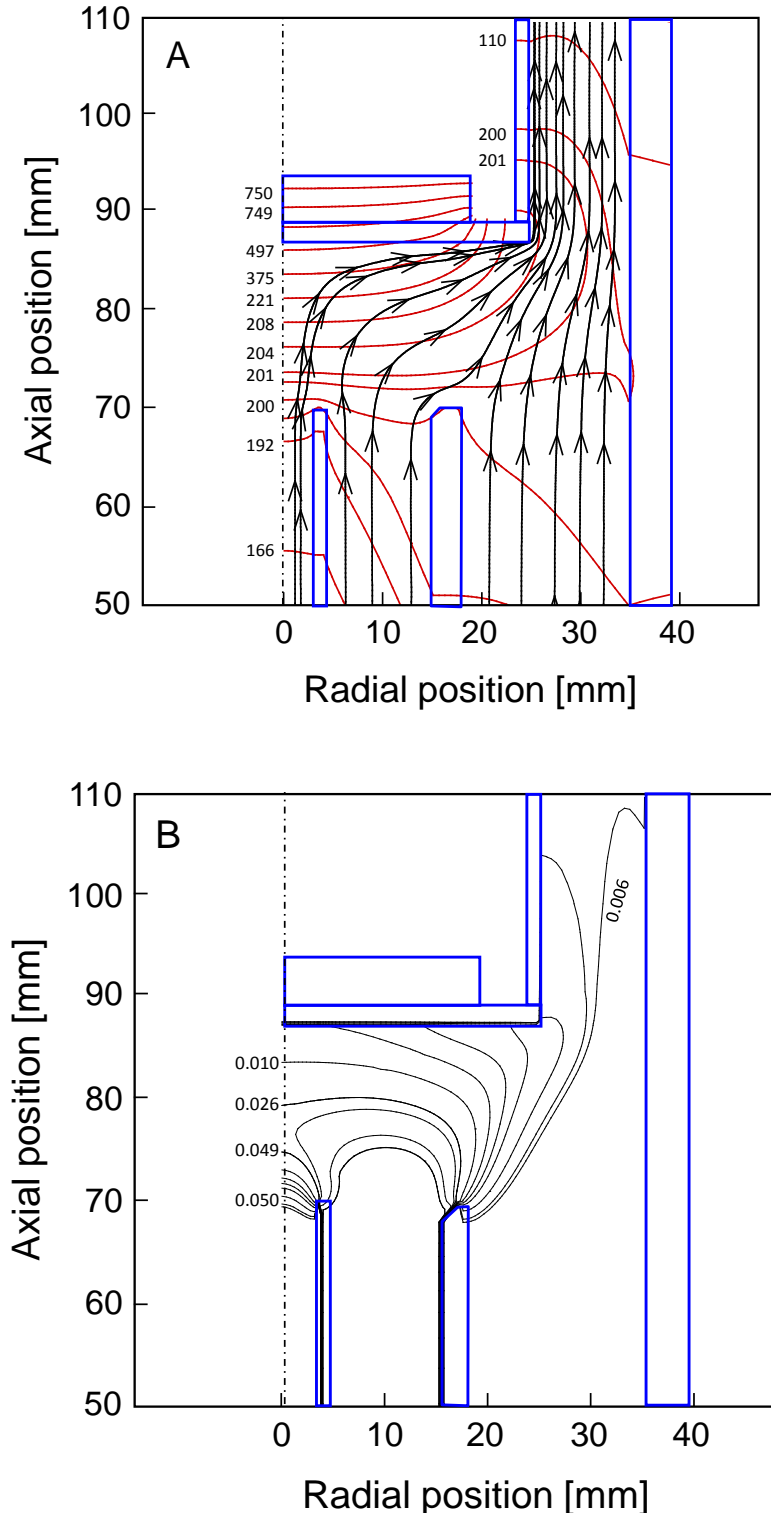


Figure 4-2. Simulated (A) temperature contours (unit is shown as °C) and streamlines and (B) concentration contours in the reactor when 5 % triethylgallium with nitrogen carrier gas at 700 °C.

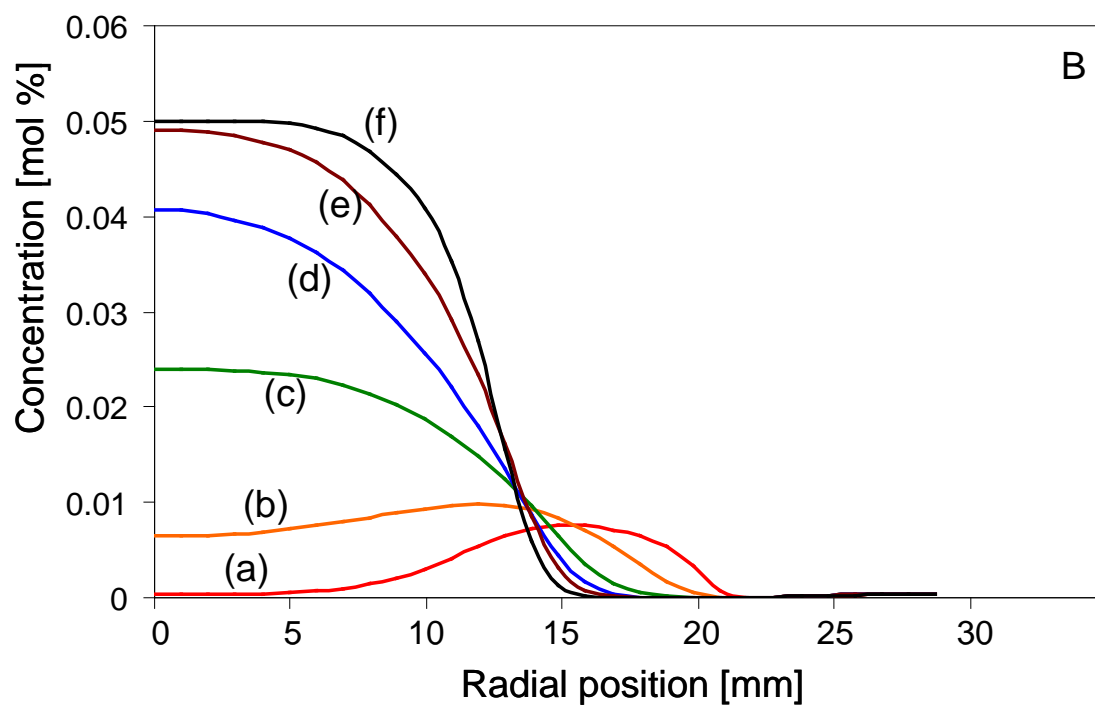
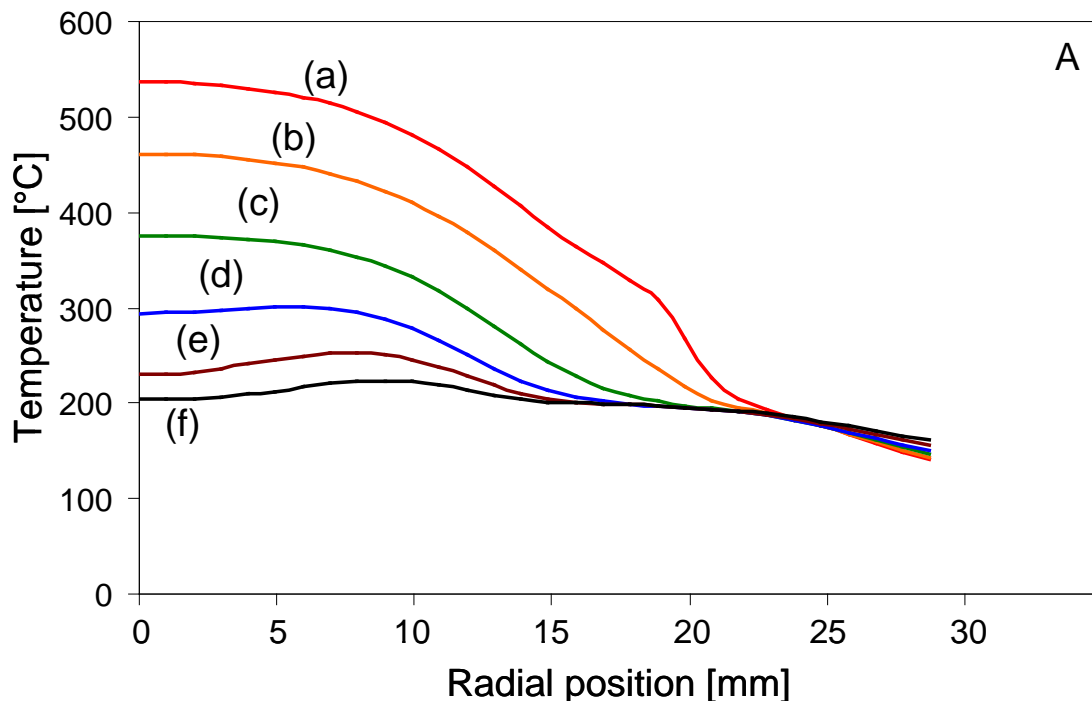


Figure 4-3. Radial triethylgallium (A) temperature and (B) concentration profile at different axial positions: distances from the heated susceptor are (a) 0.3, (b) 2,(c)4, (d) 6, (e) 8, and(f) 10 mm.

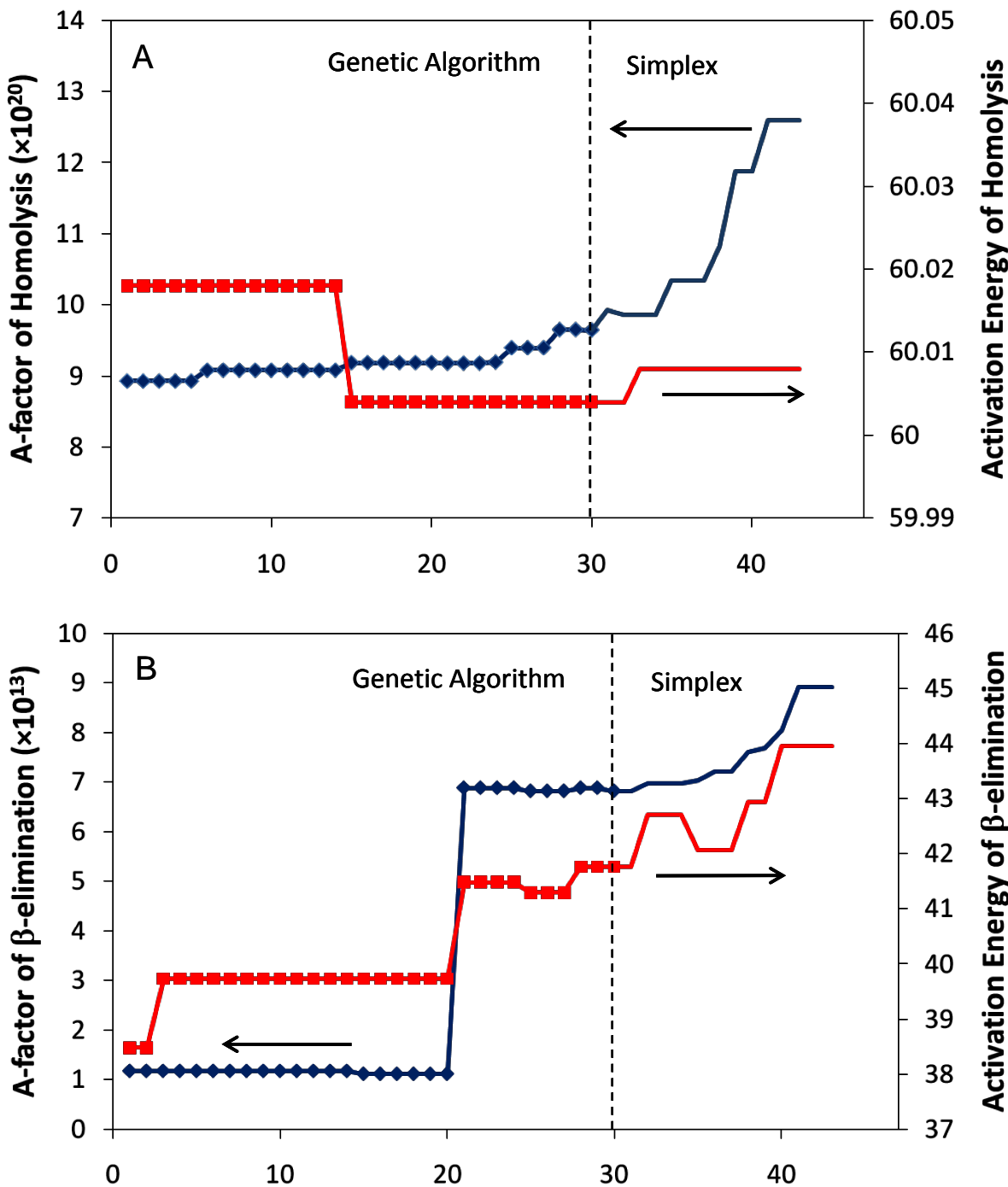


Figure 4-4. Optimization process using genetic algorithm followed by simplex method for solving inverse problem. (A) and (B) denote detailed process of A-factor (pre-exponential factor) and activation energy of homolysis and  $\beta$ -hydride elimination, respectively. (C) describes trace for goodness of fit during the process of (A) and (B).

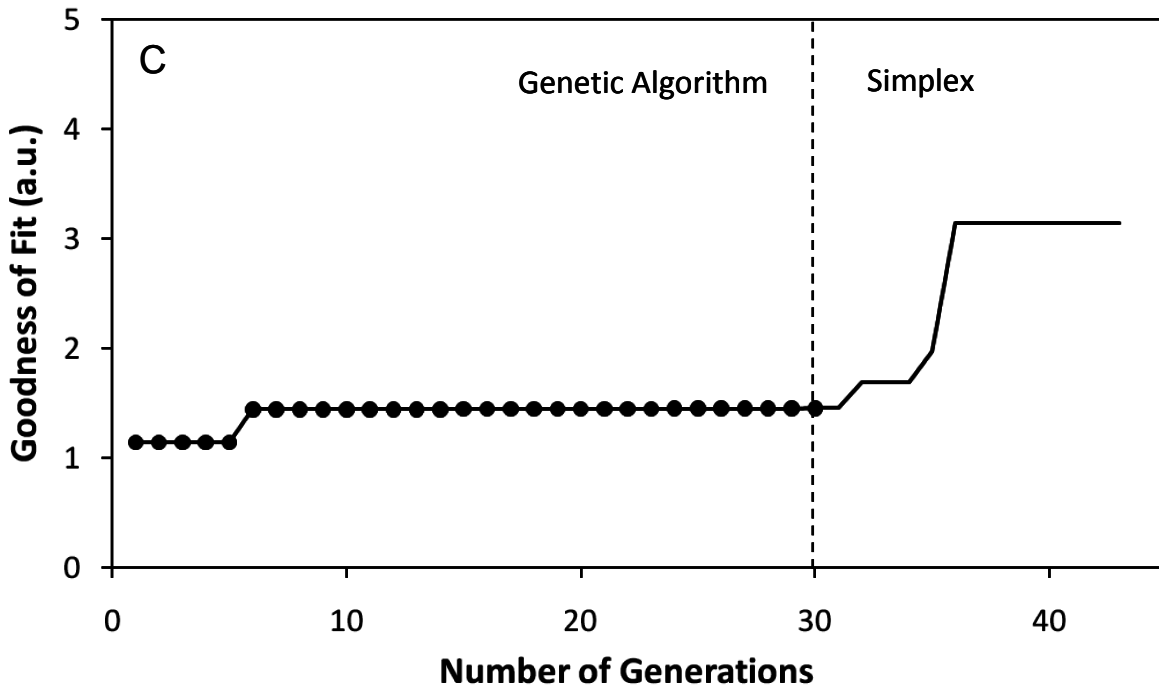


Figure 4-4. Continued.

Table 4-4. A-factor and activation energy value of homolysis and  $\beta$ -hydride elimination reaction before and after optimization

	Homolysis		$\beta$ -hydride elimination	
	A-factor	Activation energy	A-factor	Activation energy
Before optimization	$4.68 \times 10^{22}$	65.0	$1.95 \times 10^{13}$	40.3
After optimization	$1.26 \times 10^{21}$	60.0	$8.9 \times 10^{13}$	44.0

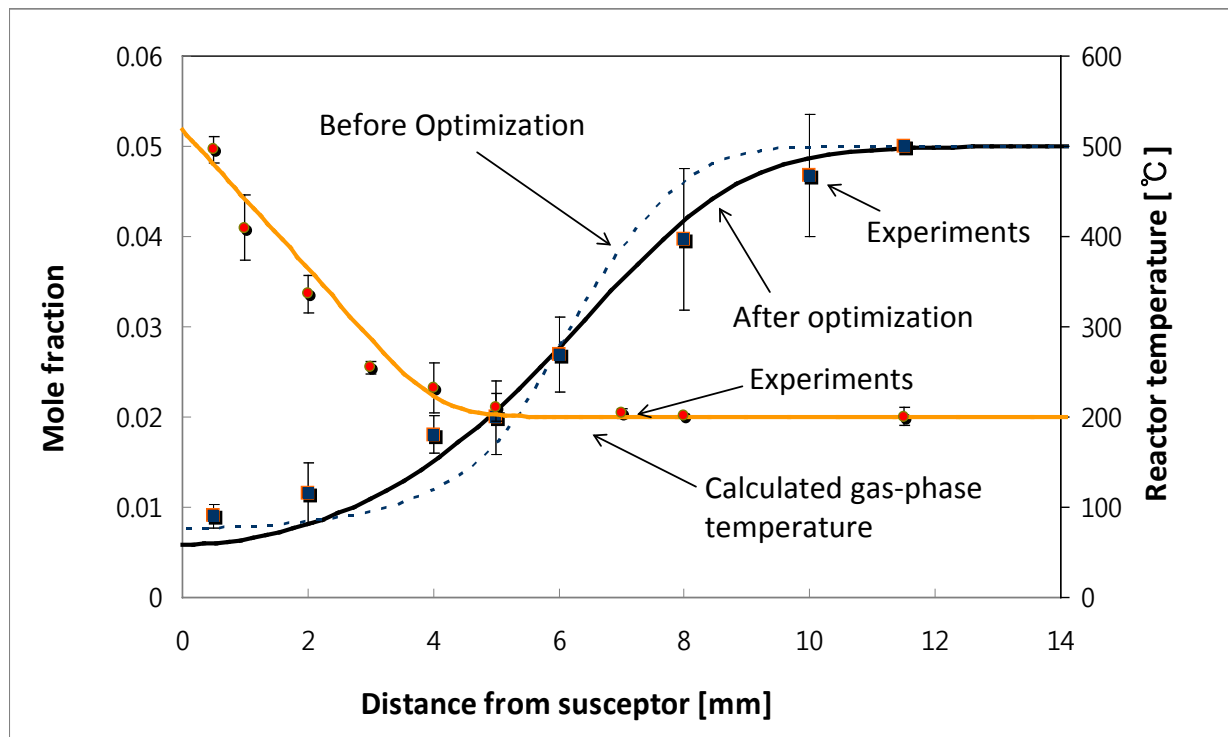


Figure 4-5. Concentration and temperature profile of gas phase triethylgallium.

CHAPTER 5  
INVESTIGATION OF THE THERMAL DECOMPOSITION OF TRIETHYLGALLIUM  
USING IN SITU RAMAN SPECTROSCOPY AND DFT CALCULATIONS

**Overview**

Gallium-based compound semiconductors have played an important role in many electronic and optoelectronic devices, and MOCVD is often the preferred method of film deposition. The electronics industry has developed several useful Ga-related materials and is still experiencing expansion. Among the commercially available Ga precursors, TEGa ( $(C_2H_5)_3Ga$ , Triethylgallium) and TMGa ( $(CH_3)_3Ga$ , Trimethylgallium) have been most widely used in the CVD of Ga-based semiconductor materials such as GaAs, GaSb or GaN[96-98]. Although TEGa and TMGa are widely used for MOCVD, there are only few reports on the gas phase thermal decomposition mechanism of TEGa. Most of the research describes thermal decomposition on a surface such as GaAs or Si[6, 98, 99]. Those studies gas phase decomposition mechanisms for TEGa only suggest either simple homolysis of the C–Ga bond or  $\beta$ -hydride elimination as the initial step[7, 8, 100]. As summarized in Table 5-1, the reported experimental activation energy for removal of the first ethyl group ranges from 22.6 to 47.2 kcal/mol, and frequency factor ranges from  $8.1 \times 10^4 s^{-1}$  to  $4.8 \times 10^{15} s^{-1}$ [7, 75, 101].

To a certain extent, the reason why frequency factors show the large deviation is because each experiment was carried out at different conditions, e.g. carrier gas, reactor temperature, and reaction that was taken place. Unfortunately, this wide range in the values of the rate parameters produces large uncertainties in reactor modeling results. These deviations may in part be attributed to chemical effects on the decomposition reactions arising from selection of carrier gas (i.e., toluene or hydrogen)

and reaction conditions that may favor one mechanism over another. In addition to these values derived from experimental data, the activation energy values 60.0 kcal/mol for simple homolysis and 44.0 kcal/mol for  $\beta$ -hydride elimination were calculated using *ab initio* calculations (restricted Hartree-Fock MO method) by Tsuda et al. [74]. DFT calculation results from this work suggest activation energy values of 65.0 kcal/mol for simple homolysis and 40.3 kcal/mol for  $\beta$ -hydride elimination, and pre-exponential factors of  $4.7 \times 10^{22} \text{ s}^{-1}$  and  $1.9 \times 10^{13} \text{ s}^{-1}$ , respectively.

In this study, the TEGa homogeneous decomposition kinetics were investigated using *in situ* Raman spectroscopy in a vertical up-flow, cold-wall CVD reactor. The results of this nonintrusive measurement technique were used to estimate rate parameters using a detailed reactor model. Theoretically, its reaction pathways are going to be validated with DFT calculations were used to assist in assignment of Raman shifts and estimating rates and thermodynamic driving forces for selected reaction pathways.

### **Experimental and Theoretical Methods**

To better understand the decomposition mechanisms of TEGa, this study used experimental CVD reactor shown in Fig. 5-1 that is interfaced with a Raman spectrometer (Ramanor U-1000, Jobin Yvon), which includes a double additive monochromator and uses the 532.08 nm line of Nd:YAG solid-state laser as the light source. As described in detail elsewhere [91, 102], this CVD reactor is an up-flow impinging jet reactor designed to produce a stable 2-D flow condition while isolating the reactants from the reactor walls to prevent wall deposition. The entire CVD reactor assembly could be translated x-y-z to allow measurement of temperature and composition profiles. Three concentric inlet tubes are incorporated into the design with

the reactant input into the center tube. Each tube is packed with 3mm glass beads to provide an equal velocity, parallel-flow inlet boundary condition.

TEGa as a metalorganic precursor is introduced through a center line and N<sub>2</sub> carrier gas envelops is introduced through the annular and outer inlets to prevent wall deposition of precursors or reaction products. Based on the previous study[91] that developed and validated a steady-state, two dimensional mass transport model and performed a CH<sub>4</sub> tracer experiment, conditions were used that assure no recirculation flows in the reactor.

The measurement of temperature using Raman spectroscopy is well established. In low density flows, several authors have succeeded in measuring local temperatures with oxygen rotational spectrum at 1 atm ranging from 243 to 343 K[103]. Because Raman scattering does not disturb the flow, it can give relatively accurate results. It has been used to determine temperature in reactive flows[104], flames[24, 105], and in the atmosphere[23]. It was reported that temperature measurements with rotational state distribution using Raman spectroscopy can be accurate to less than 7 % uncertainty in the range of 20-2230 °C[18]. From the modified equation for Stokes-Raman scattering intensity of Eq. 5-1, temperature distributions are obtained from linear regression of experimental data.

$$\ln \left\{ \frac{(2J+3)I}{(\nu_o - \nu_{J+2,J})^4 g_J(J+1)(J+2) R(J)f(J)} \right\} = C_1 - \frac{F(J)hc}{k_B T} \quad (5-1)$$

where  $C_1 = \ln \left\{ 7NC_0 / 30 \sum_J g_J(2J+1) \exp[-F(J)hc/k_B T] \right\}$  and this is a constant at a given experimental setup and  $\nu_o$  is the wavenumber of the incident light.  $J$ ,  $h$ ,  $k_B$ ,  $T$ ,  $R(\nu)$  and  $F(J)$  are rotational quantum number, Planck constant, Boltzmann constant, spectral

response of the spectrometer and the correction to the anisotropy of the polarizability, respectively. If  $R(\nu)$  and  $F(J)$  are known, the temperature is determined from the linear regression method from a set of rotational peaks.

With the nitrogen Q-branch standard, the relative Raman cross-section  $\Sigma_k$  for vibration mode  $k$  is defined as:

$$\Sigma_k \equiv \frac{(d\sigma_k / d\Omega)}{(d\sigma_{N_2} / d\Omega)} \cdot \frac{(\tilde{\nu}_0 - \tilde{\nu}_{N_2})^4}{(\tilde{\nu}_0 - \tilde{\nu}_k)^4} \frac{1 - \exp(-hc\tilde{\nu}_k / kT)}{1 - \exp(-hc\tilde{\nu}_{N_2} / kT)} \quad (5-2)$$

where  $\tilde{\nu}_k$  and  $\tilde{\nu}_{N_2}$  are, respectively, the wavenumbers of the molecular vibration and Q-branch of  $N_2$  carrier gas. Relative Raman cross section of  $k^{\text{th}}$  material can be calculated with Eq. 5-2 using Q-branch of the  $N_2$  vibrational motion of  $\tilde{\nu}_{N_2}$  which is found stably with relatively high intensity at  $2331 \text{ cm}^{-1}$ . In Eq. 5-2, the exponential Boltzmann factor for nitrogen can be omitted at ambient temperature. A relationship between the Raman intensity ratio and the number density ratio for two components is necessary to perform the concentration measurement in a detection region. One should note that the quantity  $\Sigma_k$  is closely related to the relative scattering coefficient and the scattering activity.

When performing concentration measurement with Raman spectroscopy, measured Raman apparent intensity and the number density ratio are to be calculated at the region of interest. Using Eq. 5-2 and equation of thermal population at temperature T, the relationship between the number density ratio,  $N_{N_2} / N_k$ , and the intensity ratio is described as follows:

$$\frac{N_{N_2}}{N_k} = \frac{I_{N_2}}{I_k} \frac{(d\sigma_{N_2} / d\Omega)}{(d\sigma_k / d\Omega)}$$

$$= \frac{I_{N_2}}{I_k} \frac{(\tilde{\nu}_0 - \tilde{\nu}_k)^4}{(\tilde{\nu}_0 - \tilde{\nu}_{N_2})^4} \frac{1 - \exp(-hc\tilde{\nu}_{N_2}/kT)}{1 - \exp(-hc\tilde{\nu}_k/kT)} \Sigma_k \quad (5-3)$$

For a binary system, the mole fraction of component k is given by

$$\begin{aligned} x_k &= \frac{N_k}{N_k + N_{N_2}} \\ &= 1 / \left[ 1 + \frac{N_{N_2}}{N_k} \right] \\ &= 1 / \left[ 1 + \frac{I_{N_2}}{I_k} \frac{(\tilde{\nu}_0 - \tilde{\nu}_k)^4}{(\tilde{\nu}_0 - \tilde{\nu}_{N_2})^4} \frac{1 - \exp(-hc\tilde{\nu}_{N_2}/kT)}{1 - \exp(-hc\tilde{\nu}_k/kT)} \Sigma_k \right] \end{aligned} \quad (5-4)$$

However, one should note that the relative normalized Raman cross-section has to be measured to use Eq. 5-4.

Although the relative Raman cross section for most of the metal-organic sources is not known, various methods such as relative Raman intensity measurement with using circumventive materials and solvents[106] and density functional theory calculation[107] provide different techniques for understanding optical characteristics better than ever.

In a preliminary experiment, the relative Raman cross-section of TEGa was measured in the reactor at room temperature and atmospheric pressure. In this experiment, 2.5 cm/s steady flow of 5 mol % TEGa in N<sub>2</sub> as a carrier gas in the center line was used. For the annulus and sweep flows, pure N<sub>2</sub> gas was delivered with the same flow rate (2.5 cm/s) and sufficient gas flow time before measurements was allowed for form a steady-state and stable flow pattern. Then the 1.5W Nd:YAG solid-state laser line was used to excite TEGa source and the Ga-C<sub>3</sub> vibrational Raman excitation line (490cm<sup>-1</sup> line) was recorded (Fig.5-2).

Although the scattered intensity of TEGa is much weaker than other group II, III metal sources as shown in Table 5-2, the signal to noise ratio was sufficient to quantify the TEGa concentration from the recorded  $490\text{cm}^{-1}$  excitation line. With repeated measurements (10 times) and long integration time (5 s) at room temperature, the relative Raman cross section was estimated to be 2.7. This value is relatively low in comparison with other well-known metalorganic sources, e.g. 17.5 for trimethylgallium, 21.0 for dimethylcadmium.

By connecting experimental observations with computational calculations, one can identify intermediate Raman signals and provide thermal decomposition mechanisms. All calculations were performed using Gaussian 03 program suite[73]. For all bond dissociation, activation energy and frequency calculations, the density functional theory level with the spin polarized hybrid density functional B3LYP together with the LanL2DZ for all elements was used. The reference experimental value of Ga–C<sub>3</sub> bond length and Ga–C–C bond angle that was measured with diffractometer from the TEGa single cylindrical crystals of 0.3mm diameter[71] were used for choosing model chemistry. After the discreet comparison of a large number of cross-combinations of methods (HF, B3LYP, MP2, MP4) and basis sets (6-31G\*, 6-31G\*\*, 6-311G, 6-311G\*\*, SDD, LanL2DZ) as well as the split basis set of B3LYP/(LanL2DZ for Ga, 6-311G for other elements), the B3LYP/LanL2DZ model chemistry was chosen by comparing the experimental Ga–C<sub>3</sub> average bond length ( $1.966 \sim 1.996\text{\AA}$ ) and the Ga–C–C bond angle ( $113.3 \sim 116.1^\circ$ ) with the former ( $1.995\text{\AA}$ ) and the latter ( $115.3^\circ$ ) of computational calculation results. According to the crystallographic data, there are two forms of TEGa structure. Three of the four molecules are found in a propeller-like arrangement with C<sub>3</sub>

symmetry and only one molecule does not exhibit the same symmetry and has two ethyl groups pointing at each other. Mitzel et al.[71] also reported that the wide Ga-C-C angles in the TEGa structure resemble those in the B-C-C structure of solid  $B(C_2H_5)_3$ , which was explained by hyperconjugation of the boron *p* orbital into C-H orbitals[108]. The “tight” convergence option was used for the TEGa geometry optimization, especially for the Ga–C<sub>3</sub> vibrational frequency, since this investigation focuses on the precise frequency value among the many kinds of Ga–C vibrations of expected intermediates. As described above, calculated values using B3LYP/LanL2DZ model chemistry will be used for validating the frequencies of reaction intermediates.

## Results and Discussion

**DFT Calculations** The basic procedure in using DFT calculations to understand gas phase reactions is to first identify possible reaction pathways, perform DFT calculations on the relevant gas phase species to estimate their thermodynamic properties, and then envision transition states for each reaction and perform DFT calculations to estimate rate constants. Two major routes have been proposed for the initial stages of thermal decomposition of TEGa by several researchers for gas-phase reaction as well as adsorbed forms on surfaces such as GaAs or Si[6, 8, 98-100]. One mechanism is homolysis of the C-Ga bond to yield an ethyl radical and another is  $\beta$ -hydride elimination, both of which could occur homogeneously or heterogeneously. Specific studies have proposed either just one of the mechanisms[99] or both mechanisms[8, 98, 100] based on the detected decomposition products. It is noted that detection of butane or ethylene is decisive evidence to discriminate between homolysis or  $\beta$ -hydride elimination, respectively. To the best of this investigator’s knowledge, however, subsequent reactions such as dimerization of two radicals or

association of two intermediate products, have not been studied either computationally or experimentally. Since these two major mechanisms are not exclusive, this study assumes initially both routes are possible.

DFT calculations were performed to represent species in the TEGa decomposition system. Based on the TEGa structure data, the B3LYP level calculation with LanL2DZ basis set was also chosen to investigate the NBO (Natural Bond Orbital) analysis and evaluate the thermodynamic properties enthalpy, entropy, and Gibbs energy. Two initial stages, i.e. homolysis and  $\beta$ -hydride elimination, are supported by the Wiberg bond index in the NBO analysis. In the case of homolysis, the Wiberg bond index between Ga and  $C_\alpha$  (0.5976) is much smaller than that between  $C_\alpha$  and  $C_\beta$  (1.0563), the products from  $C_\alpha$ – $C_\beta$  breakage such as  $\bullet CH_3$  from the ethyl group are thus not considered as a thermal decomposition pathway. For the  $\beta$ -hydride elimination case, it is more complicated since the transition state which includes the imaginary bond between hydrogen connected with  $C_\beta$  and gallium center should be considered. Additional information on the imaginary ring which consists of gallium,  $C_\alpha$ ,  $C_\beta$  and hydrogen connected with  $C_\beta$  was analyzed from Wiberg indices change. These changes with TEGa energetics and schematized TEGa structure are shown in Fig.5-3. The four numbers beneath the type of structure indicate Wiberg bond indices for bonds 1 ~ 4 depicted in the schematized TEGa structure. From Fig.5-3, the transition of the bond strength for the four membered Ga– $C_\alpha$ – $C_\beta$ –H imaginary ring can be easily investigated.

As clearly shown in Fig. 5-3, bonds **1** and **3** are increasing in strength and bonds **2** and **4** are becoming weaker during the first  $\beta$ -hydride elimination. From the Wiberg indices profiles, one can suggest the feasibility of  $\beta$ -hydride elimination of TEGa.

The theoretical enthalpy ( $\Delta H$ ), entropy ( $\Delta S$ ) and Gibbs energy ( $\Delta G$ ) changes of the selected association and dissociation reactions including homolysis and  $\beta$ -hydride elimination reactions in the thermal decomposition pathways of TEGa at 298 and 900K as well as all the possible reaction pathways leading to formation of the 4-membered-ring,  $(\text{MEG})_4$ , consisted of 35 species and 39 reactions including three transition states of  $\beta$ -hydride elimination. These results are summarized in Table 5-3.

R1-R3 and R5-R7 in Table 5-3 describe  $\beta$ -hydride elimination reactions and homolysis reactions, respectively. T1 through T5 describe transition state energy changes for TEGa,  $(\text{Et})_2\text{GaH}$  and  $(\text{Et})\text{GaH}_2$  in the middle of the  $\beta$ -hydride eliminations. One should pay attention to the fact that some reactions are connected with others. For example, R8-R11, R12-R14, R15-R18, R19-R20, R25-R26, R27-R28, and R29-R31, respectively, are under competition. Moreover R19 and R23 are indispensable reactions for R21-R24 and R27-R28, respectively. That means if R19 is not available, R21-R24 are not feasible and then R27-R28 will not be favorable automatically.

As described above, two natural forms of TEGa should be included for three consecutive  $\beta$ -hydride elimination reactions. Each transition structure is constructed from the different TEGa structure. TEGa transition structure 1 (TEGa TS1 $\ddagger$ ) comes from the structure that has two ethyl groups pointing at each other and TEGa transition structure 2 (TEGa TS2 $\ddagger$ ) comes from the propeller-like arrangement. For the  $(\text{Et})_2\text{GaH}$  transition state structures, two different types ( $(\text{Et})_2\text{GaH}$  TS1 $\ddagger$  and TS2 $\ddagger$ ) were constructed and these two structures are available from any two TEGa transition structures. Lastly, the  $(\text{Et})\text{GaH}_2$  transition structure has only one transitional form, and these schemes are depicted in Fig.5-4. As stated in the Table 5-3, because the first (T1

and T2) and second (T3 and T4)  $\beta$ -hydride elimination steps have almost same energy barriers, initial structure of TEGa would not be very critical.

Contrary to the transition state structure of the  $\beta$ -hydride elimination, simple elongations of the ethyl group from Ga center constitute homolysis and its energy variation profile shows a smooth curve without a sudden upturn in potential energy. One could confirm the potential energy profile that shows continuous decrease during the elongation of ethyl radical. Based on the potential energy surface calculation for the elongation of the ethyl radical from TEGa molecule, the potential energy of TEGa follows the singlet state for short separation distance and triplet state at longer separation distance. A Morse potential fit and these two potential energy surface calculations show very good agreement. A more detailed computational calculation was performed for two initial stages of TEGa thermal decomposition using same model chemistry as shown in Fig. 5-5.

To the best of this investigator's knowledge, since there is no previous research which dealt with entire mechanism of TEGa thermal decomposition and proposed evidences, thermodynamic properties of these reactions was used for selection priority. The first screen was on the basis of  $\Delta H$  and  $\Delta G$  values. From the detailed calculation results of two main reaction series considering five transition state structures shown in Fig. 5-5 and minute investigation of selected decomposition pathways, 17 feasible reactions were screened on the basis of reaction enthalpies as shown in Fig. 5-6. Many reactions were eliminated due to too high reaction energy and absence of source intermediates.

## TEGa Thermal Decomposition Experiments Using *in situ* Raman Spectroscopy

To investigate TEGa thermal decomposition pathways in an up-flow, impinging jet cold-wall CVD reactor, a set of experiments was performed under strictly controlled conditions. As described earlier, 5% TEGa was introduced by the pure N<sub>2</sub> into the reactor centerline. Nitrogen was selected as a carrier gas, since it has a large relative Raman cross-section and it gives a strong Raman band that is used to normalize the peaks of intermediates. The susceptor heater was set at 750°C to provide sufficient energy for the thermal decomposition. The relative mole fraction of each gas-phase chemical species in the reactor was obtained from the ratio of peak integral of the primary peak [Ga–C<sub>3</sub>] at 490cm<sup>-1</sup> to that of the N–N vibration at 2331cm<sup>-1</sup>. Fig.5-7 shows the Raman spectrum that was recorded by measuring several centerline points from the susceptor to the inlet.

Fig.5-7 shows five ranges of Raman spectra suggestive of gas-phase TEGa and detectable intermediates. The data were acquired in a series of scans over the full range of wavenumbers. Four bands at, i.e. 517, 537, 555, and 785cm<sup>-1</sup>, may indicate an unknown intermediate vibrations. There are also observations for expected hydrocarbon products around 3100cm<sup>-1</sup> Raman shift. Given the large number of possible hydrocarbon products and motions, it is not easy to assign these signals to the exact vibrational motions.

Although spectral lines for Ga–Ga vibration are proof of the presence of many di-gallium intermediates such as (DEGa)<sub>2</sub>, (Et)GaH–GaH<sub>2</sub> and (GaH<sub>2</sub>)<sub>2</sub>, those spectral lines are not apparent in the scans. From DFT calculations the Ga–Ga vibration spectral lines are expected in the region around wavenumber of 190 through 200cm<sup>-1</sup>. Because intensities of nitrogen rotational transition lines are periodical and considerably

stronger than those of other signals in the region of  $\sim 220\text{cm}^{-1}$ , it is difficult to make assignments. Based the known characteristics of the nitrogen rotational bands, the spectral lines for vibration of Ga–Ga are not easy to detect in the measured spectrum, which overlaps with the rotational transitions of the nitrogen carrier molecules. If more evidence can be supplied from the Raman spectrum, it will not be difficult to assign each spectrum to a certain molecule. However, quantum calculations have shown that they can predict Raman shifts of intermediate molecules with considerable exactness[109].

The concentration of TEGa was calculated from measured Raman scattering intensities using Eq. 5-2 and the temperature profile inside the reactor was calculated with Eq. 5-1. Fig.5-8 represents the measured TEGa concentration at the centerline below the susceptor heated to  $750^\circ\text{C}$ . It should be noted that experimental results with error bars agree well with concentration profile which considers both reactions, i.e., homolysis and  $\beta$ -hydride elimination. As shown in the Fig.5-8, the experimental concentration cannot be explained using only one specific reaction. This suggests both  $\beta$ -hydride elimination and homolysis reactions are active during TEGa thermal decomposition.

Fig.5-8 also indicates temperature (orange solid line) and concentration (thin black solid line) profile simulated using the 2-D axisymmetric reactor model. This reactor model is described in more detail elsewhere[91, 110] and those references contain its validation procedures. In short, the 2-D axisymmetric reactor model was developed to describe the experimentally observed temperature and concentration profiles and it uses the finite element Galerkin method (FEM) to simulate heat, momentum, and mass

transfer mechanisms simultaneously. For optimization of the frequency factor and activation energy from measured data on the disappearance of TEGa, a genetic algorithm followed by simplex algorithm was implemented. The parameter estimation was performed by minimizing the objective function that is the sum of squares of the differences between experimental data and simulated data for total 8 measurements. More detailed description of optimization scheme is reported elsewhere[91]. Fig.5-9 shows the values of the frequency factor and activation energy for two main reactions at each step during the optimization. Optimized activation energies are 60.0 and 44.0 kcal/mol and frequency factors are  $1.26 \times 10^{21} \text{ s}^{-1}$  and  $8.9 \times 10^{13} \text{ s}^{-1}$  for homolysis and  $\beta$ -hydride elimination, respectively. Interestingly, rate parameters of homolysis are increased and those of  $\beta$ -hydride elimination are decreased after optimization.

### **The Comparison of DFT Calculation with Experimental Results**

A value of  $474 \text{ cm}^{-1}$  was produced for the symmetrical Raman active [Ga–C<sub>3</sub>] stretching from the B3LYP/LanL2DZ model chemistry. Based on the DFT calculations and the experimental results, a scaling factor of 1.0408 was produced. Eleven species including TEGa related to the 17 screened reactions were examined and corrected with scaling factor using same model chemistry(see Table 5-4). This table shows the calculated and corrected Raman frequencies for each selected species from the stable reactions accompanied by the Ga–C symmetric motions.

The scaling factor of 1.0408 mentioned above is applied only to the Ga–C stretching mode and frequencies from calculation results were corrected. As stated in Table 5-4, four frequencies related to three molecules matched well with experimental Raman shifts. Especially, one of the two corrected frequencies for (DEGa)<sub>2</sub> shows exact matching with  $517 \text{ cm}^{-1}$  experimental Raman shift. Moreover, another corrected

frequency of  $(DEGa)_2$ , frequency from  $(Et)GaH-Ga(Et)_2$  and one from  $(Et)GaH-GaH_2$  is in good agreement with 555, 537, and  $555\text{cm}^{-1}$ , respectively. Although there are two candidates for  $555\text{cm}^{-1}$ , it is not obvious which frequency is more accurate since relative Raman cross-sections of two molecules are not known. Moreover, although long absorption time is not mandatory for Raman spectroscopic measurement, in the case of depleting intermediate materials simultaneously such as trimethylindium decomposition reaction[111], the lifetime of these molecules can be critical. Investigation of Table 5-4 firmly suggests the presence of  $(DEGa)_2$ ,  $(Et)GaH-GaH_2$ , and  $(Et)GaH-Ga(Et)_2$ . According to the presence of  $(DEGa)_2$  as a reaction product of the DEGa, presence of the homolysis reaction which make DEGa and MEGA radical can be supported though energy barrier of homolysis reaction pathway is higher than that of  $\beta$ -hydride elimination reactions. Moreover, the presence of  $(Et)GaH-GaH_2$ , and  $(Et)GaH-Ga(Et)_2$  evidences  $\beta$ -hydride elimination decomposition. Based on these results, it is suggested that both homolysis and  $\beta$ -hydride elimination reactions take place during the thermal decomposition of TEGa in the CVD reactor.

### Concluding Remarks

An analysis of the decomposition kinetics for TEGa with  $N_2$  carrier gas in a custom up-flow, cold-wall CVD reactor was shown that both  $\beta$ -hydride elimination and homolysis reactions are present in the reaction zone of the reactor. This was evidenced by observation of  $(DEGa)_2$ ,  $(Et)GaH-GaH_2$ , and  $(Et)GaH-Ga(Et)_2$  using *in situ* Raman spectroscopic and values of the reaction enthalpy preferences computed by DFT calculations at the B3LYP/LanL2DZ chemistry level. Raman shifts of 490, 517, 537, and  $555\text{cm}^{-1}$  were found and assigned to TEGa,  $(DEGa)_2$ ,  $(Et)GaH-Ga(Et)_2$ ,  $(Et)GaH-GaH_2$ , respectively. The concentration profile for TEGa and the temperature distribution

of reactor centerline were measured and these were compared to those from the simulated results using finite element Galerkin method. Activation energy and frequency factor for both reactions were optimized using genetic and simplex algorithm and optimized rate parameters show better fit with experimental results. The similarity confirmed from experiment and DFT calculation results is remarkable and suggests this methodology can be considerable for metal-organic materials research with *in situ* Raman spectroscopy, which does not interrupt the flow pattern in the CVD reactor.

Table 5-1. Experimental and calculated rate parameters for first ethyl group dissociation

T(K)	$k_0$	Ea (kcal/mol)	Method	Ref
610 ~ 749	$4.8 \times 10^{15}$	47.2	Flow system, toluene carrier	[7]
543 ~ 1023	$8.0 \times 10^7$	22.7	Flow system, hydrogen atmosphere	[75]
573 ~ 653	$8.1 \times 10^4$	22.9	Static system	[75]
553 ~ 673	$2.4 \times 10^{10}$	32.0	desorption on GaAs	[9]
585	-	37.8	decomposition on GaAs(100)	[6]
600	-	38.7	decomposition on GaAs(100)	[6]
750 ~ 850	-	60.0	Hartree-Fock (Homolysis)	[74]
750 ~ 850	-	43.6	Hartree-Fock ( $\beta$ -hydride elimination)	[74]
400 ~ 900	$4.7 \times 10^{22}$	65.3	DFT (homolysis)	This work
400 ~ 900	$1.9 \times 10^{13}$	40.5	DFT ( $\beta$ -elimination)	This work

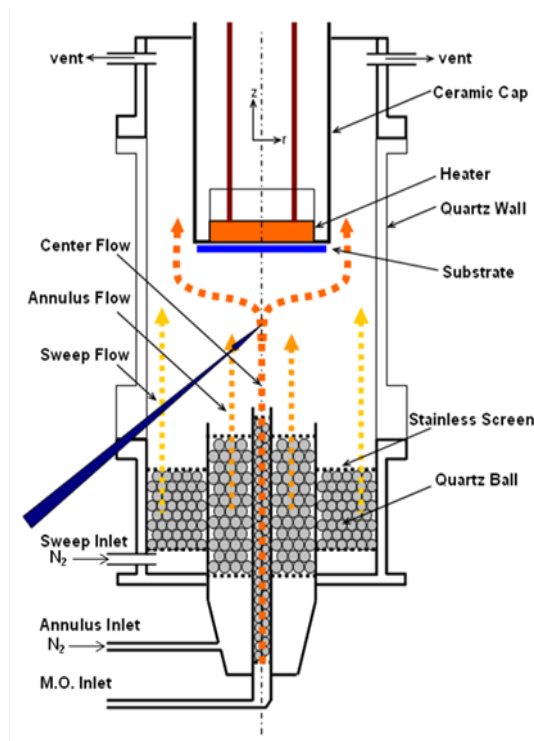


Figure 5-1. Schematic of the experimental reactor for *in situ* Raman spectroscopic measurements.

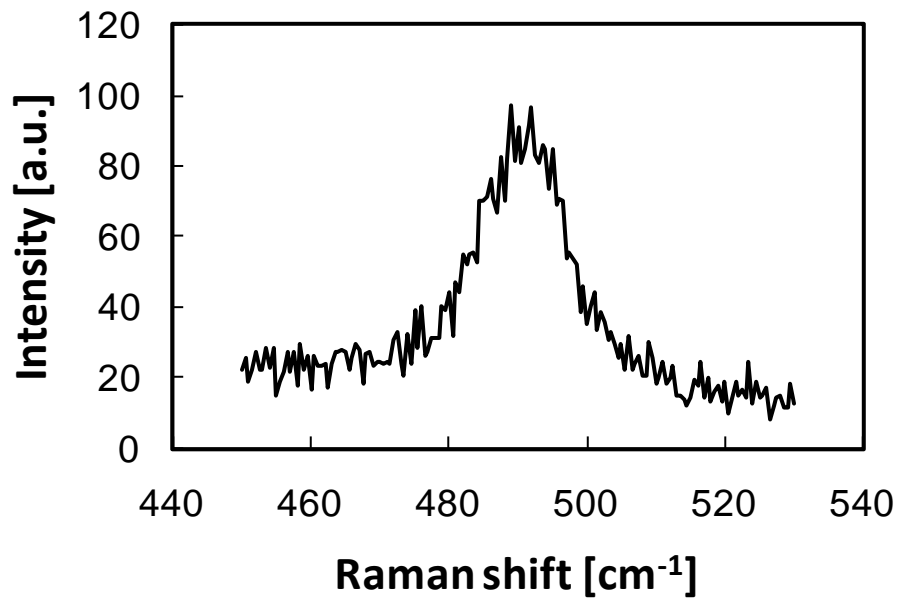


Figure 5-2. Recorded Ga–C<sub>3</sub> vibrational measurement of 490cm<sup>-1</sup>line.

Table 5-2. Reported relative Raman cross section for group II, III metal-organic sources

Precursor	DMCd	TMGa	TMIn	DEZn	TEGa
Relative Raman Cross-section	21.0 <sup>a</sup>	17.5 <sup>b</sup>	22.3 <sup>c</sup>	4.2 <sup>a</sup>	2.7 <sup>d</sup>

(a : Ref.[109], b : Ref.[112], c : Ref.[113], d: this work)

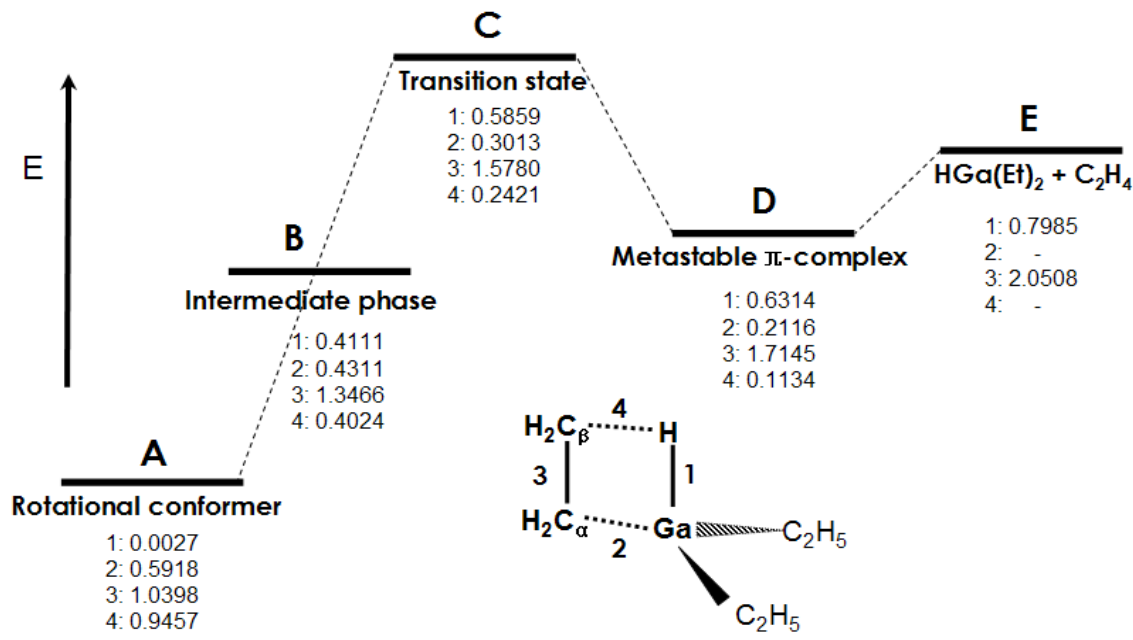


Figure 5-3. Schematized TEGa structure and energetics during first  $\beta$ -hydride elimination with Wiberg indices.

Table 5-3. Computed enthalpies ( $\Delta H$ , kcal/mol), entropies ( $\Delta S$ , cal/mol·K) and Gibbs free energies ( $\Delta G$ , kcal/mol) for selected gas-phase decomposition reactions at 298K and 900K using B3LYP/LanL2DZ model chemistry (Et : ethyl group, –C<sub>2</sub>H<sub>5</sub>)

	298K		900K			
	$\Delta H$	$\Delta S$	$\Delta G$	$\Delta H$	$\Delta S$	$\Delta G$
R1 (Et) <sub>3</sub> Ga = (Et) <sub>2</sub> GaH + C <sub>2</sub> H <sub>4</sub>	25.47	32.64	15.74	24.62	29.47	-1.90
T1 (Et) <sub>3</sub> Ga = (Et) <sub>3</sub> Ga TS1‡	38.60	-2.16	39.24	39.75	-0.48	40.19
T2 (Et) <sub>3</sub> Ga = (Et) <sub>3</sub> Ga TS2‡	38.33	-3.16	39.27	39.46	-1.54	40.84
R2 (Et) <sub>2</sub> GaH = (Et)GaH <sub>2</sub> + C <sub>2</sub> H <sub>4</sub>	26.46	38.90	14.86	26.85	-7.58	38.25
T3 (Et) <sub>2</sub> GaH = (Et) <sub>2</sub> GaH TS1‡	37.18	-0.70	37.39	38.30	0.91	37.48
T4 (Et) <sub>2</sub> GaH = (Et) <sub>2</sub> GaH TS2‡	37.03	-1.21	37.39	38.15	0.40	37.79
R3 (Et)GaH <sub>2</sub> = GaH <sub>3</sub> + C <sub>2</sub> H <sub>4</sub>	26.06	28.75	17.49	25.30	25.79	2.09
T5 (Et)GaH <sub>2</sub> = (Et) <sub>3</sub> Ga TS‡	34.88	-5.94	36.65	34.76	-6.84	40.91
R4 GaH <sub>3</sub> = Ga + 3/2H <sub>2</sub>	32.85	34.48	22.58	33.69	36.07	1.23
R5 (Et) <sub>3</sub> Ga = (Et) <sub>2</sub> Ga• + •C <sub>2</sub> H <sub>5</sub>	65.24	51.81	49.81	63.22	40.78	26.52
R6 (Et) <sub>2</sub> Ga• = (Et)Ga• + •C <sub>2</sub> H <sub>5</sub>	73.02	44.42	59.78	73.12	43.62	33.86
R7 (Et)Ga• = Ga + •C <sub>2</sub> H <sub>5</sub>	8.61	29.48	-0.18	8.81	29.26	-17.53
R8 2(Et) <sub>2</sub> GaH = (Et)HGa-Ga(Et) <sub>2</sub> + C <sub>2</sub> H <sub>6</sub>	-7.06	-8.15	-4.63	-9.23	1.27	-11.60
R9 2(Et) <sub>2</sub> GaH = ((Et)GaH) <sub>2</sub> + C <sub>2</sub> H <sub>6</sub> + C <sub>2</sub> H <sub>4</sub>	19.45	36.24	8.65	18.81	34.38	-12.13
R10 2(Et) <sub>2</sub> GaH = ((Et) <sub>2</sub> Ga) <sub>2</sub> + C <sub>4</sub> H <sub>10</sub>	0.17	1.55	-0.30	0.42	2.42	-1.76
R11 2(Et) <sub>2</sub> GaH = ((Et) <sub>2</sub> Ga) <sub>2</sub> + H <sub>2</sub>	2.86	2.52	2.11	7.17	11.82	-3.47
R12 2(Et)GaH <sub>2</sub> = ((Et)GaH) <sub>2</sub> + H <sub>2</sub>	1.29	-12.56	5.03	2.03	-10.52	11.50
R13 2(Et)GaH <sub>2</sub> = (Et)HGa-GaH <sub>2</sub> + C <sub>2</sub> H <sub>6</sub>	-9.63	-1.80	-9.10	34.19	28.42	8.62
R14 2(Et)GaH <sub>2</sub> = (GaH <sub>2</sub> ) <sub>2</sub> + C <sub>4</sub> H <sub>10</sub>	-15.60	-11.24	-12.25	-17.53	-14.82	-4.19
R15 (Et)GaH <sub>2</sub> + (Et) <sub>2</sub> GaH = ((Et)GaH) <sub>2</sub> + C <sub>2</sub> H <sub>6</sub>	-7.00	-2.66	-6.21	-8.03	-3.87	-4.55
R16 (Et)GaH <sub>2</sub> + (Et) <sub>2</sub> GaH = (Et)HGa-GaH <sub>2</sub> + C <sub>4</sub> H <sub>10</sub>	-17.02	2.08	-17.64	28.27	34.71	-2.97
R17 (Et)GaH <sub>2</sub> + (Et) <sub>2</sub> GaH = (Et)HGa-Ga(Et) <sub>2</sub> + H <sub>2</sub>	1.24	-18.06	6.62	0.84	-17.42	17.32
R18 (Et)GaH <sub>2</sub> + (Et) <sub>2</sub> GaH = (Et)HGa-GaH <sub>2</sub> + C <sub>2</sub> H <sub>6</sub>	-9.32	-2.69	-8.52	-10.31	-3.79	-6.89
R19 C <sub>2</sub> H <sub>6</sub> = 2•CH <sub>3</sub>	83.06	41.04	70.83	84.98	43.30	46.01
R20 C <sub>2</sub> H <sub>6</sub> = C <sub>2</sub> H <sub>4</sub> + H <sub>2</sub>	34.75	28.99	26.11	36.92	31.60	8.48
R21 (Et)Ga• + 2•CH <sub>3</sub> = (Et)Ga(CH <sub>3</sub> ) <sub>2</sub>	-151.54	-74.05	-129.48	-151.27	-71.43	-86.98
R22 (Et) <sub>2</sub> Ga• + •CH <sub>3</sub> = (Et) <sub>2</sub> Ga(CH <sub>3</sub> )	-71.72	-36.87	-60.73	-71.03	-34.43	-40.04
R23 •C <sub>2</sub> H <sub>5</sub> + •CH <sub>3</sub> = C <sub>3</sub> H <sub>8</sub>	-80.42	-45.60	-66.83	-81.93	-47.08	-39.56
R24 (Et)Ga• + •CH <sub>3</sub> + •C <sub>2</sub> H <sub>5</sub> = (Et) <sub>2</sub> Ga(CH <sub>3</sub> )	-144.74	-81.29	-120.51	-144.15	-78.05	-73.90
R25 2•C <sub>2</sub> H <sub>5</sub> = C <sub>2</sub> H <sub>6</sub> + C <sub>2</sub> H <sub>4</sub>	-58.52	-17.61	-53.27	-60.49	-21.00	-41.59
R26 2•C <sub>2</sub> H <sub>5</sub> = C <sub>4</sub> H <sub>10</sub>	-77.80	-52.31	-62.22	-78.88	-52.95	-31.22
R27 (Et) <sub>2</sub> Ga• + C <sub>3</sub> H <sub>8</sub> = (Et) <sub>2</sub> Ga(CH <sub>3</sub> ) + •C <sub>2</sub> H <sub>5</sub>	19.84	17.18	8.93	21.87	12.65	10.49
R28 (Et) <sub>2</sub> Ga• + C <sub>3</sub> H <sub>8</sub> = (Et) <sub>3</sub> Ga + •CH <sub>3</sub>	15.17	-6.21	17.02	18.71	6.29	13.04
R29 (Et) <sub>2</sub> Ga• + C <sub>4</sub> H <sub>10</sub> = (Et) <sub>2</sub> Ga(CH <sub>3</sub> ) + •C <sub>3</sub> H <sub>7</sub>	8.72	4.23	7.46	9.68	5.67	4.57
R30 (Et) <sub>2</sub> Ga• + C <sub>4</sub> H <sub>10</sub> = (Et) <sub>3</sub> Ga + •C <sub>2</sub> H <sub>5</sub>	12.56	0.50	12.41	15.66	12.17	4.71
R31 (Et) <sub>2</sub> Ga• + C <sub>4</sub> H <sub>10</sub> = (Et) <sub>2</sub> Ga(C <sub>3</sub> H <sub>7</sub> ) + •CH <sub>3</sub>	11.72	-4.64	13.11	13.18	-2.54	15.46
R32 2(Et) <sub>2</sub> Ga• = ((Et) <sub>2</sub> Ga) <sub>2</sub>	-52.16	-31.19	-42.86	-47.80	-21.42	-28.53
R33 3(Et)Ga• = ((Et)Ga) <sub>3</sub>	-152.76	-74.97	-130.42	-150.97	-69.51	-88.41
R34 4(Et)Ga• = ((Et)Ga) <sub>4</sub>	-249.20	-117.35	-214.22	-244.76	-105.44	-149.87

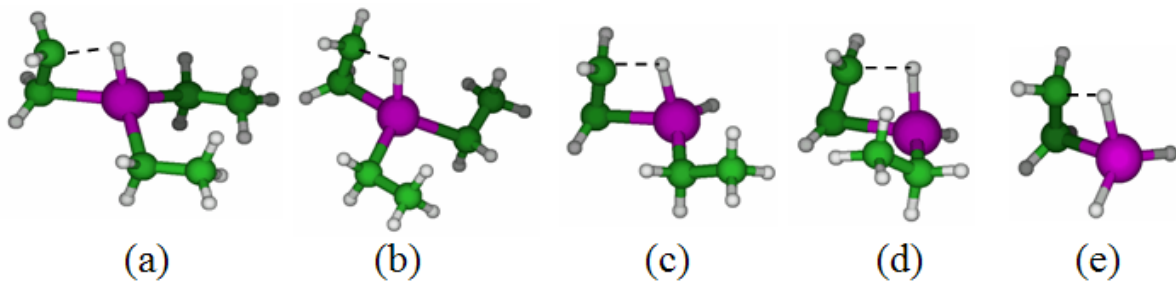


Figure 5-4. Schematics of  $\beta$ -hydride elimination transition state structures ((a) TEGa TS1 $\ddagger$ , (b) TEGa TS2 $\ddagger$ , (c) (Et)<sub>2</sub>GaH TS1 $\ddagger$ , (d) (Et)<sub>2</sub>GaH TS2 $\ddagger$ , (e) (Et)GaH<sub>2</sub> TS $\ddagger$ ).

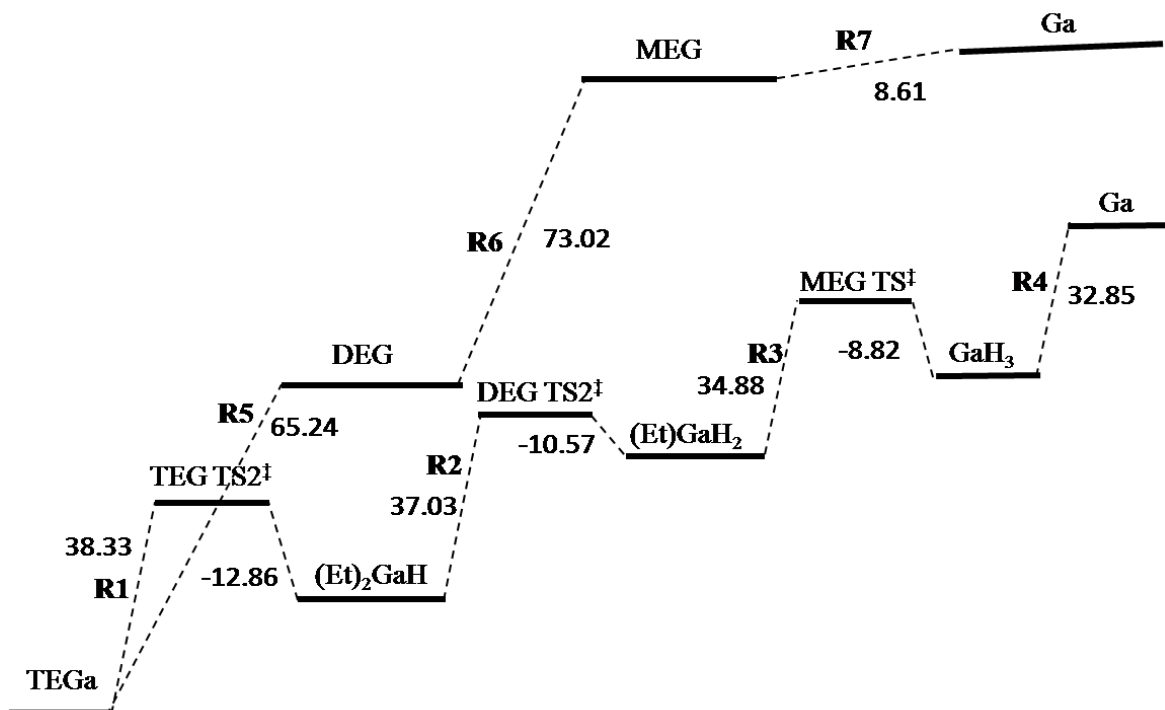


Figure 5-5. Calculated energetics of the two major thermal decomposition pathways of TEGa with reaction enthalpies [kcal/mol] listed.

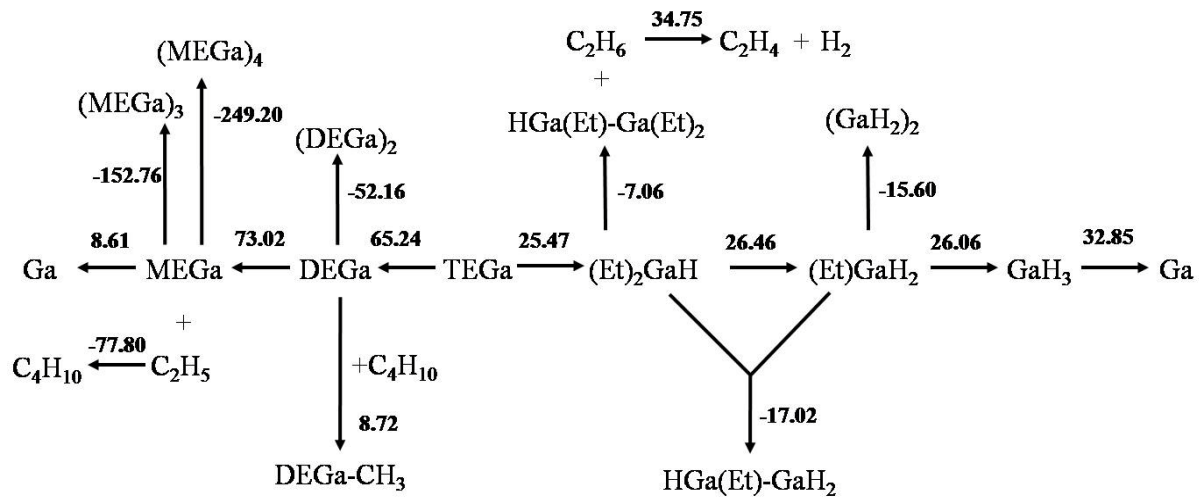


Figure 5-6. 17 screened reaction pathways out of 34 with reaction enthalpies [kcal/mol] listed.

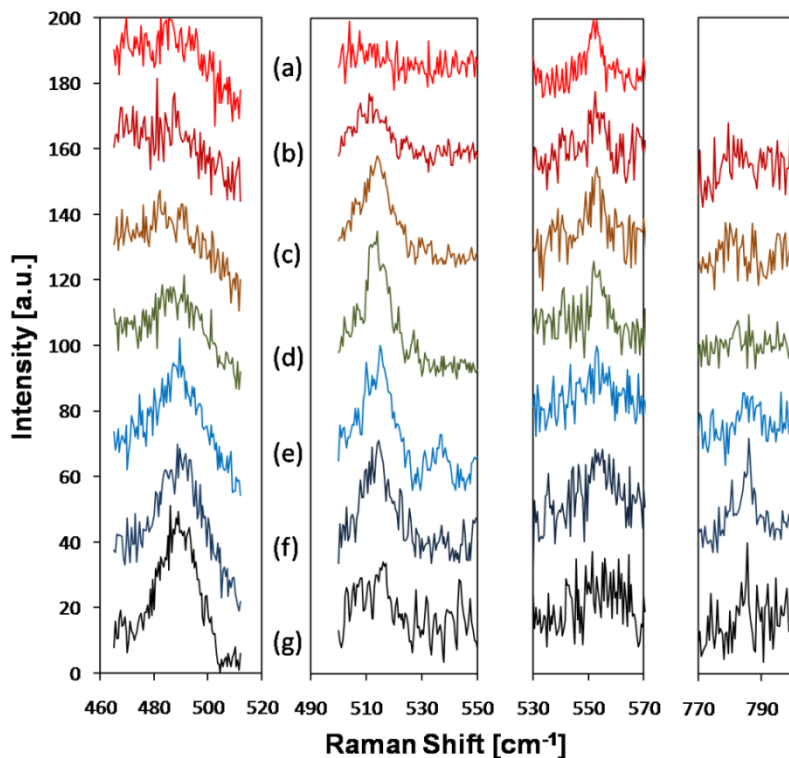


Figure 5-7. Raman spectrum of gas-phase TEGa. Different horizontal line means different height measurement along the centerline. ((a) 1mm (b) 2mm (c) 4mm (d) 6mm (e) 8mm (f) 10mm (g) 11mm from the heated susceptor).

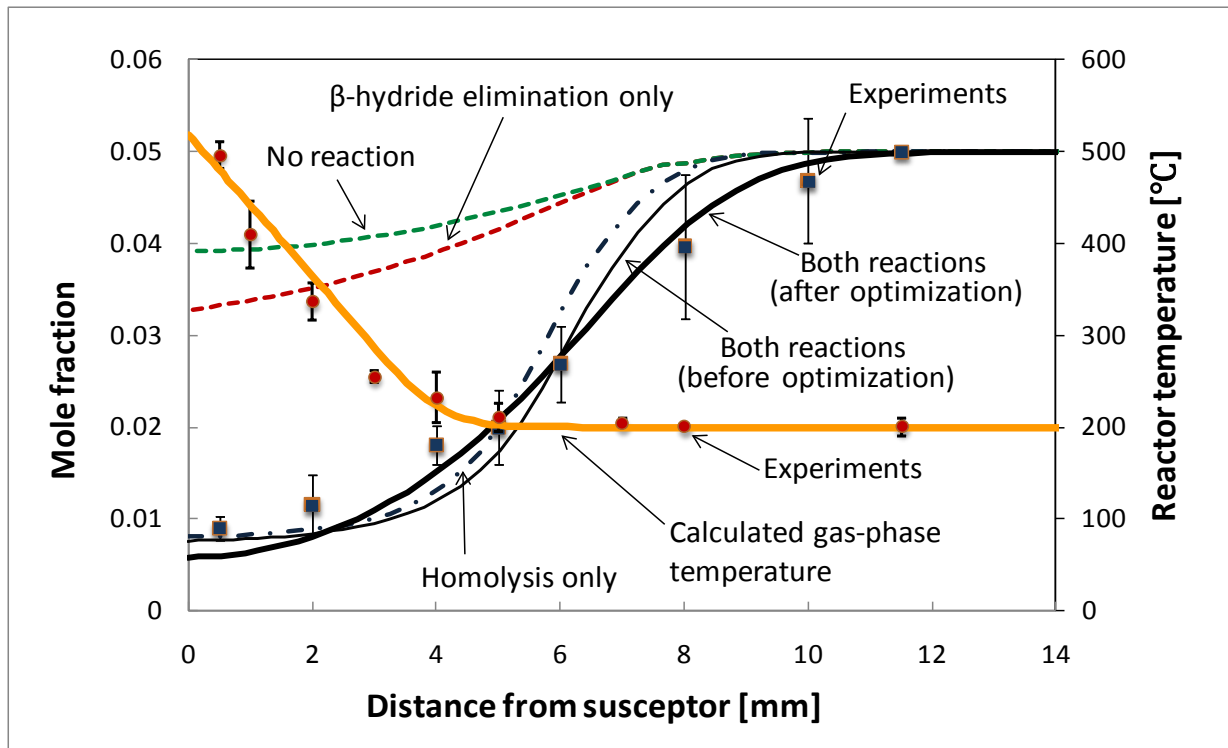
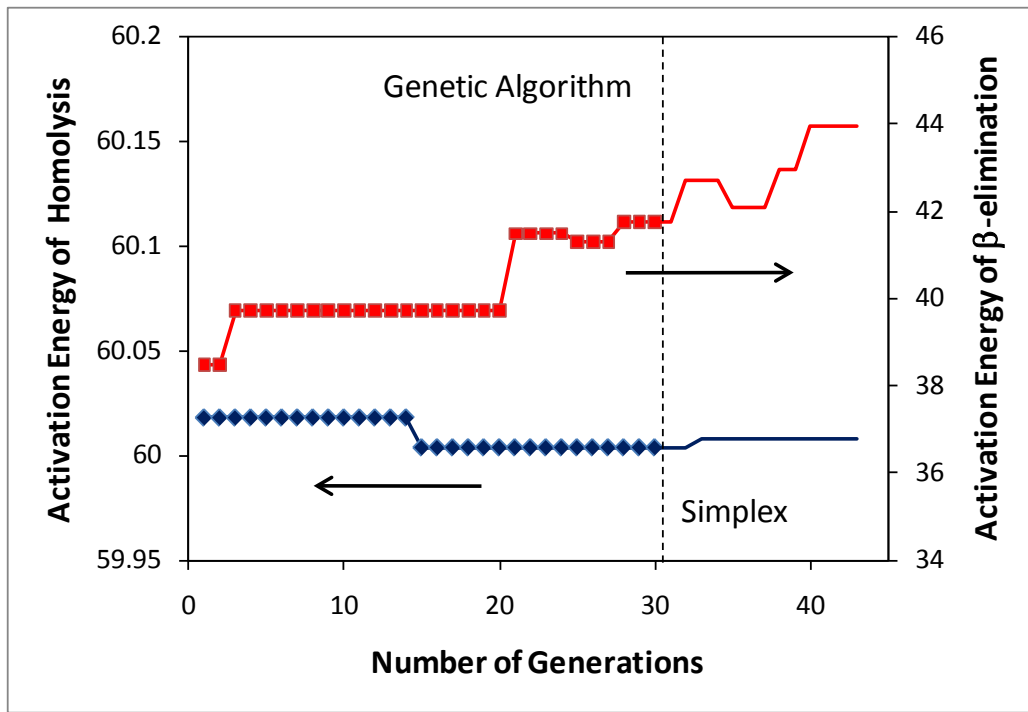
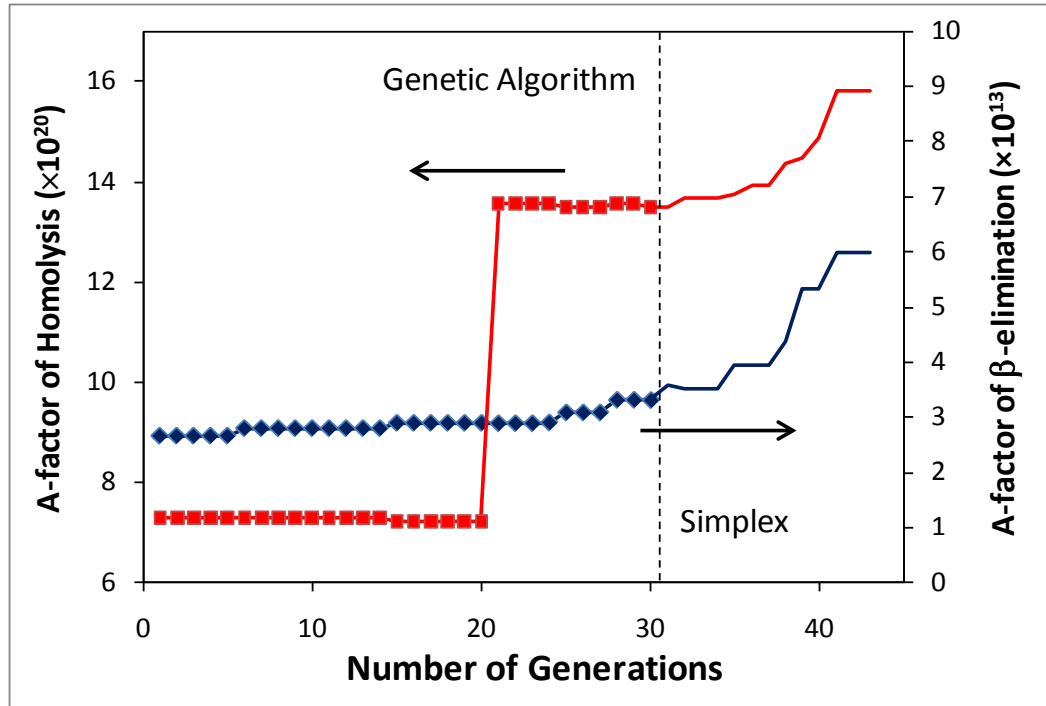


Figure 5-8. Simulated and experimental concentration profile of TEGa in the reactor.



A



B

Figure 5-9. Optimized values of rate parameters of two main reactions for (A) activation energy and (B) A-factor (pre-exponential factor).

Table 5-4. Calculated and corrected Raman active Ga–C stretching frequencies only for the symmetric motions (Lowercase s, m and w attached to the calculated frequencies mean strong, medium and weak intensity, respectively)

	Calculated	Experimental	Scaling Factor	Corrected
TEGa	470.8 s	490	1.0408	<b>490</b>
DEGa	453.9 s		1.0408	472.4
MEGa	336.4 m		1.0408	350.1
(Et) <sub>2</sub> GaH	490.8 m		1.0408	510.8
(Et)GaH <sub>2</sub>	450.5 m		1.0408	468.9
	563.1 m		1.0408	586.1
(Et)GaH–Ga(Et) <sub>2</sub>	513.4 m	537	1.0408	<b>534.3</b>
(Et)GaH–GaH <sub>2</sub>	533.0 w	555	1.0408	<b>554.7</b>
DEGa–CH <sub>3</sub>	486.0 m		1.0408	505.8
(DEGa) <sub>2</sub>	496.8 m	517	1.0408	<b>517.1</b>
	531.0 m	555	1.0408	<b>552.7</b>
(MEGa) <sub>3</sub>	493.0 s		1.0408	513.1
(MEGa) <sub>4</sub>	526.4 s		1.0408	547.9

**CHAPTER 6**  
**HOMOGENEOUS THERMAL DECOMPOSITION STUDIES OF**  
**TRIETHYLALUMINUM(TEAL): EFFECT OF NH<sub>3</sub>**

**Overview**

Aluminum nitride is a wide and direct band-gap semiconductor (6.2 eV at 300K) and a refractory ceramic with a high thermal conductivity (285 W/mK). In recent years the properties of aluminum nitride thin films make this material interesting for various applications such as blue and UV photodetectors and light-emitting diodes[114, 115]. However, most interest is focused toward the properties of its alloys with GaN which can be fabricated AlGaN-based devices. Among various deposition technique, metalorganic chemical vapor deposition (MOCVD) provides a useful strategy to grow III-V compound semiconductor. For AlN film, trialkylaluminum compounds, such as triethylaluminum (TEAl) and trimethylaluminum (TMAI), are the most widely used metalorganic aluminum sources. However, AlN films deposited using TMAI usually contain very high levels of carbon[116]. Since TEAl has three ethyl groups and these can be eliminated through consecutive  $\beta$ -hydride eliminations even under relatively low temperature, TEAl has been focused as one of the good alternatives, such as, triisobutylaluminum (TIBAl), dimethylaluminum hydride (DMAH), triethylamine alane (TEAA) and trimethylamine alane (TMAA)[116]. Ho et al. have deposited films that have comparatively better crystallinity with TEAl and NH<sub>3</sub> at 723 ~ 1173K[117]. Although TMAI and TEAl are commonly used for MOCVD, it is very difficult to find studies for the gas phase thermal decomposition, especially, considering the effect of ammonia on the mechanism. Like the other triethyl-metal precursors, such as TEGa and TEIn, TEAl has two major decomposition routes, i.e.,  $\beta$ -hydride eliminations and homolysis and Smith and his coworker have reported both reactions using IR and mass spectrometry by

detecting hydrocarbons such as  $C_2H_4$  and  $C_4H_{10}$ , possibly products of  $\beta$ -hydride eliminations and homolysis, respectively[118].

In this study, TEAI decomposition kinetics in a vertical, impinging jet, cold-wall CVD reactor were investigated and reaction intermediates were identified. In addition to TEAI study, ammonia effect on TEAI decomposition mechanism was studied using gas phase *in situ* Raman spectroscopy and DFT calculations by Raman shift corrections.

### **Experimental and Theoretical Methods**

To elucidate homogeneous thermal decomposition mechanisms of TEAI in CVD reactor, the reactor configuration in Fig.6-1 was used. CVD reactor shown in Fig.6-1 was interfaced with *in situ* Raman spectrometer (Ramanor U-1000, Jobin Yvon) that has double additive monochromator for better resolution. 532.08nm line of Nd:YAG solid-state laser was used as the excitation of metalorganic precursor. As described in detail elsewhere[119], this CVD reactor is custom-designed cold wall, up-flow impinging jet reactor to study the gas phase decomposition kinetics of TEAI.

Metalorganic precursor and carrier gas including co-reactant such as ammonia can be introduced to CVD reactor through three concentric inlet tubes – center, annulus and sweep flows. All three tubes are packed with 3 mm glass beads to supply parallel flow from inlet to susceptor. Moreover,  $N_2$  sweep flow envelops metalorganic gas not to make wall deposition ( $Al_2O_3$ ). In the case of introducing ammonia with TEAI, to prevent adduct formation of TEAI and ammonia before inlet, TEAI and ammonia were introduced center and annulus tube, respectively. Pure  $N_2$  was introduced into the reactor through three inlets at 21 °C as a carrier gas. The gas velocity was set at 2.5 cm/s for all inlets and sufficient residence time was allowed to maintain stable flow. The vapor pressure of TEAI is much lower than trimethylaluminum (TMAI) leading to its

application and massive deposition be limited. However, owing to ethyl group, TEAI has advantage on low carbon contamination on film compositions. The vapor pressure of TEAI was estimated using Eq.6-1:

$$\log P(\text{mmHg}) = 9.00 - \frac{2361.2}{T(K) - 73.8} \quad (6-1)$$

where T stands for temperature in Kelvin. Bubbler of TEAI was maintained 90 °C and the vapor pressure was calculated 6.91 mmHg (0.9 %) in the current experiment. Usually aluminum alkyls exist dimer form of  $\text{AlR}_3$  ( $\text{R}=\text{CH}_3, \text{C}_2\text{H}_5, \text{n-C}_3\text{H}_7, \text{n-C}_4\text{H}_9, \text{i-C}_4\text{H}_9$ , etc) in the liquid phase, however, most of those have monomer form in the gas phase[120]. In the case of TEAI, the entropy of vaporization (176.6 J/mol K) is almost exactly two times larger than the value of 88 J/mol K calculated by Trouton's rule. This indicates that 1 mole of liquid is converted into 2 moles of vapor in the process of vaporization. Therefore, one can conclude TEAI dimers are present in the liquid, however the vapor consists of monomeric TEAI. Based on this information, gas phase TEAI introduced to CVD reactor is complete monomeric TEAI since the lowest temperature of CVD reactor is around 128 °C. Raman scattering signals were recorded along with the centerline of the reactor and heater temperature was set at 500 °C. Not to interrupt the flow pattern in the reactor, temperature measurement was performed with spectroscopic method. Since this technique does not make any hindrance in the reactor, it can make very accurate results and Raman spectroscopic temperature measurement could be accurate with less than 7% uncertainty in the range of 20~2230°C[18]. From the modified equation for Stokes Raman scattering intensity, temperature distributions are obtained from linear regression of experimental data.

To study ammonia effect on thermal decomposition mechanism of TEAI, two types of experiments were performed. First set of experiment used pure TEAI through center inlet and second experiment introduced 5 % ammonia into annulus inlet with nitrogen. Since ammonia was introduced annulus inlet and Raman scattering measurement was obtained at the reactor centerline, one can easily expect ammonia concentration would be increase from inlet to the heated susceptor in an up-flow reactor.

The spin polarized hybrid density functional B3LYP with the LanL2DZ calculations using Gaussian 03 program[73] were performed to assist experimental results. Using this model chemistry, optimized geometry, activation energy, vibrational frequency were calculated at temperature range of 298~1000 K.

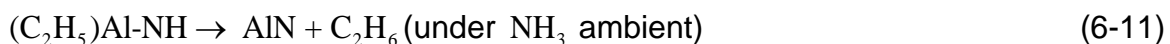
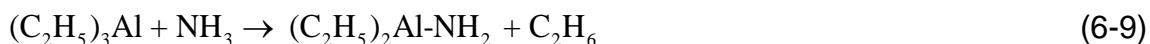
## Results and Discussion

### Homogeneous TEAI Thermal Decomposition Experiments

A few decades ago, Smith and his coworker have studied the thermal decomposition of TEAI in static systems over the temperature range of 162~192 °C[118]. Even though that previous research was performed in static systems and under narrow temperature range, it can have a few similarities in decomposition mechanisms. They have followed the partial pressure of TEAI according to the duration of reaction and it could make them for having kinetic parameters. From the Arrhenius plot for aluminum-ethyl bond decomposition between 162.0 and 192.4 °C, the value for the activation energy,  $E_a$ , was 29 kcal/mol, and the 'A' factor was  $1.6 \times 10^8 \text{ s}^{-1}$ . Like other ethyl containing metal compound, such as triethylgallium (TEGa), TEAI also has possibility to decompose with two main directions:  $\beta$ -hydride elimination and homolysis reaction. Usually  $\beta$ -hydride elimination and homolysis reaction proceed following manner.

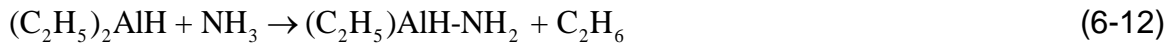


Through Eqs. 6-2 to 6-8, TEAI can produce metal aluminum. Similar to TEGa,  $\beta$ -hydride elimination would have energy barrier for transition state to form hydride molecule and homolysis reaction proceeds through elongation of bond between Al and ethyl group. Since intermediates from  $\beta$ -hydride elimination have metal–H bond, it would arise distinct signal other than C–H bond ( $\sim 2000\text{ cm}^{-1}$  and  $\sim 3000\text{ cm}^{-1}$  for metal–H and C–H, respectively). However, if it decomposes with co-reactant, ammonia in this case, those two main mechanisms might be interrupted from co-reactant. In other words, any intermediates can react with ammonia and following steps would be changed.



Jiang and his coworker have reported AlN thin film and powder with TEAI with ammonia following above reactions, i.e., Eqs. 6-9 to 6-11 by chemical vapor deposition[121]. Certainly, Eqs. 6-9 to 6-11 have to be considered adduct formation in

between reactants and products, respectively. Other than these reactions, because  $\beta$ -hydride elimination and/or homolysis reaction products can react with ammonia, one can assume following side reactions.



To study TEAI thermal decomposition pathways in an up-flow, cold-wall CVD reactor as described before, experiments were performed under well controlled conditions. 0.9 % of TEAI was introduced into the reactor centerline with pure  $N_2$ .

Nitrogen rotational Raman signals give us temperature information in the reactor and it has a large relative Raman cross-section so that gives a strong Raman band that is used to normalize the peaks of intermediates. Sufficient residence time was allowed for stable flow in the reactor under the heater set at 500 °C. Although Kvisle and his coworker measured monomeric IR spectroscopy of TEAI[122] and Yamamoto had dimeric TEAI Raman spectroscopic measurement[123], to the best of my knowledge, no gas phase monomeric TEAI Raman signals have been reported. Since Al–C stretch at 648  $cm^{-1}$  has been observed from IR spectroscopy, one can expect Raman signal might be observed at similar region. Unfortunately even the repetitive experiments, signals for aluminum–ethyl vibration were not observed. However, a few signals for intermediates have been observed and it would give enough information for determining reaction mechanism. Fig.6-2 shows Raman spectrum profile from the cold inlet to the heated susceptor for pure gas phase TEAI. From this first set of experiment, it is confirmed that the observed signals of 600, 1989, 2025, 2580, 2835, 2849, 2900, 2918, 2939, 3173  $cm^{-1}$ .

Raman shift of  $600\text{ cm}^{-1}$  can be assigned to H wagging of Al–H in DEAlH (diethylaluminum hydride). This will be specified in detail on following chapter. Unlike  $600\text{ cm}^{-1}$ , signals at the region over  $2800\text{ cm}^{-1}$  are not easy to assign since various C–H vibrations have similar IR and/or Raman frequencies. To elucidate ammonia effect on TEAl thermal decomposition mechanisms, 5 % of ammonia was introduced through annulus inlet. Fig.6-3 shows Raman spectrum observation along the reactor centerline from cold inlet to the heated susceptor.

Raman shift at  $449\text{ cm}^{-1}$  is from  $\text{NH}_3$  rotational spectrum and 934, 964, 3219,  $3334\text{ cm}^{-1}$  are from  $\text{NH}_3$  vibrational spectra. However, one can find  $452\text{ cm}^{-1}$  shoulder attached to  $449\text{ cm}^{-1}$  signal and 1462, 1525, 1639, 2580,  $2838\text{ cm}^{-1}$  Raman shifts. Since observed spectra from two different sets of experiments have only small overlap, one can assume most intermediates produced by  $\beta$ -hydride elimination or homolysis reaction are consumed right after being produced not to be observed or TEAl decomposition with ammonia are carried out with different routes compared with neat TEAl experiment. From these expectations, decomposition mechanism can be supposed and it would be confirmed and described in detail later.

Although there are various complexes that can consume ammonia based on Fig.6-3, experimental ammonia concentration profile in CVD reactor can provide information on mechanism. Fig.6-4 shows ammonia concentration profile in CVD reactor for two cases, with and without reaction. And temperature profile that was measured by laser is also shown in the Fig.6-4. This technique that measures nitrogen rotational state distribution with focused laser does not make any hindrance to flow and

shows high accuracy. Solid line with temperature measurement is simulated profile with FEM reactor modeling described in detail elsewhere[119].

Ammonia concentration profile was measured for two cases, i.e., (a) without reaction and (b) with reaction. For case (a), 5 % ammonia was used at 500 °C without TEAI introduction to the reactor, and for case (b), same 5 % ammonia with 0.9 % TEAI were introduced to the reactor and ammonia concentration profile was dramatically changed at around 9 mm from susceptor. And then concentration of case (b) has increasing gap compared with case (a). One should note that ammonia concentration with reaction shows equilibrium at ca. 4 mm from susceptor. Numerous possibility can be supposed for this equilibrium, for instance, TEAI:NH<sub>3</sub> adduct can release NH<sub>3</sub> at higher temperature. Unexpectedly, this flat concentration region was shown at temperature ramping area.

### DFT Calculations

In TEAI/NH<sub>3</sub> systems, TEAI molecule makes a stable Lewis acid-base adduct bound to ammonia, i.e., (C<sub>2</sub>H<sub>5</sub>)<sub>3</sub>Al:NH<sub>3</sub>[114, 124]. The adduct formation is supported by NBO (Natural Bond Orbital) analysis even though various researchers have considered it fundamental reaction. By tracking Wiberg bond indices of each bond, it can be clearly explained. As described above, B3LYP method with LanL2DZ basis set was used for DFT calculations.

From Wiberg indices shown in Fig.6-5, one can assure that N in ammonia makes strong bond with Al. Moreover Al–C bond is weakened and ethyl group with H in ammonia forms new moiety, i.e., C<sub>2</sub>H<sub>6</sub>, during reaction coordinate. It should be noted that each bond in four-membered ring, Al–C–H–N has similar bond strength at the transition state. Al–N bond strength of product is approximately three times higher than

adduct. Detailed reaction mechanism with optimized geometry for TEAl adduct with ammonia is described in Fig.6-6. This energy change shows small differences with results from Ikenaga's study even though he used same level of theory.[124]

Due to Lewis acid-base interactions between TEAl and ammonia, adduct forms stable complex that has lower energy by 22.8 kcal/mol than reactants. And DEAI-NH<sub>2</sub> and C<sub>2</sub>H<sub>6</sub> are produced via transition state that has slightly higher energy than initial reactants. Other than 1:1 ratio for TEAl and ammonia, one can suppose the possibility of reacting more ammonia with TEAl. If TEAl molecules are in the presence of excess ammonia, TEAl makes a stable complex with two ammonia molecules without potential energy barrier. This tendency is applied to other trialkyl metal compound with the form of R<sub>3</sub>M (R= -CH<sub>3</sub>, -C<sub>2</sub>H<sub>5</sub>, M=Al, Ga, In)[124].

Interestingly, overall scheme in Fig.6-7 does not show much difference with Fig.6-6. Adduct, transition state and final products have similar relative energy compared with simple ammonia adduct case, i.e., TEAl:NH<sub>3</sub>. One of the products, H<sub>2</sub>Al-NH<sub>2</sub> can form dimer or trimmer before deposition of AlN thin films. In this study, only dimer and trimmer were considered to make tetramer and hexane, respectively as shown in Fig.6-8.

There can be numerous possible alternative pathways to produce tetramer and hexane during the course of structural growth. In this study, only a specific route to the desired target is investigated computationally. One can find out detailed review of broad coverage from Timoshkin's work[125]. As an analogous complex, Hwang et al. have reported the thermal conversion of cyclotrigallazane, [H<sub>2</sub>GaNH<sub>2</sub>]<sub>3</sub>, to cubic GaN at 150

°C [126] and Jegier and his coworkers showed the formation of  $[\text{HGaNH}]_n$  from diamidogallium hydride and characterized IR spectroscopy[127, 128].

### The Comparison of Experimental Results with DFT Calculations

For assigning frequencies to intermediates, simulated frequencies using the B3LYP/LanL2DZ level of theory and reference data were used. DFT calculations suggest vibrational frequencies for intermediates suggested in the proposed decomposition mechanisms. Experimental Raman active stretching frequencies with calculated and corrected values for all complexes including values for ammonia are shown in Table 6-1.

One should note that three bands at 2835, 2841, 2849  $\text{cm}^{-1}$  are mixed in together and it should be deconvolved into each signal. Spectrum was deconvolved for more precise analysis using PeakFit v4.12. And one can confirm the ammonia effect on spectrum around 2840  $\text{cm}^{-1}$  as shown in Fig.6-9. Moreover, intermediates produced by  $\beta$ -hydride elimination such as DEAIH and DEAI-AIH<sub>2</sub> were not observed at the experiment of TEAI + NH<sub>3</sub> system and ammonia related intermediates, i.e., H<sub>2</sub>Al-NH<sub>2</sub> and H<sub>2</sub>N-AIH-NH-AIH<sub>2</sub>, were observed. From these results, DEAIH and DEAI-AIH<sub>2</sub> would react with ammonia fast enough not to be detected after the first  $\beta$ -hydride elimination. Sauls et al. have reported TEAI:NH<sub>3</sub> adduct forms  $[(\text{Et})_2\text{AlNH}_2]_3$  (i.e., amide six-membered ring) and it forms AlN via  $[\text{EtAlNH}]_n$  (i.e., imide six-membered ring)[129]. However, amide formation was processed under liquid phase with (TEAI)<sub>2</sub> at 50 °C. The peak at 1639  $\text{cm}^{-1}$  would be assigned to NH<sub>2</sub> scissoring mode of H<sub>2</sub>Al-NH<sub>2</sub> and this assignment is also supported by computed result and Raman characteristic group frequency.

Certainly one can see the lack of peak B in Fig.6-9b. Peaks A, B, and C were assigned to C–H stretching of MEAIH<sub>2</sub>, TEAl:NH<sub>3</sub> and MEAIH-AlH<sub>2</sub>, respectively, by frequency analysis. From above analysis, proposed decomposition mechanism of TEAl with and without ammonia as shown in Fig.6-10 and it shows ammonia effect on TEAl decomposition process.

Fig.6-10 shows small overlap in mechanisms, (Et)AlH–AlH<sub>2</sub> formation and two β-hydride elimination products. And one should note that homolysis intermediates such as diethylgallium dimer, (Et)<sub>2</sub>Ga-Ga(Et)<sub>2</sub> or C<sub>4</sub>H<sub>10</sub>, were not detected from both experiments. Possibly relatively low operating temperature could prohibit homolysis reaction that has higher energy barrier. The fact that TEAl + NH<sub>3</sub> system did not show homolysis intermediates can be one of evidences that homolysis is not a main process in these systems. When it comes to ammonia effect on TEAl decomposition, ammonia attacks TEAl and (Et)AlH<sub>2</sub> directly and makes adducts with them. Although H<sub>2</sub>N–AlH–NH–AlH<sub>2</sub> was observed, four-membered ring, [HAINH]<sub>2</sub> or higher-membered rings were not detected, unfortunately. However, this observation can show one of stepping-stones to AlN film formations.

### Concluding Remarks

A study for ammonia effect on the thermal decomposition kinetics of TEAl with N<sub>2</sub> carrier gas in a custom up-flow, cold-wall CVD reactor was shown that combination of ammonia with β–hydride elimination product produce H<sub>2</sub>Al–NH<sub>2</sub> that is the another reactant for AlN film formation in the reaction zone of the reactor. By suggesting the presence of TEAl:NH<sub>3</sub> adduct, DEAIH, TEAl:NH<sub>3</sub> TS, H<sub>2</sub>N–AlH–NH–AlH<sub>2</sub>, H<sub>2</sub>Al–NH<sub>2</sub>, MEAIH<sub>2</sub>, MEAIH–AlH<sub>2</sub> and DEAI–AlH<sub>2</sub>, ammonia effect on TEAl decomposition mechanism was confirmed using *in situ* Raman spectroscopy and DFT calculations at

the B3LYP/LanL2DZ level of chemistry. Raman shifts of 600, 1989, 2025, 2580, 2835, 2849, 2900, 2918, 2939, and 3173 cm<sup>-1</sup> were found at the experiment of neat TEAI, and 452, 1462, 1525, 1639, 2580, 2853, 2841, and 2849 cm<sup>-1</sup> were found at the experiment of TEAI with ammonia. In addition to that, four vibrational spectra of 930, 965, 3230, and 3334 cm<sup>-1</sup> for ammonia were observed with high intensity. The temperature distribution of reactor centerline was measured and this was compared to the simulated results using custom-FEM Galerkin method. Those measured and simulated temperature profiles agree very well. This methodology that compares the results from the experiment using *in situ* Raman spectroscopy with DFT calculations and FEM reactor model suggests considerable way to investigate the thermal decomposition mechanism in the CVD reactor since this method does not interrupt the flow pattern and reaction pathways.

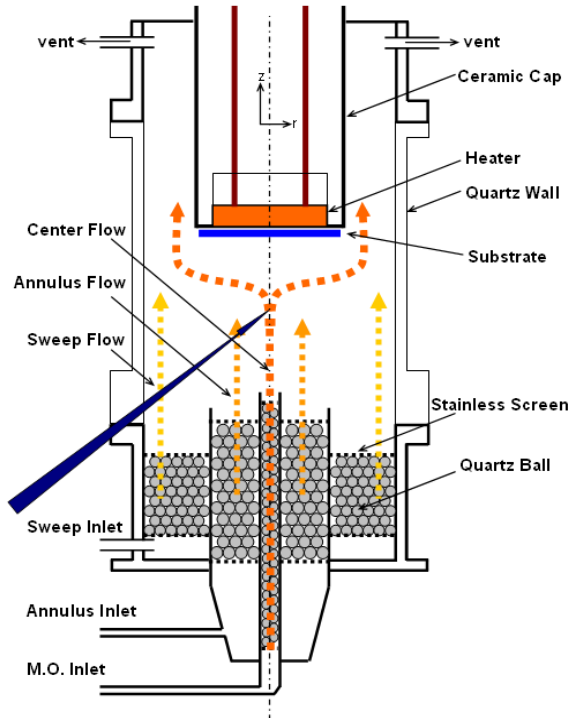


Figure 6-1. (Color online) Schematic drawing of the CVD reactor interfaced with in situ Raman spectrometer.

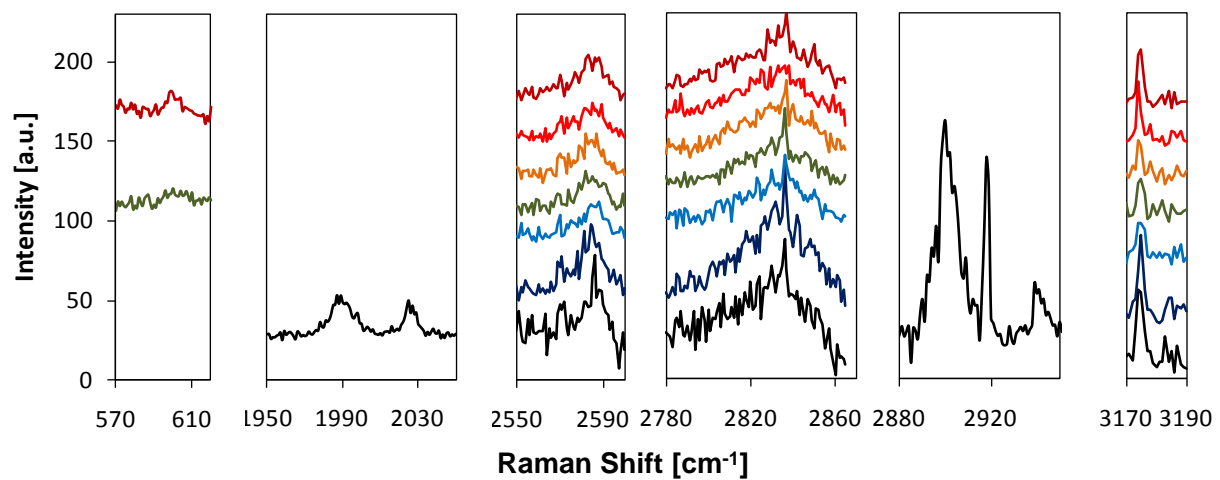


Figure 6-2. (Color online) Raman spectrum of gas-phase TEAl. Different horizontal signal means different height measurement along the centerline from the cold inlet (black bottom signals) to the heated susceptor (red top signals).

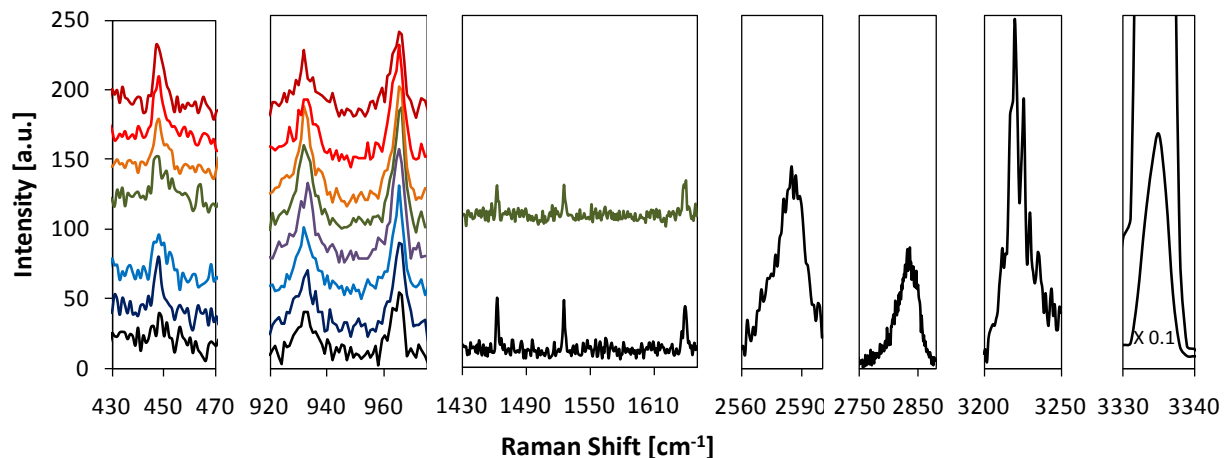


Figure 6-3. (Color online) Raman spectrum of gas-phase TEAl with ammonia. Different horizontal signal means different height measurement along the centerline from the cold inlet (black bottom lines) to the heated susceptor (red top lines).

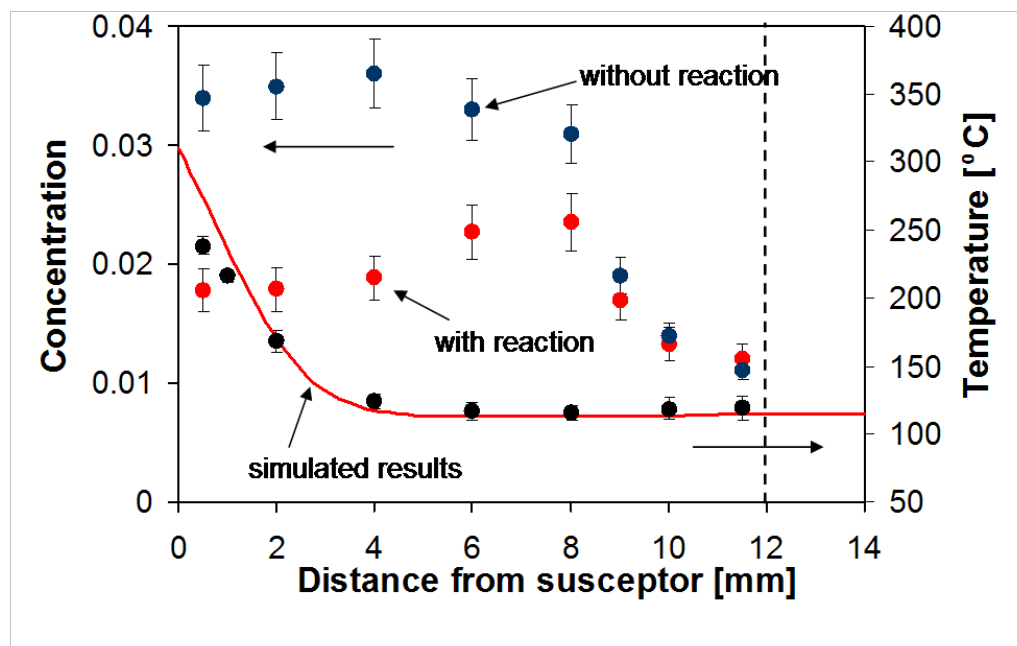


Figure 6-4. (Color online) Measured and simulated temperature and ammonia concentration profile (with and without reaction) in CVD reactor.

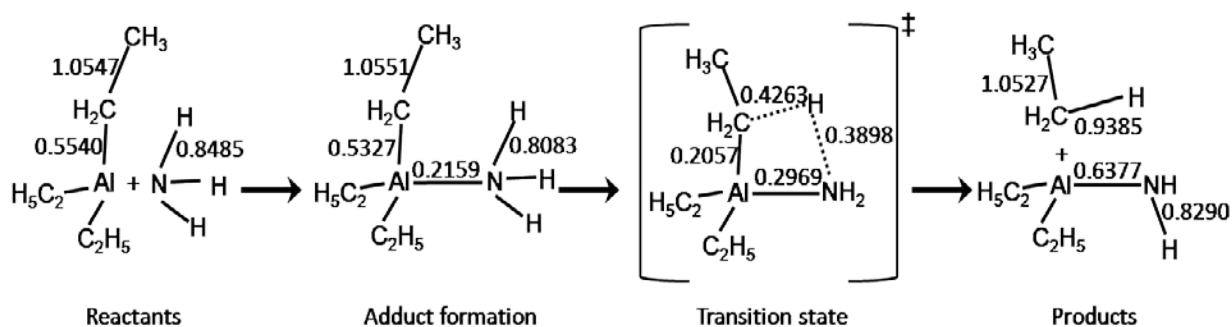


Figure 6-5. Wiberg indices tracking of  $\text{C}_2\text{H}_6$  elimination from TEAI: $\text{NH}_3$  adduct.

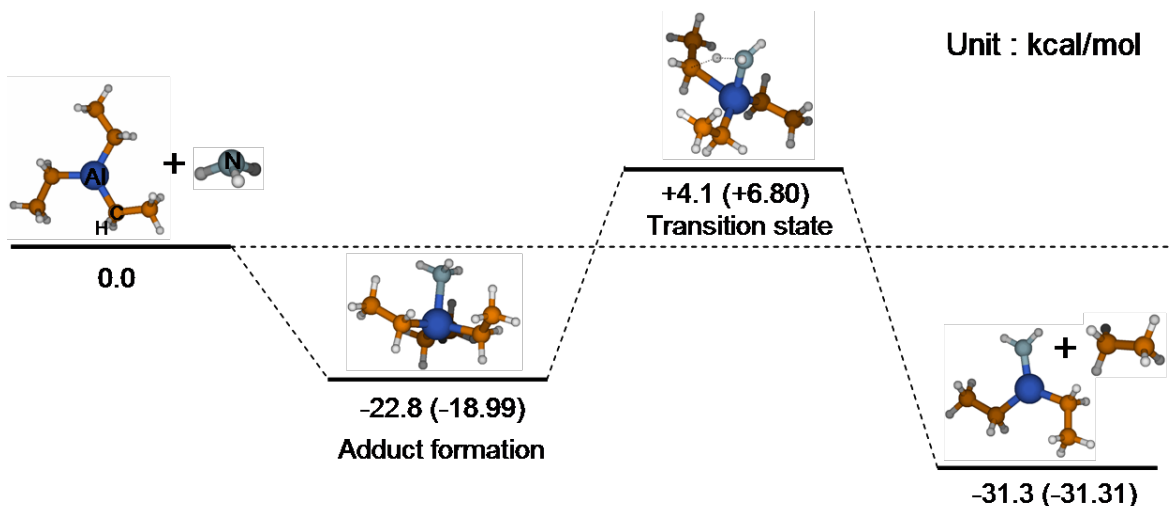


Figure 6-6. (Color online) Relative energy diagram of  $\text{C}_2\text{H}_6$  elimination from TEAI: $\text{NH}_3$  adduct (Energies in parenthesis are from Ref.[124]).

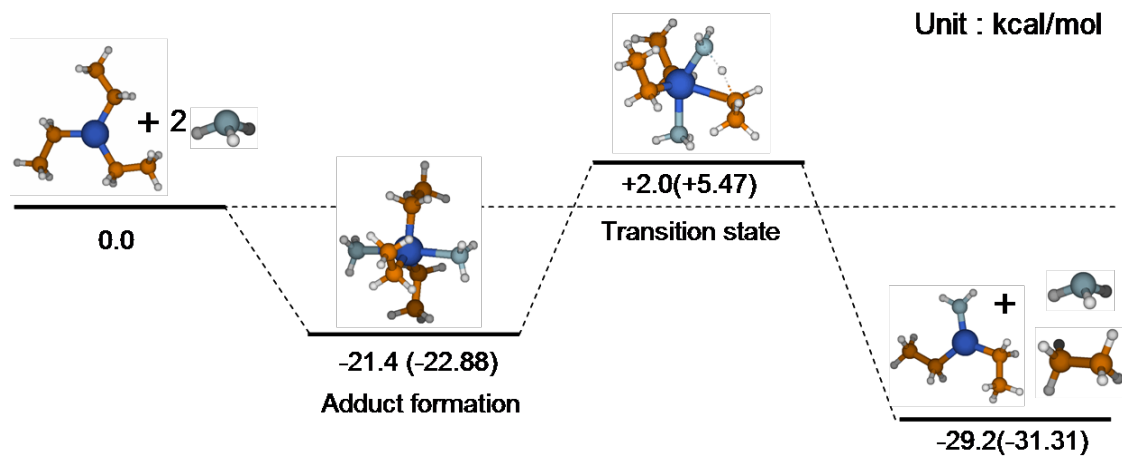


Figure 6-7. (Color online) Relative energy diagram of  $\text{C}_2\text{H}_6$  elimination in the case of excess ammonia (Energies in parenthesis are from Ref.[124]).

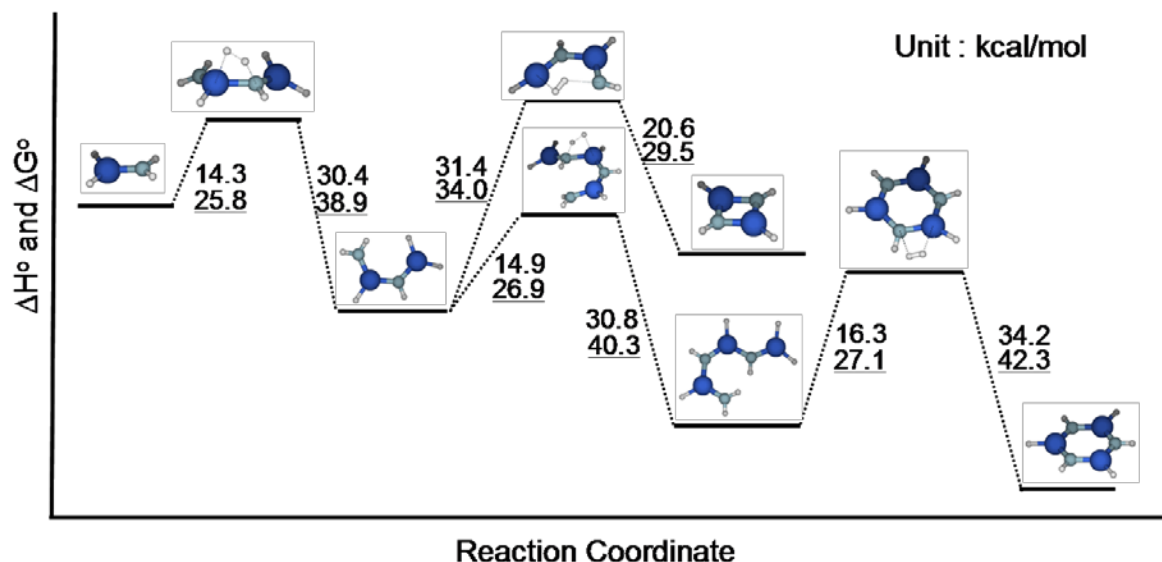


Figure 6-8. (Color online) Simulated tetramer and hexane formation from  $\text{H}_2\text{Al}-\text{NH}_2$  with enthalpy change and free energy change (underlined) at 298K.

Table 6-1. Calculated and corrected Ramanactive stretching frequencies

Molecule	Experimental (without NH <sub>3</sub> )	Experimental (with NH <sub>3</sub> )	Calculated	Corrected	Assignment
TEAI:NH <sub>3</sub>		452	467	454	Al-C str
DEAIH	600		616	601	Al-H wagging
NH <sub>3</sub>		930	-	-	N-H str
NH <sub>3</sub>		965	-	-	N-H str
TEAI:NH <sub>3</sub> TS		1462	1496	1459	Al-H-N br
H <sub>2</sub> N-AIH-NH-AIH <sub>2</sub>		1525	1565	1526	NH str
H <sub>2</sub> Al-NH <sub>2</sub>		1639	1664	1622	NH sci
	1989				
	2025				
	2580	2580			
MEAIH <sub>2</sub>	2835	2835	2997	2829	C-H str
TEAI:NH <sub>3</sub>		2841	3012	2843	C-H str
MEAIH-AIH <sub>2</sub>	2849	2849	3023	2854	C-H str
DEAI-AIH <sub>2</sub>	2900		3077	2905	C-H str
DEAI-AIH <sub>2</sub>	2918		3093	2920	C-H str
MEAIH-AIH <sub>2</sub>	2939		3106	2932	C-H str
	3173				
NH <sub>3</sub>		3230	-	-	NH str

(Abbreviations for the internal coordinates: vib, vibrational; sci, scissor; br, bridging; str, stretching)

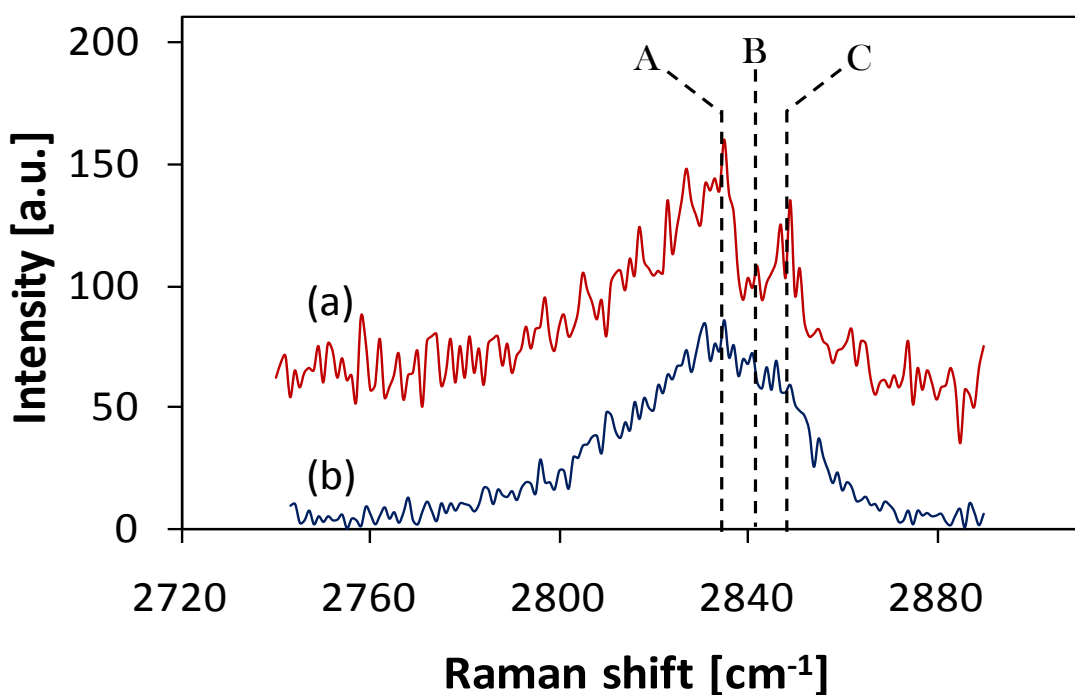


Figure 6-9. (Color online) Comparison of Raman spectra at  $2840\text{cm}^{-1}$  for two cases, (a) without ammonia, (b) with ammonia.

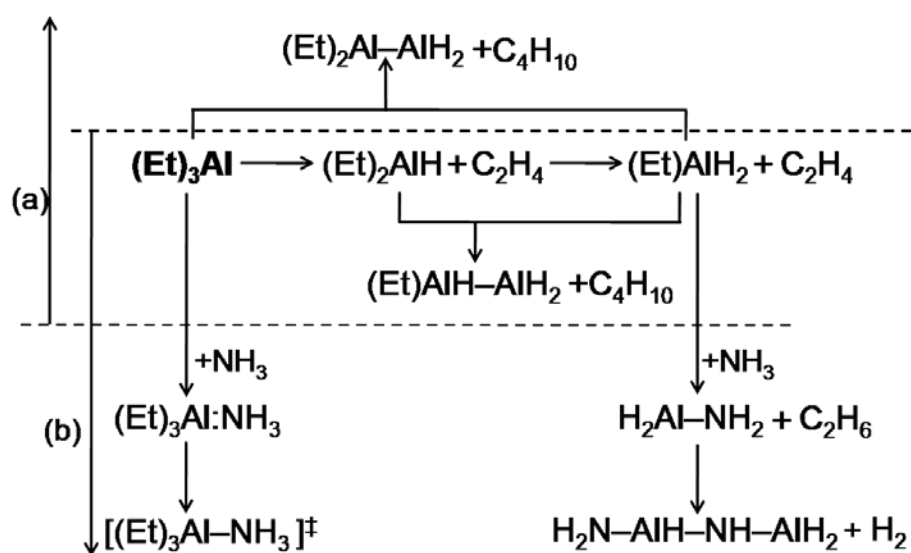


Figure 6-10. Proposed overall decomposition mechanism from (a) neat TEAI and (b) TEAI with ammonia experiment (Et = ethyl group;  $-\text{C}_2\text{H}_5$ ).

CHAPTER 7  
EXPERIMENTAL AND COMPUTATIONAL STUDIES OF THE HOMOGENEOUS  
THERMAL DECOMPOSITION OF THE TUNGSTEN DIMETHYLHYDRAZIDO  
COMPLEX  $\text{Cl}_4(\text{CH}_3\text{CN})\text{W}(\text{NNMe}_2)$  DURING DEPOSITION OF  $\text{WN}_x\text{C}_y$  THIN FILMS

**Overview**

Continual reduction of the average feature size found in integrated circuits and the concomitant changes in via and line resistivity, current density, and RC (Resistive-Capacitive) time delays have driven the gradual replacement of Al-based metallization to that based on Cu given its lower electrical resistivity and higher resistance to electromigration. Use of Cu metallization requires prevention of Cu migration into the underlying Si and  $\text{SiO}_2$ , which can produce an increase in contact resistance, leaky p-n junctions, variations in the barrier height, and contact layer embrittlement [130, 131]. To avoid Cu-Si interaction an amorphous diffusion barrier layer at a thickness well below the via dimension is conformally deposited at low temperature. As these requirements become more demanding, a chemical deposition method will likely be required.  $\text{WN}_x\text{C}_y$  films grown by both chemical vapor deposition (CVD) [132, 133] and atomic layer deposition [134] have shown promise as a suitable diffusion barrier material. Tungsten-based barriers have demonstrated improved adhesion to Cu and ease of chemical mechanical planarization as compared to the commonly used  $\text{TaN}_x$ . It was recently reported the preparation of the diorganohydrazido(2-) tungsten complexes  $\text{Cl}_4(\text{CH}_3\text{CN})\text{W}(\text{NNR}_2)$  ( $\text{R}_2 = \text{Me}_2, \text{Ph}_2$ , and  $-(\text{CH}_2)_5-$ ) and  $\text{Cl}_4(\text{pyridine})\text{W}(\text{NNPh}_2)$  [135] as precursors for the CVD of  $\text{WN}_x\text{C}_y$  films for use as Cu diffusion barriers [10, 136].

To probe the mechanism of precursor decomposition under deposition conditions, the gas-phase decomposition kinetics of the hydrazido complex

$\text{Cl}_4(\text{CH}_3\text{CN})\text{W}(\text{NNMe}_2)$  (**1a**) were investigated using *in situ* Raman spectroscopy in a vertical up-flow, cold-wall CVD reactor. Additional experiments involved NMR kinetics and observation of the dissociation of **1a** under ion cyclotron resonance conditions. Comparison of the experimental results with literature data and DFT calculations was used for assignment of the observed Raman bands and evaluation of likely decomposition pathways.

### Experimental and Theoretical Methods

The homogeneous thermal decomposition of the tungsten dimethylhydrazido complex **1a** and its benzonitrile derivative  $\text{Cl}_4(\text{PhCN})\text{W}(\text{NNMe}_2)$  (**1b**) was studied in a custom designed CVD reactor (Fig.7-1). The reactor is interfaced with an *in situ* Raman spectrometer (Ramanor U-1000, Jobin Yvon), which uses the 532.08 nm line of Nd:YAG solid-state laser as the light source and includes a double additive monochromator fitted with a diffraction grating of 1800 grooves/mm. The Raman system was calibrated against the 546.07 nm emission line of mercury. As described elsewhere [119], this up-flow, impinging-jet CVD reactor was designed to produce a stable 2-D flow pattern while isolating the reactants from the reactor walls to prevent parasitic reactions. Since the entire CVD reactor chamber assembly could be translated in the x-y-z directions, it was possible to measure gas-phase composition and temperature profiles inside the reactor to quantitatively study the gas phase decomposition kinetics of complex **1a**. The three concentric inlet tubes shown in Fig.7-1 are packed with 3 mm glass beads to supply an equal velocity and uniform-flow inlet boundary condition. Aerosol-assisted CVD (AACVD) was carried out for the Raman experiment with **1a** because this complex has low volatility[10]. Solid **1a** was dissolved in benzonitrile (PhCN, 0.0174 mol/L), which generates a mixture of **1a** and **1b** in

solution. The solution is then pumped into a nebulizer from a syringe. A piezoelectric material in the nebulizer vibrates at a frequency of 1.44 MHz, which generates an aerosol of precursor **1a/1b** (hereafter referred to as "**1a**") and benzonitrile. The aerosol is introduced into the reactor with N<sub>2</sub> (99.999 %, Airgas) carrier at a flow rate of 2.5 cm/s, which transports the mixture of **1a** and solvent that was injected at a rate of 1.0 mL/h. For the concentric annular and sweep flows, pure N<sub>2</sub> gas was delivered with the same flow velocity (2.5 cm/s) and sufficient gas flow time was allowed for the reactor to reach steady state before measurements were made. Based on a previous study [91] that validated a steady-state, two-dimensional mass transport model and included CH<sub>4</sub> tracer experiments, disruptive recirculation flow patterns in the reactor are not anticipated. A 3W Nd:YAG solid-state laser line (532.08nm) was used to excite the mixture of **1a**, benzonitrile, while the N<sub>2</sub> vibrational Raman excitation lines were recorded along the centerline to estimate the temperature profile. In addition to bands for gas phase benzonitrile, several other bands were observed.

To assist in the assignment of these additional Raman bands as well as to assess possible reaction pathways, DFT calculations were performed using the Gaussian 03 program suite [73]. For all bond dissociation, recombination, activation energy, thermodynamic properties, and frequency calculations, the spin polarized hybrid density functional B3LYP was combined with the LanL2DZ basis set for all elements. Crystallographic structure data [135] of complex **1a** collected at 173 K were used to obtain the starting geometry for calculations.

NMR kinetic studies of the dissociation of acetonitrile from **1a** were conducted on a Varian Inova at 500 MHz. Compound **1a** along with a molar equivalent of acetonitrile

was dissolved in toluene-d<sub>8</sub>. The <sup>1</sup>H spectrum displayed signals for **1a** at 0.53 ppm and acetonitrile at 0.83 ppm with a ratio of 1:2.09.

## Results and Discussion

### Kinetics of Acetonitrile Dissociation from **1a**

To estimate the rate of loss of acetonitrile from **1a** in the CVD reactor, the kinetics of acetonitrile exchange were determined via variable temperature NMR (Nuclear Magnetic Resonance) spectroscopy. The exchange rate k was determined by line shape analysis in the temperature interval 50 to 84 °C. A plot of ln(k/T) vs. 1/T (Fig.7-2) afforded an activation enthalpy of  $23.0 \pm 0.2$  kcal/mol and an activation entropy of  $28.8 \pm 0.6$  cal/mol·K, consistent with dissociative exchange. The corresponding Gibbs free energy of activation is 14.4 kcal/mol, indicating that dissociation of acetonitrile should be facile under CVD conditions.

Based on these results it can be assumed that benzonitrile solutions of **1a** have been converted almost completely to **1b** by exchange of the acetonitrile ligand with solvent before the solution is introduced into the CVD reactor. Thus complex **1b** can be considered as the predominant precursor species during deposition of WN<sub>x</sub>C<sub>y</sub> from solutions made from **1a**.

### Ion Cyclotron Resonance Experiments

It was previously demonstrated that mass spectrometry can provide insight into the gas phase dissociation chemistry of the related tungsten imido complexes Cl<sub>4</sub>(CH<sub>3</sub>CN)W(NR) where R = iPr, Ph and allyl [132, 137, 138] as well as the series of tungsten hydrazido complexes Cl<sub>4</sub>(CH<sub>3</sub>CN)W(NNR<sub>2</sub>) [135]. However, the chemical ionization mass spectra of **1a** were anomalous in that the tungsten nitrido fragment Cl<sub>4</sub>WN<sup>+</sup>, which is a marker for the ability of the imido complexes to deposit high quality

films at low temperatures, could not be detected unambiguously in the spectra of **1a**, despite the fact that **1a** is an excellent CVD precursor for  $\text{WN}_x\text{C}_y$ . To further investigate the gas phase ion dissociation pathways of **1a** and their relevance to the deposition conditions, an ion cyclotron resonance study was carried out.

### ***In situ* Raman Experiments**

To investigate the thermal decomposition of hydrazido complex **1a**, *in situ* Raman experiments were performed using a susceptor set point temperature of 850 °C. Fig.7-3 shows the observed Raman bands along the centerline at seven distances below the heated susceptor (labeled a-g in Fig.7-3). Estimation of the local gas phase temperature along the reactor centerline was made by analysis of the  $\text{N}_2$ rotational state distribution with accuracy 20 to 30 °C in the temperature range of interest [18].The measured temperature is plotted in Fig.7-4 as a function of reactor position and the value associated with each spectrum is listed in Fig.7-3. To minimize the influence of blackbody radiation, Raman signals of the blank reactor were recorded and subtracted for each measurement position. For the results shown in panel A and D, each spectrum was deconvolved using Gaussian-Lorentzian peak shape routine in the commercial software package PeakFIT (v4.12).

Measurements on neat benzonitrile provided frequency values for C-H in plane bending coupled with C–CN stretching ( $1182 \text{ cm}^{-1}$ )and the C-H in plane bending ( $1198 \text{ cm}^{-1}$ ) modes in this region. Other modes detected in this region include C-H in plane bending, W–N1 and W–N3 stretching with C–N–C torsion ( $1193 \text{ cm}^{-1}$ ), C–CN stretching for complex **1b**( $1178 \text{ cm}^{-1}$ ), and W≡N1 stretching with methyl scissoring for complex **2** ( $1189 \text{ cm}^{-1}$ ), with the assignments based on DFT calculations. The peak deconvolution

results are shown in Fig.7-4A and concentration profiles were obtained as shown in Fig.7-4B. In Fig.7-4B, measurements were not possible closer than 3 mm from the heated susceptor in this range.

Using the results shown in panel D (Fig.7-3), two C≡N vibrational modes were detected. However, since this region also includes signal from the periodic vibration of excited N<sub>2</sub>, these two vibrations can be extracted from the spectra in panel D by comparison with the gas-phase data from authentic benzonitrile. Peak deconvolution results show six components: four peaks for the N<sub>2</sub> vibrational mode and two for C≡N stretching as shown in Fig.7-5A. Examination of the spectra at four different reactor positions (a-d) shown in Fig.7-5B reveal the four periodic N<sub>2</sub> vibrational peaks (spectrum a) at 2220.5, 2229, 2237, and 2245 cm<sup>-1</sup>. Two additional C≡N stretching frequencies are detected at 2234 and 2241 cm<sup>-1</sup> as shown in Fig.7-5B panels b, c, and d. These last two frequencies lie in the reported ranges for  $\nu_{CN}$  of benzonitrile as observed in gas-phase Raman experiments[139-141] and the origin of the second band under our experimental conditions is not yet understood.

To probe for additional Raman active species that were not detected in the gas-phase experiments, supplementary liquid phase Raman experiments for title compound dissolved in benzonitrile were performed. Using a standard liquid chamber, the 532.08 nm Nd:YAG solid-state laser line at 0.1 W was used to excite neat benzonitrile and the vibrational Raman excitation lines were recorded in the range 100~4000 cm<sup>-1</sup>. Solution phase Raman spectra of **1a** (0.0174 mol/L in benzonitrile) and pure benzonitrile were measured and spectra for three selected wave number ranges are shown in Fig.7-6. It is evident that the higher liquid phase density affords strong scattering intensity to produce

very good signal to noise (S/N) ratio. It is also evident that spectra for the liquid samples show features not be detected in the gas-phase experiments. Specifically, the three spectra show peaks at  $361\text{ cm}^{-1}$ , associated with the W–Cl<sub>4</sub> vibrational mode,  $1133\text{ cm}^{-1}$ , assigned to the C–N–C asymmetric vibrational mode, and  $1396\text{ cm}^{-1}$  assigned to the symmetrical umbrella mode of two terminal CH<sub>3</sub> groups. Although these Raman shifts were not detected in the gas-phase experiments, more detailed experiments are in progress.

### DFT Calculations

To better understand the experimental results and model some of the possible mechanistic steps in the thermal decomposition of **1a**, DFT calculations were performed. The initial calculations were a geometry optimization (B3LYP/LanL2DZ) using experimentally determined bond lengths and angles for **1a**[135] as the starting point as a test of the computational method. Although the results of the NMR study indicate that **1a** will have been converted to **1b** before it is injected into the reactor, only the substituent of the nitrile ligand is different and the critical bond lengths and bond angles of **1a** will carry over to **1b**. The computationally optimized geometry of **1a** is summarized in Table 7-1 along with experimental data[135] and previous calculations using a split valence basis set[142]. For most of the calculated values in Table 7-1, the B3LYP/LanL2DZ geometry optimization more closely approximates the experimental solid state structure.

Since the dissociation of acetonitrile from **1a** was observed to be facile near room temperature, further calculations assumed that loss of the nitrile was a rapid first step in decomposition of **1a** in the reactor. Further calculations on possible intermediates thus began with Cl<sub>4</sub>W(NNMe<sub>2</sub>) (**2**), the product of acetonitrile loss from **1a**. The experimental

observation of dimethylamine and methylmethylenimine among the decomposition products suggest two possible dissociative reactions of **2** as depicted in Fig. 7-8. Both dissociation reactions were considered since AACVD from **1a** involves high deposition temperature. Values for the enthalpy and Gibbs energy of W–N1 and N1–N2 dissociation (Table 7-2) were obtained using statistical thermodynamics. Homolysis of W–N1 affords open shell products and the spin states were set accordingly during calculations. In the case of N1–N2 homolysis, the products are doublets. The calculated W–N1 bond dissociation enthalpy is significantly higher than the N1–N2 dissociation energy over the 298 to 900 K temperature range. These bond strengths can be viewed in terms of the limiting resonance structures A and B (Fig.7-9). Crystallographic data are consistent with representation B being the major contributor, which is in accord with calculated N1–N2 BDE(Bond Dissociation Energy) values that are higher than the experimental value for free 1,1-dimethylhydrazine (49.6 kcal/mol) [143].

The dissociation of benzonitrile to form  $\text{Cl}_4\text{W}(\text{NNMe}_2)$  (**2**) (Fig. 7-8) is postulated to be the first step in thermal decomposition of **1b** on the basis of the nitrile dissociation rates for conversion of **1a** to **1b**. The assumed parallel between the reactivity of **1a** and  $\text{Cl}_4(\text{CH}_3\text{CN})\text{W}(\text{N}^{\text{i}}\text{Pr})$  is consistent with computational assessment of the bond strength between W and N3 using the Wiberg bond index in the natural bond orbital (NBO) analysis of complex **1a**. As shown in Fig.7-10, the coordinate covalent bond of the acetonitrile ligand with W has the weakest bond order (0.3310).

Dimethylaminyl radical (**3**) [144-146] and 1,1-dimethyldiazene(**5**) have been previously generated by other methods and their reactions have been reported.

Dimerization of 1,1-alkyldiazenes is known to form tetrazene derivatives, which in the case of **5** would afford tetramethyl-2-tetrazene (**7**). Since decomposition of **7** affords two equivalents of dimethylaminyl radical **3** (Fig. 7-12), the critical reactive intermediate from cleavage of either the W–N1 or N1–N2 bond of **2** (Fig. 7-8) will be **3**.

Known reactions of dimethylaminyl radical (disproportionation, dimerization, dissociation and rearrangement) are summarized in Fig. 7-13. Two dimethylaminyl radicals can yield methylmethylenimine (**8**) and dimethylamine (**9**) [147-149] or tetramethylhydrazine (**7**) by disproportionation or recombination, respectively[145, 150](Fig. 7-13a). Since bimolecular reactions of radicals have low activation energies, products of recombination and disproportion are expected to be formed in similar quantities [151]. In addition to these reactions, dimethylaminyl radical undergoes dissociation into methylnitrene and methyl radical (Fig. 7-13b). Subsequent hydrogen shift in methylnitrene affords methyleneimine [152-154](Fig. 7-13c).

### **Comparison of Experimental Results with DFT calculations**

The analysis of this study assumes that the decomposition reactions that occur in the gas phase along the probed centerline are for inlet species **1b**, benzonitrile, and acetonitrile, and that no surface or particle formation reactions occur. The aerosol assisted delivery of the low volatility precursor complicates the analysis of the experimental results since the precursor is initially in a liquid solution but quickly evolves to a gas mixture due to the high vapor pressure of the solvent. Furthermore, the precursor is a metastable gas species and a large driving force exists for particle formation. This sequence is depicted in Fig.7-14. An analysis was performed to answer the question whether the aerosol is volatilized before decomposition occurs.

To better describe the behavior of intermediates in the CVD reactor, the calculations should include the polarizable continuum model (PCM) to model solvation, as well as gas-phase calculations if there exists liquid phase in the reactor since simple gas phase simulation is often not a good predictor of condensed phase behavior. To investigate the homogeneity of the introduced precursor, further study was performed. The initial droplet size produced by the nebulizer was first estimated using Lang's correlation [155]. This model assumes each droplet generated by the ultrasonic nebulizer is a homogeneous sphere. The droplet diameter estimated for the system used in this study is ca. 2.7  $\mu\text{m}$ . Next, the rate of evaporation was estimated by modeling the evaporation process.

The Nusselt number, Nu, is the ratio of convective to conductive heat transfer across the liquid-gas interface, and for a liquid droplet in a flowing gas, this is empirically given by the relation

$$Nu = 2.0 + 0.6 \text{Re}^{0.5} \text{Pr}^{0.33} \quad (7-1)$$

where Re is the Reynolds number and Pr is the Prandtl number.

Using this equation, the heat transfer coefficient,  $h_c$  is estimated as:

$$\frac{h_c D}{\kappa_d} = 2.0 + 0.6 \left( \frac{D \nu \rho}{\mu} \right)^{0.5} \left( \frac{C_p \mu}{\kappa_d} \right)^{0.33} \quad (7-2)$$

where  $D$  and  $\kappa_d$  are the droplet diameter and liquid thermal conductivity (0.1317 W/mK at 366.5 K). In addition,  $\nu$ ,  $\rho$ ,  $\mu$ , and  $C_p$  denote mean fluid velocity, density, viscosity, and specific heat capacity at constant pressure, respectively. With property values

mentioned above,  $Re$  and  $Pr$  have the value of  $5.45 \times 10^5$  and 3.81, respectively.

From Eq. 7-2, the heat transfer coefficient is calculated as  $9.79 \times 10^4 \text{ J/sm}^2\text{K}$ .

A model that describes the coupled heat and mass transfer of an evaporating droplet in a laminar carrier gas stream was next examined. Briefly, the energy balance equation for a benzonitrile droplet gives:

$$N_c = \frac{h_c A \Delta T}{\lambda} \quad (7-3)$$

where  $N_c$ ,  $h_c$ ,  $A$ ,  $\Delta T$  and  $\lambda$  denote the solvent evaporation rate, heat transfer coefficient across the liquid-gas ( $9.79 \times 10^4 \text{ J/sm}^2\text{K}$ ), total droplet surface area introduced to the reactor as  $6.18 \times 10^{-4} \text{ m}^2$  temperature difference between droplet surface and ambient, and latent heat of vaporization as  $3.67 \times 10^2 \text{ J/g}$ , respectively. The value of the temperature difference was assumed to be 10 K since the drop size is fairly small. If one assumes a larger temperature difference since evaporation process lowers the surface temperature, the solvent evaporation rate would be increased. Eq. 7-3 gives the value of the solvent evaporation rate as 1.65 g/s and applying this model to these reaction conditions gives a drop evaporation time of only 17 ms, which at an average 2.5 cm/s velocity yields a distance at  $4.25 \times 10^{-4} \text{ m}$ . In other words, a drop introduced to the reactor evaporates in 17 ms and only travels  $4.25 \times 10^{-4} \text{ m}$ .

The droplet diameter is predicted to show a normal distribution with standard deviation,  $\sigma$ , as follows [156]:

$$\sigma = 4.6 \times 10^{-5} \frac{\rho^{0.1}}{f^{0.41} \tau^{0.50} \mu^{0.18}} \quad (7-4)$$

where  $f$  is the nebulizer frequency [Hz],  $\tau$  is the surface tension [N/m] and  $\mu$  is the dynamic viscosity as  $1.25 \times 10^{-3}$  Pa·s. Using these values the standard deviation of drop diameter,  $\sigma$ , is 5.0  $\mu\text{m}$ . The portion of a droplet with the diameter of 17.7  $\mu\text{m}$  from the normal distribution curve, which is deviated from the mean value as much as twice the standard deviation, is only 2.3 % among total solvent and statistically it is produced only 1.8 particles per one reactor volume. Although it can reside  $2.0 \times 10^{-3}$  m in the reactor, it can be highly possible to evaporate in the center tube during approaching the inlet.

There is experimental evidence to support this conclusion. Frolov et al. [156] reported experimental results supported by calculations that show 70  $\mu\text{m}$  n-tetradecane droplets vaporize in 70 ms at a liquid surface temperature of 293.15 K and a gas temperature of 573.15 K. It is noted that n-tetradecane has higher boiling temperature (526 K) than benzonitrile (464 K) and their droplet diameter was approximately 4 times larger than that in this study. As further evidence, the spectral positions of the strongest phenyl ring breathing mode of benzonitrile were carefully measured. No displacement of peak positions along the reactor centerline was detected as shown in Fig.7-15. Based on the modeling results, comparison to experiment using a less volatile solvent, and measurement of the lack of peak shift in the phenyl ring breathing mode, the assumption of homogeneous gas-phase reaction in the whole CVD reactor can be substantiated.

The calculated vibrational frequencies can be correlated to products postulated in the proposed decomposition mechanisms (Fig. 7-8 and Fig. 7-13a). Calculated and

corrected Raman active stretching frequencies with experimental values for all compounds including the gas-phase authentic sample of benzonitrile are listed in Table 7-3.

Assignments for 9 of the observed bands attributed to benzonitrile (462, 762, 1003, 1181, 1197, 2234, 3077, 3128, 3175 cm<sup>-1</sup>) were derived from gas phase benzonitrile Raman spectra and deconvolution data as well as DFT calculations. The reported Raman bands of 1240 and 3377 cm<sup>-1</sup> of gas-phase dimethylamine [157] and DFT results were used for assigning 1247 and 3377 cm<sup>-1</sup> to the CH<sub>3</sub> rocking and N–H stretching motions in dimethylamine, respectively. In addition, 1638 cm<sup>-1</sup> was assigned to C=N stretching of methylmethylenimine (**8**). This assignment is supported by IR data [150] and the Raman characteristic group frequency [158]. Given that dimethylamine (**9**) and imine **8** would ultimately result from homolysis of the N1–N2 bond followed by disproportionation of radical **3**, observation of these products is consistent with N1–N2 cleavage. The possibility of W–N1 dissociation, however, cannot be excluded since this reaction can produce the same radical intermediate (**3**) through tetramethyltetrazene formation (Fig. 7-13).

The peak at 3426 cm<sup>-1</sup> is tentatively assigned to the N–H stretching mode of HNWCl<sub>4</sub> (**14**) based on the predicted gas phase reaction chemistry and the experimentally observed N–H vibrational frequencies of W(VI) model compounds with imido (NH) and amido (NH<sub>2</sub>) ligands [159]. The N–N cleavage reaction (Fig. 7-8) would produce the nitrogen-centered radical •NWCl<sub>4</sub> (**4**) as the inorganic product. Subsequent abstraction of a hydrogen atom by **4** would afford the W(VI) parent imido complex **14**. The N<sub>sp</sub>–H bond of **14** would be expected to have a high bond dissociation energy,

making hydrogen abstraction from several species in the reactor energetically favorable[160].

### Concluding Remarks

In the present work, using Raman spectroscopy, NMR kinetics, ion cyclotron resonance and DFT calculations at the B3LYP/LanL2DZ level of theory, the decomposition pathway of the dimethylhydrazido tungsten complex ( $\text{RCN}\text{Cl}_4\text{W}(\text{NNMe}_2)$  (**1a**) was investigated. In a custom up-flow, cold-wall aerosol-assisted CVD reactor, identifiable Raman shifts for the starting material and intermediates were detected and these frequencies were assigned using gas-phase DFT calculations and literature data. The observed complex Raman spectra were deconvolved using commercial software with high accuracy. Analytical and spectroscopic evidences provided homogeneousness of introduced precursor by performing droplet evaporation analysis. The bond cleavages of both W-N1 and N1-N2 are possible, although the calculated bond strength of W-N1 is larger than that of N1-N2. Peaks consistent with methylmethylenimine (**8**), dimethylamine (**9**), and  $\text{HNWCl}_4$  (**14**) were observed in the Raman experiments, consistent with proposed decomposition pathways for **1a**. The methods used in this study are complementary to each other and seems very promising for kinetics study, thermal decomposition of precursors in chemical and engineering perspectives.

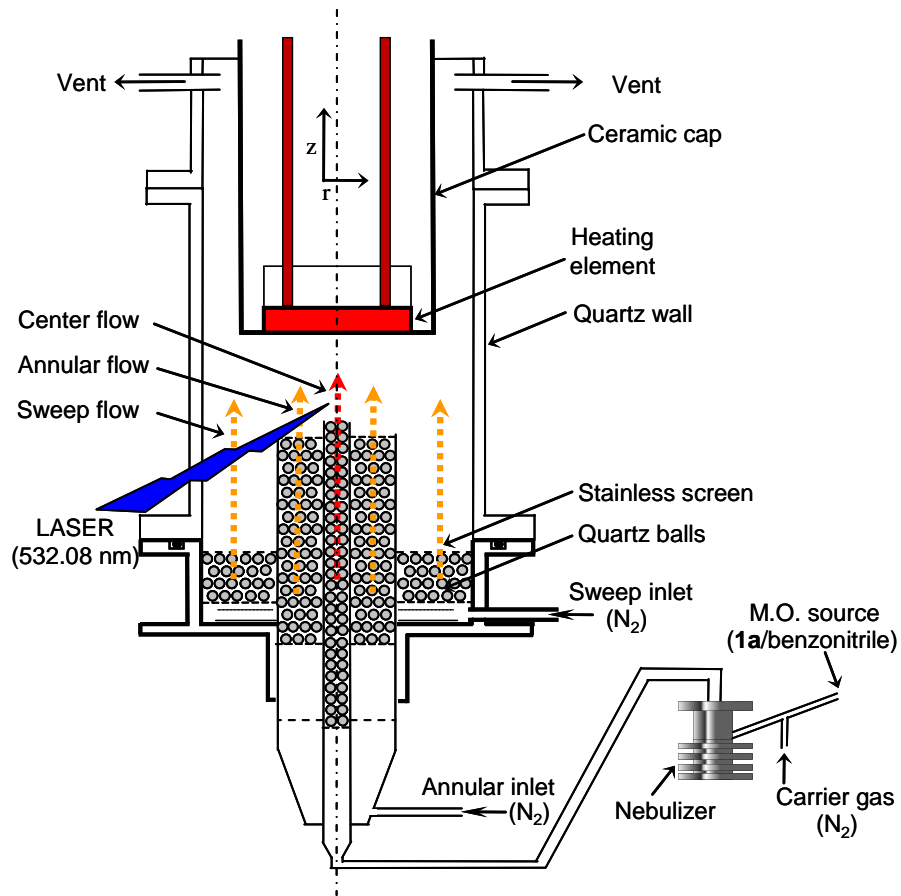


Figure 7-1. Schematic of the nebulizer-assisted experimental reactor for *in situ* Raman spectroscopic measurements.

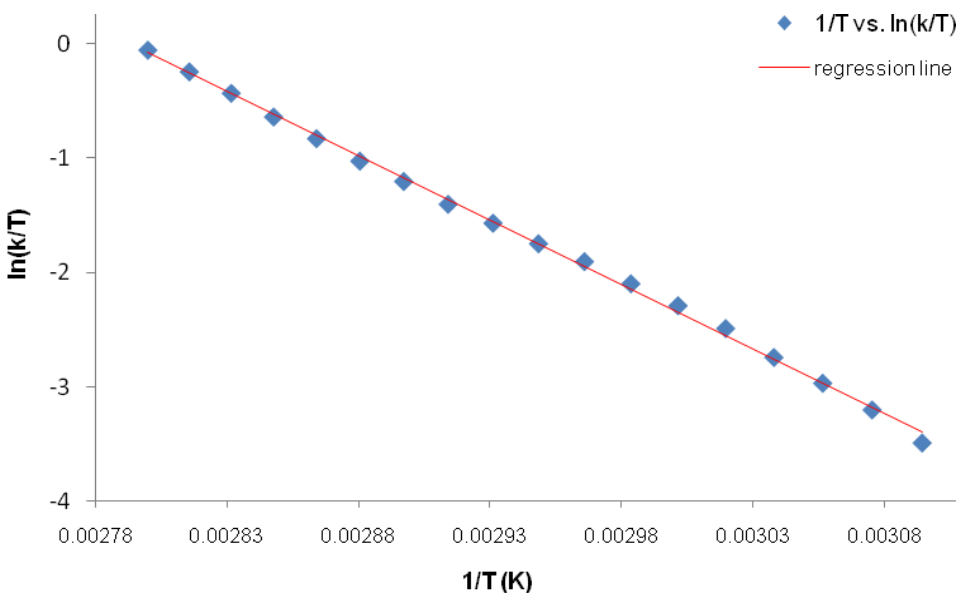


Figure 7-2. Plot of  $\ln(k/T)$  vs.  $1/T(K)$  for acetonitrile exchange in complex **1a**.

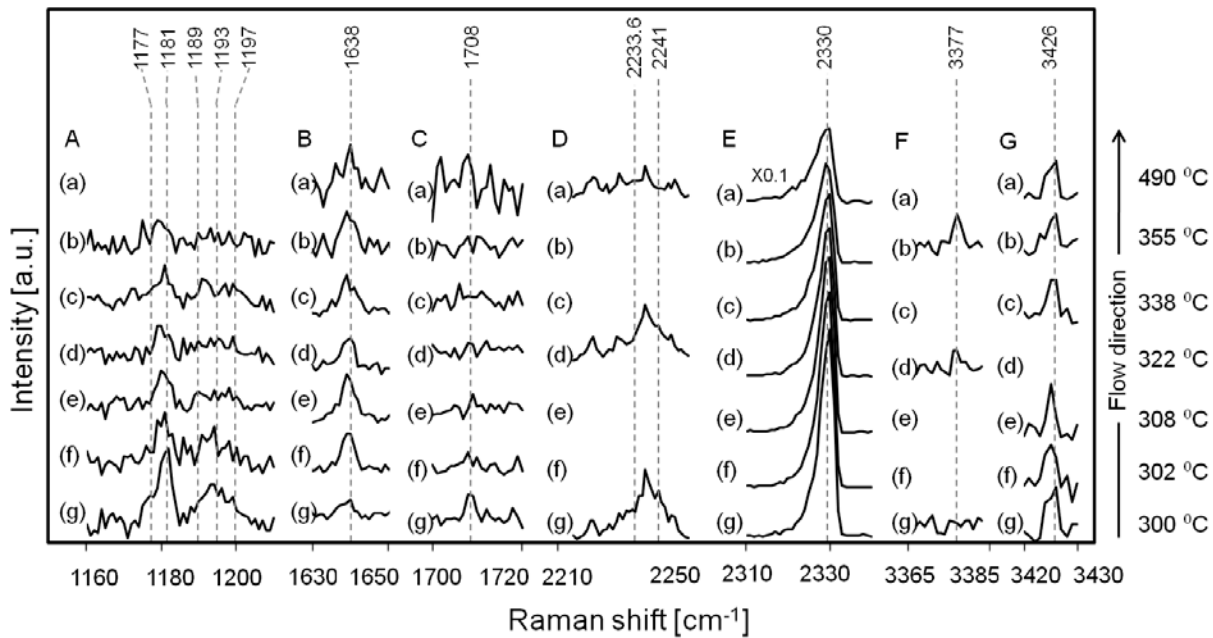


Figure 7-3. Raman spectra of gas-phase dimethylhydrazido complex **1a** in benzonitrile as a function of distance below the heated susceptor along the reactor centerline. Spectra in panel E (nitrogen vibrational mode) are marked with reduced scale for concentration reference. Raman shift values for the primary modes are specified at the top of each panel. Raman spectra profiles are marked as a function of position from the heated susceptor surface as (a) 1 mm, (b) 3 mm, (c) 4 mm, (d) 5 mm, (e) 7 mm, (f) 9 mm and (g) 11.5 mm.

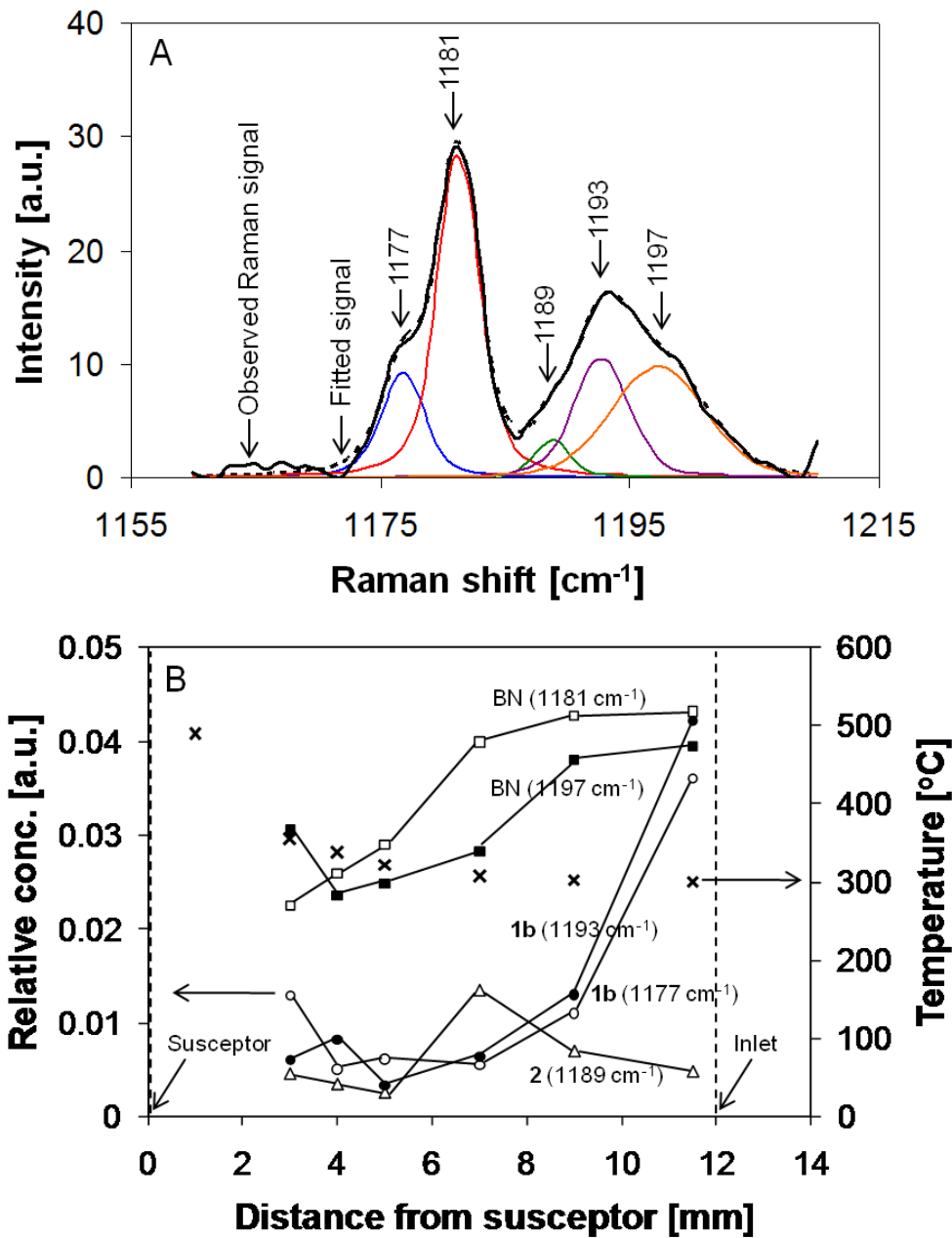


Figure 7-4. Relative species concentration and gas phase temperature profiles along the reactor centerline for benzonitrile (BN), **1b**, and **2** using results in panel A, Fig. 7-3.

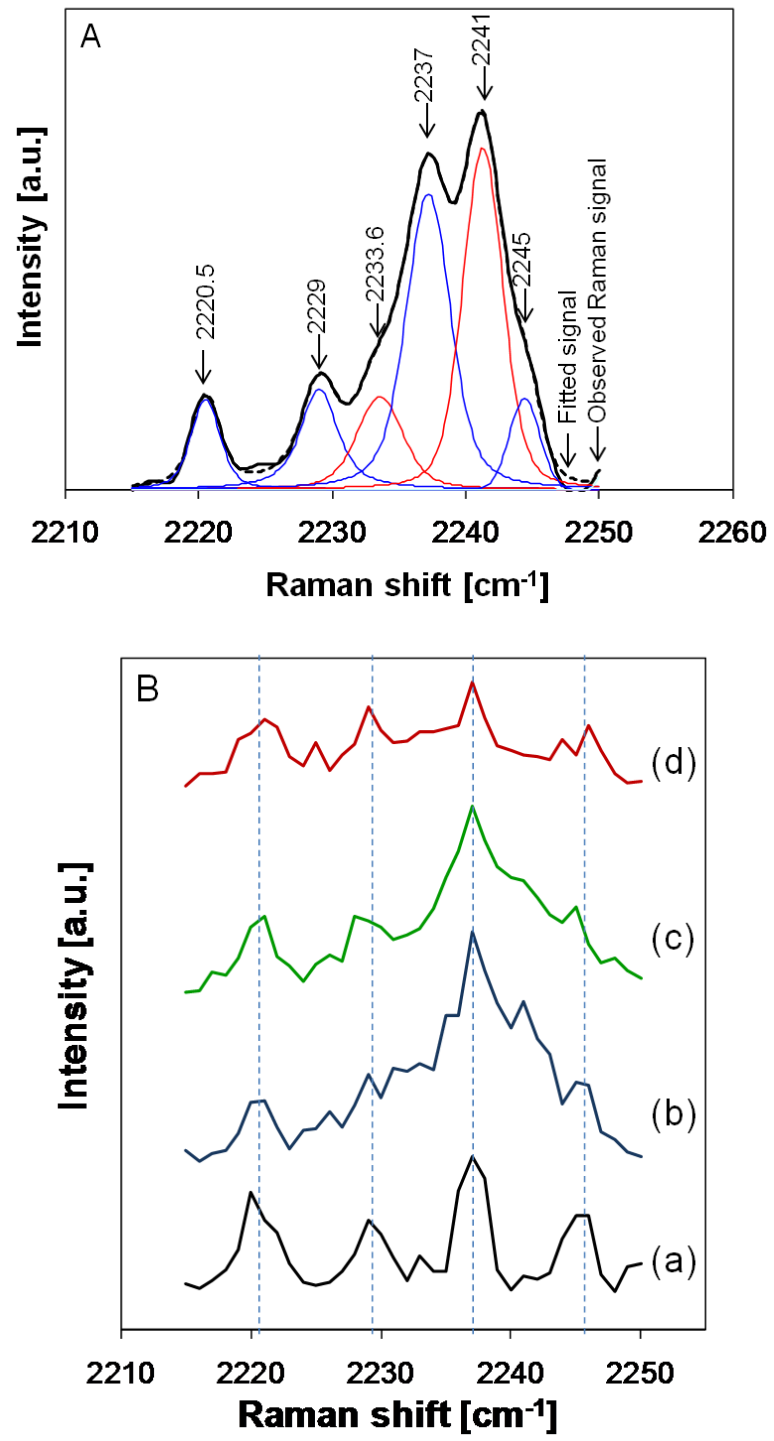


Figure 7-5. Peak deconvolution results: (A) results shown in panel D of Fig. 7-3,  $\text{N}_2$  vibrational bands (spectrum a) and (B) peaks associated with  $\text{N}_2$  vibrational modes and with  $\text{C}\equiv\text{N}$  stretching frequencies(spectra b-d).

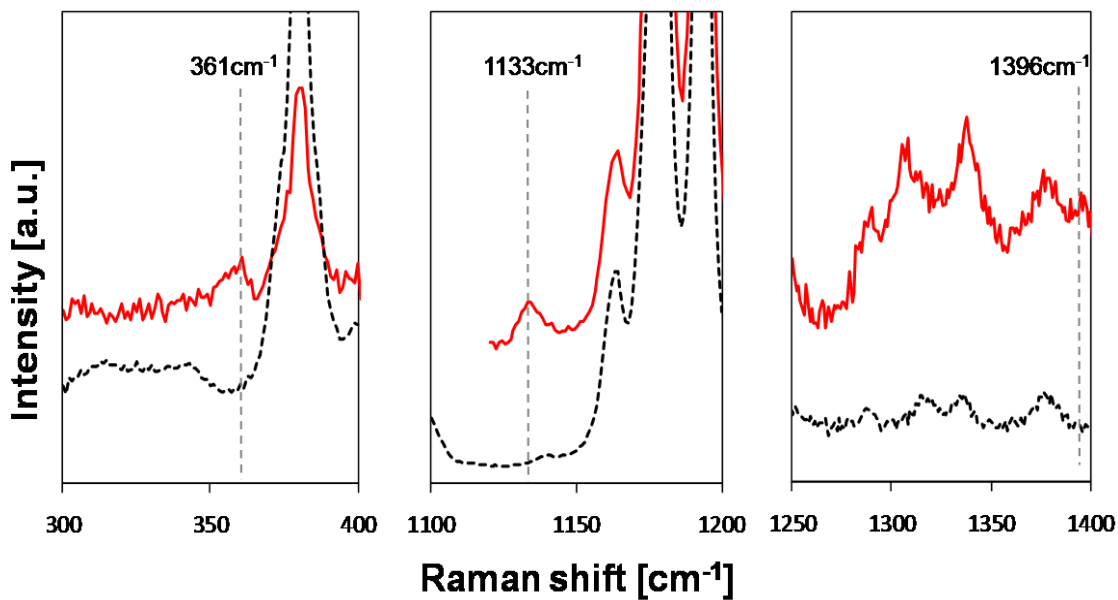


Figure 7-6. Liquid Raman spectra of **1a** in benzonitrile solution (red) compared to pure liquid benzonitrile (black). Note that the red spectra are intensity shifted for clarity.

Table 7-1. Experimental and computationally optimized bond lengths ( $\text{\AA}$ ) and bond angles ( $^\circ$ ) for complex **1a**

	Experimental [135]	Split Basis Set[142] <sup>a</sup>	This Work <sup>b</sup>
W1-N1	1.769(5)	1.749	1.757
W1-N3	2.224(7)	2.268	2.220
W1-Cl	2.347(16)	2.388	2.429
N1-N2	1.271(8)	1.289	1.283
N2-C1	1.438(7)	1.467	1.478
N1-W1-Cl	95.9(4)	96.8	96.2
N3-W1-Cl	84.07(4)	83.24	83.75
N2-N1-W1	180.0(0)	178.0	179.6

<sup>a</sup>B3LYP/LanL2DZ for W, 6-311G for other elements, <sup>b</sup>B3LYP/LanL2DZ for all elements

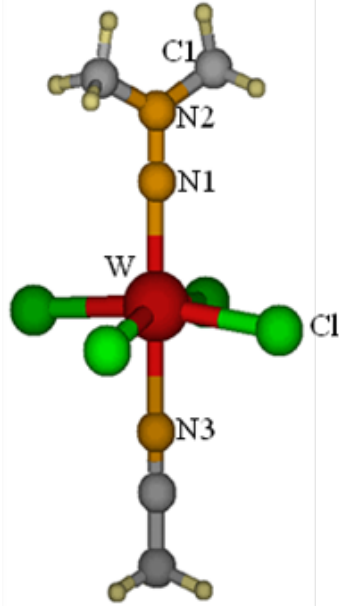


Figure 7-7. Computationally optimized geometry of **1a**.

Figure 7-8. Products of cleavage of the W–N1 and N1–N2 bonds of complex **2**. Gibbs energy values ( $\Delta G^\circ$ ) are in kcal/mol.

Table 7-2. Calculated bond dissociation enthalpy ( $\Delta H^\circ$ ) and Gibbs energy change ( $\Delta G^\circ$ ) for the W-N1 and N1-N2 bonds

	BDE(W-N1) (kcal/mol) <sup>a</sup>	BDE(N1-N2) (kcal/mol) <sup>a</sup>
$\Delta H^\circ$ (298 K)	113.1	88.0
$\Delta H^\circ$ (900 K)	111.4	86.9
$\Delta G^\circ$ (298 K)	101.0	73.2
$\Delta G^\circ$ (900 K)	77.8	43.7

<sup>a</sup>B3LYP/LanL2DZ

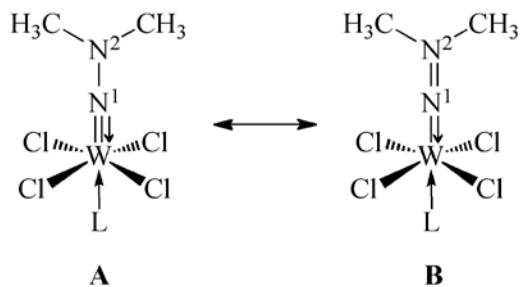


Figure 7-9. Limiting resonance structures of complexes **1a** and **1b**.

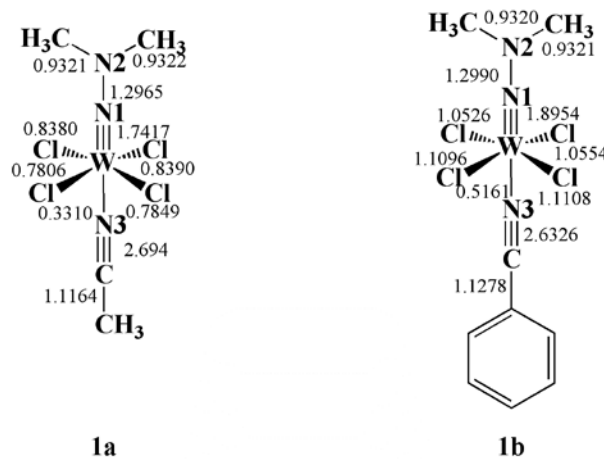


Figure 7-10. Wiberg bond indices for **1a** and **1b**.

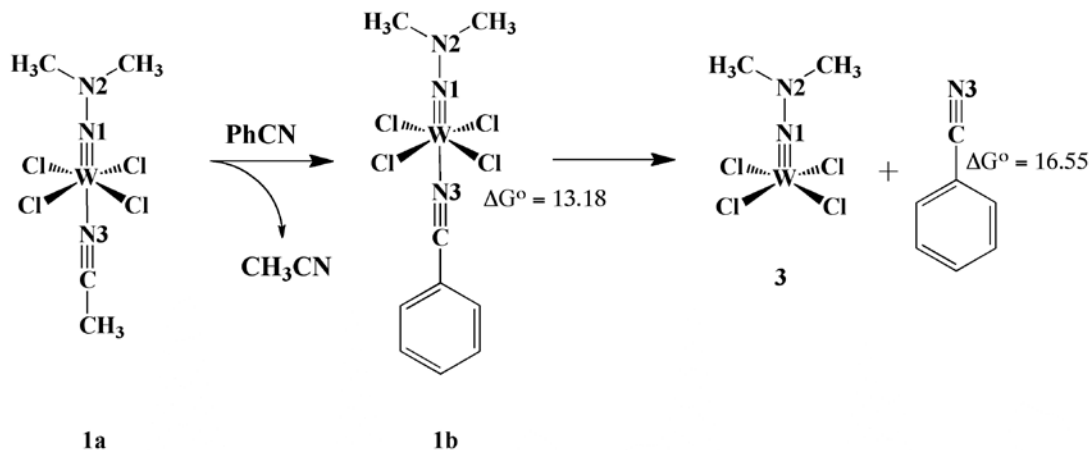


Figure 7-11. Gibbs energy change ( $\Delta G^\circ$ ) for initial ligand substitution and dissociation reactions of complex **1**. All energy values are in kcal/mol at 298 K.

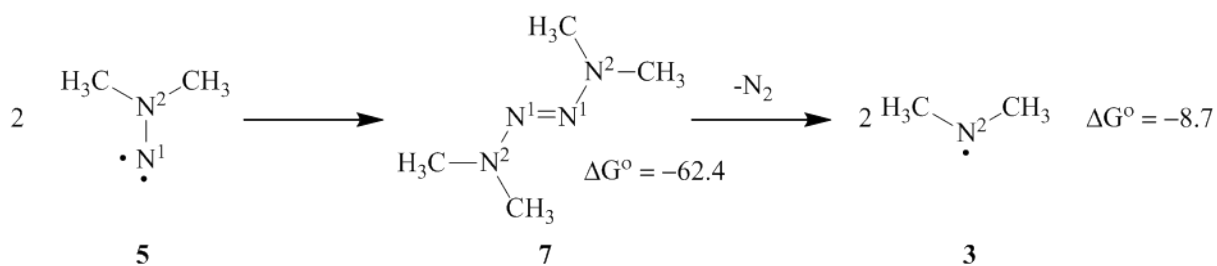


Figure 7-12. Production of dimethylaminyl radical (**3**) after W–N1 cleavage to form **5**. Gibbs energy values are in kcal/mol.

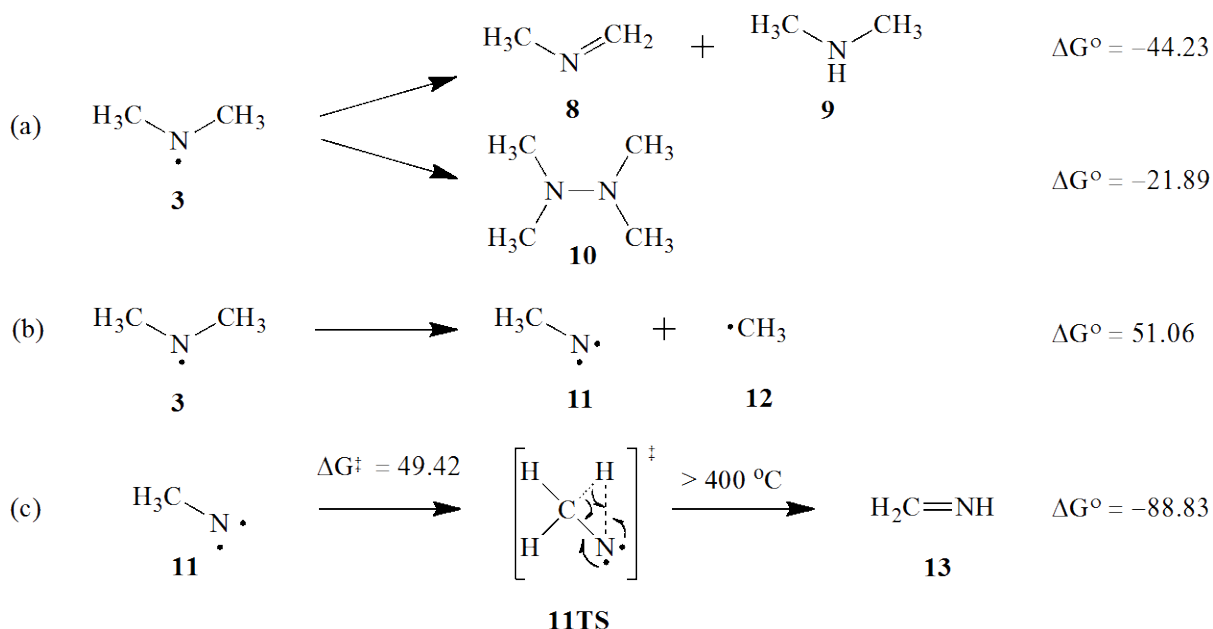


Figure 7-13. Known reactions of dimethylaminyl radicals and their calculated (B3LYP/LanL2DZ) reaction energies at 298 K. Gibbs energy values are in kcal/mol.

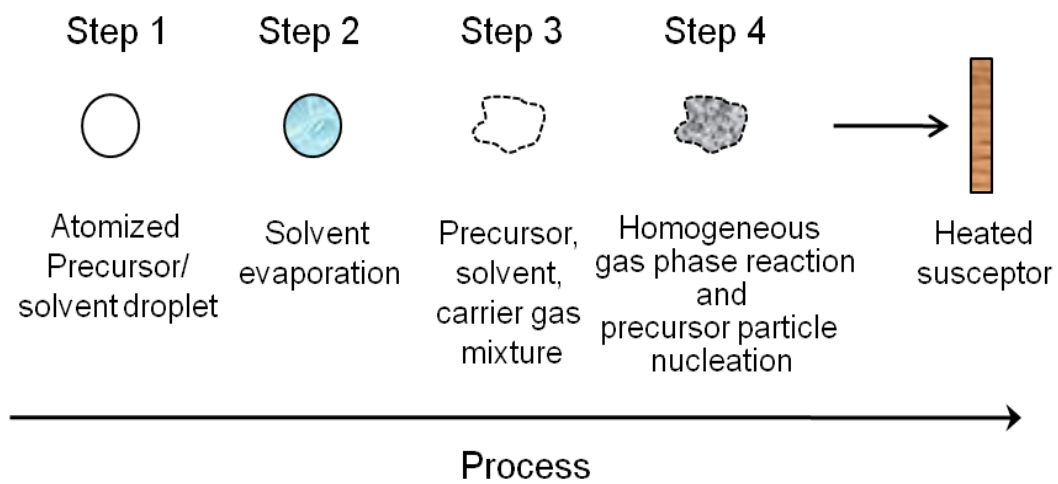


Figure 7-14. Suggested evolution of an atomized droplet as it approaches a heated susceptor.

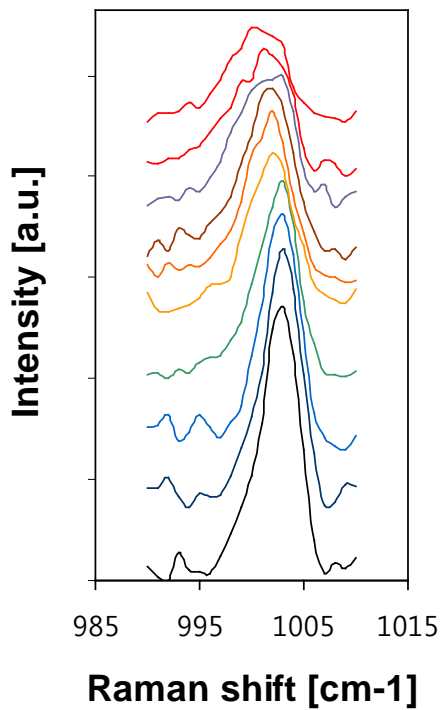


Figure 7-15. Detected Raman spectrum profile assigned to phenyl breathing mode of benzonitrile ( $1003\text{ cm}^{-1}$ ). Raman spectra are shifted for clarity. Black bottom signal is for right above inlet (cold region) and red top signal is for right below the heated susceptor.

Table 7-3. Calculated and corrected Raman active stretching frequencies

Molecule	Experimental	Calculated	Corrected	Assignment
<b>BN</b>	462	466	461	Ph ring stretching
<b>BN</b>	762	769	760.5	Ph ring stretching
<b>BN</b>	1003	1025	1004.5	Ph ring breathing
<b>1b</b>	1177	1226	1177	C-H in plane bend
<b>BN</b>	1181	1236	1186.6	C-H in plane bend+ C-CN vibration
<b>2</b>	1189	1246	1196	CH <sub>3</sub> scissoring + W≡N stretching
<b>1b</b>	1193	1243	1193	C-Ph stretching + N3-W-N1 stretching + C-N-C torsion
<b>BN</b>	1197	1248	1198	C-H in plane bend
<b>9</b>	1247	1279	1228	CH <sub>3</sub> rocking
<b>8</b>	1638	1696	1638	C=N stretching
-	1708			
<b>BN</b>	2233.6	2334.5	2236.5	C≡N stretching C≡N stretching in BN?
-	2241			
-	2516			
-	2547			
-	2580			
-	2834			CH <sub>3</sub> symmetric stretching (-N(CH <sub>3</sub> ) <sub>2</sub> ; aromatics)
<b>BN</b>	3077	3142	3079	C-H asymmetric stretching
<b>BN</b>	3128	3192	3128.2	C-H asymmetric stretching
<b>BN</b>	3175	3238	3173	
<b>9</b>	3377			NH stretching
<b>14</b>	3426			NH stretching

## CHAPTER 8

# DESIGN, SIMULATION AND SETUP OF ULTRA HIGH VACUUM SYSTEM FOR SURFACE SCIENCE AND ITS APPLICATION

### **Overview**

The increasing importance of organic and metal-organic films in semiconductor technology has led to research efforts which direct toward understanding and controlling hydrocarbon reactions with surfaces such as Si, Al<sub>2</sub>O<sub>3</sub>, Ge, etc. Although efforts to experimentally observe and analyze fundamental reaction mechanisms during thin film deposition of organic and metal-organic materials on silicon surfaces have been made for decades, single technique could not have satisfied these needs. To analyze initial step of film deposition, various techniques, for example, XPS (X-ray photoelectron spectroscopy), AES (Auger electron spectroscopy), LEED (Low energy electron diffraction), TPD (Temperature-Programmed Desorption) using QMS (Quadrupole mass spectroscopy), ATR-FTIR (Attenuated total reflection – Fourier transform infrared spectroscopy) have been used for this purposes. Understanding of first step of film deposition is very important in semiconductor field since initial step plays an important role for controlling the film composition, quality, growth rate, and so on. Among surface analysis techniques mentioned above, ATR-FTIR can be used for identifying the functional group on surface and semi-quantifying the adsorbates and it would be more powerful when using *in situ* type in UHV (Ultra high vacuum) chamber. ATR-FTIR technique which uses internal reflection element (IRE) allows the vibrational properties of the adsorbed species and this information can enhance understandings of bond between adsorbate and surface by using DFT calculations[161]. Even though some molecular vibrations are not IR active, IR technique provides strong signal compared to

Raman spectroscopy for various vibrational modes, in other words, an extremely reliable and well recognized fingerprinting method.

## Characterization of Surface Kinetics in UHV

### Temperature Programmed Desorption (TPD)

The method of temperature programmed desorption (TPD) is one of the most effective and well-known methods for the determination of bond energy in adsorption. And it has been used to study reactions at the gas-metal interface[162]. TPD offers a way to better understand the growth of metal-organic films. To control chemical processes at the atomic level during the growth of a film, information about reactions on the substrate surface such as decomposition, adsorption, desorption, and migration of chemical species is important. Once absorbed, the surface of the sample is heated according to a known temperature ramp to desorb the bonded reactant[163]. While “flash-filament” desorption method records the pressure in the system to analyze information on various adsorption parameters, a technique called TPRS (temperature programmed reaction spectroscopy) is often used to record the identity and number of species desorbing off of the surface. The difficulty of the analysis of the desorption curves using TPRS relies on if the rate determining step is the desorption of the species or the decomposition of the species on the surface. While the flash-filament analysis can be applied to the desorption curves in the former case, the basic rate equation for TPD can be given in the latter case,

$$-\frac{d\theta}{dt} = A \exp\left(-\frac{E}{RT}\right) \theta^n \quad (8-1)$$

where  $A$ ,  $\theta$ ,  $n$ ,  $T$ , and  $E$  is the pre-exponential factor, the surface coverage, the order of kinetics, the temperature at time  $t$ , and the activation energy, respectively. If

the peak temperature and heating ramp rate are known, it is possible to calculate the pre-exponential factor  $A$ . Desorption curves for the surface will be produced by numerical integration of Eq. 8-1. Desorption rate curves for argon on tungsten with various incident ion energy are depicted in Fig. 8-1. What one can determine from the shape of the peaks on the desorption rate curve is whether the activation energy is constant or a function of the surface coverage. However, there should not be any overlapping peaks to determine the dependence of activation energy of surface coverage. The only property that can be calculated is the temperature at which the desorption rate is at a maximum since Fig. 8-1 has overlapping peaks. One can find out detailed analysis from Redhead's articles[163, 164].

Recently, TPD depends on the use of a mass spectrometer, which can identify different species in the gas phase. More specifically, a mass spectrometer is used to detect the species coming off from the surface of the sample while it is being heated. In addition, mass spectrometry can be used to deduce fragmentation patterns of the precursors as they interact with the substrate surface. Fragmentation data can provide important information for bonding state and effect of the precursor to the surface.

### **Low Electron Energy Diffraction (LEED)**

LEED (Low Electron Energy Diffraction) is a technique for investigating the crystallography of surfaces and overlayers or films adsorbed on surfaces. LEED uses a beam of low energy electrons, typically 10-1000 eV[165, 166]. The electrons are incident on the surface of the sample and the resulting backscattered and secondary electrons are used to determine the position of the atoms on the surface of the sample. Diffraction of electrons occurs because of the periodic arrangement of atoms in the surface. This periodic arrangement can be conceptualized as parallel rows of atoms

analogous to grating lines in a diffraction grating. The simplest diffraction measurement is the determination of the surface or overlayer unit mesh size and shape if the electron beam is incident normal to the surface. This can be done by inspection of the diffraction pattern at any energy of the incident beam. The surface structure can be determined by a plot of intensity versus energy or accelerating voltage, which is referred to as an I-V curve. Diffraction is very useful whenever there is a distinct phase relationship between scattering units. The greater the order, the better defined are the diffraction features. Although LEED can be used for quantitative determination of atomic positions in surfaces, it is complicated by the multiple scattering of the electrons since an accurate goniometer and detection scheme are required to measure intensities for which the scattering geometry. LEED is the most powerful, widely used and developed technique for investigating periodic surface structures. It has been used very widely as a method to check surface order[165].

### **Auger Electron Spectroscopy (AES)**

AES (Auger Electron Spectroscopy) is very similar to LEED in which it depends on the use of electrons to determine the nature of the surface. AES is the most commonly used surface, thin film, or interface compositional analysis technique. AES is used to determine the elemental composition of the surface, and in many cases, the chemical bonding of the atoms in the surface region of solid sample while LEED is used to check the surface structure. Among all the electrons in the beam incident on the surface of the sample, Auger electrons have the least amount of energy. Due to the lack of energy, Auger electrons only penetrate the surface deep enough to analyze the outermost 2 through 10 atomic layers and this characteristic make AES most useful in identifying thin films grown on the substrate surface. It has very good lateral spatial

resolution which can be as low as 300 Å, relying on the electron gun used. In addition to good lateral spatial resolution, it also has very good depth resolution, as low as 20 Å depending on the characteristics of the ion beam used for sputtering[165]. And it has a good absolute detectability of 100 ppm for most elements under good conditions. It can be combined with ion-beam sputtering to remove material from the surface and to continue to monitor the composition and chemistry of the remaining surface as this surface moves into the sample.

### **Attenuated Total Reflection Using FTIR Spectroscopy (ATR-FTIR)**

#### **Current state of ATR-FTIR technique**

Attenuated total reflection is a sampling technique used in conjunction with IR spectroscopy which enables samples to be examined directly in the solid or liquid phase without further sample preparation[167]. ATR uses a property of total internal reflection called the evanescent wave, the phenomenon which was observed by Newton in the early 1700s. Total internal reflection can occur when a ray of light passes from a denser to a rarer medium. In such environments, light bends away from the normal in to the rarer medium, however, from at a certain incidence angle which is called as critical angle, the light is completely reflected back to the denser medium. Fig.8-2 shows a multiple reflection ATR system.

As seen in Fig.8-2, ATR crystal has some type of beveled edges and infrared beam go through it with one or more reflections. Fig.8-3 shows various types of ATR-FTIR system. For pursuit of diversity of sample phases, IRE has been developed for each specific sample type. Among these types, Fig.8-3(A) is the most typical one for UHV surface system.

In view of number of reflections, the more, the better. However, there are some constraints for that. The total number of reflections (N) of a given length (L) and width (W) of an ATR element is given by;

$$N = \frac{L}{W} \cot \theta_c \quad (8-2)$$

where  $\theta_c$  is the critical incidence angle. As one can see in Eq. 8-2, long and thin crystal can give more reflection numbers, however, long and thin crystal might lose uniformity and have beam focusing problem, respectively.

### **FT-IR (Fourier Transform Infrared)spectroscopy**

Every molecule is in constant motion, producing vibrations like stretching, bending, rocking, wagging and scissoring. A molecule composed of n-atoms has  $3n$  degrees of freedom, six of those are translations and rotations modes. Those  $3n-6$  degrees of vibrational freedom make different modes. And it can be symmetric or asymmetric stretches and bends and bending mode can be either in-plane or out-of-plane. If the frequency (energy) of incoming IR radiation matches that of the molecular vibration, energy is absorbed by the vibrating bonding. Since every vibrational mode has its own fingerprint region, one can assign each signal to specific vibrational mode, even though some are overlapped. In other words, C-O, C-S, C-H, N-H, S-O, etc. demonstrate their unique vibration bands in the infrared spectrum. And wavenumber for each mode can be red or blue shifted depending on its neighboring group. The report from Mui and his coworkers shows good conjunction of ATR-FTIR experiment and detailed calculation result for vibrational frequencies of adsorbed molecules including bonding energy calculations. They used ATR-FTIR technique and DFT calculations to

test the applicability of the surface proton affinity using methylamine, dimethylamine, and trimethylamine at the Si(100)-2x1 and Ge(100)-2x1 surfaces[168].

### **Applications of ATR-FTIR technique to thin film research**

As interest in the surface chemistry of group IV semiconductors such as silicon and germanium increases rapidly, technological applications as well as fundamental research is getting more important. Energetic research products for various types of surfaces, for example, flat, porous, and reactive surfaces, have been performed with surface analysis tools. The most widely used single-crystal silicon wafers of high purity are commercially available and relatively cheap. Si(100) and Si(111) is the most common surface orientations, it becomes coated with a native oxide upon air exposure. For flat silicon surface, native oxide can be removed by fluoride ion chemically or thermally under UHV environments. Moreover depending on desired electronic properties, silicon wafers can be doped as n-type or p-type with electron-donors (P, As, Sb) or electron-withdrawer (B), respectively. Compared with silicon wafers, germanium wafers is approximately 500 times more expensive due to its limited use. Disordered and water soluble  $\text{GeO}_2$  interface is one of the main obstacles for applications. Ranke reported NH<sub>3</sub> adsorption on three orientations of Ge surfaces, Ge(001), (113), and (111)[169]. Due to disordered interface, initial adsorption on Ga(111) which does not form reconstruction dimers is much weaker. And even beyond two monolayers, the layer continues to grow with different adsorption enthalpy on the different orientations and only after 4 monolayers, the whole layer rearrange irreversibly to form the usual NH<sub>3</sub>.

ATR-FTIR technique has been used widely, especially in surface functionalization research. For analyzing surface flatness and makeup of the hydride-

terminated surfaces that offer many advantages, ATR-FTIR has been put to use. Rapid and efficient preparation of Si-H hydride-terminated flat surfaces has been known and it is outlined in Fig.8-4.

Since the Si(111)-H monohydride surface has a very sharp and narrow Si-H stretch at  $2083.7\text{cm}^{-1}$  as shown in Fig.8-5, one can confirm smooth surface over nanometer-scale distances from ATR-FTIR results. Also for preparing Ge-H surface which was first published only recently in 2000[170], the roughness of this surface is related with the broad Ge-H stretching observed by ATR-FTIR at around  $2100\text{cm}^{-1}$  with  $\sim 50\text{cm}^{-1}$ line width. As shown in Fig.8-5, germanium surface was smoothened by etching with a 10% HF solution with time evolution. And Choi and Buriak[170] reported that the H-terminated Ge is stable in air for up to 1 hour.

Other than H-terminated silicon and germanium surface researches, chlorinated silicon (Si-Cl)[171], brominated silicon (Si-Br),[172] halogenated silicon (Si-X, X=Cl, Br, I), chlorinated germanium (Ge-Cl)[173], etc. have been studied using ATR-FTIR for surface functionalization.

UHV approach to Si-C bond formation is very important for metal-organic precursor initialization step with surface. Working under UHV environment (below  $10^{-10}$  Torr) provides good conditions that are as close as at the atomic level. Among various possibilities, [2+2] reactions of carbon containing unsaturated molecules with silicon surface and diels alder like ([4+2]) reactions of dienes with silicon surface have been paid attention and studied over twenty years. Bozack and his coworkers started research about small unsaturated hydrocarbons such as propylene to chemisorbed to Si(100) surfaces at room temperature[174]. From ATR-FTIR results, two new Si-C  $\sigma$

bonds form due to cleavage of the  $\pi$  bonds in the alkene and disilylene remaining the Si-Si  $\sigma$  bond intact as outlined in Fig.8-7. In addition, the reactivity of *cis*- and *trans*-1,2-dideuteroethylene by ATR-FTIR was examined and compared the stretching frequencies of the observed vibrations with calculated values with Gaussian 94. In this case due to the lack of data for ethylene adsorption to silicon surface with different stereochemistry, DFT calculations can provide definite clues for identifying peaks.

Other than the vibrational frequency calculations, various thermodynamic calculations such like adsorption/desorption energy, activation energy, reaction enthalpy, etc. can be performed with satisfactory level[168]. Filler and his coworkers adopted ATR-FTIR, TPD, and DFT calculations for elucidation of carbon and oxygen coupling in the reaction of formaldehyde on Ge(100) surface[175]. In their work, evidence that a species with an electron-deficient carbonyl group, likely a dative bond, initially exists near room temperature with a minority C-H dissociation product was elucidated by infrared spectroscopic method. And using DFT calculations, formation of a C=O [2+2] cycloaddition product was predicted. Although Konecny predicted that the [4+2] reaction will be 15-29 kcal/mol more stable than the [2+2] addition product theoretically[176], this work identified the first catalytic reaction on a group IV semiconductor surface both experimentally and theoretically.

In the case of adsorption of more complex molecules, experimental and theoretical study for mechanisms and processes in hafnium alkylamine precursor adsorption and reaction on silicon oxide and H-terminated silicon surfaces has carried out by Kelly and his coworkers[177]. From the UHV experiment of TDEAHf (Tetrakis (diethylamino) hafnium) exposure to Si-H and Si-OH surfaces, they reported conversion

of the higher hydrides to monohydride (Si-H) units on the surface through hydrogen abstraction, or change in one or more of possible back-bonds made by the local silicon atom. The structures of the Si-H IR vibrational modes for the initial surface and after various exposure doses at 25 and 250°C are shown in Fig.8-8. Comparison the spectra in Fig.8-8 indicates a broad Si-H mode, consistent with surface roughness and a variety of Si-H, Si-H<sub>2</sub>, and Si-H<sub>3</sub> surface species and the loss of these converted (or frequency shifted) Si-H bonds. By observing ATR-FTIR results and matching with DFT calculation results for each reaction step as shown in Fig.8-9, they proposed adsorption mechanism of TDEAHf on functionalized silicon surface. In Fig.8-9(A), one can confirm Si-H and O-H stretching modes of the initial surface at 2207 and 3880cm<sup>-1</sup> from the first spectrum and O-H modes disappear after reaction with TDMAHf via H transfer from OH group. While Si-H stretch remains, other modes of the adsorbed precursor appear including the N-H stretch of the adsorbed product at 3512cm<sup>-1</sup>. In the same context, after the reaction with TDMAHf via H abstraction, the Si-H mode which was shown in the first spectrum (surface group) disappears while the other modes of the adsorbed precursor appear.

For another H-terminated silicon experiment, Kosuri and his coworkers reported vapor-phase adsorption kinetics of 1-decene on Si(100) surface[178]. Adsorbed 1-decene can be detected with ATR-FTIR owing to an evanescent electric field, which gathers signal of distant functional group from surface approximately 0.5~5μm. And this distance is enough to analyze thin film surface. Proposing reaction mechanism of 1-decene on hydrogenated silicon, they obtained pre-exponential factor and activation energy with regression of Arrhenius plot experimentally. Reasonable initial and

boundary conditions of coverage were assumed and those were used to solve the rate equations. A time series of infrared absorbance spectra are taken during the Si(100) surface exposure to 1-decene as shown in Fig.8-10.

And interesting and outstanding results were reported by Kim and his coworkers. They demonstrated the layer-by-layer growth via urea coupling reaction to form an ultrathin film on Ge(100) surface between two bifunctional molecules, ethylenediamine and 1,4-phenylene diisocyanate at room temperature under vacuum environment[179]. Since multilayer functionalization under vacuum condition is not common and this developed dry method for multiple layer organic functionalization, this research is more outstanding. Moreover, since gas-phase reactants should undergo spontaneous reaction with the terminal functional groups at the surface under vacuum-based condition, this reaction should meet severe requirement. By reacting two molecules sequentially, layer-by-layer growth mechanism was discovered as shown in Fig.8-11.

In addition to that, they observed and reported characteristic infrared peak areas plotted as a function of exposure. Since one carbonyl group is created per molecule of ED or PD adsorbed beyond the first layer, the peak areas of each layer are expected to be equal and that was confirmed. Their demonstration of these layer-by-layer deposition methods could provide door to a strategy to design and produce precisely tailored organic materials.

Among various surface analysis tools, the most widely used machine would be XPS and QMS. Due to the difficulties of operating and designing barrier, ATR-FTIR is not that common so far. However, ATR-FTIR can give powerful information for surface functional group and surface analysis could be incomplete without it. Cho and his

coworkers have reported thermal decomposition of  $\text{Ti(O-iPr)}_2(\text{dpm})_2$  on Pt foil and they used QMS, XPS and AES[180]. They proposed thermal decomposition mechanism with sufficient data of TPD and binding energy as shown in Fig.8-12 and final species remaining on the Pt surfaces after the decomposition of the Ti compound at temperature above 650K with XPS data. However, they failed to explain the bond between the adsorbate and Pt surface, and functional group variation of intermediates.

Although ATR-FTIR can be used all phases (i.e. solid, liquid and gas) even for the interface[181], this review has focused on gas-phase surface reaction under vacuum. ATR-FTIR would have unlimited applications for surface science area owing to its fingerprint capability and high sensitivity. And its utilization will make surface science field more resourceful and exciting one. The unlimited technological applications of ATR-FTIR are only a matter of time. One should note its potential.

### **UHV System Design and Sample Probe Simulation Using CFD Software**

#### **UHV System Design**

Fig. 8-13 shows UHV system design and process flow diagram interfaced with QMS, LEED/AES and FTIR spectroscopy. This *in situ* system enables to analyze surface science kinetics under ultra high vacuum atmosphere. Two bubblers that typically contain metalorganic precursor are immersed in the constant temperature bath to provide sufficient vapor pressure. UHV system designed in this work consists of four chambers. Chamber 1 is loadlock to mount the sample on the sample probe and enables to save time to make chamber 2 ultra high vacuum level. Since chamber 1 is small, one can easily lower the chamber pressure to high vacuum level. Chamber 2 is deposition chamber. Two metalorganic precursors are used to deposit films on beveled edge silicon wafer. And then deposited film is conveyed to chamber 3 to analyze

spectroscopic characteristics. Chamber 3 is for ATR-FTIR chamber and deposited film is analyzed using ATR technique. To conserve IR beam source two KBr windows are adopted. Chamber 4 is analysis chamber which will perform main analysis using QMS and LEED/AES including TPD option.

Fig. 8-14 depicts perspective view of three chambers of four. For effective movement of sample probe, four chambers are connected linearly. At each chamber, sample can be rotate in one direction completely to face or align appropriately.

### **Sample Probe Simulation Using CFD Software**

The most demanding part to design is sample probe. Basically, mass and momentum transfers are not related to this simulation, conservation of energy was considered with geometry and boundary conditions specific to this sample probe geometry. Since heating and cooling of sample should be done during experiment and temperature distribution is very important for TPD experiment, temperature uniformity would be the key to success or failure. Temperature simulation was performed using FLUENT<sup>TM</sup> Computational Fluid Dynamics (CFD) commercial software.

Heating filament, heater tube and front and rear clamps are made of tungsten, Oxygen Free High Conductivity ("OFHC" hereafter) copper, and 304SS (stainless steel 304), respectively. The thermal properties used in CFD simulations are tabulated in Table 8-1.

After various trials of sample probe design, improved model was proposed and further CFD simulations were performed to investigate temperature profile mainly focused on Si wafer at the heating material temperature 1000 K as shown in Fig. 8-15. Fig. 8-15 (A) shows perspective view with IR pathway and cross-section for simulation.

However, since temperature difference ( $\Delta T = T_1 - T_2$ ) between X and Y shown in Fig. 8-15B and C was around 85 K, it requires another modification to increase temperature uniformity. The large temperature difference between both ends can give improper information about desorption temperature during TPD experiments. Based on this experience, a few modified designs were simulated as shown in Fig. 8-16.

With the simulated results with 1000 K heating material, temperature difference between both ends of beveled Si wafer is tabulated in Table 8-2. The mesh was generated using the Gambit™ software and the unstructured quadrangle grid was employed.

After initializing the values with boundary condition, the iteration process converged after 228 iterations. Fig. 8-16E shows the most uniform temperature distribution and three-dimensional model was prepared using CAD (Computer Aided Design) software as shown in Fig. 8-18. With all these simulation and analysis, prototype of UHV system is schematized as shown in Fig. 8-19.

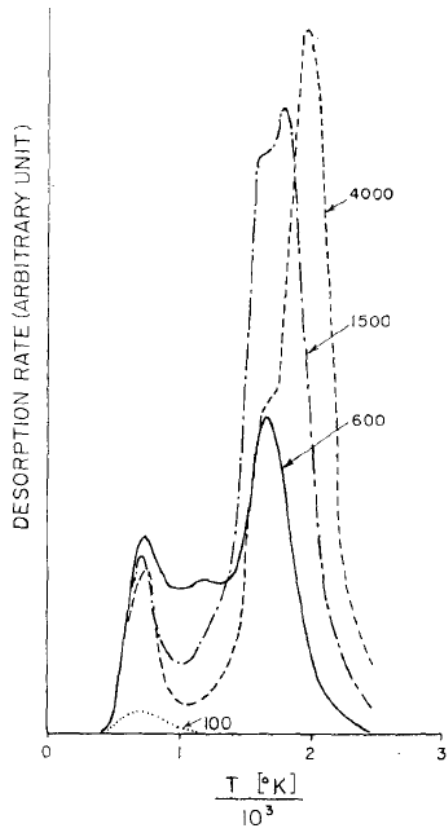


Figure 8-1. Desorption rate of argon from tungsten for various values of the incident ion energy. (taken from Ref. [163]).

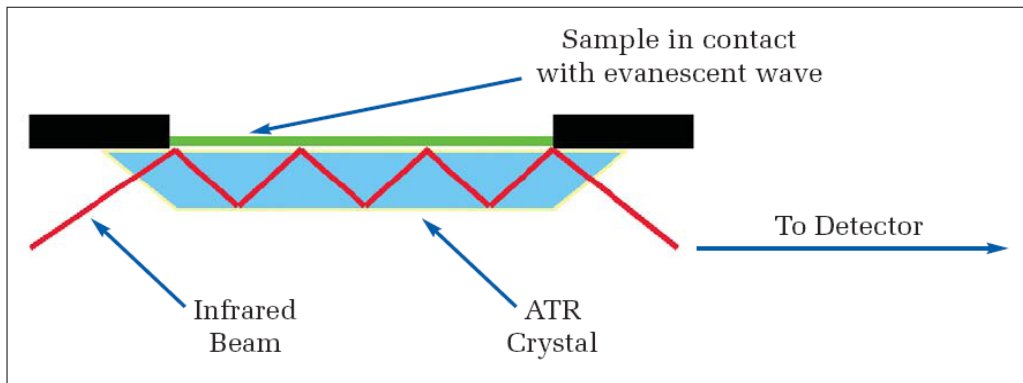


Figure 8-2. A multiple reflection ATR system (Figure was taken from Ref.[182]).

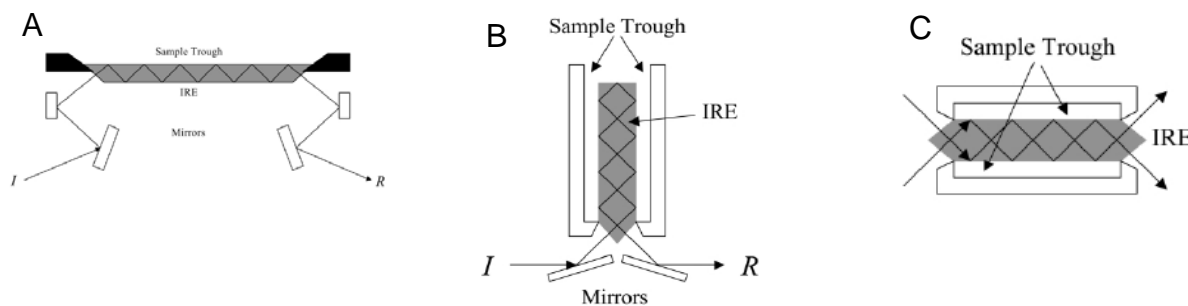


Figure 8-3. Various types of ATR-FTIR system.

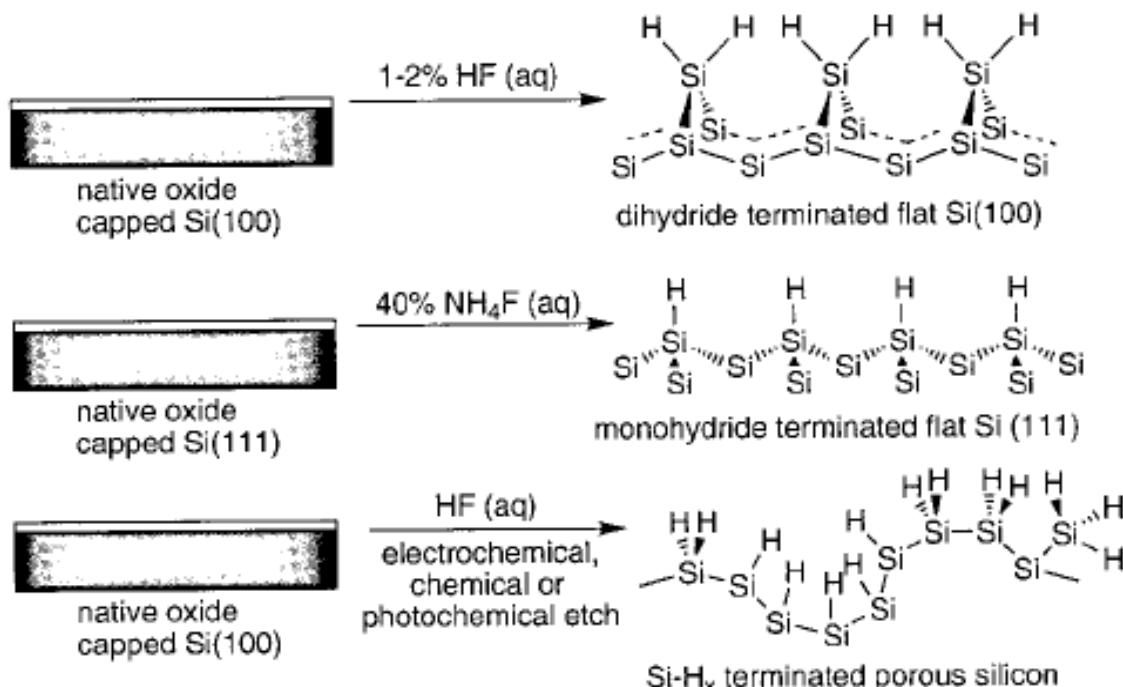


Figure 8-4. Fluoride-based etching conditions, leading to hydride-terminated flat and porous silicon surfaces. (Figure was taken from Ref.[183]).

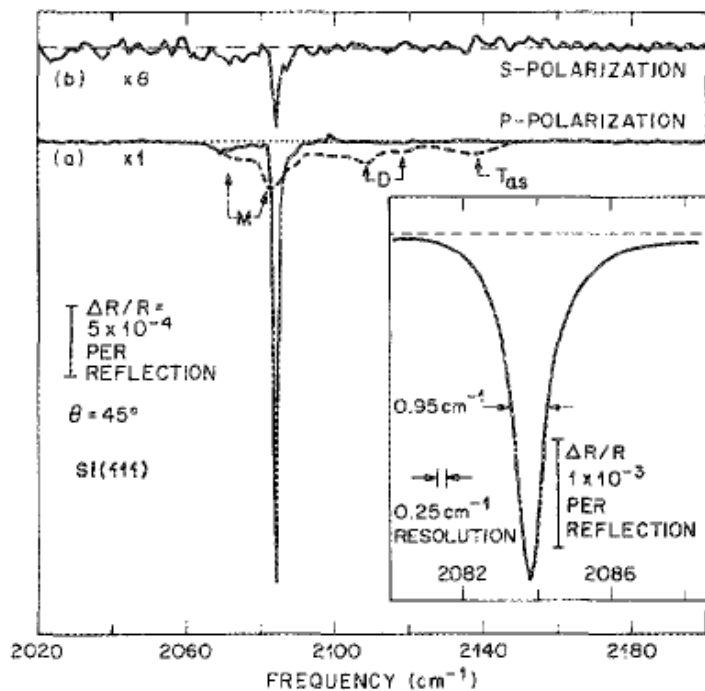


Figure 8-5. Internal reflection spectra of HF-treated Si(111) surfaces (Figure was taken from Ref.[184]).

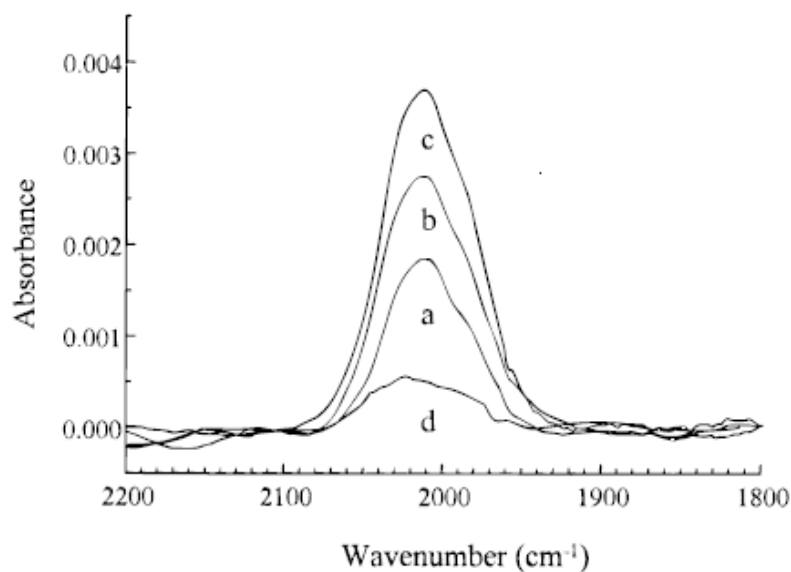


Figure 8-6. Ge-H vibrations observed by ATR-FTIR. Surfaces prepared by etching 10% HF solution. (Figure was taken from Ref.[170]).

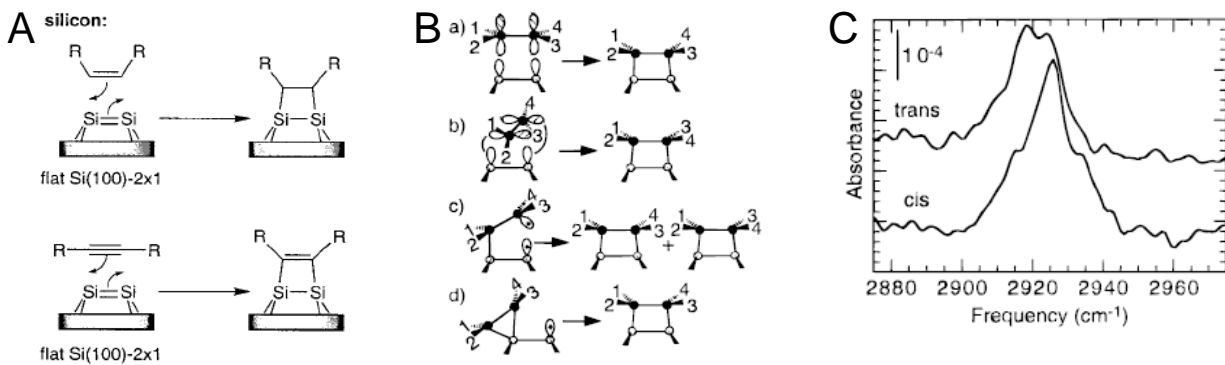


Figure 8-7. (a) [2+2] cycloadditions on Si(100) surface with alkenes and alkynes (b) possible models for adsorption of ethylene on Si(100) surface (c) FTIR spectra for *cis*- and *trans*-1,2-dideuteroethylene. (Fig.8-7(A) was taken from Ref.[183] and (B) and (D) were from Ref.[175]).

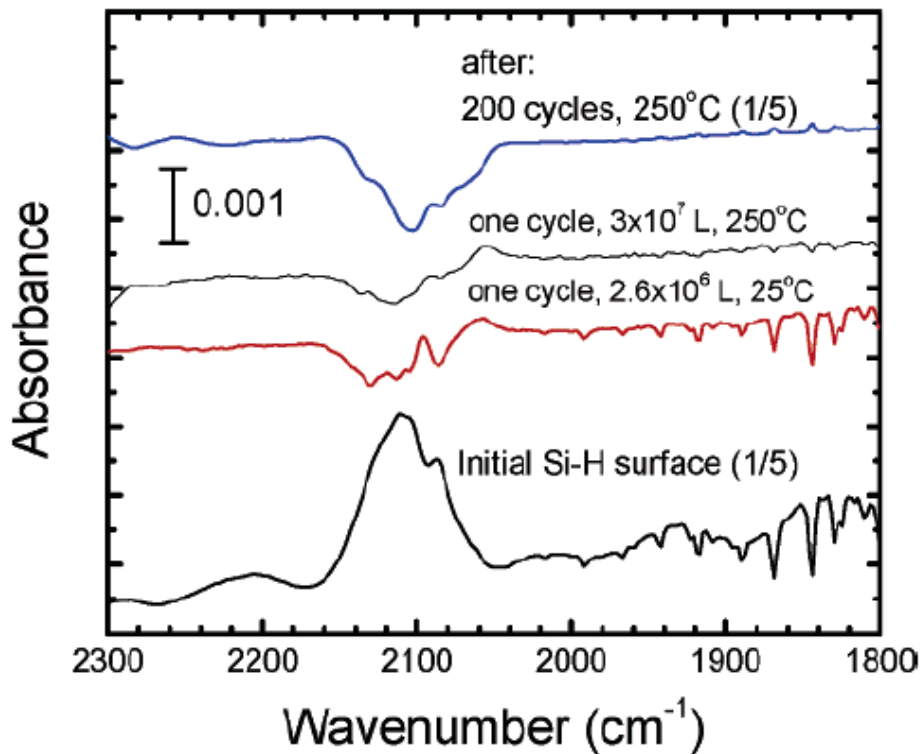


Figure 8-8. Si-H IR vibrational modes for the initial surface and after various precursor exposure doses of TDEAHf at 25 and  $250^\circ\text{C}$ . (Figure was taken from Ref.[177]).

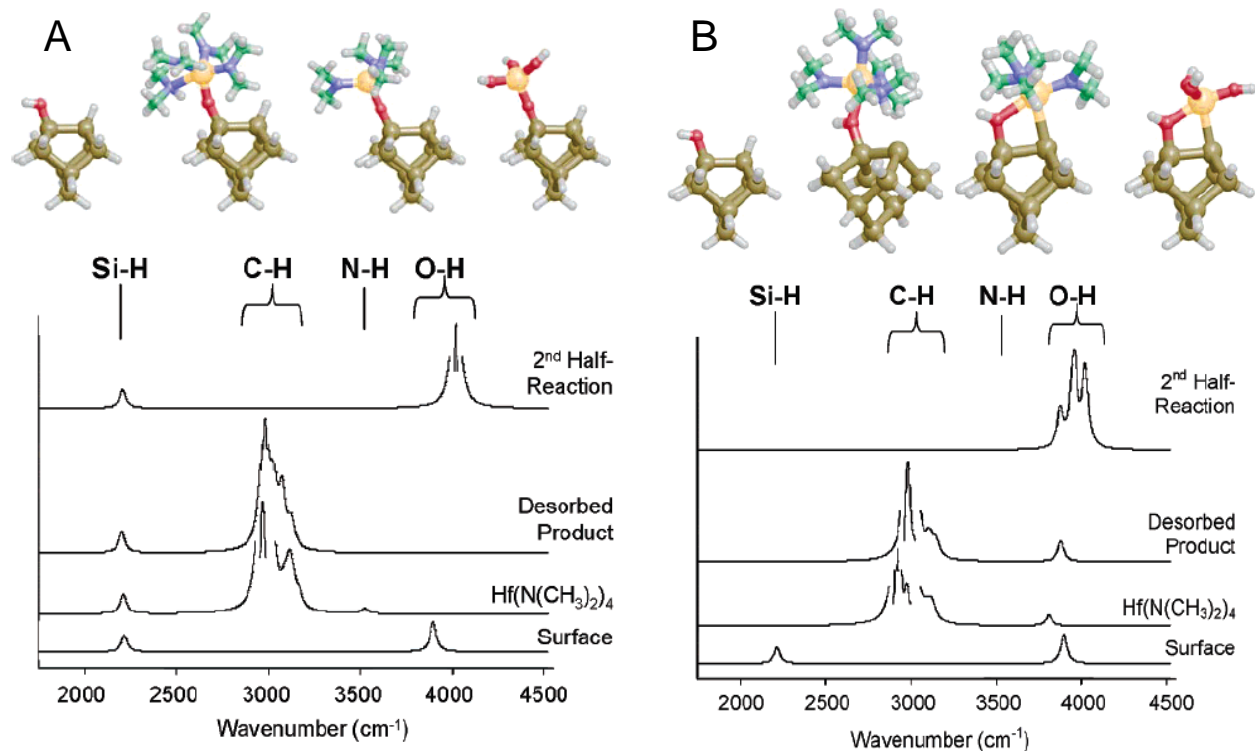


Figure 8-9. (A) Calculated vibrational spectra for the species present in the H transfer process (B) Calculated vibrational spectra for surface species in the Si-H abstraction process. (Figure was taken from Ref.[177]).

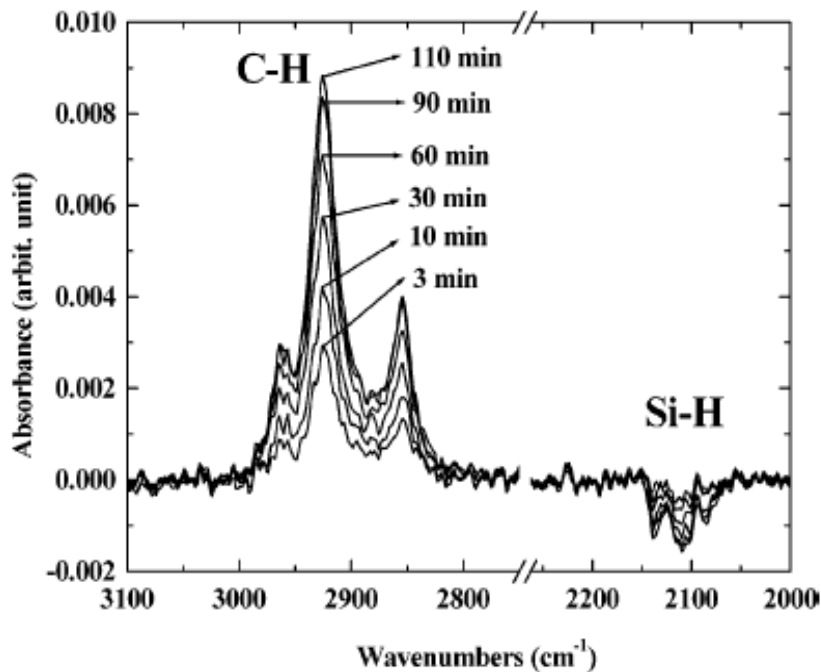


Figure 8-10. A time series of IR absorbance spectra of c-H and Si-H stretching vibrational modes. (Figure was taken from Ref.[178]).

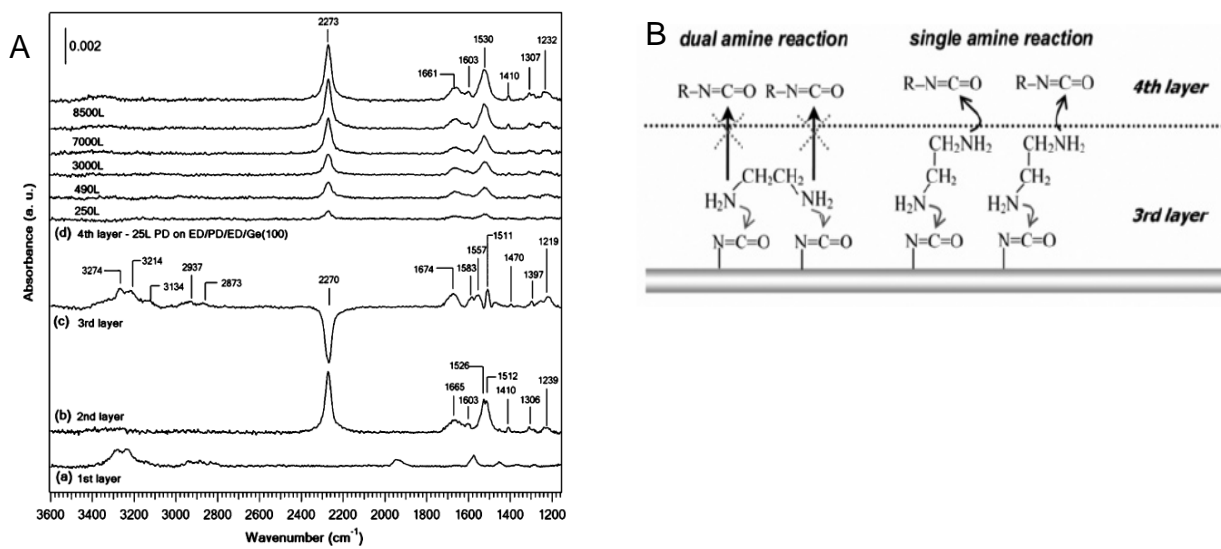


Figure 8-11. (A) Saturation infrared spectra of ED/Ge(100), PD/ED/Ge(100), ED/PD/ED/Ge(100), and PD/ED/PD/Ge(100) for 1<sup>st</sup> through 4<sup>th</sup> layer. (B) Schematic illustration of PD adsorbed on Ge(100) and second layer reaction with subsequent exposure to ED (Figure was taken from Ref.[178]).

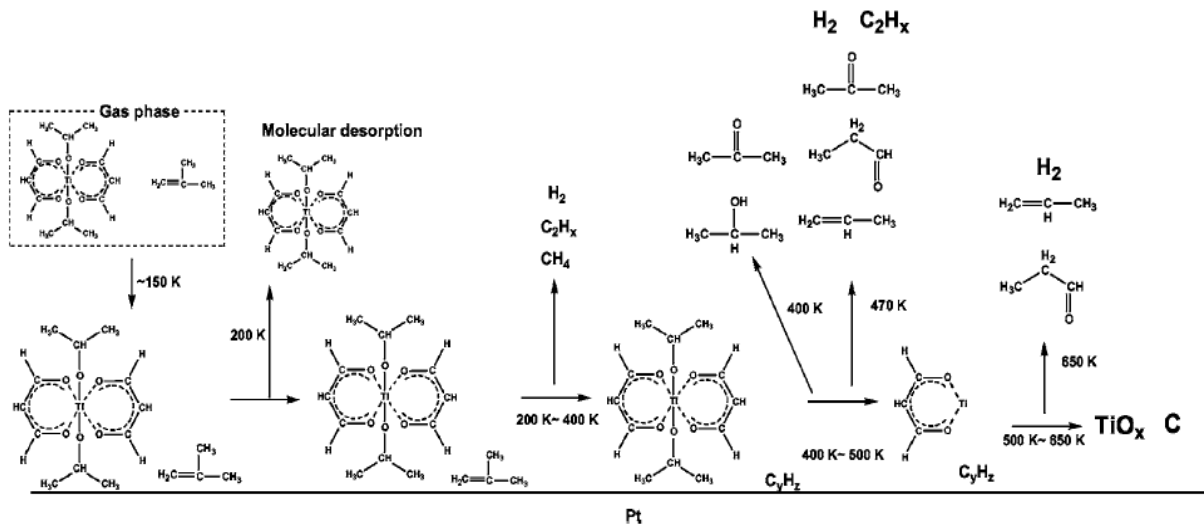


Figure 8-12. Proposed decomposition mechanism for  $\text{Ti}(\text{O}-\text{iPr})_2(\text{dpm})_2$  on a Pt surface. (Figure was taken from Ref. [179]).

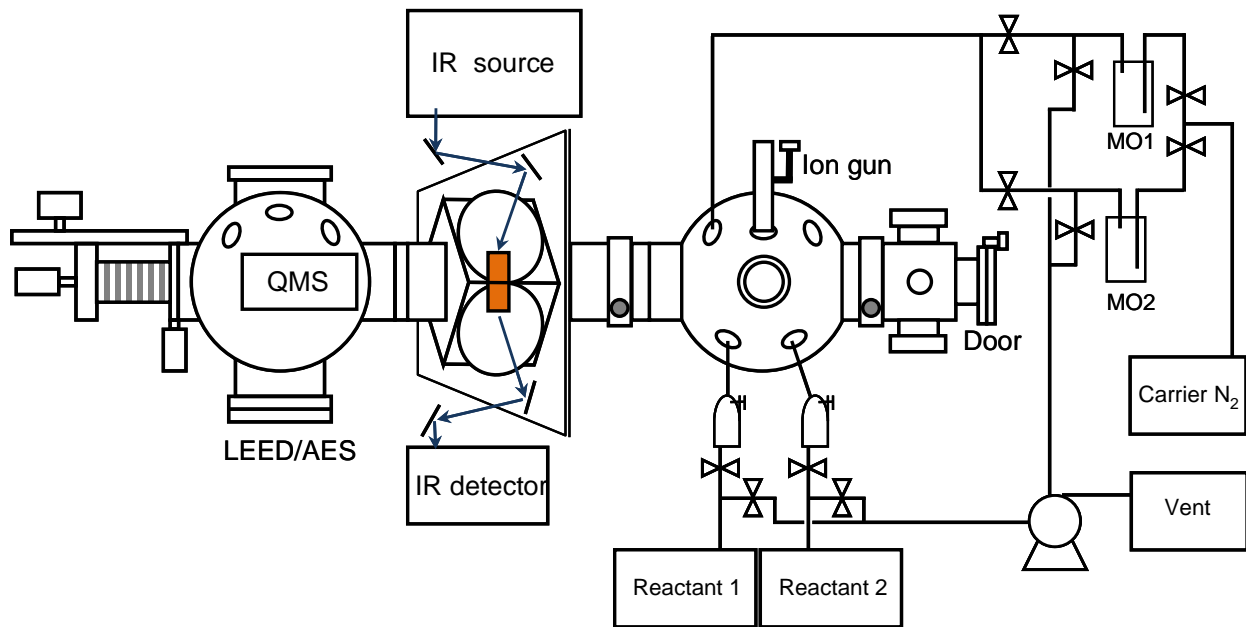


Figure 8-13. Four chamber UHV system and process flow diagram.

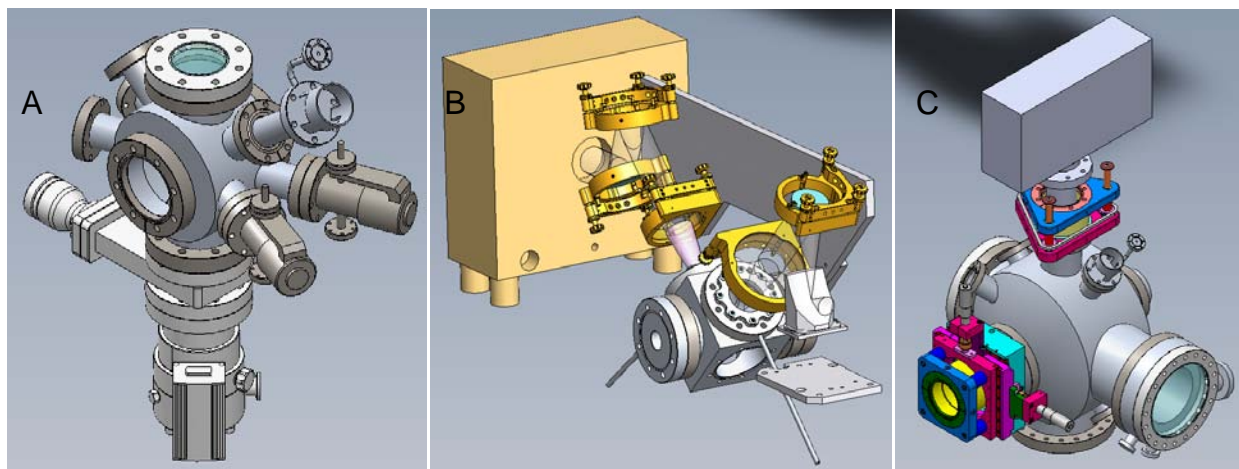


Figure 8-14. Perspective view of CAD drawing for (A) deposition chamber, (B) ATR-FTIR chamber and (C) analysis chamber.

Table 8-1. The thermal properties used in CFD simulation.

	Si	W	OFHC	304SS (Stainless steel)
Density [kg/m <sup>3</sup> ]	2329	19300	8978	8030
Cp [J/kg-K]	19.789	134.4	381	502.48
Thermal conductivity [W/m-K]	149	168	387.6	16.27

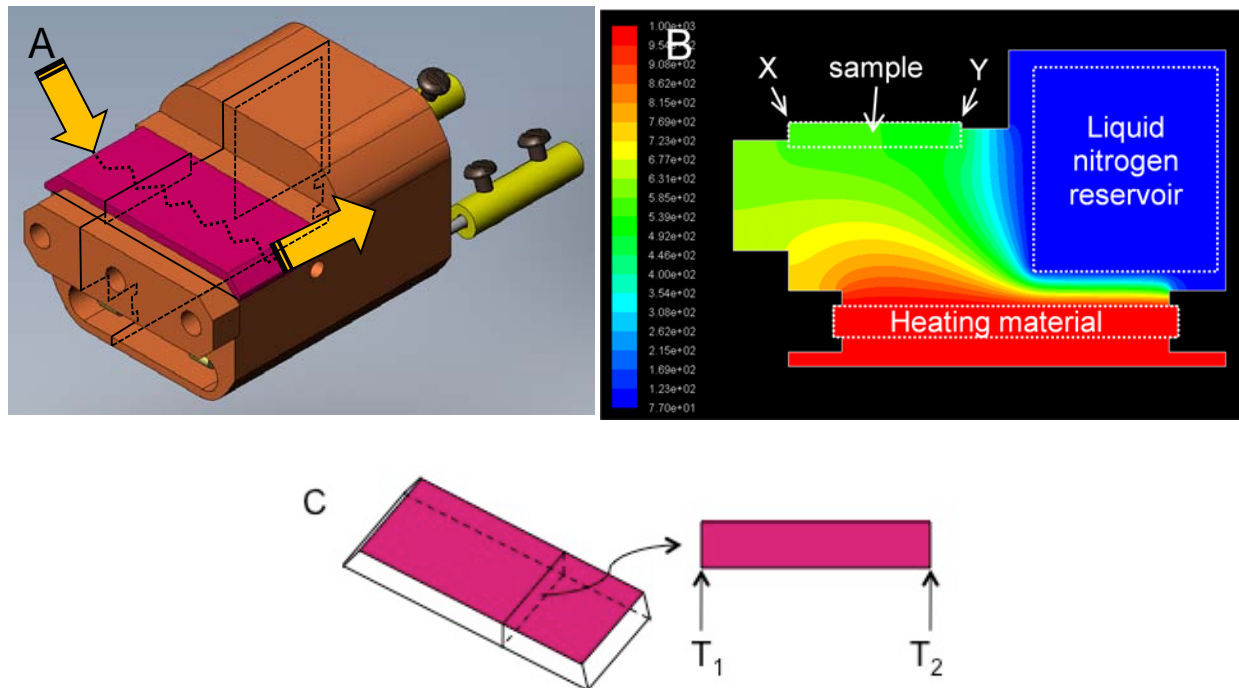


Figure 8-15. Proposed design of sample probe (A) perspective view, (B) CFD simulation profile, and (C) beveled edge Si wafer.

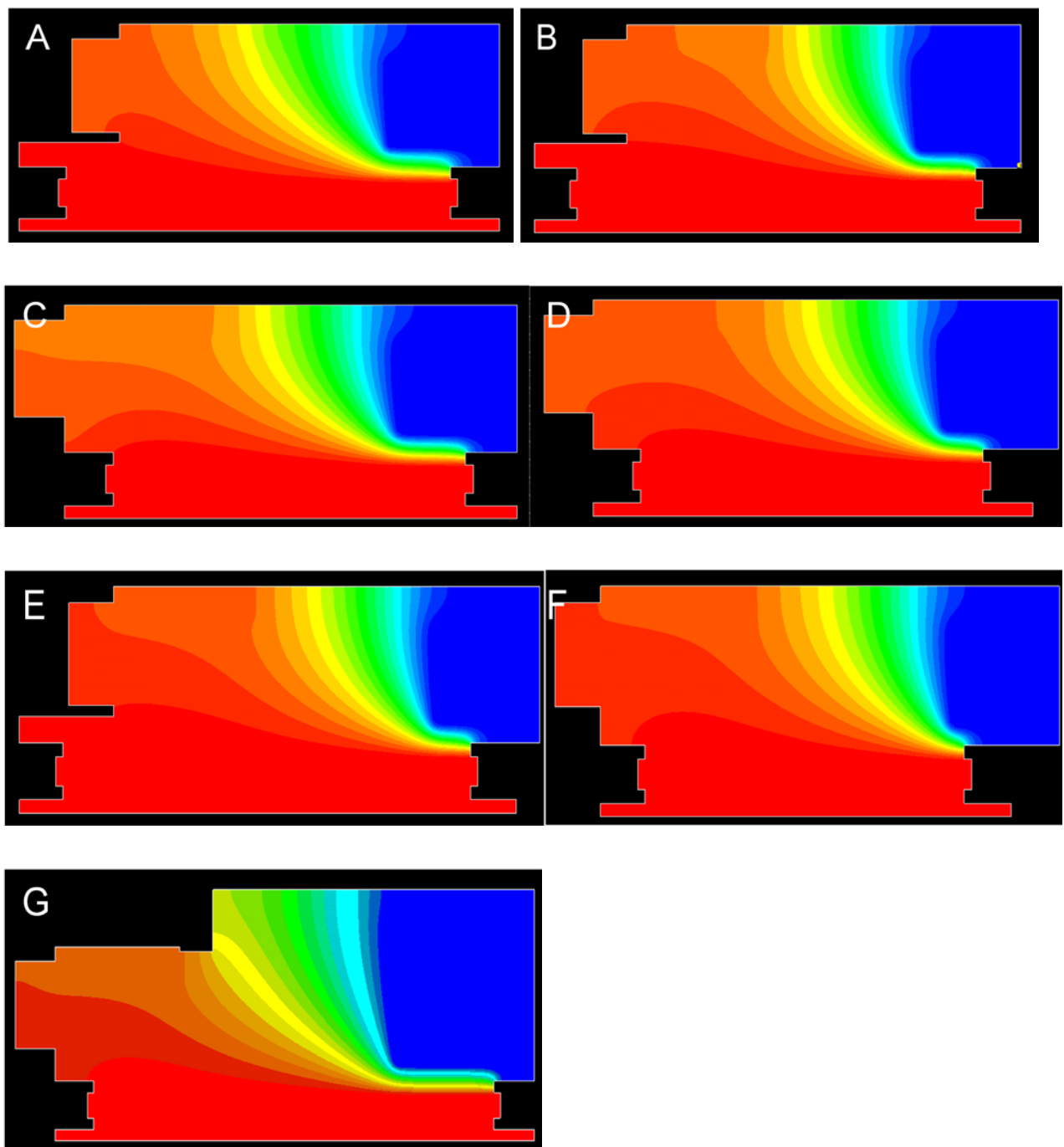


Figure 8-16. Temperature profile simulations at 1000 K for the modified designs with (A) 6 unit elongated front heating element, (B) 2 unit retracted liquid nitrogen reservoir from design A, (C) 4 unit retracted liquid nitrogen reservoir, (D) 6 unit retracted reservoir, (E) 6 unit elongated heater from design D, (F) 8 unit retracted reservoir, and (G) 6 unit retracted reservoir from Fig. 8-15 (B). (1 unit = 1.67 mm in real scale).

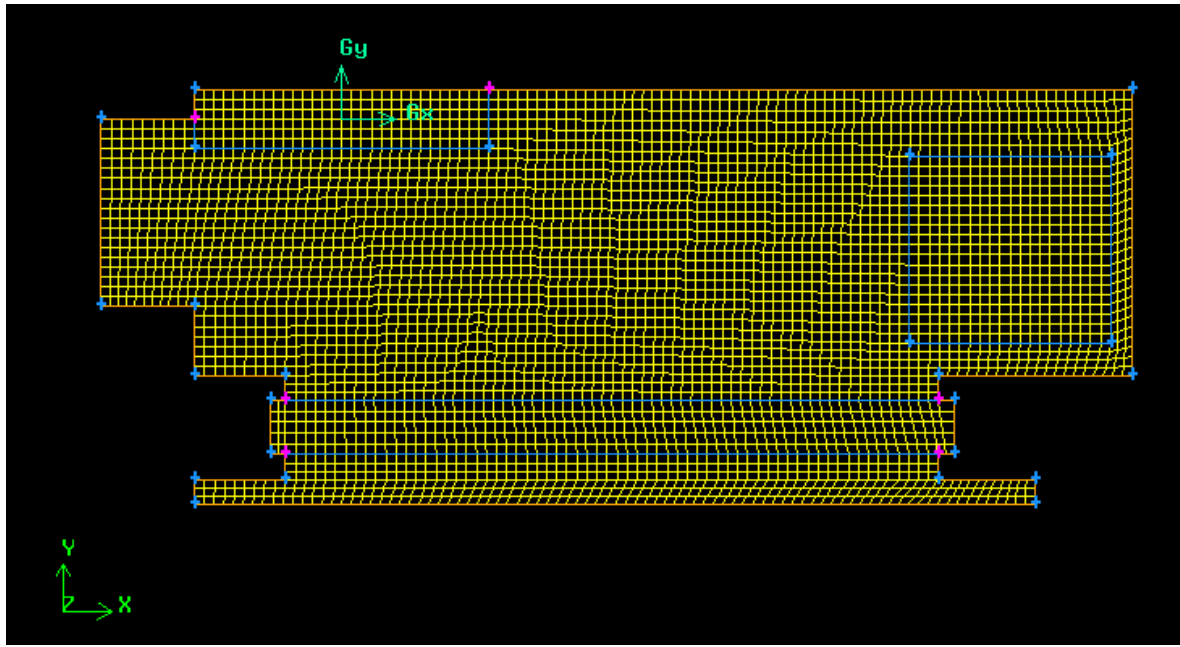


Figure 8-17. Quadrangular grid mesh for Fig. 8-16E.

Table 8-2. The temperature difference between both ends of Si wafer according to each design

Design No.	1	2	3	4	5	6	7
$\Delta T$ (K)	200	40	33	30	50	22	25

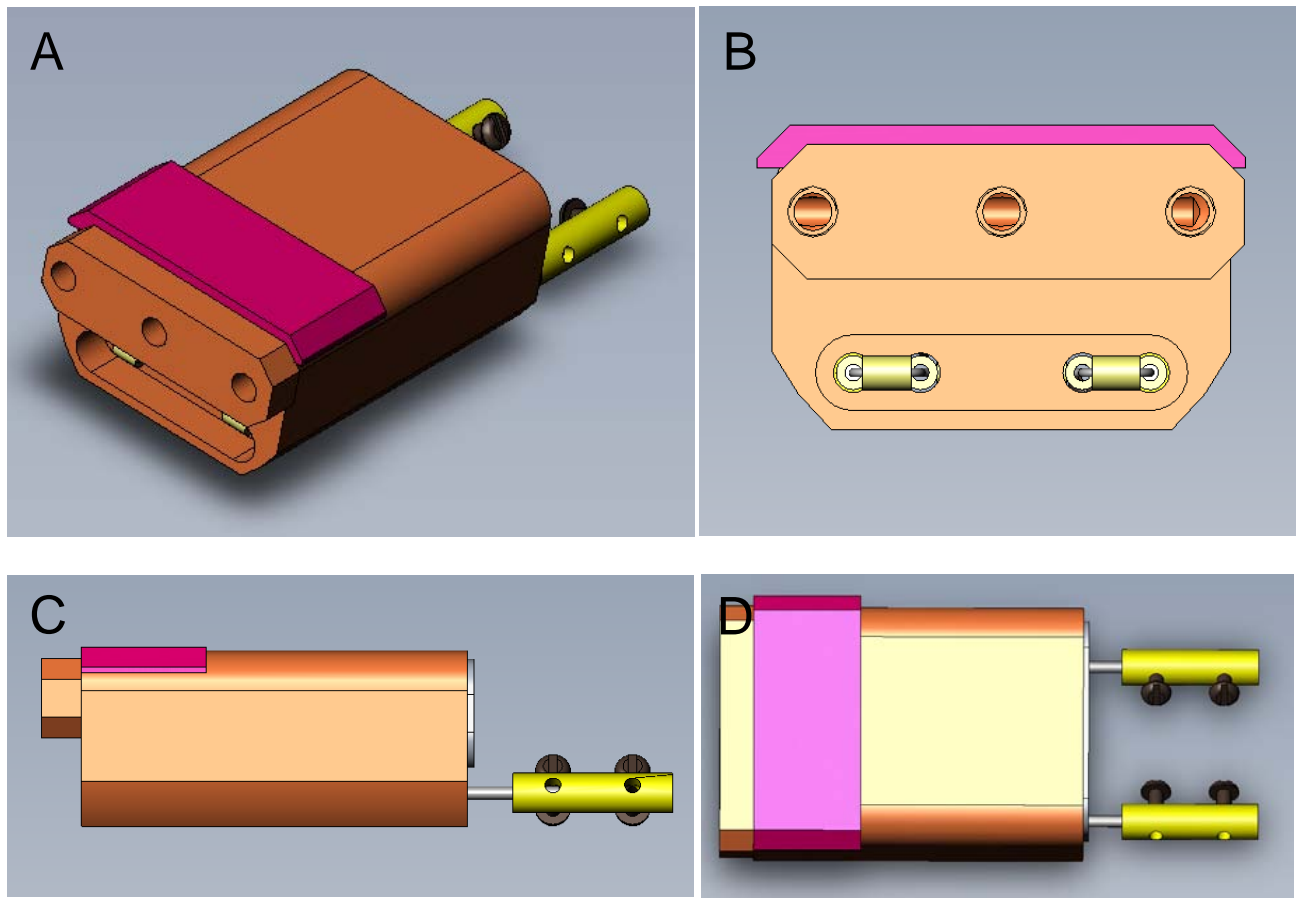


Figure 8-18. CAD drawing of sample probe (Fig. 8-16 (E)). (A) perspective, (B) front, (C) side, and (D) top view.

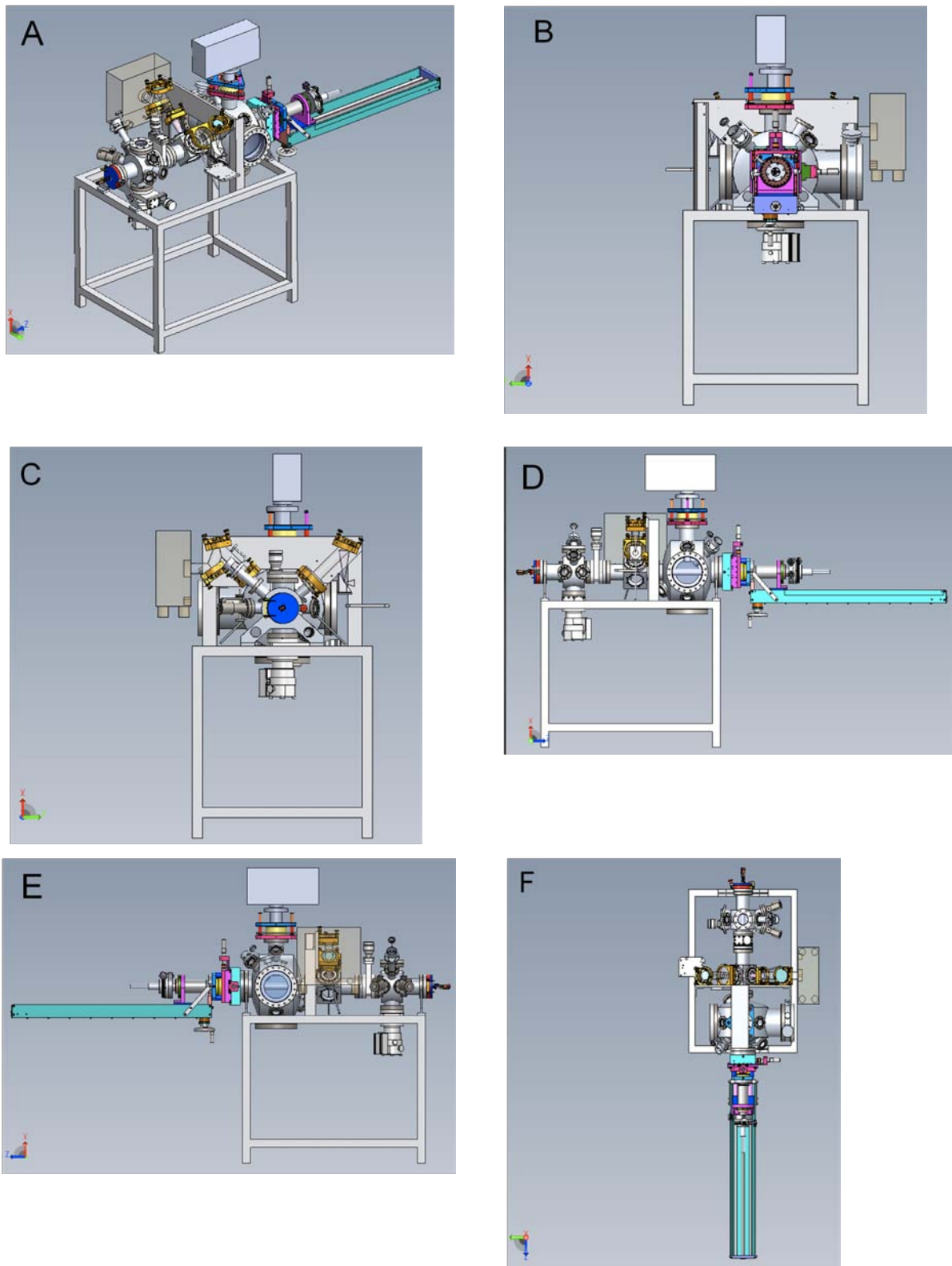


Figure 8-19. CAD drawing of designed UHV system. (A) perspective, (B) front, (C) rear, (D) side, (E) another side, and (F) top view.

## CHAPTER 9 CONCLUSIONS AND RECOMMENDATIONS

In the present study, several issues have been investigated in the homogeneous thermal decomposition of some metalorganic precursors basically using an *in situ* Raman spectroscopy and computational calculations. The CVD reactor used in this study is interfaced with an *in situ* Raman spectrometer (Ramanor U-1000, Jobin Yvon), which uses the 532.08 nm line of Nd:YAG solid-state laser and adopts a double additive monochromator with a diffraction grating of 1800 grooves/mm. DFT calculations were performed using Gaussian 03 program package to calculate molecular optimized geometry, thermodynamic properties, and rate parameters.

In triethylgallium thermal decomposition study in the CVD reactor, one can confirm the presence both of homolysis and  $\beta$ -hydride elimination experimentally. DFT calculations were performed to assist vibrational frequency prediction and assignment and thermodynamic properties estimation, etc. In this study, Raman shift measurements shown at  $490\text{cm}^{-1}$ ,  $517\text{cm}^{-1}$ ,  $537\text{cm}^{-1}$ , and  $555\text{cm}^{-1}$  were assigned to the vibrational frequencies between gallium and  $\alpha$ -carbon of  $(\text{Et})_3\text{Ga}$ ,  $(\text{DEGa})_2$ ,  $(\text{Et})\text{GaH}-\text{Ga}(\text{Et})_2$  and  $(\text{Et})\text{GaH}-\text{GaH}_2$ , respectively, by DFT calculations. Optimized activation energies are 60.0 and 44.0 kcal/mol and frequency factors are  $1.26 \times 10^{21}\text{s}^{-1}$  and  $8.9 \times 10^{13}\text{s}^{-1}$  for homolysis and  $\beta$ -hydride elimination, respectively. These results were obtained by using FEM reactor modeling and parameter optimization algorithm. And these results showed very good agreement with experimental observations.

The study of metalorganic precursor interaction with ammonia to construct group III-nitride was performed using triethylaluminum. To find out ammonia effect on triethylaluminum, two separate studies were carried out, i.e. triethylaluminum

decomposition with and without ammonia. To find out ammonia effect on triethylaluminum, *in situ* Raman spectroscopy measurement in an up-flow, cold-wall CVD reactor was used and the results of Density Functional Theory (DFT) calculations were performed. The observed Raman shifts were assigned based on references and DFT calculations as follows: TEAl:NH<sub>3</sub> (452 and 2841 cm<sup>-1</sup>), DEAlH (600 cm<sup>-1</sup>), TEAl:NH<sub>3</sub> TS (1462 cm<sup>-1</sup>), H<sub>2</sub>N-AIH-NH-AIH<sub>2</sub>(1525 cm<sup>-1</sup>), H<sub>2</sub>Al-NH<sub>2</sub>(1639 cm<sup>-1</sup>), MEAIH<sub>2</sub>,(2835 cm<sup>-1</sup>) MEAIH-AIH<sub>2</sub>(2849 and 2939 cm<sup>-1</sup>) and DEAI-AlH<sub>2</sub>(2900 and 2918 cm<sup>-1</sup>). DFT calculations using B3LYP functional combined with LanL2DZ basis set were also carried out to find the optimized geometry of each intermediate and transition structure and to calculate activation energies.

The decomposition pathways of the tungsten dimethylhydrazido complexes Cl<sub>4</sub>(RCN)W(NNMe<sub>2</sub>) (**1a**: R = CH<sub>3</sub>; **1b**: R = Ph), precursors for single source deposition of WN<sub>x</sub>C<sub>y</sub>, were investigated using a combination of experiments and calculations. Since complex **1a** has low volatility, Raman scattering studies were performed in an aerosol-assisted CVD reactor to identify reaction intermediates. Though complex **1a** is introduced as an aerosol state to reactor inlet, it can be realized that aerosol vaporizes in very short time enough to be considered as gas-phase by droplet evaporation analysis. DFT calculations (B3LYP/LanL2DZ) were used to estimate Raman active frequencies and these results were compared with experimental and literature data. methylmethylenimine (**8**), dimethylamine (**9**), and HNWCl<sub>4</sub> (**14**), products from N-N cleavage of the hydrazido ligand, were observed under deposition conditions and identified by comparison with previously reported Raman shifts and calculated frequencies.

Based on the obtained results through this study, a few modifications and future works are recommended. At first, although *in situ* Raman spectroscopic study has good aspects to investigate reaction kinetics of metalorganic precursors, infrared spectroscopy can still provide useful information. Since infrared spectroscopy is much more sensitive than Raman spectroscopy and has large number of database especially for organic materials, it can give very good supplementary information to reaction intermediates analysis. If infrared spectroscopy gives presence and concentration variation criteria for intermediate organic materials, performance of reaction kinetics analysis using Raman spectroscopy can be boosted much more. In practical perspective, attaching infrared spectrometer to the reactor used in this study is worth a try. If the reactor wall is changed to KBr or CaF<sub>2</sub> unless infrared source beam is absorbed to the wall during radiation, the present reactor scheme and movable reactor setting can still be used for *in situ* IR for analysis. Secondly, by combining kinetics study and film growth using appropriate substrate, one can reveal direct correlation between film quality or characteristics and kinds or quantity of reaction intermediates. At last, further study with two different metalorganic precursors can give more practical results by trying ternary phase study, for instance, gallium and aluminum precursors with ammonia to build AlGaN. By performing these, one can find out very useful reaction mechanisms for characteristics of doped film.

## LIST OF REFERENCES

- [1] G. Moore, Electronics, vol. 38, 1965.
- [2] J. Wu, W. Walukiewicz, K.M. Yu, J.W. Ager, E.E. Haller, H. Lu, W.J. Schaff, Y. Saito, Y. Nanishi, Applied Physics Letters 80 (2002) 3967.
- [3] B.G. Streetman, S. Banerjee, Solid State Electronic Devices, Prentice Hall, New Jersey, 2000.
- [4] W.M. Yim, E.J. Stofko, P.J. Zanzucchi, J.I. Pankove, M. Ettenberg, S.L. Gilbert, Journal of Applied Physics 44/1 (1973) 292.
- [5] O. Ambacher, Journal of Physics D: Applied Physics 31 (1998) 2653.
- [6] K.C. Wong, B.G. McBurnett, R.D. Culp, A.H. Cowley, J.G. Ekerdt, Surface Science 416 (1998) 480.
- [7] M.C. Paputa, S.J.W. Price, Canadian Journal of Chemistry 57 (1979) 3178.
- [8] Z. Mahmood, I. Hussain, R.E. Linney, D.K. Russel, Journal of Analytical and Applied Pyrolysis 44 (1997) 29.
- [9] J.A. McCaulley, R.J. Shul, V.M. Donnelly, J. Vac. Sci. Technol. A 9/6 (1991) 2872.
- [10] H.M. Ajmera, T.J. Anderson, J. Koller, L. McElwee-White, D.P. Norton, Thin Solid Films 517/21 (2009) 6038.
- [11] R.L. McCreery, Raman Spectroscopy for Chemical Analysis, A John Wiley & Sons, Inc., New York, 2000.
- [12] D. Parras, P. Vandenabeele, A.S. chez, M. Montejo, L. Moens, N. Ramos, Journal of Raman Spectroscopy 41/1 (2009) 68.
- [13] D.A. Long, Raman spectroscopy, McGraw-Hill, New York, 1977.
- [14] H.W. Schrötter, H.W. Klöckner, Raman Scattering Cross Sections in Gases and Liquids, Springer, New York, 1979.
- [15] H.A. Hyatt, J.M. Cherlow, W.R. Fenner, S.P.S. Porto, Journal of the optical society of america 63/12 (1973) 1604.
- [16] W.R. Fenner, H.A. Hyatt, J.M. Kellam, S.P.S. Porto, Journal of the optical society of america 63/1 (1973) 73.
- [17] N.C. Craig, I.W. Levin, Applied Spectroscopy 33/5 (1979) 475.

- [18] P.R.N. Childs, J.R. Greenwood, C.A. Long, Review of Scientific Instruments 71/8 (2000) 2959.
- [19] F. LaPlant, G. Laurence, D. Ben-Amotz, Applied Spectroscopy 50/8 (1996) 1034.
- [20] B.J. Kip, R.J. Meier, Applied Spectroscopy 44/4 (1990) 707.
- [21] R.J. Butcher, D.V. Willetts, W.J. Jones, Proceedings of The Royal Society (London) A 324/1557 (1971) 231.
- [22] J.J. Barrett, J. Opt. Soc. Am. 66 (1976) 801.
- [23] G. Vaughan, D.P. Wareing, S.J. Pepler, L. Thomas, V. Mitev, Applied Optics 32/15 (1993) 2758.
- [24] B.S. Samyal, R.S. Hickman, American Institute of Aeronautics and Astronautics, Fluid and Plasma Dynamics Conference, 13th (1980) 8.
- [25] M.C. Drake, Optics Letters 7/9 (1982) 440.
- [26] J.M. Alía, H.G.M. Edwards, Journal of Molecular Structure 354/2 (1995) 97.
- [27] J.M. Alía, H.G.M. Edwards, J. Moore, Spectrochimica Acta Part A: Molecular Spectroscopy 51 (1995) 2039.
- [28] J.-H. Yin, S.-Q. Gao, Z.-W. Li, Y.-N. Yu, G.-H. Lu, Y.-J. Tian, Journal of Raman Spectroscopy 35 (2004) 1042.
- [29] P.T. Araujo, A. Jorio, Phys. Stat. Sol. 245/10 (2008) 2201.
- [30] A. Jorio, R. Saito, J.H. Hafner, C.M. Lieber, M. Hunter, T. McClure, G. Dresselhaus, M.S. Dresselhaus, Physical Review Letters 86/6 (2001) 1118.
- [31] P.W. C. Silvara-Batista, J.E. Butler, and K.J. Ziegler, J. Am. Chem. Soc. 131 /35 (2009) 12721–12728.
- [32] R.K.W. W.-C. Chen, and K.J. Ziegler, ACS Appl. Mater. Interface 1/8 (2009) 1821.
- [33] A.M. Rao, J. Chen, E. Richter, U. Schlecht, P.C. Eklund, R.C. Haddon, U.D. Venkateswaran, Y.K. Kwon, D. Tom?ek, Physical Review Letters 86/17 (2001) 3895.
- [34] M.M. Mitambo, G.R. Loppnow, Chemical Physics Letters 261 (1996) 691.
- [35] S. Jeon, J. Woo, J.-B. Kyong, J. Choo, Bull. Korean Chem. Soc. 22/11 (2001) 1264.
- [36] A. Palm, J. Phys. Chem. 55/8 (1951) 1320.

- [37] B. Chu, G. Fytas, G. Zalczer, *Macromolecules* 14 (1981) 395.
- [38] M. Lee, J.-P. Lee, H. Rhee, J. Choo, Y.G. Chai, E.K. Lee, *Journal of Raman Spectroscopy* 34 (2003) 737.
- [39] O.K. Kim, W.G. Spitzer, *Journal of Applied Physics* 50/6 (1979) 4362.
- [40] C. Wetzel, W. Walukiewicz, E.E. Haller, J. Ager, I. Grzegory, S. Porowski, T. Suski, *Physical Review B* 53/3 (1996) 1322.
- [41] H.y. Kim, J. Ahn, J. Kim, *Journal of Ceramic Processing Research* 9/1 (2008) 10.
- [42] J.B. Cui, K. Amtmann, J. Ristein, L. Ley, *Journal of Applied Physics* 83/12 (1998) 7929.
- [43] J. Kim, J.J.A. Freitas, J. Mittereder, R. Fitch, B.S. Kang, S.J. Pearton, F. Ren, *Solid-State Electronics* 50/3 (2006) 408.
- [44] S. Roy, P. Guha, S.N. Kunda, H. Hanzawa, S. Chaudhuri, A.K. Pal, *Materials chemistry and physics* 73 (2002) 24.
- [45] S. Shirakata, Y. Kannaka, H. Hasegawa, T. Kariya, S. Isomura, *Jpn. J. Appl. Phys.* 38 (1999) 4997.
- [46] J.H. Ely, T.R. Ohno, T.E. Furtak, A.J. Nelson, *Thin Solid Films* 371 (2000) 36.
- [47] C. Rincon, F.J. Ramirez, *J. Appl. Phys* 72/9 (1992) 4321.
- [48] O. Ramdani, J.F. Guillemoles, D. Lincot, P.P. Grand, E. Chassaing, O. Kerrec, E. Rzepka, *Thin Solid Films* 515 (2007) 5909.
- [49] S. Shirakata, H. Kubo, C. Hamaguchi, S. Isomura, *Jpn. J. Appl. Phys.* 36 (1997) 1394.
- [50] W. Witte, R. Kniese, M. Powalla, *Thin Solid Films* 517 (2008) 867.
- [51] J. Weszka, P. Daniel, A. Burian, A.M. Burian, A.T. Nguyen, *Journal of Non-Crystalline Solids* 265 (2000) 98.
- [52] F. Lin, G.-Q. Bian, Z.-X. Lei, Z.-J. Lu, J. Dai, *Solid State Sciences* 11 (2009) 972.
- [53] M. Ramsteiner, J. Wagner, P. Koidl, *Applied Physics Letters* 59/27 (1991) 3616.
- [54] D.E. Aspnes, S.M. Kelso, R.A. Logan, R. Bhat, *J. Appl. Phys* 60/2 (1986) 754.
- [55] C. Asawaroengchai, G.M. Rosenblatt, *J. Chem. Phys.* 72/4 (1980) 2664.
- [56] M. Hizushima, *The Theory of Rotating Diatomic molecules*, Wiley, New York, 1975.

- [57] D.E. Aspnes, A.A. Studna, Physical Review B 27/2 (1983) 985.
- [58] K. Senthil, D. Mangalaraj, S.K. Narayandass, R. Kesavamoorthy, G.L.N. Reddy, Nuclear Instruments and Methods in Physics Research Section B: Beam Interactions with Materials and Atoms 173/4 (2001) 475.
- [59] H. JobinYvon, in:  
[http://www.horiba.com/fileadmin/uploads/Scientific/Documents/Raman/Semiconductors\\_01.pdf](http://www.horiba.com/fileadmin/uploads/Scientific/Documents/Raman/Semiconductors_01.pdf) (Ed.), Horiba JobinYvon.
- [60] M. Holtz, W.M. Duncan, S. Zollner, R. Liu, Journal of Applied Physics 88/5 (2000) 2523.
- [61] H. Harima, Microelectronic Engineering 83/1 (2006) 126.
- [62] C.J. Cramer, Essentials of Computational Chemistry Theories and Models, John Wiley & Sons, Chichester, England, 2006.
- [63] D.R. Burgess, M.R. Zachariah, W. Tsang, P.R. Westmoreland, Progress in Energy and Combustion Science 21/6 (1995) 453.
- [64] M.D. Allendorf, C.F. Melius, P. Ho, M.R. Zachariah, The Journal of Physical Chemistry 99/41 (1995) 15285.
- [65] P. Ho, C.F. Melius, The Journal of Physical Chemistry 99/7 (1995) 2166.
- [66] P. Ho, M.E. Colvin, C.F. Melius, The Journal of Physical Chemistry A 101/49 (1997) 9470.
- [67] H. Simka, B.G. Willis, I. Lengyel, K.F. Jensen, Prog. Crystal Growth and Charact. 35 (1998) 117.
- [68] I.N. Levine, Quantum Chemistry, Prentice Hall, Upper Saddle River, NY, 2006.
- [69] D.K. Malick, G.A. Petersson, J. John A. Montgomery, Journal of Chemical Physics 108/14 (1998) 5704.
- [70] M.J.S. Dewar, E.F. Healy, J.J.P. Stewart, J. Chem. Soc., Faraday Trans. 2 80 (1984) 227.
- [71] N.W. Mitzel, C. Lustig, R.J.F. Berger, N. Runeberg, Angewandte Chemie International Edition 41/14 (2002) 2519.
- [72] D.A. McQuarrie, Statistical Mechanics, University Science Books, Sausalito, CA, 2000.

- [73] M.J. Frisch, G.W. Trucks, H.B. Schlegel, G.E. Scuseria, M.A. Robb, J.R. Cheeseman, J.J.A. Montgomery, T. Vreven, K.N. Kudin, J.C. Burant, J.M. Millam, S.S. Iyengar, J. Tomasi, V. Barone, B. Mennucci, M. Cossi, G. Scalmani, N. Rega, G.A. Petersson, H. Nakatsuji, M. Hada, M. Ehara, K. Toyota, R. Fukuda, J. Hasegawa, M. Ishida, T. Nakajima, Y. Honda, O. Kitao, H. Nakai, M. Klene, X. Li, J.E. Knox, H.P. Hratchian, J.B. Cross, V. Bakken, C. Adamo, J. Jaramillo, R. Gomperts, R.E. Stratmann, O. Yazyev, A.J. Austin, R. Cammi, C. Pomelli, J.W. Ochterski, P.Y. Ayala, K. Morokuma, G.A. Voth, P. Salvador, J.J. Dannenberg, V.G. Zakrzewski, S. Dapprich, A.D. Daniels, M.C. Strain, O. Farkas, D.K. Malick, A.D. Rabuck, K. Raghavachari, J.B. Foresman, J.V. Ortiz, Q. Cui, A.G. Baboul, S. Clifford, J. Cioslowski, B.B. Stefanov, G. Liu, A. Liashenko, P. Piskorz, I. Komaromi, R.L. Martin, D.J. Fox, T. Keith, M.A. Al-Laham, C.Y. Peng, A. Nanayakkara, M. Challacombe, P.M.W. Gill, B. Johnson, W. Chen, M.W. Wong, C. Gonzalez, J.A. Pople, 2004.
- [74] M. Tsuda, S. Oikawa, M. Morishita, M. Mashita, Japanese Journal of Applied Physics 26/5 (1987) L564.
- [75] V.A. Yablokov, N.V. Yablokova, Russian Chemical Reviews 64/10 (1995) 953.
- [76] A.H. McDaniel, M.D. Allendorf, Chemistry of Materials 12/2 (2000) 450.
- [77] G. Keresztury, S. Holly, G. Besenyei, J. Varga, A. Wang, J.R. Durig, Spectrochimica Acta Part A: Molecular Spectroscopy 49/13-14 (1992) 2007.
- [78] D. Michalska, R. Wysokinski, Chemical Physics Letters 403 (2005) 211.
- [79] H.B. Schlegel, Geometry Optimization 1, Wiley, Chichester, 1998.
- [80] J. Ouazzani, K.-C. Chiu, F. Rosenberger, Journal of Crystal Growth 91/4 (1988) 497.
- [81] M.E. Coltrin, R.J. Kee, J.A. Miller, J. Electrochem. Soc. 133/6 (1986) 1206.
- [82] K.F. Jensen, Journal of Crystal Growth 98/1-2 (1989) 148.
- [83] D.I. Fotiadis, M. Boekholt, K.F. Jensen, W. Richter, Journal of Crystal Growth 100/3 (1990) 577.
- [84] W.L. Holstein, Prog. Crystal Growth and Charact. 24 (1992) 111.
- [85] R.B. Bird, W.E. Stewart, E.N. Lightfoot, Transport phenomena, John Wiley & Sons, New York, 2001.
- [86] W.M. Deen, Analysis of Transport Phenomena, Oxford University Press, New York, 1998.
- [87] J.L. Plawsky, Transport phenomena fundamentals, Marcel Dekker, Inc., New York, 2001.

- [88] H.A. Jakobsen, Elementary Kinetic Theory of Gases, Springer, Berlin, 2008.
- [89] P.D. Neufeld, A.R. Janzen, R.A. Aziz, The Journal of Chemical Physics 57/3 (1972) 1100.
- [90] A. Eucken, Physik. Z. 14 (1913) 324.
- [91] J.Y. Hwang, C. Park, M. Huang, T. Anderson, Journal of Crystal Growth 279/521-530 (2005).
- [92] T.-Y. Park, G.F. Froment, Industrial & Engineering Chemistry Research 40/20 (2001) 4187.
- [93] R. Span, E.W. Lemmon, R.T. Jacobsen, W. Wagner, A. Yokozeki, Journal of Physical and Chemical Reference Data 29/6 (2000) 1361.
- [94] J. Smukala, R. Span, W. Wagner, Journal of Physical and Chemical Reference Data 29/5 (2000) 1053.
- [95] H. Miyamoto, K. Watanabe, International Journal of Thermophysics 22/2 (2001) 459.
- [96] M.S. Tomar, R. Rutherford, C. New, K.A. Kuenhold, Solar Energy Material & Solar Cells 63 (2000) 437.
- [97] C.A. Wang, Journal of Crystal Growth 272 (2004) 664.
- [98] A.A. Aquino, T.S. Jones, Applied Surface Science 104/105 (1996) 304.
- [99] R. Lin, T.R. Gow, A.L. Backman, L.A. Cadwell, F. Lee, R.I. Masel, Journal of Vacuum Science and Technology B 7/4 (1989) 725.
- [100] D.K. Russell, G.P. Mills, J.B. Raynor, A.D. Workman, Chemical Vapor Deposition 4/4 (1998) 61.
- [101] A.S. Grady, R.E. Linney, R.D. Markwell, D.K. Russell, Journal of Material Chemistry 3/5 (1993) 483.
- [102] Y.S. Kim, Y.S. Won, H. Hagelin-Weaver, N. Omenetto, T.J. Anderson, Journal of Physical Chemistry A 112/4246-4253 (2008).
- [103] R.S. Hickman, L.H. Liang, The Review of scientific instruments 43/5 (1972).
- [104] R.W. Dibble, S.H. Starner, A.R. Masri, R.S. Barlow, Applied Physics B: Photophysics and Laser Chemistry B51 (1990) 39.
- [105] E.J. Burlbaw, R.L. Armstrong, Applied Optics 22 (1983) 2860.

- [106] J.D. Lorentzen, S. Guha, J. Menendez, P. Giannozzi, S. Baroni, Chemical Physics Letters 270 (1997) 129.
- [107] S.D. Williams, T.J. Johnson, T.P. Gibbons, C.L. Kitchens, Theoretical Chemical Accounts 117 (2006) 283.
- [108] R. Boese, D. Bläser, N. Niederprüm, M. Nüsse, W.A. Brett, P.v.R. Schleyer, M. Bühl, N.J.R.v.E. Hommes, Angewandte Chemie International Edition in English 31/3 (1992).
- [109] Y.S. Kim, Ph. D. Thesis, University of Florida (2007).
- [110] C.H. Park, J.Y. Hwang, M. Huang, T.J. Anderson, Thin Solid Films 409 (2002) 88.
- [111] C. Park, W. Jung, Z. Huang, T.J. Anderson, Journal of Materials Chemistry 12 (2002) 356.
- [112] M. Huang, PhD, Chemical Engineering, University of Florida, Gainesville, FL, 2003.
- [113] J.Y. Hwang, Ph. D. Thesis, University of Florida (2004).
- [114] J.N. Kidder, Jr. , H.K. Yun, J. J.W. Rogers, T.P. Pearsall, Chem. Mater. 10 (1998) 777.
- [115] B. Abdallah, C. Duquenne, M.P. Besland, E. Gautron, P.Y. Jouan, P.Y. Tessier, J. Brault, Y. Cordier, M.A. Djouadi, The European Physical Journal Applied Physics 43 (2008) 309.
- [116] D.C. Bertolet, H. Liu, J. J.W. Rogers, J. Appl. Phys 75/10 (1994) 5385.
- [117] K.-L. Ho, K.F. Jensen, J.-W. Hwang, W.L. Gladfelter, J.F. Evans, Journal of Crystal Growth 107/1-4 (1991) 376.
- [118] W.L. Smith, T. Wartik, J. Inorg. Nucl. Chem 29 (1967) 629.
- [119] J. Lee, Y.S. Kim, T. Anderson, ECS Transactions 25/8 (2009) 41.
- [120] J.E. House, Inorganic chemistry, Academic Press, Oxford, UK, 2008.
- [121] Z. Jiang, L.V. Interrante, Chem. Mater. 2 (1990) 439.
- [122] S. Kvistle, E. Rytter, Spectrochimica Acta 40A/10 (1984) 939.
- [123] O. Yamamoto, Bulletin of the Chemical Society of Japan 35/4 (1962) 619.
- [124] M. Ikenaga, K. Nakamura, A. Tachibana, K. Matsumoto, Journal of Crystal Growth 237-239 (2002) 936.

- [125] A.Y. Timoshkin, Coordination Chemistry Reviews 249 (2005) 2094.
- [126] J.-W. Hwang, S.A. Hanson, D. Britton, J.F. Evans, K.F. Jensen, W.L. Gladfelter, Chem. Mater. 2 (1990) 342.
- [127] J.A. Jegier, S. McKernan, W.L. Gladfelter, Inorg. Chem. 38 (1999) 2726.
- [128] A.Y. Timoshkin, I. Henry F. Schaefer, Inorganic Chemistry 43 (2004) 3080.
- [129] F.C. Sauls, W.J. Hurley, L.V. Interrante, P.S. Marchetti, G.E. Maciel, Chem. Mater. 7 (1995) 1361.
- [130] A.E. Kaloyerous, X.M. Chen, T. Stark, K. Kumar, S. Seo, G.G. Peterson, H.L. Frisch, B. Arkles, J. Sullivan, J. Electrochem. Soc. 146/1 (1999) 170.
- [131] E. Kolawa, P.J. Pokela, J.S. Reid, J.S. Chen, M.A. Nicolet, Applied Surface Science 53 (1991) 373.
- [132] O.J. Bchir, K.M. Green, H.M. Ajmera, E.A. Zapp, T.J. Anderson, B.C. Brooks, L.L. Reitfort, D.H. Powell, K.A. Abboud, L. McElwee-White, J. Am. Chem. Soc. 127 (2005) 7825.
- [133] H.M. Ajmera, A.T. Heitsch, T.J. Anderson, C.B. Wilder, L.L. Reitfort, L. McElwee-White, D.P. Norton, J. Vac. Sci. Technol. B 26 (2008) 1800.
- [134] S.-H. Kim, S.S. Oh, H.-M. Kim, D.-H. Kang, K.-B. Kim, W.-M. Li, S. Haukka, M. Tuominen, J. Electrochem. Soc. 151/4 (2004) C272.
- [135] J. Koller, H.M. Ajmera, K.A. Abboud, T.J. Anderson, L. McElwee-White, Inorg. Chem. 47 (2008) 4457.
- [136] D. Kim, O.H. Kim, T.J. Anderson, J. Koller, L. McElwee-White, L.C. Leu, J.M. Tsai, D.P. Norton, J. Vac. Sci. Technol. A 27 (2009) 943.
- [137] O.J. Bchir, S.W. Johnston, A.C. Cuadra, T.J. Anderson, C.G. Ortiz, B.C. Brooks, D.H. Powell, L. McElwee-White, Journal of Crystal Growth 249 (2003) 262.
- [138] O.J. Bchir, K.M. Green, M.S. Hlad, T.J. Anderson, B.C. Brooks, C.B. Wilder, D.H. Powell, L. McElwee-White, J. Organomet. Chem. 684/1-2 (2003) 338.
- [139] J.H.S. Green, D.J. Harrison, Spectrochim. Acta, Part A 32/6 (1976) 1279.
- [140] T.G. Burova, A.A. Anashkin, Optics & Spectroscopy 102/6 (2007) 825.
- [141] S. Ishikawa, T. Ebata, N. Mikami, Journal of Chemical Physics 110/19 (1999) 9504.
- [142] H.M. Ajmera, Ph. D. Dissertation, Chemical Engineering, University of Florida, Gainesville, Fl., 2007.

- [143] J.A. Kerr, Chemical Reviews 66 (1966) 465.
- [144] C.J. Michejda, W.P. Hoss, J. Am. Chem. Soc. 92/21 (1970) 6298.
- [145] J.R. Roberts, K.U. Ingold, J. Am. Chem. Soc. 95/10 (1973) 3228.
- [146] F.O. Rice, C.J. Grelecki, J. Am. Chem. Soc. 79/11 (1957) 2679.
- [147] D. Mackay, A. Waters, J. Chem. Soc. C (1966) 813.
- [148] H. Gesser, J.T. Mullhaupt, J.E. Griffiths, J. Am. Chem. Soc. 79 (1957) 4834.
- [149] B.G. Gowenlock, K.E. Thomas, J. Chem. Soc. B (1966) 409.
- [150] S. Salim, C.K. Lim, L.F. Jensen, Chemistry of Materials 7/3 (1995) 507.
- [151] Y.G. Lazarou, P. Papagiannakopoulos, The Journal of Physical Chemistry 97 (1993) 9133.
- [152] H. Shang, C. Yu, L. Ying, X. Zhao, Chemical Physics Letters 236 (1995) 318.
- [153] J. Demuynck, D.J. Fox, Y. Yamaguchi, H.F.S. III, J. Am. Chem. Soc. 102/20 (1980) 6204.
- [154] C. Richards, C. Meredith, S.-J. Kim, G.E. Quelch, H.F. Schaefer, Journal of Chemical Physics 100/1 (1994) 481.
- [155] R.J. Lang, J. Acoust. Soc. Amer. 34/1 (1962) 6.
- [156] S.M. Frolov, F.S. Frolov, B. Basara, J. Russ. Laser Res. 27/6 (2006) 562.
- [157] J.R. Durig, M.G. Griffin, P. Groner, The Journal of Physical Chemistry 81/6 (1977) 554.
- [158] G. Socrates, Infrared and Raman Characteristic Group Frequencies: Tables and Charts, John Wiley & Sons, Inc, New York, 2004.
- [159] T.E. Glassman, M.G. Vale, R.R. Schrock, Organometallics 10/12 (1991) 4046.
- [160] D.F. McMillen, D.M. Golden, Ann. Rev. Phys. Chem. 33 (1982) 493.
- [161] G.T. Wang, C. Mui, C.B. Musgrave, S.F. Bent, The Journal of Physical Chemistry B 103/32 (1999) 6803.
- [162] M. Bhattacharya, W.G. Devi, P.S. Mazumdar, Applied Surface Science 218 (2003) 1.
- [163] P.A. Redhead, Vacuum 12 (1962) 203.

- [164] P.A. Redhead, *Transactions of the Faraday Society* 57 (1961) 641.
- [165] C.R. Brundle, J. Charles A. Evans, S. Wilson, *Encyclopedia of materials characterization : Surfaces, Interfaces, Thin Films*, Butterworth-Heinemann, Greenwich, CT, 1992.
- [166] P.W. Palmberg, R.E. DeWames, L.A. Vredevoe, *Physical Review Letters* 21/10 (1968) 682.
- [167] S. Ye, T. Ichihara, K. Uosaki, *Journal of Electrochemical Society* 148 (2001) C421.
- [168] C. Mui, J.H. Han, G.T. Wang, C.B. Musgrave, S.F. Bent, *J. Am. Chem. Soc.* 124/15 (2002) 4027.
- [169] W. Ranke, *Surface Science* 342/1-3 (1995) 281.
- [170] K. Choi, J.M. Buriak, *Langmuir* 16/20 (2000) 7737.
- [171] A. Bansal, X. Li, I. Lauermann, N.S. Lewis, S.I. Yi, W.H. Weinberg, *J. Am. Chem. Soc.* 118/30 (1996) 7225.
- [172] J. He, S.N. Patitsas, K.F. Preston, R.A. Wolkow, D.D.M. Wayner, *Chemical Physics Letters* 286/5-6 (1998) 508.
- [173] G.W. Cullen, J.A. Amick, D. Gerlich, *J. Electrochem. Soc.* 109/2 (1962) 124.
- [174] M.J. Bozack, P.A. Taylor, W.J. Choyke, J.T. Yates Jr, *Surface Science* 177/1 (1986) L933.
- [175] M.A. Filler, C.B. Musgrave, S.F. Bent, *The Journal of Physical Chemistry C* 111/4 (2007) 1739.
- [176] R. Konecny, D.J. Doren, *J. Am. Chem. Soc.* 119/45 (1997) 11098.
- [177] M.J. Kelly, J.H. Han, C.B. Musgrave, G.N. Parsons, *Chemistry of Materials* 17/21 (2005) 5305.
- [178] M.R. Kosuri, H. Gerung, Q. Li, S.M. Han, B.C. Bunker, T.M. Mayer, *Langmuir* 19/22 (2003) 9315.
- [179] A. Kim, M.A. Filler, S. Kim, S.F. Bent, *J. Am. Chem. Soc.* 127/16 (2005) 6123.
- [180] Y.S. Cho, S.-I. Cho, J.S. Heo, J.C. Kim, S.H. Moon, *J. Electrochem. Soc.* 153/3 (2006) C195.
- [181] A.R. Hind, S.K. Bhargava, A. McKinnon, *Advances in Colloid and Interface Science* 93/1-3 (2001) 91.

[182] I. PerkinElmer, in:

[http://las.perkinelmer.com/content/TechnicalInfo/TCH\\_FTIRATR.pdf](http://las.perkinelmer.com/content/TechnicalInfo/TCH_FTIRATR.pdf) (Ed.), PDF, PerkinElmer Life and Analytical Sciences, 2005.

[183] J.M. Buriak, Chemical Reviews 102/5 (2002) 1271.

[184] G.S. Higashi, Y.J. Chabal, G.W. Trucks, K. Raghavachari, Applied Physics Letters 56/7 (1990) 656.

## BIOGRAPHICAL SKETCH

Jooyoung Lee was born in 1976 in Seoul, Korea. He entered Seoul National University in March 1995 and received his Bachelor of Science degree in chemical engineering in February 1999. After the Bachelor of Science degree, he started mandatory military service as a tactical driver in Yangyang-si, Kangwon-do. When he finished 26 months of service, he got married to Hankyung Seong in 2002 and he started graduate school in Seoul National University for process optimization and safety and received his Master of Science degree in chemical engineering in August, 2005. Then Jooyoung Lee decided to pursue his Ph.D. degree in the University of Florida. He started his Ph.D. program in August 2006 at the University of Florida and joined the electronic materials processing group to work with Dr. Tim Anderson and he devoted himself to chemical vapor deposition kinetics research for semiconductor processing.